Integrated Battery Charging and Powertrain Schemes for All-Wheel Drive Electric Vehicles

A thesis submitted

in partial fulfillment for the award of the degree of

Doctor of Philosophy

by

Vidya V

Department of Avionics

Indian Institute of Space Science and Technology

Thiruvananthapuram - 695547, India

January 2024

Certificate

This is to certify that the thesis titled ***Integrated Battery Charging and Powertrain Schemes for All-Wheel Drive Electric Vehicles*** submitted by **Vidya V**, to the Indian Institute of Space Science and Technology, Thiruvananthapuram, in partial fulfillment for the award of the degree of **Doctor of Philosophy** is a bona fide record of the original work carried out by him/her under my supervision. The contents of this thesis, in full or in parts, have not been submitted to any other Institute or University for the award of any degree or diploma.

Dr. R Sudharshan Kaarthik
Associate Professor
IIST

Dr. N. Selvaganesan
Professor and Head
IIST

Place: Thiruvananthapuram
Date: January 2024

Declaration

I declare that this thesis titled ***Integrated Battery Charging and Powertrain Schemes for All-Wheel Drive Electric Vehicles*** submitted in partial fulfillment for the award of the degree of **Doctor of Philosophy** is a record of the original work carried out by me under the supervision of **Dr. R Sudharshan Kaarthik**, and has not formed the basis for the award of any degree, diploma, associateship, fellowship, or other titles in this or any other Institution or University of higher learning. In keeping with the ethical practice in reporting scientific information, due acknowledgments have been made wherever the findings of others have been cited.

Place: Thiruvananthapuram
Date: January 2024

Vidya V
(SC18D027)

To my family, my teachers C K V Kurup sir and K S Sureshkumar sir ...

Acknowledgements

Firstly, I would like to express my deepest gratitude to my research advisor Dr. R Sudharshan Kaarthik for guiding me to the completion of the thesis. I am sincerely thankful for having the opportunity to work under his supervision. His course works on DC drives, PEPS, and lab experiments had significantly helped me in building the much needed base for my research works. The constant discussions with him, his insights and intuition has immensely influenced me in tackling the research problems, in the fruitful completion of this thesis and definitely in my future research works. His enthusiasm, passion, and dedication in the field of research, will always remain a motivation for me. I am also indebted for his patience and support during my personal struggles. It was demanding, but pleasant and satisfying experience to work with him.

I would sincerely thank Dr. Rajeevan P. P for his thoughtful comments and informative classes on AC drives, which has especially helped me in my research. I also wish to thank my DC committee members at IIST, Dr. Anindya Das Gupta, Dr. Anoop C, Dr. Natarajan, Dr. Manoj B S, Dr.Deepak Mishra for their insightful comments that helped me in shaping my research work. I also thank my teachers at IIST Dr. Harsha Simha, Dr. Kaushik Mukherjee, Dr. C V Anil Kumar for their informative classes on control system and mathematics.

I am happy to work in the wonderful Power Electronics and Drives Lab at IIST and like to thank Mrs. Dhanya and Mrs. Archana for their wholehearted technical and emotional support.

This would not have been a pleasant journey without the help of my lab mates, Gopika, Ranjith, Gourahari, Prasoon, Harihrishna, Pragya, Srikara, Sivakrishna, Sahal, Sai Pavan, Balwant, Mohit, Aiswarya, Sai Ram, Sreya and my friends Roshan, Anjana and Naufal. I would also like to thank all other teaching and non-teaching staffs for their direct and indirect support.

My research would not have been possible without the complete support, encouragement, love and concern of my parents, my husband and my kids. I am deeply grateful to them for their unconditional support and being my constant motivation. I am thankful to my brother, Mr. Vineeth for his emotional support and encouragement. I am also thankful to my in-laws and relatives for their moral support.

I would also like to thank all my neighbors at Nedumangad for their help and support throughout these years, especially, Mrs. Sophia, Mrs. Sheeba, Mr. Madhu, and Mrs. Saraswati.

Also, I would also like to appreciate the guidance and loving concern given to me by my mentor at Amrita Vishwa Vidyalaya Dr. T.N.P Nambiar sir and my m.tech guide at NIT Calicut, Mr. K S Suresh Kumar sir throughout these years which has always remained a strong emotional support for me.

Finally I would like to thank God, for providing me good oppurtunity, health, and people around me to complete my work in a pleasant and successful manner.

Vidya V

Abstract

In recent decades, advancements in battery technology, huge investments in electric vehicle deployment, environmental concerns, and supportive policies by governments have spurred interest in Electric Vehicles (EVs). Two and three-wheeler EVs dominate the market in developing countries like India, Thailand, and Indonesia, while, Battery Electric Vehicles (BEVs), mostly electric-Sports Utility Vehicles (e-SUVs), which are all-wheel drive vehicles (vehicles that use motors for both axles), are popular in developed countries like the US and Europe. Different types of EVs are present on Indian roads, including electric cars such as Tata Nexon EV, Tata Tiago EV, MG ZS EV, Mahindra XUV 400 EV, electric scooters such as Ather 450X, Bajaj Chetak Electric, e-rickshaws like Mahindra Treo, Piaggio Ape E-City, and several electric buses.

With improvements in electric powertrain technology, the performance of electric cars has surpassed the capability of conventional Internal Combustion Engine (ICE) cars. However, the cost of EVs and the life cycle of batteries are issues that may be solved shortly as intense research is focused on improving battery technology, which includes the development of high-power density batteries with lower cost and extended battery life cycle.

For an EV user, the main concerns are the range anxiety and the time required to charge the battery. Presently there are two types of chargers, namely onboard AC chargers which are available up to 22 kW of power capability, and DC fast chargers with high power capability, but are available only at sparsely located charging stations. Thus there is a need for a fast onboard charger that enables charging at any location or can potentially reduce the installation cost of high-power charging stations.

In this thesis, a new Integrated (onboard) Battery Charger (IBC) capable of high power level-3 charging is proposed. Furthermore, the proposed IBC scheme is extended for All-Wheel Drive (AWD) EVs, by simultaneously utilizing both the powertrains, one on the rear-wheel axle and the other on the front-wheel axle, as a part of the integrated charger, resulting in higher power conversion capability of the system. Lastly, a driving scheme for a single-motor electric powertrain for AWD vehicles is proposed using dodecagonal, octadecagonal, and 24-sided polygonal space vector structures for

all-wheel drive EVs with the advantage of better DC bus utilization with reduced voltage harmonics.

Integrated Battery Charger Using a Split Phase Machine

An integrated battery charger is developed for EVs by re-utilizing the existing powertrain components of the vehicle. This fast on-board charger can be implemented by reconfiguring the existing three-phase machine in the EV as a split-phase machine. Moreover, the existing three-legged inverter serves a dual purpose, catering to both driving and charging modes requiring minimal additional components. During driving the inverter drives the three-phase machine, while in charging mode, the inverter functions as a grid-connected front-end converter, drawing grid currents at unity power factor. The reconfigured split-phase machine windings are connected between the grid and the inverter in such a way that it would not develop any electromagnetic torque inside the machine while charging the battery. Thus an integrated on-board charger with high power capability is developed using the existing hardware inside the vehicle. However, the utilization of asymmetrical windings of the reconfigured split-phase machine as the grid-interface inductance leads to the creation of unbalanced grid currents due to the asymmetry in the grid interface inductance and pulsating magnetic flux inside the machine. A comprehensive mathematical model has been formulated, and a novel control architecture has been implemented to address this issue. These advancements effectively mitigate the current unbalance, ensuring compliance with the IEEE-519, and IEEE-1547 standards. Furthermore, this IBC is applicable for vehicle-to-grid scenarios due to its bidirectional power handling capability. Simulation and experimental results are included to verify the proposed topology.

Parallel Operation of IBCs using Split Phase Machines for All-Wheel Drive EVs

All-Wheel Drive EVs have two powertrains, one in the front-axle and the other in the rear-axle for improved drive performance. An IBC of high power capability can be developed by using the two powertrains simultaneously, in parallel operation for charging the battery. The two existing three-phase motors can be reconfigured as

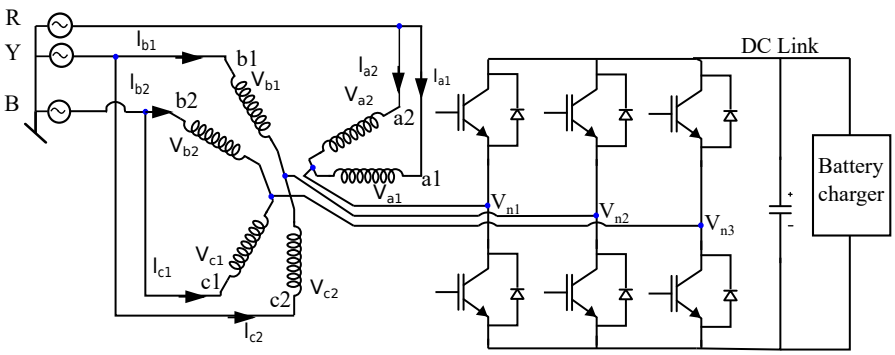

Fig. 1. Schematic of the proposed IBC using a split-phase machine.

split-phase machines. Also in this work, a new winding arrangement for the two split-phase machine windings is proposed for the parallel combination, such that the current in each of the individual IBCs will be unbalanced, but the grid current which is the sum of the two IBC currents will be balanced naturally without any additional control effort. The mathematical proof for the cancellation of unbalance with the proposed winding configuration is included in this thesis.

Also, it is found through mathematical derivation, that there is a flow of zero sequence circulating current through the two inverters, due to the difference in inductance value in each phase of IBC-1 compared to the same phase in IBC-2 leading to a difference in pole voltage of each phase of inverter-1 of IBC-1 and inverter-2 of IBC-2. This low-frequency circulating current is limited by introducing a zero-sequence current controller.

Furthermore, the proposed IBC configuration showcases bidirectional functionality, thereby allowing for its application in vehicle-to-grid scenarios.

Simulation and experimental results are included to verify the proposed concepts.

An Advanced Modulation and Driving Scheme for All-Wheel Drive EVs

In an AWD EV, even though it has two powertrains, predominantly for normal running conditions, only one primary drivetrains will be energized, and the secondary drive is mostly turned off. Both the drivetrains are used only when there is a need for extra torque, like while driving on a slippery road or through muddy terrain. In this thesis, a new driving scheme during normal running conditions is proposed, where in the

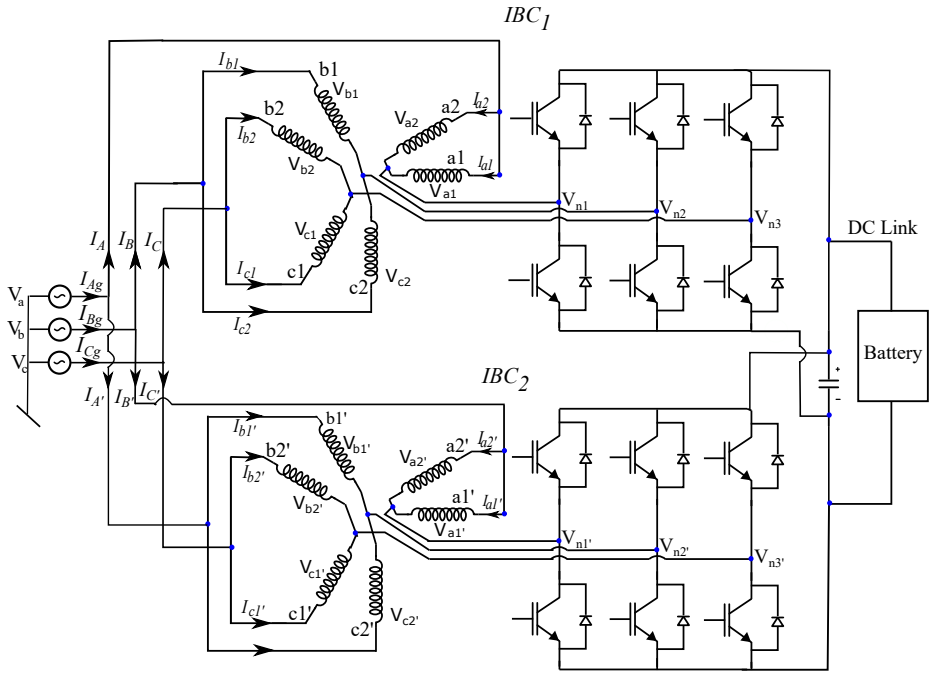

Fig. 2. Proposed configuration of parallel IBCs for AWD vehicles; (R-Y-B and Y-R-B phase sequences for IBC1 and IBC2 respectively are shown.)

primary motor is driven as an open-end wound machine by utilizing the inverters of both the powertrains. This reconfiguration helps in implementing multi-sided space vector schemes like dodecagonal, octa-dodecagonal, and 24-sided polygonal space vector schemes, with the same hardware resulting in better utilization of the battery voltage with reduced harmonics.

Also in this topology, the secondary inverter acts as a switched capacitor without any DC source. The voltage across the capacitor can be maintained constant without needing any closed-loop voltage control. For each multi-sided space vector scheme, there is a different magnitude of stable capacitor voltage, where the capacitor will go and settle naturally using the switching scheme presented in this thesis. The mathematical analysis for the stability of the capacitor voltage is derived in detail for the different multi-sided space vector schemes in this thesis.

Furthermore, a switching scheme is implemented to linearize the inverter gain between the input voltage and the fundamental component of output voltage in the over-modulation region. This is important when operating at higher speeds, as the main advantage of a multi-sided space vector scheme is the reduction in voltage harmonics when operating in the extreme modulation region. The mathematical expressions for the different regions in each of the multi-sided space vector schemes

are included in the thesis. Simulation and experimental results are included to verify the proposed concepts.

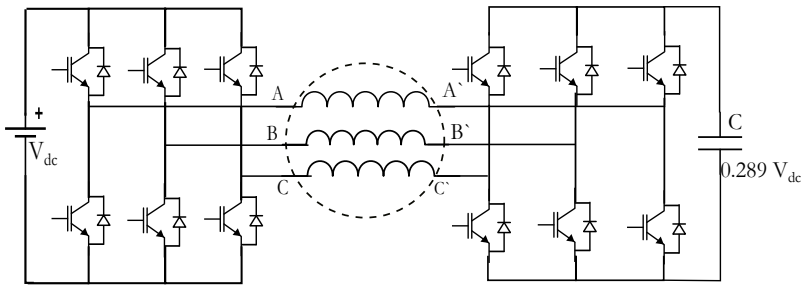

Fig. 3. Schematic for dodecagonal space vector scheme using one DC source.

Summary and Critical Overview of the thesis

A new and fast integrated battery charging scheme is developed for EVs with the existing three-phase machine and three-legged powertrain inverter. The proposed scheme is the only scheme reported that can reuse the three-phase inverter in the vehicle. All other reported works require five or six-legged inverter to operate as IBC using the multiphase machine. Currents are drawn from the grid at a unity power factor with lower THD (within the IEEE-519 standards). The proposed scheme can be used to charge the EV from any place where AC power is available and is limited to the power capability of the Electric Vehicle Supply Equipment (EVSE) and the maximum power of the inverter. Furthermore, the power rating of the IBC can be up to twice the power rating of the motor in the vehicle. As the proposed IBC scheme is bidirectional, the system can also be used for vehicle-to-grid applications. Further research can be done for implementing this topology using permanent magnet synchronous machines as it has become a popular motor in EVs.

The concept of IBC is then introduced for AWD EVs. A high-power integrated charging scheme is proposed for All-Wheel Drive EVs, using the two motor drives inside the vehicle. This charging scheme can also be implemented for heavy-duty electric trucks, which are always on the run, and it helps users to charge the battery from any location where the AC supply is available. Furthermore, by implementing the proposed parallel IBC winding configurations, the distortions in the grid currents can be inherently reduced without using any additional control effort. This scheme can also be used for vehicle-to-grid applications because of its bidirectional nature. In

cases where front axle and rear axle powers are different, unbalance in the current is mitigated as opposed to complete elimination.

Furthermore, a driving scheme with better inverter DC voltage utilization for AWD EVs is proposed by engaging the two inverters (present on both the front axle and rear axle) inside the vehicle. The motor (front/ rear axle) is run as an open-end winding motor along with the two inverters inside the vehicle. Three space vector modulation schemes, namely the 12, 18, and 24-sided polygonal space vector structures, are implemented using the same hardware, that is, the open-end winding motor with the two two-level inverters. The main advantage is the reduction in voltage harmonics in the phase voltages of the motor, resulting in reduced torque pulsations.

This scheme is implemented using a single DC source, with the second inverter fed by a DC link capacitor (operating as a switched capacitive filter). A switching scheme is implemented, where the capacitor voltage is regulated naturally without any closed-loop control. Furthermore, linearization of the overmodulation region is developed to utilize the existing battery voltage to its maximum limit effectively.

This work aims to solve a few significant problems that impede EV adoption. An IBC to enable high-power (level-3) charging wherever AC power is available is attempted. This charging method will also effectively reduce the capital cost of EV charging facilities as powertrain equipment is reused as the AC-DC converter. A decrease in capital cost will increase the number of charging stations. The proposed scheme is adaptable to be used for AWD vehicles. As e-SUVs typically have larger batteries, high power capabilities of e-SUV powertrains as parallel IBCs should be exploited for the benefit of fast charging. Lastly, by using the dual inverter topology for the open-end wound motor, the efficiency of the powertrain can be improved. In summary, this thesis proposes methods to use existing power electronic hardware in an EV for charging and driving motors more efficiently. As the cost of adopting these schemes is relatively minimal, the proposed schemes are a viable alternative to traditional charging and driving methods. The proposed methods are validated through simulations and exhaustive experimental results.

Contents

List of Figures

List of Tables

Chapter 1

Introduction

The automobile industry is undergoing a transformative shift from traditional internal combustion engine (ICE) vehicles to more sustainable Electric Vehicles (EVs). The advancements in battery technology, environmental concerns, and supportive government policies have spurred interest in electric vehicles. Major auto manufacturers around the world are heavily investing in electric vehicle deployment and introducing a variety of EV models for different preferences and budgets. Moreover, the expansion of charging infrastructure has also assured EV users to charge the vehicle, thus increasing the appeal for EV mobility. A market analysis of the EV industry worldwide, particularly in India, is given in the following sections.

1.1 Global Electric Vehicle Market: A Comprehensive Analysis

The global EV market has witnessed substantial growth and transformation in recent years. The global EV market had a sale of 8.151 million units in 2022. It is expected to reach around 40 million units by 2030 [1]. The various government policies, subsidies, and tax rebates have forced the automobile companies to manufacture diverse models of electric vehicles. China is the front runner in global electric car sales [2]. More than half of the electric cars on roads worldwide are now in China. Europe is the second largest market, which saw a 15% increase in electric car sales in 2022. The United States is the third largest market of electric vehicles.

Electric car sales which were generally low outside major markets saw a rise in sales in 2022 in India, Thailand, and Indonesia. Battery Electric Vehicles (BEVs), mainly for Sports Utility Vehicles (SUVs) and large cars dominate the EV market in

China, Europe, and mostly in the United States. In developing economies two and three-wheelers EV sales outnumber the sales of cars. In India 50 % of three-wheelers sold in 2022 were electric.

There is a growth in electric light commercial vehicles which mainly include public transport buses. Also, there is an intense research focus on electrifying heavy-duty vehicles. These include Tesla Semi [3] powered by three motors and Volvo VNR electric [4].

New alternatives for Lithium-ion batteries are also on the rise, for example sodium-ion batteries. China is the main supplier of battery minerals worldwide.

1.2 Electric Vehicle Market in India

The Indian electric vehicle market size was USD 3.21 billion in 2022 and is projected to grow to USD 113.99 billion by 2029 at a Compound Annual Growth Rate (CAGR) of 66.52% in the forecast period, 2022-2029 [5]. Indian EV market shows strong growth due to favorable government policies like the Faster Adoption and Manufacturing of Electric Vehicles (FAME) scheme, GST benefits, foreign direct investment, etc. Uttar Pradesh (UP) held the maximum share in EV sales in India in 2021, followed by Karnataka and Tamilnadu. There is a rising trend in micro-mobility vehicles like two-wheelers and three-wheelers in the Indian EV market. UP leads in the three-wheeler segment, while others on two-wheeler and four-wheeler segments. The Battery Electric Vehicles (BEVs) had the peak demand in the four-wheeler segment with the TATA motors two models, Nexon and Tigor having the highest sales in India in 2022.

The different types of Electric Vehicles that are present on Indian roads include electric cars like the Tata Nexon EV, Tata Tiago EV, Mahindra XUV 400 EV, Hyundai Kona Electric, MG ZS EV, and Mahindra eVerito, electric scooters like the Ather 450X, Bajaj Chetak Electric, TVS iQube, Hero Electric Optima, electric auto rickshaws also called e-rickshaws like Mahindra Treo, Ape E-City, Kinetic Safar, etc and electric buses.

1.3 All-Wheel Drive EVs in India

Apart from these, electric-Sports Utility Vehicles (e-SUVs) which are mainly all-wheel drive vehicles are also popular in the 4-wheeler EV market due to their enhanced driving performances. They have two powertrains, one for the front axle and the other

Fig. 1.1. Volkswagen ID.4 All Wheel Drive car with two motor drives [6].

for the rear axle which helps in providing extra traction when required, to all the wheels of the vehicle. Fig 1.1 shows an all-wheel drive car by Volkswagen, wherein the two motor drives, one on the rear axle and the other on the front axle are visible.

A list of AWD EVs by different car manufacturers that are popular in the Indian market is given in Table. 1.1 and is described below.

- *Audi e-tron*: The German car maker had sale of 4,187 units (EVs and ICE vehicles) in 2022. The e-Tron series was the first all-wheel drive EV car introduced in India by Audi. It uses two different motors on both axles. A Permanent magnet synchronous motor on the rear-axle (RM) which is constantly engaged under all working conditions and an asynchronous motor on the front-axle (FM) which is powered when there is a need for higher torque [7]. Audi has also launched a three-motor all-wheel drive model, the Audi e-tron S sports back in the US where two motors are on the rear axle and one motor is on the front axle [8]. The twin rear wheel motor actively distributes torque to each wheel.

- *BMW iX , BMW i7*: BMW had a sale of 347 units of EVs in 2022. BMW iX, an all-wheel drive luxury SUV had a huge success in its sales in India. This German car also utilized two motors, both of which were Permanent Magnet Synchronous Motors (PMSMs).

- *Mercedes Benz EQB, EQS*: Both these models of Mercedes Benz cars are all-wheel drives. The model EQB has an asynchronous motor (AM) connected to the front-axle and PMSM connected to the rear-axle. For the model EQS both the powertrain utilizes PMSMs.

- *KIA EV6 GT-Line AWD*: KIA EV6 has an all-wheel drive option which includes two PMSMs on both the front and rear-axle.

- *Porsche Taycan Turbo S*: Porsche Taycan Turbo S uses two PMSMs of different power ratings for the front and rear axles.

- *VOLVO XC40 Recharge*: Volvo XC40 has a total powertrain capacity of 300 kW with a range of 358 kms, and uses two PMSMs for its two axles.

- *TATA Motors*: Tata Motors are planning to launch TATA harrier EV and AVINYA (showcased in auto expo 2023 [9]), which will have all-wheel drive capability using dual motors.

Table 1.1. Various All-Wheel Drive EV Models with specifications available In the Indian Market

Model	**Motors (Power, Torque)**	**Capacity**	**Performance 0 to 100 km/h**	**Battery**	**Maximum power AC Charger**	**Maximum power DC Charger**	**Range**
50 e-tron quattro [10]	PMSM 150 kW, AM 80kW	230kW 540Nm	6.8sec	76.6 kWh	22 kW	125 kW	264-379 kms (WLTP)
Audi e-tron GT [11]	PMSM and AM	390kW 630Nm	4.1sec	93.4 kWh	22 kW	270 kW	388-500 kms (WLTP)
BMW iX [12]	2 PMSMs	240kW 630Nm	6.1sec	76.6 kWh	11 kW	150 kW	372-425 kms (WLTP)
BMW i7 [13]	2 PMSMs	400kW 745Nm	4.7sec	105.6 kWh	11 kW	150 kW	590-625 kms (WLTP)
Mercedes EQB [14]	PMSM and AM	215kW 520Nm	6.2 sec	66.5 kWh	11 kW	100 kW	388-423 kms (WLTP)
Mercedes EQS [15]	2 PMSMs	560kW 1020Nm	3.4 sec	107.8 kWh	11 kW	200 kW	526-580 kms (WLTP)
KIA EV6 [16]	2 PMSMs	325kW 605Nm	5.2 sec	77.4 kWh	11 kW	350 kW	708 kms (WLTP)
Porsche Turbo S [17]	2 PMSMs	460kW 1050Nm	2.8 sec	93.4 kWh	11 kW	270 kW	482 kms (WLTP)
VOLVO XC40 [18]	2 PMSMs	300kW 670Nm	4.9 sec	78 kWh	11 kW	150 kW	358 kms (WLTP)

1.4 All-Wheel Drive EVs in Global Market

All-wheel drive EVs are quite popular in the EV market around the world especially in developed countries, due to their increased grip and traction on varying terrains, especially in ice-capped regions. Some of the globally popular AWDs, with electrical specifications, are listed in Table. 1.2 and are described below.

- *Tesla Model S P85D*: Tesla first launched the Model S in 2012 and there were many modifications from then on. The all-wheel drive version of Model S was

first introduced in 2014. This model uses a 193 kW Asynchronous AC Motor (AM) on its front axle and a 375 kW Asynchronous AC motor [19], on its rear axle.

- *Tesla Model X*: This is an AWD electric SUV using a Permanent Magnet Synchronous motor on both the front-axle and rear axle. A faster version, the Tesla model X Plaid was also launched which uses two PMSMs in the rear axle and one PMSM in the front axle. This car can accelerate from 0 to 100 kms/h in just 2.5 seconds.

- *Jaguar i pace*: Different models of this car have been launched in the market with varying specifications. In contrast to other all-wheel drive cars, it used two motors with the same power rating on the front axle and rear axle.

- *Volkswagen ID.4*: This is the first electric SUV by Volkswagen. This uses a PMSM motor for the rear axle and IM for the front axle.

Table 1.2. Various All-Wheel Drive Models with specifications in the Global Market

Model	**Motors (Power, Torque)**	**Capacity**	**Performance 0 to 100 km/h**	**Battery**	**Maximum power AC Charger**	**Maximum power DC Charger**	**Range**
Tesla Model S P85D [20], [21]	2 Asynchronous motors	671kW 657 Nm	4 sec	85 kWh	11 kW	120 kW	469 kms (EPA)
Tesla Model X [22]	2 PMSMs	500kW	3.8sec	100 kWh	11.5 kW	150 kW	548 kms (EPA)
Jaguar i Pace [23]	2 PMSMs (150kW each)	290kW 696Nm	4.8sec	90 kWh	11 kW	100 kW	470 kms (WLTP)
Volkswagen ID.4 GTX [6]	PMSM and AM	220kW 696Nm	6.2sec	77 kWh	11 kW	125 kW	484 kms (WLTP)

1.5 Electric Vehicle Charging Standards

An important feature of EVs is the duration and characteristics of charging the battery. A brief review of various types of charging levels and connectors is described in this section. Charging can happen conductively or inductively (wireless charging). In this thesis, we will be discussing different methods to charge battery via conduction.

The block diagram of a level-2 ac charging system is shown in fig 1.2. The various parts of the charging system are given below [24].

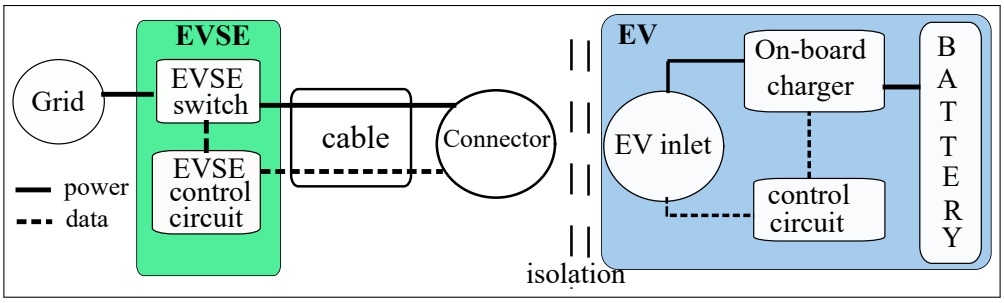

Fig. 1.2. Block diagram of various components in a level 2 AC charging system

- *Electric Vehicle Supply Equipment (EVSE):* The conductors, including the ungrounded, grounded, and equipment grounding conductors, the electric vehicle connectors, attachment plugs, and all other fittings, devices, power outlets, or apparatuses installed specifically to deliver energy from the premises wiring to the electric vehicle. Charging cords with NEMA 5-15P plugs are considered EVSEs.

- *Connector*: A conductive device that by insertion into a vehicle inlet establishes an electrical connection to the electric vehicle for the purpose of transferring energy and exchanging information.

- *Charger*: An electrical device that converts alternating current energy to regulated direct current for replenishing the energy of an energy storage device (i.e., battery) and may also provide energy for operating other vehicle electrical systems.

- *Off-Board Charger*: A charger located off of the vehicle

- *On-Board Charger*: A charger located on the vehicle

1.5.1 Various Charging Modes

There are various standards of EV charging which are defined for the different regions where they are being operated [24–27]. In North America, the SAE-J1772 standards are implemented for EV charging specifications, instead in Europe, the IEC-62196 standards are applied for charging specifications. In China, GB/T-20234 standards are applied. The North American standard, SAE-J1772, classified the charging mode mainly based on the type of supply as listed in Table. 1.3.

Table 1.3. Charging Mode Classification based on the SAE-J1772 standards [28]

Charge Method	Volts	Max Current (Amp - Continuous)	Maximum Power
AC Level 1	120 V AC	16 A	1.9 kW
AC Level 2	240 V AC	80 A	19.2 kW
DC Level 1	200 to 500 V DC maximum	80 A	40 kW
DC Level 2	200 to 500 V DC maximum	200 A	100 kW

The IEC-62196 standard classifies the charging mode into four categories as listed out in Table. 1.4.

Table 1.4. Charging Mode Classification based on the IEC-62196 standards [29]

Charge Method	Phase	Max Current	Max Voltage	Max Power
Mode 1 (Slow)	AC Single AC Three	16 A	230 - 240 V 480 V	3.8 kW 7.6 kW
Mode 2 (Semi-fast)	AC single AC Three	32 A	230 - 240 V 480 V	7.6 kW 15.3 kW
Mode 3 (Fast)	AC Three	32 - 250 A	480 V	120 kW
Mode 4 (Ultra fast)	DC	250 - 400 A	1000 V	400 kW

Guobiao Standards (GB) created the GB/T-20234 standard for charging infrastructures of electric vehicles in China and the classifications based on the type of power supply are listed in Table. 1.5.

The main drawbacks of AC charging are given below.

1. AC power needs to be converted into DC power with a power converter placed inside the car, and as with the increase in power of the charger, the size and weight of the on-board charger will increase, because of which the on-board charger circuit has a limited power rating in most EVs.

2. Due to the limited power levels, these chargers take a longer time to charge the battery, and are typically not suitable for charging in between a long journey.

The disadvantages of DC charging include

Table 1.5. Charging Mode Classification based on the GB/T standards [30]

Charging Mode	Standard	Rated Voltage	Rated Current	Maximum Power
2	GB/T-20234.2-2015	250 V AC	10 A	27.7 kW
			16 A	
			32 A	
3		440 V AC	16 A	
			32 A	
			63 A	
4	GB/T-20234.3-2015	750 V - 1000 V AC	80 A	250 kW
			125 A	
			200 A	
			250 A	

1. The initial high cost of installing high-power charging stations as well as the operation and maintenance cost.

2. Different voltage ratings and connectors for different EV manufacturers around the world.

3. The availability of charging stations, especially in remote locations.

1.5.2 Connectors

There exists a wide variety of connectors for charging EVs.

- J1772-2009 / IEC-62196 - Type 1: Type 1 is used for charging with AC supply. It has 5 pins, two AC pins to supply the power, a ground connection, a control pin to communicate with the vehicle, and proximity detection pins, which will not allow the vehicle to move while charging the battery. These connectors are also included in IEC-62196 standards as Type 1 connectors. They are mainly found in charging equipment of EVs in North America and Japan. They are used by car companies like Nissan, Chevrolet, Mitsubishi, Ford, and Toyota.

- IEC-62196 - Type 2 (Mennekkes): This connector has seven pins. Four pins for the three phases and neutral, one for ground, and two for data communication. In Europe, the Middle East, Africa, and Australia, these connectors are used to connect the EVSE to the EV.

- Continuous Charging System (CCS) combo 1 and combo 2: These are extensions of IEC-62196 Type 1 and Type 2 connectors along with two additional contacts

for DC supply for high power fast charging applications. They are compatible with Mahindra, Tata Motors, General Motors, and Volkswagen EV cars.

- IEC-62196 Type 4 / CHAdeMO: They were developed in Japan and were promoted by TEPCO (Tokyo Electric Power Company). They are mainly found in EV charging equipments in Japan but are also used in Europe and the US. The first version of these connectors had a power handling capability of 62.5 kW of power with 125 A DC current and up to 500 V DC voltage limit. The latest version of this, named as the third generation of CHAdeMO connectors (Chaoji) is expected to handle a power of up to 900 kW safely [31]. The connector can also be used for data connection using the CAN bus protocol in addition to transferring electric power. They can only used for DC supply. Hence for AC charging an additional connector is needed. Therefore, the demand for these connectors has reduced in numbers in the present market, but are still compatible with the DC charger inlet of older models of Nissan and Mitsubishi vehicles. These connectors have ten pins, two for DC supply, one for ground, and seven for data communication and control.

- GB/T 20234: This connector is mostly used in China. There is a standard connector for the AC supply and another one for the DC supply. It has a maximum power handling capability of 250 kW with up to 1000 V DC voltage limit.

- Tesla / North American Charging Standard: Tesla cars have their own connector, which is common for Level 1, Level 2, and DC fast charging applications. They can carry around 48 A of AC and 400 A of DC current and are capable of handling DC power of 250 kW.

The various connectors are shown in fig 1.3.

1.6 Charging levels and connectors used in India

In India, two-wheeler EVs and three-wheeler EVs are more popular than four-wheelers. Hence level-2 AC chargers are found in more numbers compared to DC fast charging stations.

1. Charging at home: The single phase 230 V/15 A plug can deliver power between 2 kW to 3 kW at residential houses.

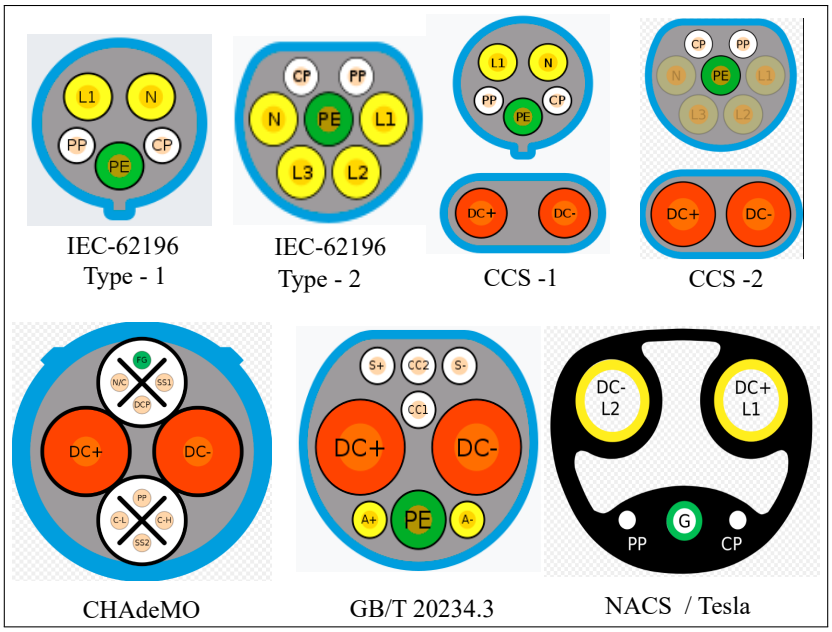

Fig. 1.3. Different connectors of EV chargers.

2. Bharat AC -001 [32]: These are public metered AC outlets that provide AC input to vehicles that have an on-board charger. They provide 3 rated output terminals of 230 V single phase voltage with a maximum current of 15 A / output and maximum power of 3.3 kW / output with IEC 60309 connector. It takes power from the three-phase grid.

3. Bharat DC-001 [32]: Each of these EVSE takes 3-phase input and provides a single DC output capable of handling a maximum power of 15 kW at 48 V /60 V /72 V. The maximum current capability is 200 A. They use the GB/T 20234.3 connector. For higher power levels, India is yet to develop its standards. However, car manufacturers in India are mostly using CCS-2 and CHAdeMo protocols that are globally popular [33].

   The electrical specifications of various chargers used in India [34] are shown in Table.1.6.

Battery Swapping: A battery Swapping station allows the replacement of a discharged battery with a fully charged battery in the EV. This system is popular in China, especially for the electric two-wheelers (Gogoro [35]). Gogoro also has 6 operational battery swapping stations in Delhi-NCR.

Sun Mobility is a prominent player in India's battery swapping industry by developing smart batteries and running battery swapping stations for two-wheelers,

Table 1.6. Electrical specification of different EV connectors used in India [34]

Charging Level	Voltage (V)	Power (kW)	Type of Vehicle	Type of connector
Level 1 (AC)	240 V	$\leq$ 3.5 kW	4w,3w,2w	Type 1 (J1772), Bharat AC-001(IEC 60309)
Level 1 (DC)	$\leq$ 48 V	$\leq$ 15 kW	4w,3w,2w	Bharat DC-001(GB/T 20234.3)
Level 2 (AC)	380-400 V	$\leq$ 22 kW	4w,3w,2w	Type 2 (Mennekes), GB/T
Level 3 (AC)	200-1000 V	$\leq$ 22-43 kW	4w	Type 2
Level 3 (DC)	200-1000 V	Up to 400 kW	4w	CCS2

three-wheelers, and e-buses. They aim to provide one million EVs by 2025 in India and save 8.5 million tons of CO_2 [36]. Battery Smart, a company funded in 2019, has completed 12 million swaps and has more than 650 live swap stations across 25 cities in India [36].

Honda Powerpack Energy India Private Ltd (HEID) in association with the Bangalore Metro Rail corporation Ltd (BMRL), has launched battery swapping service for three wheelers in India in 2022 [37].

1.7 Battery Management System

Battery Management System (BMS), is the key element in the safe, efficient and reliable utilization of batteries inside the EVs. Using its sophisticated circuit and control algorithms, it controls the operating conditions of the battery and estimates the State of Charge (SoC), State of Health (SoH) and thermal conditions of the battery. The battery cost, its lifetime, power delivery and safety are major concerns while using batteries in an EV.

The data acquisition module in the BMS, collects the battery voltage, current and temperature data at proper sampling time and the estimation algorithm module will analyze these data. With the help of a battery model, BMS predicts the SoC, SoH State of Life (SoL) of the battery. The key features of BMS are given in fig 1.4. There are various works published on Soc estimation algorithms, cell balancing and battery modeling [38–41].

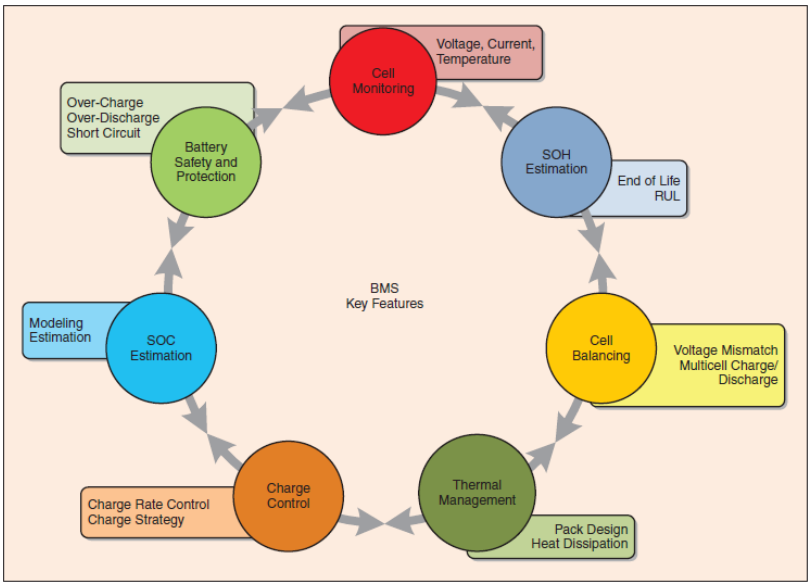

Fig. 1.4. Battery Management System-Key features where RUL represents remaining life until End of Life [38]

1.8 Key Challenges in the Electric Vehicle Market

Even with much research and development work happening in the field of EV technology, they are facing some key challenges which are as follows.

1. *Range Anxiety and Availability of Charging infrastructure:* The reliable distance that can be covered by the EV in a single charge is still a concern for EV customers, especially during long drives. Also, the availability and accessibility of public fast-charging DC stations along highways, especially in remote areas is a key challenge. Many EV manufacturers along with governments across the world are trying to overcome this concern by planning to install EVs after every specified distance.

2. *Charging Compatibility and Standards:* The use of different charging standards causes compatibility issues among different EV users. For example, Tesla Motors has a proprietary charging network that can only be used by owners of Tesla automobiles. China has its own charging standards. Similar is the case in Europe and Japan. In India, the charging station has to provide multiple connector options as the different EV requirements are different. The need for interoperability and standardized charging solutions across all EV models is crucial for a seamless charging experience.

3. *Charging Speed and Time:* Charging speed and time are significant concerns for EV owners. While home charging solutions offer convenience, they often require several hours to fully charge the vehicle. Public fast-charging stations can provide a significant charge in a shorter time, typically 30 minutes to 1 hour, but their availability is limited. Also, there is a concern for battery life with the use of fast chargers.

4. *Battery Technology*: Batteries are one of the most important components of EV as they directly affect the performance and overall cost of the vehicle. Research is focused on improving the energy density, battery life cycle, and durability of the batteries. High energy density batteries can improve the range of the vehicle as well as reduce the overall weight and size of the battery pack. Lithium-ion (Li-ion) batteries are the most common type of battery used in EVs due to their high energy density, relatively long cycle life, and lightweight design. Within the category of lithium-ion batteries, various chemistries are employed, including lithium nickel cobalt aluminum oxide (NCA), lithium nickel manganese cobalt oxide (NMC), and lithium-iron phosphate (LFP). Also, advancements include the development of solid-state batteries, which offer even higher energy densities, faster-charging rates, and improved safety compared to traditional lithium-ion batteries.

   Furthermore, the battery management systems need to be accurate in measuring the state of charge of the battery as well as managing the temperature of the battery, for the longer life cycle of the battery.

5. *Affordability:* The upfront cost of EVs, primarily due to battery cost, remains a barrier for many consumers.

6. *Environmental Concerns:* Even though EVs claim to be environmental friendly compared to internal combustion engine vehicles because of zero emissions, but they can't be truly sustainable until their manufacturing, usage, disposal, and recycling stages are environmentally safe. The major concerns include the mining of raw materials for batteries, the electricity consumed and emissions generated during the battery manufacturing process [42], the source of electrical energy consumed to charge the batteries [43], battery disposal, and recycling.

1.9 Focus of this thesis

This thesis focuses on new charging and driving schemes for EVs, especially AWD EVs. From the previous sections, it was observed that the existing on-board chargers are of limited power rating, because they had an extra charger circuit along with the driving hardware inside the EV, and for a given vehicle dimension, the size of the external charger circuit needs to be limited. A new integrated on-board charger is proposed using the existing driving hardware of the EV, with minimum additional power electronic hardware. Consequently, this retrofit EV charger has the advantage of being launched to the market in the shortest possible time. This IBC can be considered as a level 3 on-board charger as it uses the power driving hardware as the charger, and can be charged at any location where the supply is available. The main aspect of IBC, where the motor has to be still while charging the battery is taken care of with the existing three-phase machine and three-legged inverter without using any additional power electronic components.

However, when the machine windings are used as interface inductance between the grid and the converter, there exists an issue of unbalance in grid currents caused due to the difference in inductance between each phase especially using asymmetrically spaced machine windings in the presence of a pulsating magnetic field. The solution for the unbalance in grid currents, using detailed mathematical analysis and control solutions is dealt with in this thesis. Different control schemes are implemented and the harmonics in the grid currents are limited within the IEEE-519 standards.

Subsequently, the implementation of IBCs in all-wheel drive EVs where there are two motor drives is also focused, as these vehicles typically have higher battery capacity and require faster charging. Also, a new topology is proposed which would cancel the unbalance in grid current naturally by using the two motor drives already existing inside the AWD EV. The proposed IBC has a higher power rating and hence faster charging can be obtained, which can also be implemented in heavy-duty EV trucks, which are always in the long run and have huge battery capacity.

Finally, a driving mechanism using open-end configuration is proposed for AWD EVs with the existing star-connected motor by using the existing inverters inside the EV. The main advantages of this driving scheme include the use of existing hardware in the EV for a better driving scheme with higher battery utilization and reduced torque ripple. Also, higher speed operation can be obtained with this existing hardware and battery instead of the conventional methods of going with higher switching frequencies.

Some of the basic concepts that are needed for this work are discussed in the next section.

1.10 Key Fundamentals

This thesis mainly deals with integrated battery chargers, split phase machines, front-end converters, open-end winding machines, over-modulation regions, and their linearisation methods.

1.10.1 Integrated Battery Chargers

There are mainly two types of battery chargers for EVs, on-board chargers and off-board chargers. On-board chargers have the freedom to charge the battery from any point where a proper electric supply is available, but are limited by the size, weight, and space utilized inside the EV and hence are usually made of lower power ratings ($\leq$ 3.5 kW - Level 1 AC chargers and $\leq$ 19.2 kW - Level 2 AC chargers). This implies to charge a 70 kWh battery of an EV completely, it will take around 20 hours for a level 1 charger and around 3.6 hours for level 2 chargers. Fig 1.5 shows the block diagram of an EV with an AC on-board charger.

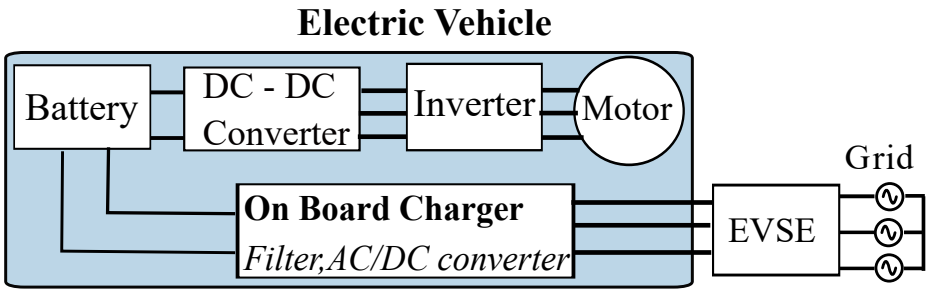

Fig. 1.5. Block Diagram of On board Level 2 charger

With the increase in battery capacity and range of vehicles, the time taken to charge the batteries completely will be higher, especially for four-wheelers, buses, and heavy duty trucks. Thus to have faster charging, Level 3 fast charging DC stations were introduced which directly charge the battery with a DC supply. Presently there are DC fast chargers with power ratings up to 250 kW. But with an increase in the number of EVs, building large number of charging stations is an economic burden. Fig 1.6 shows the block diagram of an EV connected with a DC fast charger.

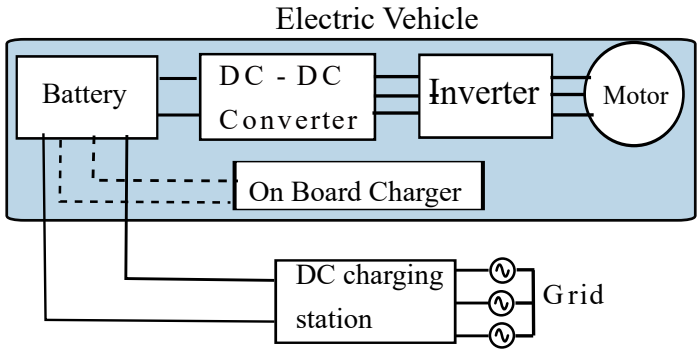

Fig. 1.6. Block Diagram of Off board charger

Naturally, an on-board charger with a higher power capability is a fruitful solution if the charger can be accommodated within the space constraints of the existing EV. The integrated battery charger is a high-powered on-board charger, which utilizes the driving hardware (the inverter and motor) to charge the battery with minimum external components, thus utilizing the existing space inside the EV. Fig 1.7 gives the block diagram of an integrated battery charger.

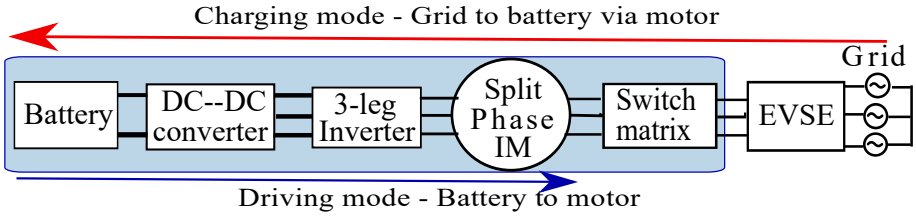

Fig. 1.7. Block Diagram of an Integrated Battery Charger

As seen from the figure, the same driving motor and inverter are used to convert the grid voltage to the required DC voltage to charge the battery. The machine windings act as the interface inductance between the grid and the pulse width modulated rectifier (three-legged inverter working as a front-end converter). By modulating the magnitude and angle of each phase voltage of the converter, the real and reactive power drawn from the grid can be controlled. The inductor (machine windings), determines the current that can flow through the system. But while the windings carry the AC current, they should not produce any torque inside the machine. Hence the windings should energized in such a way that the grid currents won't produce any rotating magnetic field inside the machine. Also while acting as an on-board charger, the inverter working as the front-end converter will ensure that the grid current is at unity power factor. Thus there is no need for any external converters or additional 50 Hz

bulk inductors for an integrated battery charger. Also since the driving motor and inverter are rated for higher power, the charger power capability can be as high as twice the motor power rating.

The main criterion while working the system as a charger is the following.

- The motor shall not produce torque while charging the battery.
- The grid currents drawn from the grid to charge the battery should have THD within the IEEE-519 standards. It should not be unbalanced or have high harmonic content.

1.10.2 Split Phase Machine

Split-phase machines or asymmetrical six-phase machines are multiphase machines. It has the advantage of also being developed by modifying an existing three-phase machine. The split phase motor configuration is achieved by splitting each of the phase belts of the three-phase motor into halves with a 30° electrical phase shift between the two as shown in fig 1.8. For a three-phase machine, the total number of slots are

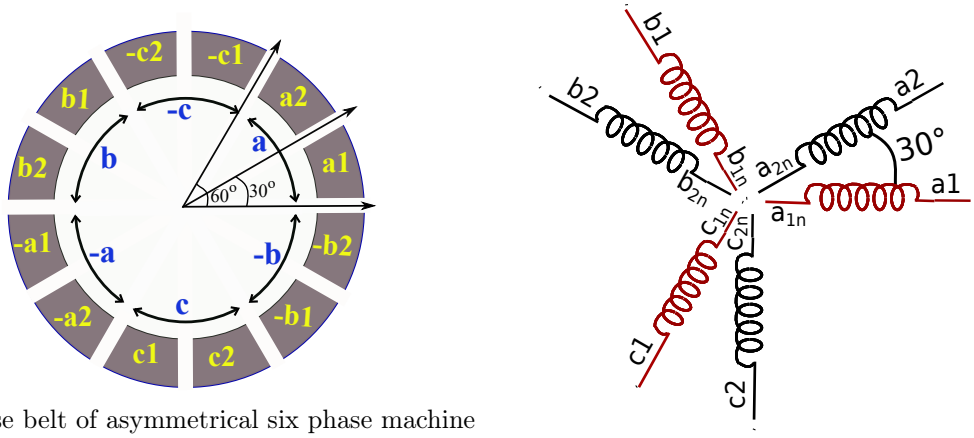

(a) Phase belt of asymmetrical six phase machine and three phase machine

(b) Six windings of split phase machine

Fig. 1.8. Split phase machine reconfigured from three phase machine

equally divided between the three phases, and the coils belonging to the same phase (Phase belt) are connected in series with their end connections coming outside the slots. To split the phase belt, the end connection at the center of the phase belt (half the number of slots per phase) is split into two coil groups with an electrical phase shift of 30° [44–47]. The slot-wise distribution of conductors for a three-phase 24-slot, 2 pole machine, and the derived split phase machine is shown in fig 1.9.

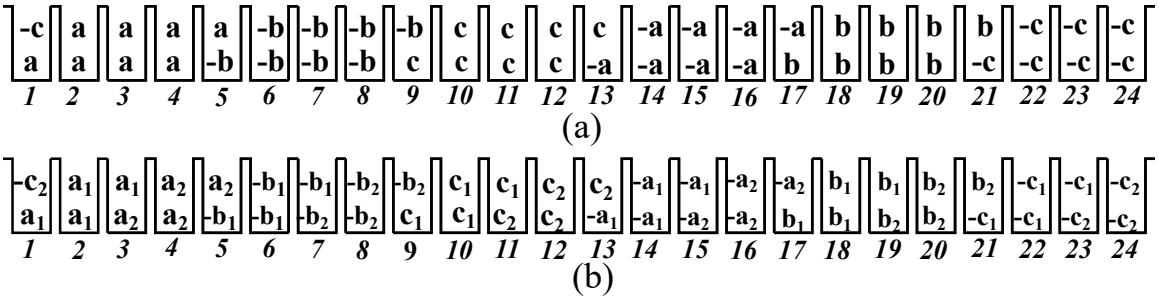

Fig. 1.9. Slot-wise winding arrangement of (a) Three Phase machine (b) Split Phase machine

The advantages of using a split phase machine include

- Elimination of 6th harmonic torque ripple in split phase drives.
- By using two inverters with DC-link voltage of $\frac{V_{DC}}{2cos(15°)}$, the maximum value of peak phase fundamental voltage that can be obtained using SVPWM is $0.643V_{DC}$ compared to $0.577V_{DC}$ for hexagonal SVPWM with three phase machine.
- It can be reconfigured from an existing three-phase machine.

Since this motor can be reconfigured from the existing three-phase machine, it is used in the integrated battery charger that is explained in chapter 2 and chapter 3. Using this motor, the instantaneous torque inside the motor can be made zero using proper excitation of the six windings.

1.10.3 Space Vector Modulation Scheme

Consider a two-level inverter shown in fig 1.10a driving a star-connected three-phase induction motor. In each leg of the inverter, both the switches cannot be turned on together as it will cause the DC link to be short-circuited. Hence the switches in each leg of the inverter are turned on in a complimentary fashion. When the top switch of each leg is turned on / turned off, the output pole voltage concerning the negative terminal of the DC-link of the inverter can be either V_{DC} or zero volts, which can be named as '1' / '0' respectively. Based on the switching combination of the three legs of the inverter, there can be eight possible switching states which are namely 1 (100), 2 (110), 3 (010), 4 (011), 5 (001), 6 (101), 7 (111) and 0 (000). The vectors 7 and 0 are called the zero voltage vectors. Consider a switching state 1 (100). In this state, the top switch of A leg is turned on, and the bottom switch of B and C leg is turned on. The pole voltage V_{AO}, V_{BO} and V_{CO} will be V_{DC}, 0 and 0 respectively.

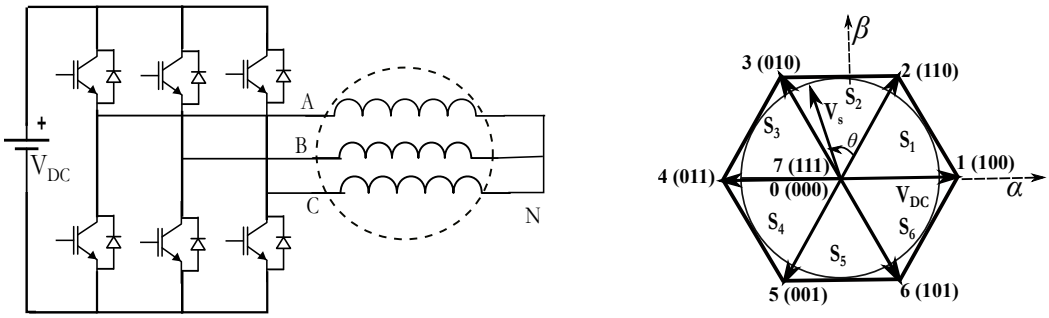

(a) A two-level inverter driving an induction motor

(b) Space vector diagram

Fig. 1.10. Space vector modulation scheme for a two-level inverter

A single voltage vector V_s can be defined instead of three different pole voltages as in (1.1) given below [48], [49].

$$\overrightarrow{V_s} = V_{AO} + V_{BO}e^{j120^\circ} + V_{CO}e^{j240^\circ} \tag{1.1}$$

This space vector can also be represented in $\alpha - \beta$ plane and the space vector can be divided into two components $V_{s\alpha}$ and $V_{s\beta}$ with α-axis defined along the a-phase winding as defined in (1.2).

$$\begin{aligned} V_{s\alpha} =& \frac{2}{3}(V_{AO} + V_{BO}\cos(120^\circ) + V_{CO}\cos(240^\circ)) \\ V_{s\beta} =& \frac{2}{3}(V_{BO}\cos(30^\circ) - V_{CO}\cos(30^\circ)) \end{aligned} \tag{1.2}$$

Table. 1.7 shows the eight switching states of the inverter and the corresponding voltage space vector location in $\alpha - \beta$ plane. It can be seen from the table that there are only seven locations for the voltage space vector corresponding to each switching state of the inverter.

Consider the inverter feeding an induction motor. Now the input phase voltage to the motor is given by (1.3).

$$V = iR + L\frac{di}{dt} + e \tag{1.3}$$

where e is the back emf, R is the winding resistance and i is the stator current of one phase of the motor. The three-phase voltages produce a magnetic flux inside the machine. The three-phase currents drawn by the machine also can be converted into a single current vector. The reference current vector, is required to generate the constant

Table 1.7. Switching states and space vector location of a two level inverter

Space vector	Switching state	Voltage space vector
1	(100)	$V_{DC}\angle(0°)$
2	(110)	$V_{DC}\angle(60°)$
3	(010)	$V_{DC}\angle(120°)$
4	(011)	$V_{DC}\angle(180°)$
5	(001)	$V_{DC}\angle(240°)$
6	(101)	$V_{DC}\angle(300°)$
7	(111)	$0\angle(0°)$
0	(000)	$0\angle(0°)$

rotating flux under all load conditions, and the error in the current phasor from the reference value can be found. The voltage vector required to reduce this current error to zero at every sampling time T_s, can be named as V_{ref}. The space vector V_s (which has only 7 fixed locations corresponding to the switching states of the inverter) has to generate the voltage vector V_{ref} in every sampling time T_s by switching the existing vectors in an average sense. The switching should happen in such a way that there is only a minimum change in switching from one vector to another. Also, only three switching states needs to be used in one sampling time.

The timing calculation for the switching of adjacent vectors in each sector is defined below. The angle θ is the local angle of the voltage space vector in each sector and varies from $0° \leq \theta \leq 60°$.

$$\begin{aligned} T_1 &= \frac{|V_s| T_s \sin(60° - \theta)}{V_{DC} \sin(60°)} \\ T_2 &= \frac{|V_s| T_s \sin(\theta)}{V_{DC} \sin(60°)} \\ T_0 &= T_s - (T_1 + T_2) \end{aligned} \tag{1.4}$$

Consider fig 1.10b, the voltage vector V_s is in sector S_2, thus vector 2 will be switched for T_1 duration, vector 3 will be switched for T_2 duration and 7 and 0 vectors together are switched for $\frac{T_0}{2}$ duration. The sequence in which the vectors are switched also affect the harmonics of the phase voltages of the inverter. If the zero vectors are not switched on, the space vector will trace along the hexagon of the space vector thus leading to the square wave mode of operation of the inverter.

Usually with space vector modulation, there is an increase in DC bus utilization of 15.5% compared to sinusoidal pulse width modulation. In the next section, different

multi-sided space vector modulation schemes are discussed using open-end winding machine, which can eliminate the lower order harmonics in the phase voltages of the inverter (square wave mode of operation) compared to the voltage harmonics in a two-level inverter driving a star connected motor.

1.10.4 Open-End Wound Machine

Open-end wound induction motor drive was introduced at the time when there was a requirement of high power, high-speed voltage source inverters to drive motors with lower switching frequency and higher efficiency [50]. The neutral of the three-phase induction motor is disconnected, thus both ends of each phase windings are accessible, which makes it an open-end wound induction motor. This motor can be driven from both sides with converters, thus different levels of phase voltage across motor windings can be obtained [51–54].

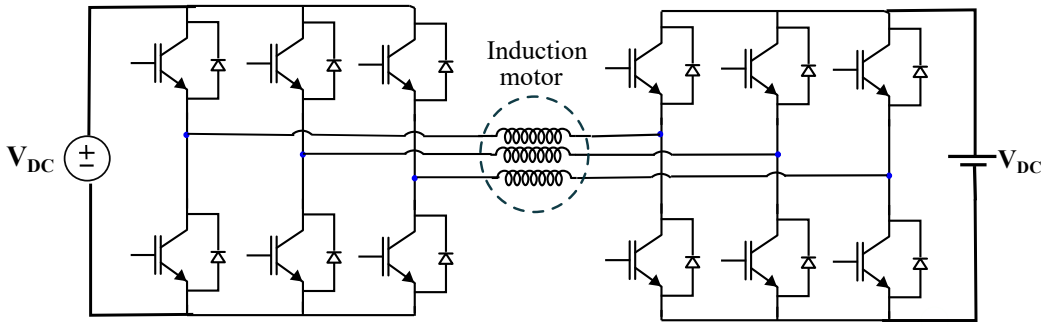

Fig. 1.11. Schematic of two inverter fed induction motor drive with isolated DC sources

Fig 1.11 shows the circuit diagram of open end winding induction motor drive using dual inverters with isolated DC sources.

Each inverter can have 8 switching states which are named from 0 to 7 for inverter-1 and 0' to 7' for inverter-2 as shown in fig 1.12a. By doing the vector sum of inverter-1 and inverter-2, 64 voltage space vector positions can be obtained for the motor windings as shown in fig 1.12b. The switching frequency of inverters in the OEW IM drive scheme can be made lower than that of 2-level and 3-level voltage source inverters by proper selection of vector combinations of inverter-1 and inverter-2 [55]. The switching scheme was such that for one instant inverter-1 will remain at a single position and only inverter-2 will be switching, for example, for sector 1, (88', 85', 84', 87') and vice versa for the other instant (87', 17', 27', 77'). At first, open-end winding space vector schemes were implemented using two inverters with isolated DC sources to limit the

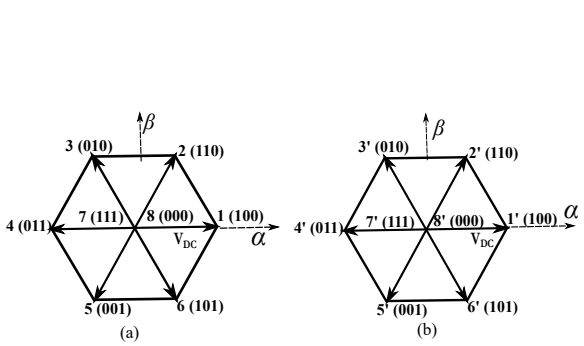

(a) Space vector positions of (a) inverter-1 and (b) inverter-2

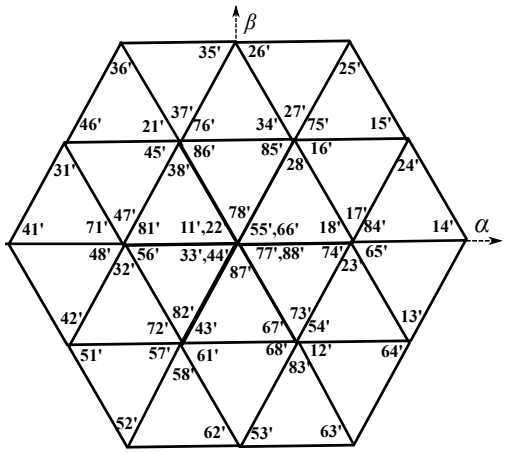

(b) Voltage Space vectors as a vector combination of inverter-1 and inverter-2

Fig. 1.12. Open end winding space vector scheme using separate DC source

flow of common mode current through the motor windings [55]. Later on, space vector modulation methods were utilized which blocked any common mode current from flowing through the windings when using a common DC source both the converters of the open-end winding (OEW) IM [56] as shown in fig 1.13a. Also in [57] by selecting certain locations in the space vector among the total 64 locations, only those vector locations were chosen which will not produce any common mode voltage across the OEW of the Induction Motor. The corresponding space vector locations are shown in fig 1.13b.

In [58], a dodecagonal space vector scheme was developed using two different magni-

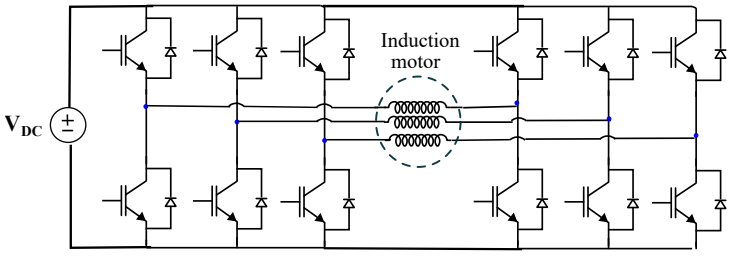

(a) Schematic of two inverter-fed induction motor drives with a common DC-link

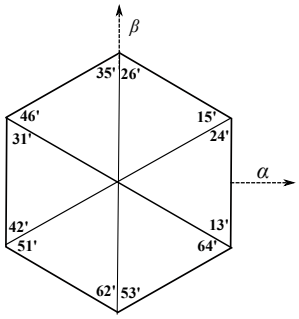

(b) Voltage Space vector locations with zero common mode voltage

Fig. 1.13. Open-end winding space vector scheme with a common DC source

tudes of DC source based dual 2 level inverter on both sides of the OEW IM. This scheme has the advantage of eliminating lower-order harmonics in the motor voltages

when it is operating in square wave mode at higher speeds. The circuit diagram is shown in fig 1.14(a). The isolated DC voltage of inverter-1 and inverter-2 are in the ratio of 1:0.366. The resultant space vectors which is the vector combination of the two inverters form a dodecagon with each sector having an angle of 30° as shown in fig 1.14.

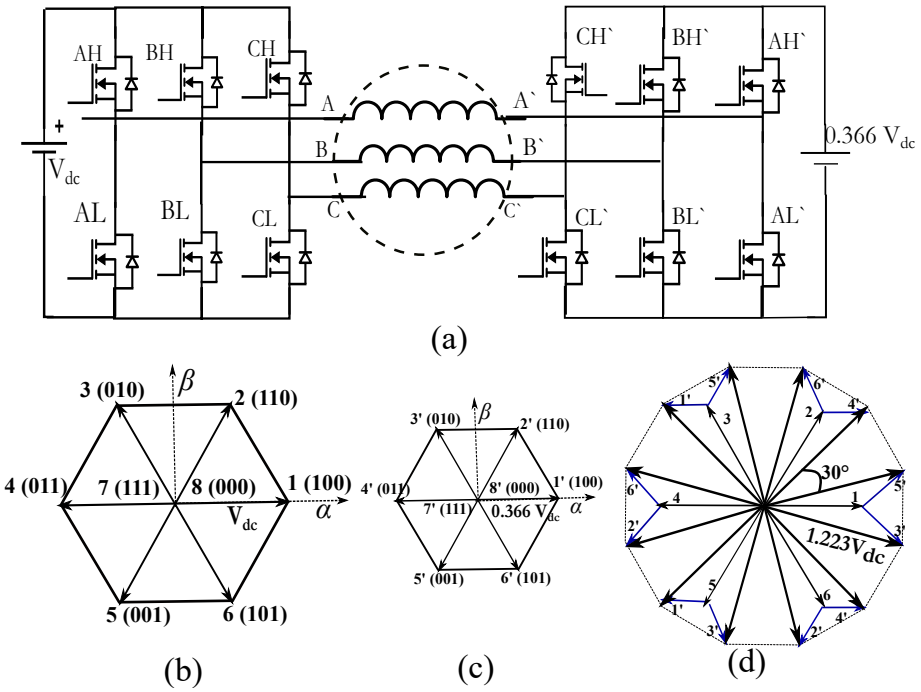

Fig. 1.14. (a) Circuit Diagram for Dodecagonal Space vector scheme for OEW IM (b) Voltage space vector for inverter-1 (c) Voltage space vector for Inverter 2 (d) Dodecagonal voltage space vector.

Only certain combinations of vectors of inverter-1 and inverter-2 are selected amongst all the valid 64 combinations to form the dodecagon. They were divided mainly into two sets of vectors (13', 24', 35', 46', 51', 62') and (15', 26', 31', 42', 53', 64'). A vector among these two sets was switched alternatively after every 30° interval as shown in fig 1.14(d). The main advantage of this scheme is the elimination of lower-order harmonics. The $6n \pm 1$ harmonics for n = 1,3,5,7... in the motor phase voltage is zero. The 11^{th} and 13^{th} harmonics are suppressed and the next main harmonic component is $6n \pm 1$ where n = 4,6...

A dodecagonal space vector modulation scheme using a single DC source and a capacitive filter (Inverter 2 with a DC-link capacitor) was developed in [59]. The capacitor voltage was maintained at a constant value using a voltage controller. In

chapter 4 a dodecagonal space vector scheme using only one DC source and inverter-2 with a capacitor is explained in detail. In this thesis, it has been mathematically proven that the capacitor voltage is regulated *without any voltage controller*.

1.10.5 Linear and over-modulation regions in Pulse Width Modulation techniques

There are several pulse width modulation techniques for voltage source inverters [60]. The most popular modulation method is the sinusoidal PWM method, where the reference waveform is compared with a high-frequency carrier waveform to turn on/off the switches of the inverter. A factor called amplitude modulation index 'm_a' was defined as the ratio of the peak value of the sinusoidal reference waveform to the peak value of the carrier waveform. The sinusoidal PWM method was implemented for the range of amplitude modulation index $0 \leq m_a \leq 1$. This region is defined as the linear region of modulation (fig 1.15a) where there is a linear relationship between the input DC voltage of the inverter and the peak value of the fundamental output voltage of the inverter as given by

$$V_{fund} = m_a.\frac{V_{dc}}{2} \tag{1.5}$$

Thus the maximum value of the fundamental voltage for a given dc source of magnitude V_{dc} is $0.5V_{dc}$ when m_a is 1. However, if the inverter were to operate in square wave mode of operation, as seen in fig 1.15a(c), the maximum peak value of fundamental voltage is

$$V_{6fund} = \frac{4}{\pi}\frac{V_{dc}}{2} \tag{1.6}$$

Hence it can be seen that using sinusoidal space vector PWM, the DC source of inverter is not fully utilized in the linear region. If the amplitude of reference voltage is increased above the linear region as shown in fig 1.15a(b), it can be seen that pulse dropping will happen and fundamental voltage will not have a linear relationship with the DC voltage as described in (1.5).

To improve the DC bus utilization different methods were developed [62], including harmonic injection techniques, [63], [64], mainly the third harmonic injection was proposed in [65]. Space vector modulation scheme, which is similar to the third harmonic injection scheme, also had a better utilization of dc link voltage [66], [67] by 15.5%. For the space vector modulation scheme, the peak value of the fundamental

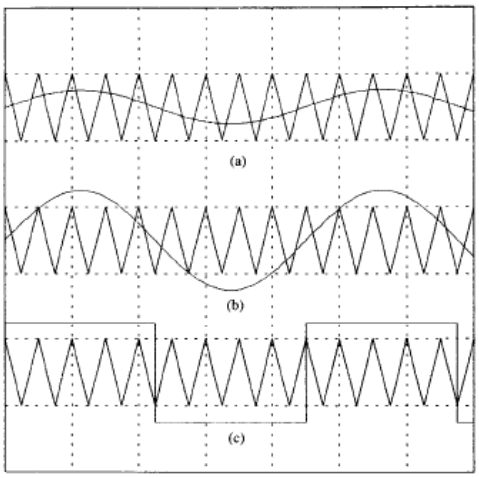

(a) Regions of PWM operation (a) Linear Region (b) Over modulation region (c) Six step operation [61]

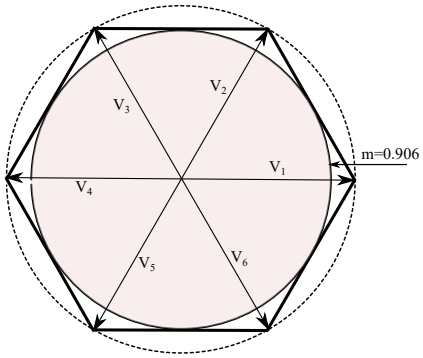

(b) linear region and over-modulation region

Fig. 1.15. Over-modulation region

voltage is given by

$$V_{sv,fund} = 0.577 V_{dc} \tag{1.7}$$

Thus, there is an increase in the dc voltage utilization of 15.5% compared to sine PWM in (1.5). The reference signal cannot be sinusoidal in shape in the over-modulation region because it will lead to pulse dropping as seen from fig 1.15a. The region above the linear region up to the square-wave operation is named the over-modulation region. A new definition for modulation index is defined as given in the below equation [68].

$$m = \frac{V_{m1}}{V_{6fund}} \tag{1.8}$$

where V_{m1} is the fundamental voltage generated using the modulation method and V_{6fund} is the fundamental voltage of the six-step operation which is already described in (1.6). For sine PWM, the maximum value of m is found to be 0.785 for the linear region. For space vector modulation, the maximum value of m is found to be 0.906. Thus for a two-level inverter, different regions are defined based on the modulation index as follows.

$$\begin{aligned} &\text{For} \quad 0 \leq m \leq 0.906, \quad \text{Linear region} \\ &\text{For} \quad 0.906 \leq m \leq 1, \quad \text{Over modulation region} \end{aligned} \tag{1.9}$$

In fig 1.15b, the shaded region which is within the inscribed circle of the hexagon

is the linear region where $0 \leq m \leq 0.906$. The over-modulation region is divided again into two regions based on the reference signal.

Linear region —- Sinusoidal reference signal.

Over-modulation region 1 —- Distorted continuous reference signal.

Over-modulation region 2 —- Distorted discontinuous reference signal.

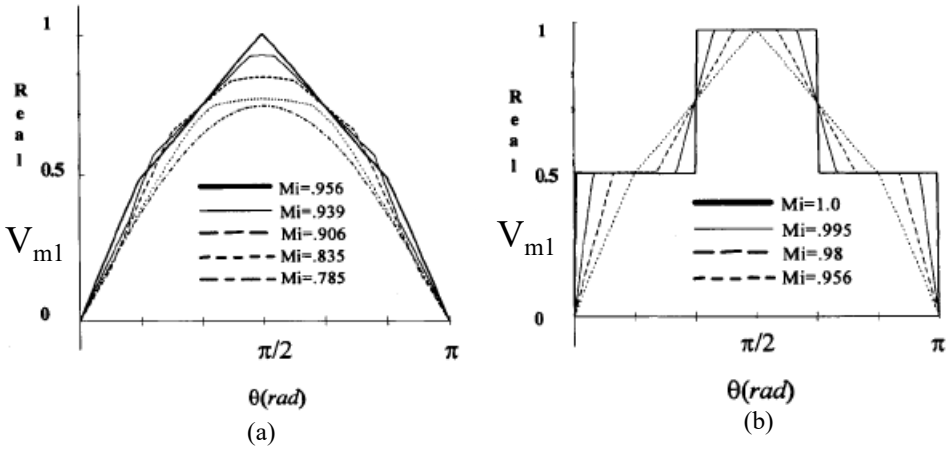

Fig. 1.16. Modulation index and the Reference signal for (a)over-modulation region 1 (b) over-modulation region 2 [62].

Different modulation techniques have been proposed to linearize the over-modulation region [62, 63, 68–71]. As seen from fig 1.16, the over-modulation region 1 ends when the reference signal stops being a continuous signal. The over-modulation region 1 for six-step waveform was defined for a modulation range of $0.906 \leq m \leq 0.952$ and over-modulation region 2 was defined from $0.952 \leq m \leq 1$. In [71], the modulation techniques for linearization of the two different regions are discussed in detail and implemented. In chapter 4, linearization of 12-sided, 18-sided, and 24-sided space vector schemes is discussed in detail.

1.10.6 Front-End Converters

The diode bridge rectifiers were used to convert the AC supply to a DC supply. However, it is an uncontrolled process and the currents drawn from the grid were found to be spiky in nature and thus disturbed the grid. A new rectification method was needed to convert the AC to DC without drawing peak currents. Front End Converter (FEC) is a controlled rectifier that will draw sinusoidal currents from the grid without any distortion. The circuit diagram of a three-phase front-end converter is shown in fig 1.17. This converter is called so because it is connected to the line side

of the motor drive or any load. This converter is also called a Pulse Width Modulation (PWM) rectifier, wherein the inverter voltages are controlled using PWM methods to control the power flow and hence the input grid current and its power factor. fig 1.17(b) shows the single-phase equivalent line diagram of the FEC.

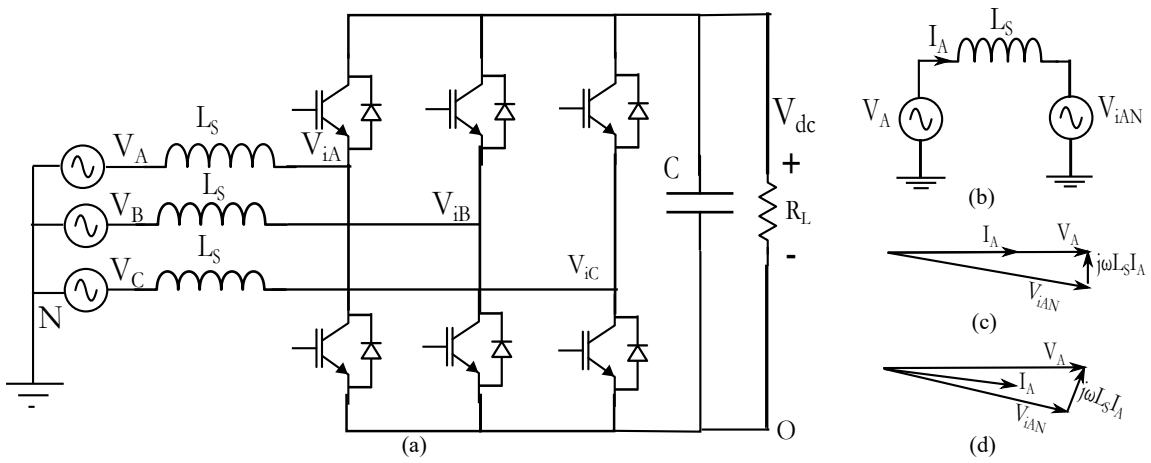

Fig. 1.17. (a) Circuit diagram of three phase front-end converter (b)Single phase diagram (c)Phasor diagram at unity power factor (d)Phasor diagram at lagging power factor

The phasor diagram for unity power factor and lagging power factor operation is shown in fig 1.17(c),(d). Here V_A is the phase voltage of the grid,
I_A is the grid phase current,
L_S is the filter inductance,
ω is the grid frequency,
V_{iAN} is the grid frequency component of phase voltage of inverter (excluding the high switching frequency components),
δ is the load angle,
ϕ is the power factor angle.

The real power, P and reactive power Q transferred from the grid to the rectifier can be defined as

$$\begin{aligned} P &= 3\frac{|V_A||V_{iAN}|\sin(\delta)}{\omega L_S} \\ Q &= 3\frac{|V_A|(|V_A| - |V_{iAN}|\cos(\delta))}{\omega L_S} \end{aligned} \tag{1.10}$$

Real and reactive power can be controlled by controlling the inverter phase voltage

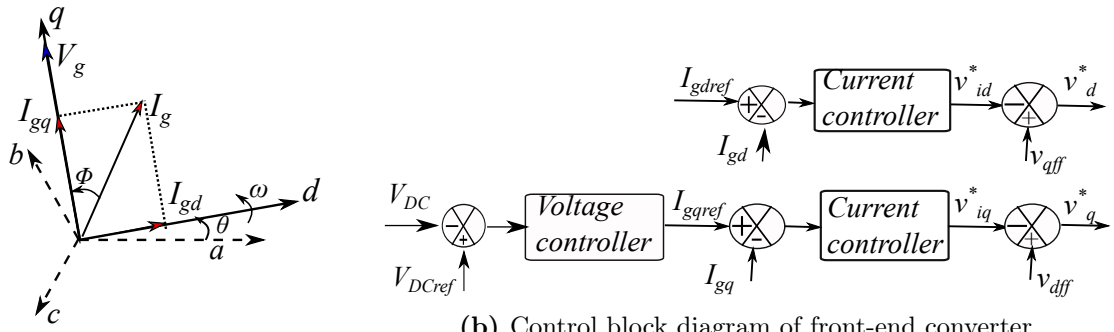

(a) Synchronous rotating reference frame

(b) Control block diagram of front-end converter

Fig. 1.18. Reference frame and control block diagram of FEC

V_{iAN}. However the independent control of real and reactive power was found to be difficult using this method. The control of power was found to be much simpler in synchronously rotating reference frame by transferring all the variable into $d-q$ frame [72–75]. Park transformation is used to convert the variables in $a-b-c$ domain to synchronously rotating $d-q$ reference frame as shown in (1.11). The grid voltage and inverter voltages can transformed into synchronously rotating $d-q$ reference frame using the park transformation.

$$\begin{bmatrix} I_d \\ I_q \\ I_o \end{bmatrix} = \frac{2}{3} \begin{bmatrix} \cos(\theta) & \cos\left(\theta - \frac{2\pi}{3}\right) & \cos\left(\theta - \frac{4\pi}{3}\right) \\ -\sin(\theta) & -\sin\left(\theta - \frac{2\pi}{3}\right) & -\sin\left(\theta - \frac{4\pi}{3}\right) \\ \frac{1}{2} & \frac{1}{2} & \frac{1}{2} \end{bmatrix} \begin{bmatrix} I_A \\ I_B \\ I_C \end{bmatrix} \tag{1.11}$$

The grid angle θ information is obtained by using a Phase Locked Loop (PLL), and by forcing the d-component of grid voltage to be zero. Thus the complete grid voltage vector V_g is aligned along the q-axis for simplified control of the real and reactive power. The synchronous rotating reference frame is shown in fig 1.18a. The dynamic model of FEC in $d-q$ reference frame is given by (1.12).

$$\begin{aligned} 0 &= R_S i_{gd} + L_S \frac{di_{gd}}{dt} - \omega L_S i_{gq} + v_{id} \\ v_{gq} &= R_S i_{gq} + L_S \frac{di_{gq}}{dt} + \omega L_S i_{gd} + v_{iq} \\ \frac{d}{dt} v_{DC}^2 &= \frac{2}{C}\left(\frac{2}{3}(v_{gq} i_{gq}) - v_{DC} i_{DC}\right) \end{aligned} \tag{1.12}$$

where v_{id}, v_{iq} are the inverter voltages in d and q axis and v_{DC}, i_{DC} are the DC-link currents of the FEC. There are two rotationally induced emf in d and q axis, that

is an emf is induced in q-axis due to current in d-axis, that is $\omega L_S i_{gd}$ and an emf in d-axis due to current in q-axis, that is, $-\omega L_S i_{gq}$. Now the real and reactive power in $d-q$ reference frame is defined in (1.13).

$$\begin{aligned} p &= \frac{2}{3}(v_{gd}i_{gd} + v_{gq}i_{gq}) = \frac{2}{3}(v_{gq}i_{gq}) \\ q &= \frac{2}{3}(v_{gd}i_{gq} + v_{gq}i_{gd}) = \frac{2}{3}(v_{gq}i_{gd}) \end{aligned} \tag{1.13}$$

Thus the control of real and reactive power transfer simplifies to the control of grid current in $d-q$ reference frame as shown in fig 1.18b. To have decoupled control of $d-q$ currents, the rotation emf terms are given as feed-forward terms.

At start, the input current drawn from the grid will be very high. Hence pre-charging of the DC-link of FEC has to be done, by running the FEC as a diode bridge rectifier, the FEC should only be started after getting the grid angle θ information and the reference output DC voltage has to be gradually increased.

1.11 Objectives of the thesis

This thesis concentrates on the charging and driving scheme for AWD EVs. A new integrated charging scheme using the existing hardware is proposed. A new driving scheme with an open-end winding motor using the existing system inside the vehicle is also proposed in this thesis. The thesis can be mainly divided into three objectives as detailed in the next sections.

1.11.1 Integrated battery chargers for electric vehicles

In chapter 2, a detailed discussion is done on Integrated Battery Charger (IBC) for electric vehicles. This is an on-board battery charger that can have a power rating above 22 kW or 40 kW (based on the motor power rating), that is it can be called a Level 3 on- board charger. The main disadvantage of the existing on-board charger was that it had a lower power rating mainly because of the limitation on its size and weight. Chapter 2 mainly addresses this issue. The new integrated charger that is presented in chapter 2 can charge the battery at a higher speed due to its high power rating without any need for extra space or weight to place the high power charger. Conversely, this IBC requires minimum space compared to the present on-board chargers in the market as it re-utilizes the existing motor and inverter inside the vehicle for charging the

battery. It uses minimum external components to make an on-board charger. Thus this charger can be used to charge the vehicle at any location where there is a rated EVSE for handling the power [76–79]. It can be installed in residential areas, offices, and parking lots and the charging speed can be made faster compared to the present slow on-board charger.
fig 1.19 shows the block diagram of an integrated battery charger using a split-phase machine, where the driving hardware is re-utilized for charging the battery.

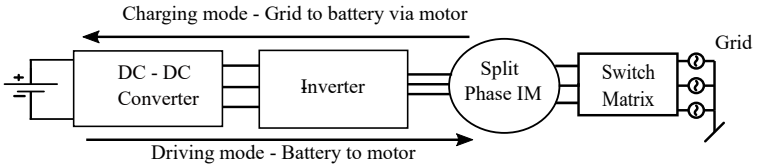

Fig. 1.19. Block Diagram of the integrated Battery Charger using Split phase IM

Another main advantage of this IBC is that the existing three-phase machine can be reconfigured and used for charging and driving purposes instead of other proposed IBCs where the existing machine had to be replaced with a multi-phase machine and multi-leg inverter.
While using the split phase machine for charging the battery, the current flow through the windings should be such that the motor won't rotate. The supply for the machine during the charging process is given accordingly. Using the Split phase machine, there was an issue of unbalance in the grid currents that was mitigated to a large extent using feed-forward control methods. A hardware prototype of IBC is implemented using a split-phase induction motor and three-legged inverter.

1.11.2 Integrated Battery Charger for All Wheel Drive Electric Vehicles

In chapter 3, a parallel combination of Integrated Battery chargers for EVs, especially AWDs, that have two motor drives is presented. An on-board charger topology is developed which has double the power capability of that mentioned in chapter 2, by using the two motor drives in parallel. In all-wheel drive EVs, there is one motor on the front axle and another motor drive on the rear axle. While charging the battery, the existing two motor drives in the AWDs can be utilized to double the power capability of the charger. Thus the idea of connecting two IBCs in parallel using split-phase machine was proposed and is presented in chapter 3.

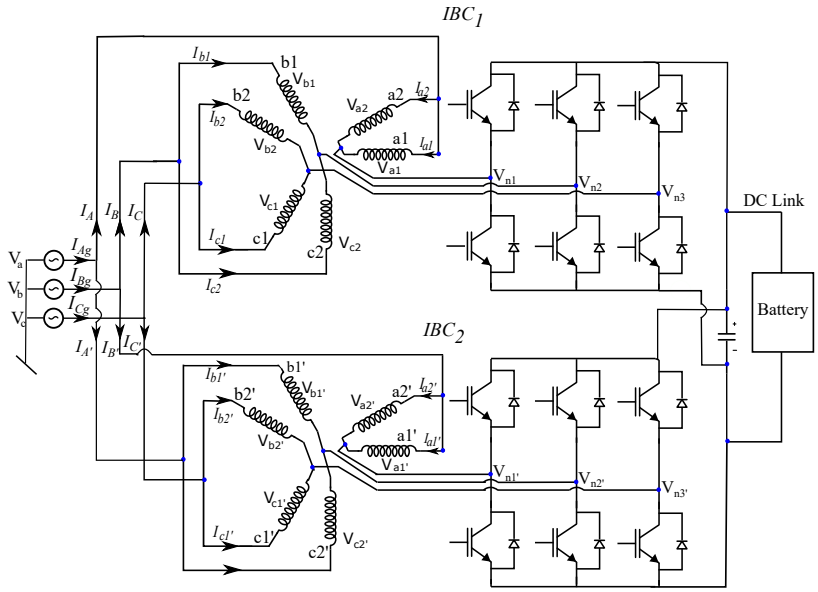

Fig. 1.20. Topology of the parallel combination of two motor drives for an on-board charger for AWD EVs.

Fig 1.20 shows the circuit diagram of the proposed on-board charger using a parallel combination of two motor drives of an AWD EV.

Also, the issue of unbalance caused by a single IBC using split-phase machine could be mitigated in the proposed parallel combination of IBCs. The motor windings of both IBCs are energized in such a way that the unbalance in the grid currents is minimized. A mathematical proof is included to verify the proposed concept. The issue of zero sequence currents that can flow when two IBCs are connected in parallel is also addressed in this chapter. Also for AWDs, the motor power rating of the front axle motor and rear axle motor may not be the same, usually, the rear axle motor drive has a higher power rating. Hence the case for unequal power sharing between the two motor drives is also discussed. Simulation and experimental results are included to validate the proposed concepts.

1.11.3 Efficient Driving Scheme for All Wheel Drive EVs

An efficient driving scheme for the AWDs is discussed in chapter 4. In AWD vehicles only one motor drive will be constantly engaged. The other drive is only engaged when there is a need for extra traction like starting/ acceleration or while driving in limited traction conditions like snowy/muddy roads. Thus for most of the driving conditions,

one motor drive is not utilized. In chapter 4, a new driving scheme is presented where while driving the rear motor of an all-wheel drive vehicle, both the front and rear converters are engaged which can improve the performance of the vehicle. The motor neutral is disconnected and it now runs as an Open End Winding (OEW) motor. Also, the DC-link voltage of the second inverter is of lower voltage with no DC source but only a DC-link capacitor. The second inverter basically acts as a switched capacitor.

Thus with the motor now connected in open-end winding configuration, using two two-level inverters, three different multi-sided space vector modulation schemes are discussed in chapter 4 which are 12-sided, 18-sided, and 24-sided SVM schemes. Using these multi-sided SVM schemes, there is the elimination of lower order harmonics in the phase voltages of the motor, thus eliminating the lower order torque ripples while driving the machine. In all these schemes the DC-link voltage of the second inverter (switched capacitor) is maintained constant without any voltage controller. The switching schemes and the proof for maintaining capacitor voltage constant naturally without any closed loop control are included in this chapter.

A linearization method for the over-modulation region in the space vector is also proposed in chapter 4. Thus for the same battery voltage, the region outside the linear region can be properly controlled thus allowing better utilization of the battery.

Thus the advantages of the above schemes are summarized below.

1. For the same machine, by implementing multi-sided space vector modulation schemes using OEW configuration, the lower order harmonics in the motor phase voltages are eliminated.

2. With the reduction in harmonics from the motor phase voltages, more fundamental voltage can be supplied to the motor using the same DC source, and thus the motor phase currents can be reduced for the same power level. Thus the conduction losses inside the motor windings on both the stator and rotor can be reduced.

3. The second inverter acts as a switched capacitor. The voltage of the capacitor is naturally maintained constant at a lower value compared to the DC source, without any closed loop voltage controller.

4. The harmonics in the motor phase voltage in the square wave mode of operation is reduced as the number of sides in the space vector polygon is increased.

5. The second inverter has a lower DC-link voltage in this proposed driving scheme, thus it has lower switching losses.

6. Linearization of the over-modulation region is also implemented to utilize the battery to its maximum capacity.

Mathematical proofs, simulation, and experimental results are included which verify the proposed concepts.

Chapter 2

An Integrated Battery Charger using Split Phase Machine

2.1 Introduction

Electric vehicle industry has evolved over the past few years; there are different models of EVs with wide ranging prices that are being launched by the EV manufacturers. However, the battery cost and the charging time are still a major concern among the EV users. As discussed in chapter 1, the presently available on-board chargers are slow with limited power capability, and the fast DC off-board chargers are confined to limited locations. Also fast charging stations require huge investment and operational costs. The concept of high-powered integrated battery charger, can be a solution to the existing problem, as they can be used to charge the battery from any location where the supply is available, at a much faster rate compared to the present on-board charger, and with reduced investment cost, compared to the DC fast chargers. The concept of IBC was already discussed in chapter 1, section 1.10.1.

In this chapter , a new topology of integrated battery charger using split-phase machine is introduced [76–79]. The advantage of the proposed IBC topology is that it uses the existing three-phase motor and inverter unlike other IBCs which require the replacement of existing machines with multiphase machines and/or multi-leg inverters. The concept of split-phase machine as a modification of three-phase machine is already discussed in section 1.10.2.

In the proposed IBC, the machine windings are connected as interface inductance between the grid and the converter in such a way that ensures the torque developed inside the motor is zero while charging the battery. However, due to the asymmetrical nature of the machine windings, the grid currents will be normally unbalanced. They

will not be pure sinusoidal in shape and the rms values of the three-phase currents will not be the same. To understand the unbalance, the mathematical model of the system is derived in $a-b-c$, $\alpha-\beta$ and synchronously rotating reference frames. With the help of the derived model, new control schemes are developed to make the grid currents balanced and within the IEEE-519 and IEEE-1547 standards.

Simulation and experimental results are included to verify the above concepts. The experimental prototype was built using a split-phase induction machine that was reconfigured from a three-phase induction machine.

Section 2.2 provides a detailed review on the existing IBC topologies in literature. Section 2.3 describes the working of the proposed IBC using split-phase machine. The issue of unbalance in grid currents in the system due to the unsymmetrical nature of machine windings is dealt in section 2.4. The mathematical modeling of the system is thoroughly dealt with in section 2.5. The control structure and the method of feed forward control is presented in section 2.6 and the simulation and experimental results are presented in section 2.9. Section 2.10 concludes all the features of the proposed IBC topology using split-phase machine.

2.2 A review on Integrated Battery Chargers

Many research works have been published in the field of IBCs over the years [25,80–87]. The concept of IBC was first introduced using single-phase grid supply [88–91]. In [89], the driving system consists of a three-phase motor, three-legged inverter and a DC battery. When it is used for charging purpose, a single-phase AC grid is connected via a bridge rectifier to provide the rectified DC output for the battery. The motor windings / leakage inductance, act as the inductor for the unity power factor single-phase boost-regulated battery charger, formed using one of the legs of the inverter. The other two legs of the inverter are turned off while in charging mode. This was of a lower power rating charger. In [92], a similar topology of diode bridge and boost converter was used to charge the battery (fig 2.1(a)).

Interleaved boost converter topology along with diode bridge rectifiers were used in [93,94] as shown in fig 2.1(b). The disadvantage of unidirectional converter is that there is a high stress on semiconductors when operating in two modes as the current and voltage levels for the switches vary for the two modes of operation even at the same power level. Also Vehicle to Grid (V2G) mode of operation is not possible in these topologies as they are unidirectional in nature.

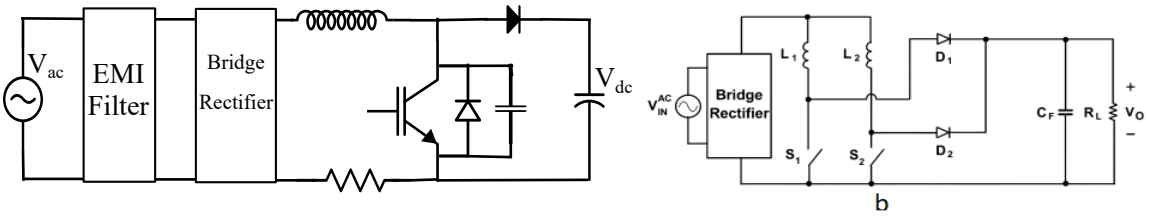

Fig. 2.1. Unidirectional IBC using Power Factor correction boost converter

Bidirectional IBCs developed with single-phase supply without using any external diode bridge rectifier reduced the complexity of the system. Here the inverter was made to operate as a front-end converter [95–98]. But IBCs using single-phase supply had a limit on in its power rating. Single phase IBCs were more focused on charging two-wheeler and three-wheeler EVs. To have a high power capability, especially for charging the batteries of four-wheeler EVs, buses and trucks, research works were directed on implementing IBCs using three-phase supply. But the three-phase machine had to be blocked using some external mechanism while using a three-phase supply.

IBCs can be classified into isolated and non-isolated IBCs based on how the motor windings are connected in the charging mode. In isolated IBCs, the motor windings are connected to work as transformer for isolation purpose [99, 100] (fig 2.2), while the motor windings are connected as filter inductance for the non-isolated IBCs. In most of the isolated IBCs, the motor generates a torque and an external system is needed to block the motor from rotating.

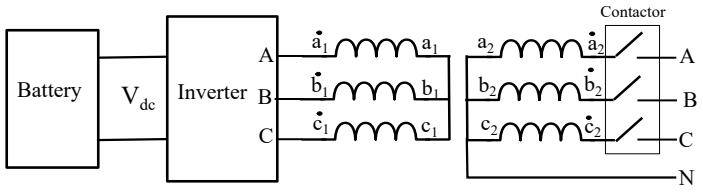

Fig. 2.2. Isolated IBC using the stator windings of an Interior Permanent Magnet Synchronous machine connected as a transformer by splitting the phase windings [100]

IBCs can also be classified based on the type of the motor that is used. Nowadays permanent magnet synchronous machines are widely used in EVs because of its high power density, compactness and reduced rotor loss compared to induction machine drives. IBCs based on PMSM machines [101–105], switched reluctance machines [106, 107] and induction machines are present in literature. This thesis focuses on IBCs using induction machines.

In non- isolated IBCs, the machine windings will be used as filter inductance by

passing the grid currents through it. The criterion to generate zero torque inside the motor, while charging the battery is one of the main requirements of non-isolated IBCs. External mechanism (clutch or another interface converters) were used to block the motor from rotating while charging the machine in [25]. This objective can be met more efficiently with the development of multiphase machines as they have additional degrees of freedom.

In [108], an integrated battery charger is developed using a symmetrical six-phase machine connected to H-bridges. Equal grid currents are passed in opposite direction through each half of the phase windings by the switching of converter legs, resulting in cancellation of flux, and in-turn producing zero torque. No hardware reconfiguration is needed between charging and driving mode operation. But it requires a symmetrical six-phase machine and a six-legged cascaded H-bridge inverter for its operation, which increases the cost of the system. Integrated battery charging system consisting of nine-phase, symmetrical six-phase and five-phase machines are discussed in [109–112]. However these topologies require the replacement of existing three-phase machine and three-legged inverter with a new multiphase machine and multi-legged inverter. In [113] an integrated battery charger topology with torque cancellation strategy is proposed with a symmetrical six-phase, split-phase and a dual-three-phase permanent magnet synchronous machine with phase displacement of 60°, 30° and 0° respectively.

Table 2.1. Comparison of different topologies of IBC using multiphase machine

Ref	**Traction Motor**	**Reuse of existing 3 leg converter**	**Retrofit ability of 3-phase motor**	**Use of 3-phase supply**	**External components**
[114]	Nine phase PMSM	No (6 leg)	No	Yes	Contactors
[113]	Six phase PMSM	No (6 leg)	No	Yes	Contactors
[115]	Three phase PMSM	Yes	Yes	Yes	Filter, 3 phase interface converter, Contactors
[116]	Three phase IPM	Yes	Yes	Yes	Rectifier, smoothing reactor, Contactors
[109]	Five phase IM	No (5 leg)	No	Yes	Contactors
[111]	Nine phase IM	No (9 leg)	No	Yes	Contactors
[112]	Symmetrical six-phase IM	No (6 leg)	No	No (6 phase)	Contactors
[117]	Asymmetrical six-phase IM	No (6 leg)	Yes	No (6 phase)	Contactors
[118]	Asymmetrical six-phase IM	No (6 leg)	Yes	Yes	Contactors
[119]	Split three-phase IM	Yes	No	Yes	Contactors
Proposed	**Asymmetrical six-phase IM**	**Yes**	**Yes**	**Yes**	**Contactors**

In [117] an integrated charger using a six-legged-inverter and an asymmetrical six-phase machine excited with six-phase supply is proposed. Here, a three-phase

transformer with two secondary windings is needed to obtain six-phase supply from the available three-phase grid which makes the system bulky. In [118], an IBC is implemented with an asymmetrical six-phase machine with a six-legged inverter, but without the need of any six-phase supply. The IBC is excited with a three-phase supply and hence the use of transformer with two secondaries is avoided. But it still requires a six-legged inverter for charging and driving the vehicle, thereby increasing the overall cost of the system. In [119], a torque cancellation strategy by re-configuring three-phase machine winding as a split three-phase machines is proposed. The machine is configured by tapping out the mid-point of each phase winding in a double layered three-phase machine. This topology uses a three-phase supply with a three-legged inverter. But it needs a three-phase machine with double layer winding which requires a change in stator design, if the existing machine is a single layer wound three-phase machine.

In this chapter an IBC using split-phase induction machine is discussed in detail. The proposed topology has the following advantages.

1. Existing motor and inverter inside the EV is reused: The existing three-phase machine windings are reconfigured as split-phase machine without affecting the winding structure by simply splitting the phase belt in the middle. The motor windings connections during driving / charging are such that a three-legged converter is sufficient, both in driving and charging modes.

2. Torque generated by the machine is zero: The proposed topology ensures that the torque generated inside the motor is zero naturally without using any extra components.

3. The power rating of the IBC can be twice the power rating of the motor (maximum power limited by the power handling capacity of the inverter).

4. The grid currents are at unity power factor: The front-end converter ensures that the grid currents are at unity power factor. Also, the current controller ensures that the grid current are balanced and its THD is within IEEE 519 standards.

5. The IBC uses minimal external components: It requires only small relay based contactors to switch the machine windings from charging mode to driving mode.

6. Vehicle to Grid (V2G) mode of operation: The proposed IBC is bidirectional in nature and can be used for V2G applications.

2.3 IBC Using a Split-Phase Machine

The block diagram of the proposed integrated battery charger using a split-phase machine is shown in fig 2.3. The six windings of the split-phase machine, namely, $a1, a2, b1, b2, c1$ and $c2$, reconfigured from the three-phase machine by splitting the phase belt into two equal halves are shown in the fig 2.3. These six machine windings are connected between the three-phase grid and the three-legged converter as interface inductance. The leakage inductance provided by the machine windings helps to determine the grid current that can flow through the converter.

The normal rectifiers which convert AC to DC draws peaky currents from the grid. In this proposed topology, the three-legged converter works as a front-end converter (pulse width modulated rectifier as described in section 1.10.6). The modulating signals given to this converter is such that it will draw sinusoidal currents from the grid at any desired power factor. In the proposed IBC, for charging the battery, the grid currents are drawn at unity power factor.

The winding configuration of the machine and the working of the system in charging mode and driving mode are discussed in detail in the following sections.

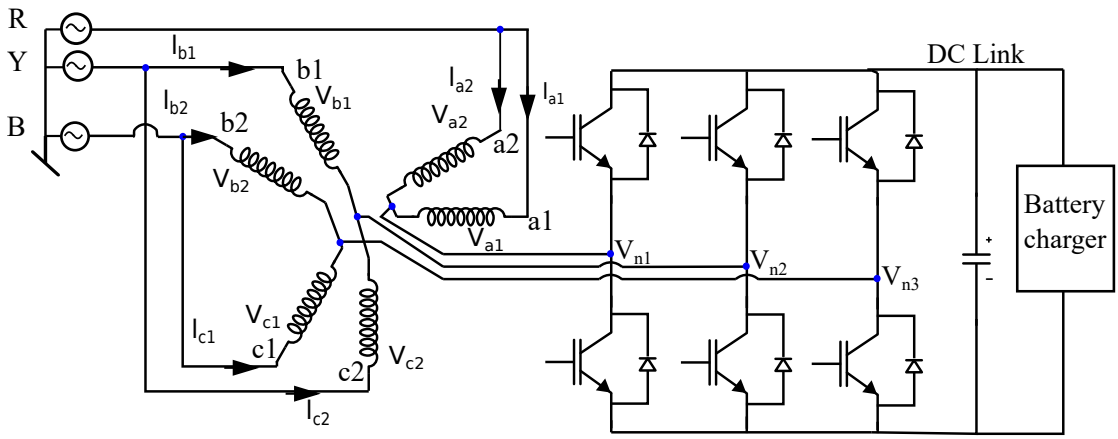

Fig. 2.3. Circuit schematic of proposed IBC using a Split-phase machine [78].

2.3.1 Charging mode of operation

While charging the battery from the grid, the motor should remain standstill even though the grid current flows through its windings. Hence the currents through the

motor windings should not induce any rotating magnetic field inside the motor. The following section describes how it is implemented.

Let the six windings of the split-phase machine be considered as two sets of three-phase windings, namely $a1, b1, c1$ and $a2, b2, c2$ that are phase sifted by 30°. One set of windings, that is, $a1, b1, c1$ can be connected to R, Y, B phase sequence and the other set of windings $a2, b2, c2$ can be connected to R, B, Y phase sequence so that the flux produced by both sets are rotating with equal speed but in opposite directions as shown in fig 2.4a. Hence the net flux inside the motor will be pulsating in nature and the motor will not rotate while charging the machine. Also, the axis of the pulsating field will be geometrically along the middle of these windings as shown in the fig 2.4a.

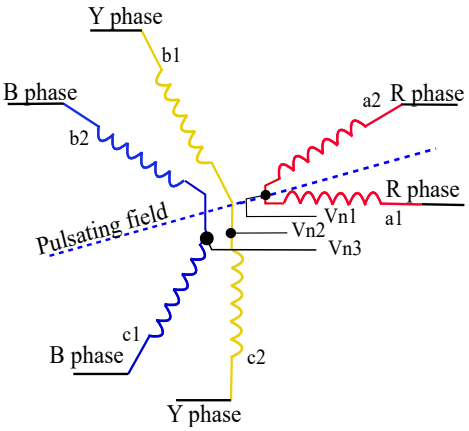

(a) Split-phase machine winding configuration during charging.

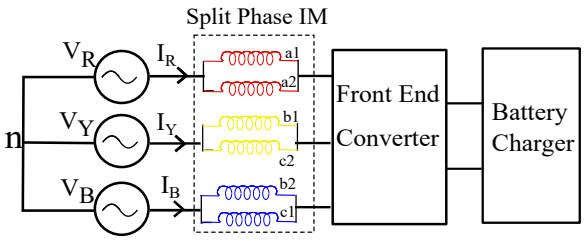

(b) Parallel combination of machine windings while charging

Fig. 2.4. Split phase machine connection when used in charging mode of operation.

The stator windings of the motor connected between the grid and the converter is shown in fig 2.4b. The windings $a1$ and $a2$ are connected in parallel between the $R-phase$ of the supply (Point of Common Coupling, at the output of EVSE) and the corresponding inverter leg V_{i1}, similarly $b1$ and $c2$ are connected in parallel between $Y-phase$ and V_{i2}, and $b2$ and $c1$ are connected in parallel between $B-phase$ and V_{i3} (fig 2.4b). The net flux that is pulsating as a function of grid current along the middle of these windings is also shown in the figure.

2.3.1.1 Instantaneous electromagnetic torque generated inside the machine is zero

Consider the spatial arrangement of the split-phase machine windings with respect to the pulsating magnetic field as shown in fig 2.4a. The parallel windings $a1$ and $a2$

are placed symmetrically with respect to the axis of pulsating magnetic field. Same is the case for the other two sets of parallel windings. The flux that links both $a1$ and $a2$ windings are the same. Also, the voltage across the windings are same. Hence the $R-phase$ currents will be equally divided between $a1$ and $a2$ windings. Similarly the other two phase currents will be equally divided between their respective parallel windings. Thus there will be a component of current if taken along the pulsating axis, but there wont be any component of current along an axis perpendicular to the axis of the pulsating flux. Similarly the induced rotor current will only have component along the axis of pulsating flux, and zero rotor component of current along the axis perpendicular to the axis of the pulsating field. By substituting these conditions in the torque equation, it can be found that the instantaneous torque generated inside the machine is zero. The mathematical derivation for zero instantaneous torque is presented in section 2.5.1.1.

2.3.1.2 Power rating of the proposed IBC

The power rating of the charger is calculated by assuming that the magneto-motive force (mmf) produced by the machine during charging should be same as the rated magneto motive force generated inside the machine during driving. The mmf generated when current flows through the stator winding is defined below.

$$\begin{aligned} MMF =& NI_{a1}\cos 15^\circ + NI_{a2}\cos 15^\circ + NI_{b1}\cos 105^\circ \\ &+ NI_{b2}\cos 135^\circ + NI_{c1}\cos 225^\circ + NI_{c2}\cos 255^\circ \end{aligned} \tag{2.1}$$

where, N is the number of turns in each winding and $I_{a1}, I_{a2}, I_{b1}, I_{b2}, I_{c1}$ and I_{c2} are the currents passing through $a1, a2, b1, b2, c1$ and $c2$ windings respectively.

During driving, $I_{a1} = I_{a2} = I_a,\ I_{b1} = I_{b2} = I_b$ and $I_{c1} = I_{c2} = I_c$ as the windings are connected in series. Consider an instant where $I_a = I$ and $I_b = I_c = -\frac{I}{2}$. Substituting in (2.1), mmf during driving is found to be

$$MMF_d = 2.89NI \text{ Ampere Turns} \tag{2.2}$$

During charging $I_{a1} = I_{a2} = \frac{I_a}{2},\ I_{b1} = I_{c2} = \frac{I_b}{2}$ and $I_{c1} = I_{b2} = \frac{I_c}{2}$ as explained in section . Considering the instant when the current through a phase is maximum and substituting the conditions in the MMF equation (2.1) the mmf during charging is

calculated to be

$$MMF_c = 1.445NI \text{ Ampere Turns} \tag{2.3}$$

Hence it is found that MMF_d is twice MMF_c. Hence the power rating of the IBC can be up to twice that of the driving motor. But the existing inverter inside the EV is rated corresponding to the power rating of the driving motor and hence the power of the IBC is limited by the maximum power handling capability of the existing inverter.

2.3.2 Driving mode of operation

The split-phase machine can be reconfigured back to three-phase machine by connecting the proper windings in series [44] and the motor runs as a three-phase induction motor with a three-leg inverter. The motor windings $a1 - a1'$ and $a2 - a2'$ are connected in series, $b1 - b1'$ and $b2 - b2'$ are connected in series, and $c1 - c1'$ and $c2 - c2'$ are connected in series (fig 2.5a) and run as a three-phase induction motor.

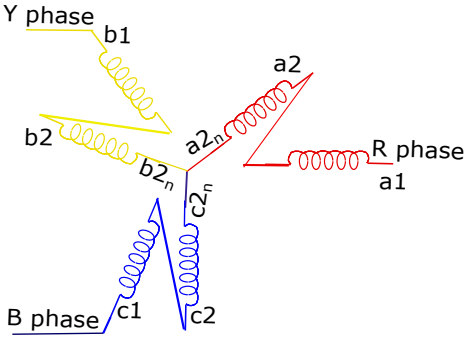

(a) Winding configuration during driving mode.

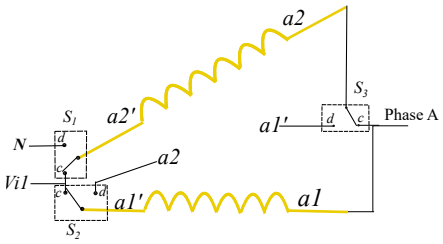

(b) Winding reconfiguration from driving mode to charging mode.

(c) Contactors -TE Kilovac EV600

Fig. 2.5. Split phase machine winding configuration in driving mode and the changeover using contactors from driving mode to charging mode.

Thus the same three-phase induction machine can be used in driving and charging mode.

2.3.3 Reconfiguration from charging mode to driving mode

To reconfigure the windings of split-phase machine from charging to driving mode and vice-versa, relay type SPDT switches (contactors) as shown in fig 2.5c are used. The use of contactors is sufficient as switching/reconfiguration is required only when the battery needs to be charged and when the motor is standstill and de-energized. As

shown in fig 2.5b, S_1, S_2 and S_3 are the contactors used which move from contact point d in driving mode to contact point c in battery charging mode.

2.4 Unsymmetrical nature of machine windings and unbalanced grid currents

While charging the battery, the windings of the split-phase machine are connected as shown in fig 2.4a to ensure zero torque generation. It can be noted that the phase sequence of the two sets of winding $a1, b1, c1$ and $a2, b2, c2$ are different. So, the flux (ϕ_1) produced by the winding group $a1, b1, c1$ will be rotating in a direction opposite that of winding group $a2, b2, c2$, flux (ϕ_2), even though the magnitudes of both the fluxes are equal. Hence the resultant flux (ϕ) inside the air gap of the machine will be a pulsating with a function of the grid angle θ, and is inclined 15° to $a1$ winding (fig 2.4a). As seen from the figure, the windings of the split-phase machine are not connected symmetrically during charging mode, and the flux that links each winding at every instant is different. The parallel combination of $a1$ and $a2$ windings forms the R-phase grid-interface inductance L_R (fig 2.6), and maximum pulsating flux is linked to these windings. Similarly, the parallel combination of $b1$ and $c2$ windings form the Y-phase grid-interface inductance, L_Y and minimum amount of flux is linked with these windings during charging. Finally, the parallel combination of $b2$ and $c1$ windings form the B-phase grid-interface inductance, L_B. Hence, the interface inductance of $R, Y,$ and$B$ phases are unequal and leads to an unbalanced system. This means that the current in each phase will be different if the converter is modulated using conventional controllers even if the grid supply is balanced. To understand and control the unbalance in the grid currents, the system has to be modeled. Modeling the system helps to find the dependence of the different phase currents, inverter voltages and inductances on the pulsating field generated inside the motor.

2.5 Mathematical modeling of IBC with a split-phase machine

It has been discussed from the previous section that the grid currents drawn by the IBC are not balanced, that is, the three-phase currents will not be sinusoidal

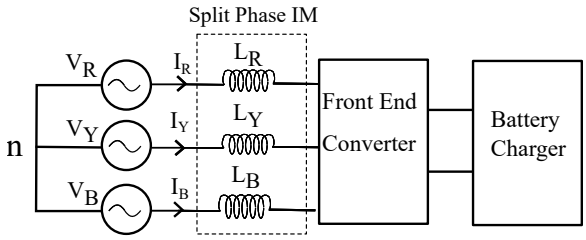

Fig. 2.6. Machine windings of IBC as inductance during charging mode of operation.

in shape and their rms values will not be the equal in all the three-phases. From the asymmetrical positioning of stator windings, it can be geometrically understood that the self inductance of each phase is different from one another and the mutual inductance between each phase will also be unequal. However, quantitative analysis needs to be implemented to understand the nature of these inductances.

Thus a mathematical model is derived in the stationary reference frame and the synchronously rotating reference frame which will be discussed in detail in the following sections.

2.5.1 IBC model in stationary reference frame

The mathematical model of the IBC is derived for the stationary reference frame and synchronously rotating reference frame. The model is derived by considering the split-phase machine as two sets of three-phase windings , that is $a1, b1, c1$ and $a2, b2, c2$ that are phase shifted by 30°. Flux ϕ_1 is assumed to be generated by $a1, b1, c1$ set of windings, and is rotating in the counter clockwise direction. Flux ϕ_2 is assumed to be generated by $a2, b2, c2$ set of windings, and is rotating in the clockwise direction as shown in fig 2.7a(a). The net flux ϕ is assumed to be pulsating in nature as shown in the figure along the axis 15° from the winding $a1$. The stationary reference frame α is assumed along the axis of pulsating magnetic field, ϕ (fig 2.7a). β axis is perpendicular to α axis as shown in the figure. Let the voltage across the two sets of windings be V_{a1}, V_{b1}, V_{c1} and V_{a2}, V_{b2}, V_{c2}. Let these two sets of voltages be transformed to stationary reference frame as $V_{\alpha 1}, V_{\beta 1}$ and $V_{\alpha 2}, V_{\beta 2}$ respectively. The transformation from $a-b-c$ reference frame to $\alpha-\beta$ reference frame is given in (2.4) and (2.5).

$$\begin{bmatrix} V_{\alpha 1} \\ V_{\beta 1} \end{bmatrix} = \begin{bmatrix} \cos(15^\circ) & \cos(105^\circ) & \cos(225^\circ) \\ \cos(105^\circ) & \cos(15^\circ) & \cos(135^\circ) \end{bmatrix} \begin{bmatrix} V_{a1} \\ V_{b1} \\ V_{c1} \end{bmatrix} \tag{2.4}$$

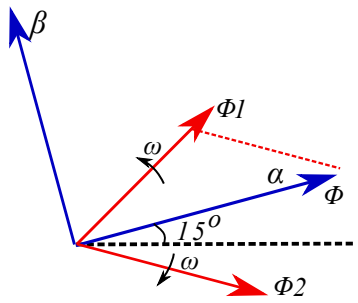

(a) Stationary reference frame, $\alpha - axis$ aligned in the direction of pulsating magnetic field.

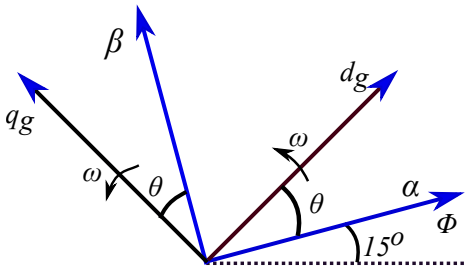

(b) The synchronous reference frame $d_g - q_g$, aligned with the grid angle ωt.

Fig. 2.7. Stationary and synchronous reference frames

$$\begin{bmatrix} V_{\alpha 2} \\ V_{\beta 2} \end{bmatrix} = \begin{bmatrix} \cos(15°) & \cos(135°) & \cos(255°) \\ \cos(75°) & \cos(45°) & \cos(165°) \end{bmatrix} \begin{bmatrix} V_{a2} \\ V_{b2} \\ V_{c2} \end{bmatrix} \tag{2.5}$$

During charging mode, the winding set $a1, b1, c1$ are connected to the grid supply V_a, V_b, V_c and the winding set $a2, b2, c2$ are connected to V_a, V_c, V_b respectively. The windings $a1$ is parallel with $a2$, $b1$ is parallel $c2$, and $b2$ is parallel with $c1$. Hence it can be written that,

$$V_{a1} = V_{a2} \ ; \ V_{b1} = V_{c2} \ ; \ V_{c1} = V_{b2} \tag{2.6}$$

Hence from (2.4) and (2.5) , it can be shown that

$$V_{\alpha 1} = V_{\alpha 2} \ \text{ and } \ V_{\beta 1} = -V_{\beta 2} \tag{2.7}$$

The model of the machine is derived by transforming the flux linkage of each winding of the split-phase machine [79] into the new reference frame defined above. The derived

model is given in (2.8) to (2.13).

$$V_{\alpha 1} = R_s I_{\alpha 1} + L_{ss}\frac{dI_{\alpha 1}}{dt} + L_{ss}(1-\sigma_{12})\frac{dI_{\alpha 2}}{dt} + L_{sr}\frac{dI_{r\alpha}}{dt} \tag{2.8}$$

$$V_{\beta 1} = R_s I_{\beta 1} + L_{ss}\frac{dI_{\beta 1}}{dt} + L_{ss}(1-\sigma_{12})\frac{dI_{\beta 2}}{dt} + L_{sr}\frac{dI_{r\beta}}{dt} \tag{2.9}$$

$$V_{\alpha 2} = R_s I_{\alpha 2} + L_{ss}\frac{dI_{\alpha 2}}{dt} + L_{ss}(1-\sigma_{12})\frac{dI_{\alpha 1}}{dt} + L_{sr}\frac{dI_{r\alpha}}{dt} \tag{2.10}$$

$$V_{\beta 2} = R_s I_{\beta 2} + L_{ss}\frac{dI_{\beta 2}}{dt} + L_{ss}(1-\sigma_{12})\frac{dI_{\beta 1}}{dt} + L_{sr}\frac{dI_{r\beta}}{dt} \tag{2.11}$$

$$V_{r\alpha} = R_r I_{r\alpha} + L_{sr}\frac{dI_{\alpha 1}}{dt} + L_{sr}\frac{dI_{\alpha 2}}{dt} + L_{rr}\frac{dI_{r\alpha}}{dt} \tag{2.12}$$

$$V_{r\beta} = R_s I_{r\beta} + L_{sr}\frac{dI_{\beta 1}}{dt} + L_{sr}\frac{dI_{\beta 2}}{dt} + L_{rr}\frac{dI_{r\beta}}{dt} \tag{2.13}$$

where, $I_{\alpha 1}, I_{\beta 1}$ are currents transformed from stator $a1, b1, c1$ reference frame to $\alpha - \beta$ reference frame, $I_{\alpha 2}, I_{\beta 2}$ are currents transformed from stator $a2, b2, c2$ reference frame to $\alpha - \beta$ reference frame. Similarly, $V_{r\alpha}, I_{r\alpha}$ are rotor voltages and currents along α-axis, L_{ss} is per-phase stator inductance of split-phase motor, L_{sr} is per-phase (stator referred) stator to rotor leakage inductance of split-phase machine, $(1-\sigma_{12})L_{ss}$ is the stator mutual inductance (coupling coefficient) between split-phase stator groups, ω is the grid frequency, R_s is stator resistance per-phase, and R_r is the stator referred rotor resistance per phase. Using (2.7), (2.8) to (2.10), the following equation is derived.

$$I_{\alpha 1} = I_{\alpha 2} \text{ and } I_{\beta 1} = -I_{\beta 2} \tag{2.14}$$

2.5.1.1 Motor Electromagnetic Torque - Charging Mode

The current components in stationary reference frame are defined as shown below.

$$\begin{bmatrix} I_{\alpha 1} \\ I_{\beta 1} \end{bmatrix} = \begin{bmatrix} \cos(15^\circ) & \cos(105^\circ) & \cos(225^\circ) \\ \cos(105^\circ) & \cos(15^\circ) & \cos(135^\circ) \end{bmatrix} \begin{bmatrix} I_{a1} \\ I_{b1} \\ I_{c1} \end{bmatrix} \tag{2.15}$$

$$\begin{bmatrix} I_{\alpha 2} \\ I_{\beta 2} \end{bmatrix} = \begin{bmatrix} \cos(15^\circ) & \cos(135^\circ) & \cos(255^\circ) \\ \cos(75^\circ) & \cos(45^\circ) & \cos(165^\circ) \end{bmatrix} \begin{bmatrix} I_{a2} \\ I_{b2} \\ I_{c2} \end{bmatrix} \tag{2.16}$$

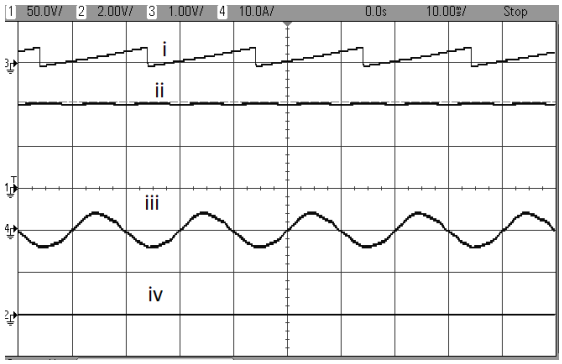

(a) Experimental results: (i) Estimated grid angle θ, (ii) DC-link voltage (50V/div), (iii) Y-phase current (10A/div), (iv) Estimated torque (from DAC) [78].

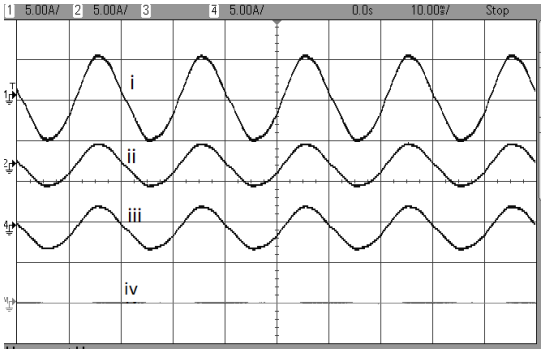

(b) (i) Y phase current (5A/div), (ii) Current through b1(5A/div), (iii) Current through c2 (5A/div), (iv) Current: (ii)-(iii).

Fig. 2.8. Experimental results on zero instantaneous torque inside the motor (experimental set up explained in 2.9)

.

Now, consider (2.14). Substituting this condition in (2.15) and in (2.16), the following condition can be concluded.

$$I_{a1} = I_{a2} \ ; \ I_{b1} = I_{c2} \text{ and } I_{c1} = I_{b2} \tag{2.17}$$

From (2.17), it can be noted that during charging mode of operation, the current from grid in each phase is equally divided between the corresponding parallel windings. Furthermore, this ensures that the flux in the air-gap is aligned along the α-axis and hence the emf induced in rotor will only be along α-direction. Hence $V_{r\beta}$ and $I_{r\beta}$ will be zero. Furthermore, the stator current along β axis is zero. These conditions are substituted for the generated instantaneous torque equation in (2.18).

$$\tau = \frac{2}{3} L_{sr} \left(I_\beta I_{r\alpha} - I_\alpha I_{r\beta} \right) = 0 \tag{2.18}$$

torque generated at every instant is zero and the machine will not even vibrate while charging the battery. There is no need of any eternal circuit or components to block the machine. Fig 2.8a shows the experimental result which will verify that the instantaneous torque generated inside the split-phase machine is zero (motor remains standstill) during the charging mode of operation.

2.5.2 Model in synchronous (grid) reference frame

From the stationary reference frame model, it was found that the currents through each parallel combination is equally divided and also that the instantaneous torque generated inside the machine is zero. But for the better understanding of the effect of pulsating flux on the unsymmetrical nature of stator windings and on the nature of grid currents drawn by the system, modeling is done in the rotating synchronous reference frame. The new reference frames are defined as d_g and q_g which are rotating synchronously in the same direction with the grid angle θ. The voltage vectors of the winding set $a1, b1, c1$ will rotate in the same direction of the reference frame as they have the same sequence as the grid voltage, but the winding set $a2, b2, c2$ will rotate in the opposite direction of the reference frame.

Let the voltages V_{dg1} and V_{qg1} be the transformed voltages in synchronously rotating reference frame corresponding to the voltages across the windings $V_{a1}, V_{b1}\text{and}V_{c1}$. Similarly let V_{dg2} and V_{qg2} be the voltages transformed from V_{a2}, V_{b2} and V_{c2} to the synchronously rotating reference frame. The transformation equations are shown in (2.19) to (2.21).

$$V_{dg1} + jV_{qg1} = (V_{\alpha 1} + jV_{\beta 1})\, e^{-j\theta} \tag{2.19}$$

$$V_{dg2} + jV_{qg2} = (V_{\alpha 2} + jV_{\beta 2})\, e^{j\theta} \tag{2.20}$$

$$V_{rdg} + jV_{rqg} = (V_{r\alpha} + jV_{r\beta})\, e^{-j\theta} \tag{2.21}$$

where, V_{rd_g}, V_{rq_g} represent rotor voltage vectors in $d-q$ axis. Now by substituting these equations, using the stationary reference frame model, the rotating reference model is derived as given in (2.22)-(2.27).

$$\begin{aligned} V_{d_{g1}} =& R_s I_{d_{g1}} + L_{ss} p I_{d_{g1}} + L_{ss}(1-\sigma_{12})(pI_{d_{g2}}\cos(2\theta) + pI_{q_{g2}}\sin(2\theta)) - \omega L_{ss} I_{q_{g1}} + \\ & \omega L_{ss}(1-\sigma_{12})(I_{q_{g2}}\cos(2\theta) - I_{d_{g2}}\sin(2\theta)) + L_{sr} p I_{rd_g} - \omega L_{sr} I_{rq_g} \end{aligned} \tag{2.22}$$

$$\begin{aligned} V_{q_{g1}} =& R_s I_{q_{g1}} + L_{ss} p I_{q_{g1}} + L_{ss}(1-\sigma_{12})(pI_{q_{g2}}\cos(2\theta) - pI_{d_{g2}}\sin(2\theta)) + \omega L_{ss} I_{d_{g1}} - \\ & \omega L_{ss}(1-\sigma_{12})(I_{d_{g2}}\cos(2\theta) + I_{q_{g2}}\sin(2\theta)) + L_{sr} p I_{rq_g} + \omega L_{sr} I_{rd_g} \end{aligned} \tag{2.23}$$

$$\begin{aligned} V_{d_{g2}} =& R_s I_{d_{g2}} + L_{ss} p I_{d_{g2}} + L_{ss}(1-\sigma_{12})(p I_{d_{g1}} \cos(2\theta) - p I_{q_{g1}} \sin(2\theta)) + \omega L_{ss} I_{q_{g2}} - \\ & \omega L_{ss}(1-\sigma_{12})(I_{q_{g1}} \cos(2\theta) + I_{d_{g1}} \sin(2\theta)) + L_{sr}(p I_{rd_g} \cos(2\theta) - p I_{rq_g} \sin(2\theta)) \\ & - \omega L_{sr}(I_{rd_g} \sin(2\theta) + I_{rq_g} \cos(2\theta)) \end{aligned} \tag{2.24}$$

$$\begin{aligned} V_{q_{g2}} =& R_s I_{q_{g2}} + L_{ss} p I_{q_{g2}} + L_{ss}(1-\sigma_{12})(p I_{q_{g1}} \cos(2\theta) + p I_{d_{g1}} \sin(2\theta)) - \omega L_{ss} I_{d_{g2}} + \\ & \omega L_{ss}(1-\sigma_{12})(I_{d_{g1}} \cos(2\theta) - I_{q_{g1}} \sin(2\theta)) + L_{sr}(p I_{rd_g} \sin(2\theta) + p I_{rq_g} \cos(2\theta)) \\ & + \omega L_{sr}(I_{rd_g} \cos(2\theta) - I_{rq_g} \sin(2\theta)) \end{aligned} \tag{2.25}$$

$$\begin{aligned} 0 =& R_r I_{rd_g} + L_{rr} p I_{rd_g} - L_{rr} \omega I_{rq_g} - \omega L_{sr} I_{q_{g1}} + L_{sr} p I_{d_{g1}} + L_{sr} p I_{d_{g2}} \cos(2\theta) + \\ & L_{sr} p I_{q_{g2}} \sin(2\theta) + \omega L_{sr} I_{q_{g2}} \cos(2\theta) - \omega L_{sr} I_{d_{g2}} \sin(2\theta) \end{aligned} \tag{2.26}$$

$$\begin{aligned} 0 =& R_r I_{rq_g} + L_{rr} p I_{rq_g} + L_{rr} \omega I_{rd_g} + L_{sr} p I_{q_{g1}} + \omega L_{sr} I_{d_{g1}} + L_{sr} p I_{q_{g2}} \cos(2\theta) - \\ & L_{sr} p I_{d_{g2}} \sin(2\theta) - \omega L_{sr} I_{d_{g2}} \cos(2\theta) - \omega L_{sr} I_{q_{g2}} \sin(2\theta) \end{aligned} \tag{2.27}$$

where, $I_{d_{g1}}, I_{q_{g1}}$ represent stator currents in $d-q$ axis transformed from $a1, b1, c1$ reference frame, $I_{d_{g2}}, I_{q_{g2}}$ represent stator current in $d-q$ axis transformed from $a2, b2, c2$ reference frame, I_{rd_d}, I_{rq_g} represent rotor currents in $d-q$ axis, L_{rr} is the stator referred rotor self-inductance of split-phase machine.
The two three-phase winding sets are connected in parallel during charging mode. Hence the total grid current in rotating reference frame I_{d_g} and I_{q_g}, that is the $d-q$ components of the grid currents are given by

$$I_{d_g} = I_{d_{g1}} + I_{d_{g2}} \quad \text{and} \quad I_{q_g} = I_{q_{g1}} - I_{q_{g2}} \tag{2.28}$$

Adding (2.22) and (2.24) and substituting (2.28) gives (2.29).

$$\begin{aligned} V_{d_g} =& R'_s I_{d_g} + L'_{ss} p I_{d_g} - \omega L'_{ss} I_{q_g} + L'_{ss}(1-\sigma_{12})(p I_{d_g} \cos(2\theta) - p I_{q_g} \sin(2\theta)) - \\ & \omega L'_{ss}(1-\sigma_{12})(I_{q_g} \cos(2\theta) + I_{d_g} \sin(2\theta)) + L'_{sr}(p I_{rd_g} \cos(2\theta) - p I_{rq_g} \sin(2\theta)) - \\ & \omega L'_{sr}(I_{rd_g} \sin(2\theta) + I_{rq_g} \cos(2\theta)) \end{aligned} \tag{2.29}$$

Subtracting (2.25) from (2.23) and substituting (2.28) gives (2.30).

$$\begin{aligned} V_{q_g} =& R'_s I_{q_g} + L'_{ss} p I_{q_g} + \omega L'_{ss} I_{d_g} - L'_{ss}(1-\sigma_{12})(pI_{q_g}\cos(2\theta) + pI_{d_g}\sin(2\theta)) + \\ & \omega L'_{ss}(1-\sigma_{12})(-I_{d_g}\cos(2\theta) + I_{q_g}\sin(2\theta)) - L'_{sr}(pI_{rd_g}\sin(2\theta) + pI_{rq_g}\cos(2\theta)) + \\ & \omega L'_{sr}(-I_{rd_g}\cos(2\theta) + I_{rq_g}\sin(2\theta)) \end{aligned} \tag{2.30}$$

where, $R'_s = \frac{R_s}{2}, L'_{ss} = \frac{L_{ss}}{2}$ and $L'_{sr} = \frac{L_{sr}}{2}$. (2.29) and (2.30) represent mathematical equations of the stator voltages in the synchronous rotating frame. From these equations, it can be seen that the voltages contain even harmonic terms, especially the second harmonic terms, in addition to the constant terms. Usually for a balanced system, the synchronous reference frame components will have only constant terms. This shows that the currents are unbalanced and they have even harmonic components in their $d-q$ components. To understand the unbalance further, the inductance matrix considering only the stator voltages and stator currents in $d-q$ reference frame (2.31) is given below.

$$\begin{bmatrix} V_{d_g} \\ V_{q_g} \end{bmatrix} = \begin{bmatrix} L_d\frac{d}{dt} - \omega M_1 & -\omega L'_{ss} - \omega M_2 - L_{dq}\frac{d}{dt} \\ \omega L'_{ss} - \omega M_2 - L_{dq}\frac{d}{dt} & L_q\frac{d}{dt} + \omega M_1 \end{bmatrix} \begin{bmatrix} I_{d_g} \\ I_{q_g} \end{bmatrix} \tag{2.31}$$

where, L_d(inductance in d-axis) $= L'_{ss} + L'_{ss}(1-\sigma_{12})\cos(2\theta)$
L_q(inductance in q-axis) $= L'_{ss} - L'_{ss}(1-\sigma_{12})\cos(2\theta)$
$M_1 = L'_{ss}(1-\sigma_{12})\sin(2\theta)$
$M_2 = L'_{ss}(1-\sigma_{12})\cos(2\theta)$ and
L_{dq}(Inductance between $d-q$ axis) $= L'_{ss}(1-\sigma_{12})\sin(2\theta)$
The following can be concluded from the above mathematical model.

1. For a system with symmetric winding and rotating magnetic field, the d-axis self inductance and q axis self inductance will be constant and equal. But as seen from the matrix, for the proposed IBC, the inductance L_d is different from L_q.

2. The inductance L_d and L_q are not constant values, but vary as a function of the grid angle θ.

3. For a balanced system there won't be any mutual coupling between the $d-axis$ and $q-axis$ induced voltage terms. But here a mutual coupling inductance term L_{dq} exists.

4. The $d-axis$ and $q-axis$ components of the grid current consists of even harmonic along with the dc terms, especially 100 Hz component which will not be present in a balanced system.

A proper controller needs to be designed to limit these even harmonic components in the current and make the grid currents balanced.

2.5.3 Verification of the proposed Mathematical Model

To verify the proposed mathematical model, the IBC was simulated using three different methods. In the first method, the split-phase machine model [44] was used. The six windings were given supply from the three-phase supply, and the windings were properly connected to act as interface inductance as described in the proposed configuration. In the second method, the mathematical model in stationary reference frame [(2.8) to (2.13)] were used and the IBC was simulated. In the third method, the mathematical model in synchronously rotating reference frame[(2.29) and (2.30)] were used and the IBC was simulated for the same condition. All the three models gave the same output at every instant. The d-axis current of the grid for all the three methods is shown in fig 2.9 and it is found to be equal at every instant, verifying the accuracy of the model even under transient conditions.

2.6 Control Structure of the IBC

The control block of IBC is shown in fig 2.12. The control of the system mainly has two steps, firstly the integration of IBC with the grid using the PLL, and secondly, the control of power flow between the grid and the inverter DC-link, thereby maintaining a constant DC-link voltage (instead of battery in the hardware setup) by proper control of front-end converter. In this, new current control methods are implemented to limit the unbalance in the grid currents, which will be discussed in the following sections.

2.6.1 Phase Locked Loop

A phase locked loop is used to synchronize the IBC to the grid. It consists of a PI controller that will force the grid voltage vector to align along any one of the axis of synchronous reference frame and the corresponding angular frequency is determined.

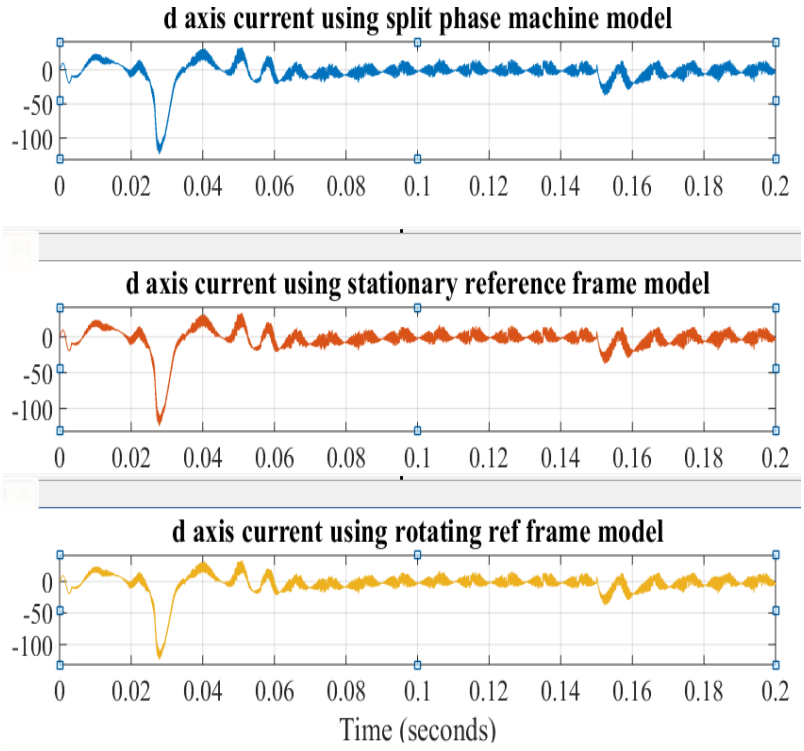

Fig. 2.9. Simulation results: Transient response phase current with step change in DC link voltage at 0.03 secs and step change in load current at 0.15 sec (i) d- axis current using split-phase machine model (ii) d- axis current using stationary reference frame model (iii) d- axis current using rotating reference frame model.

In the proposed IBC, the three-phase grid voltages are transformed into the $d-q$ reference frame described in 2.5.2. The components in $d-axis$ and $q-axis$ are named as V_{sd} and V_{sq} as shown in fig 2.10a. PLL is used to obtain the angular frequency of the grid, and thus the grid angle when the grid voltage is aligned along the q-axis. For that, as seen in fig 2.10b, the PI controller forces V_{sd} to become zero and the corresponding grid angular frequency is determined [120]. By integrating the angular frequency, the grid angle,θ is obtained. This will ensure that the resultant grid voltage vector V_s will be equal to the voltage vector along q-axis, V_{sq}. A deviation in grid frequency can cause an increase in error in grid frequency and the PI controller will force the error to become zero. However, if the frequency is known, feedforward term ω_{ff} (value nearer to the angular frequency) is added to the calculated angular frequency to eliminate the tracking error.

The grid angle, θ thus obtained, is used in the control of front-end converter by converting the different voltage and current variables into synchronously rotating frame which will rotate with the same frequency of the grid voltage.

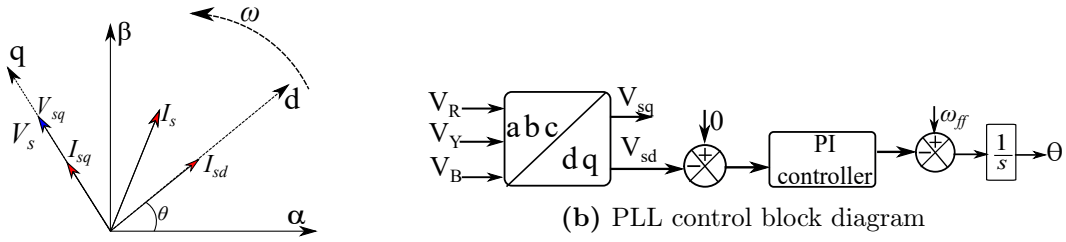

(a) Reference frame: Resultant grid voltage aligned along q-axis.

(b) PLL control block diagram

Fig. 2.10. PLL reference frame definition and the control block diagram.

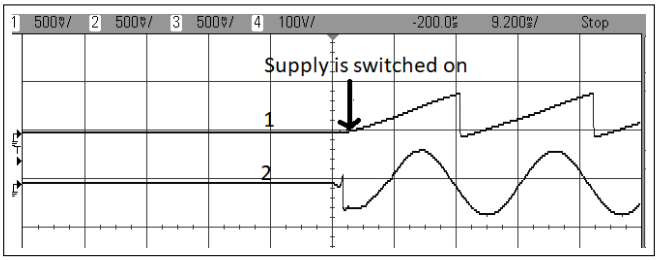

Fig. 2.11. Experimental result PLL output when the grid supply is switched on at: (1) Grid angle θ (2) Grid phase voltage (100 V/div)

The experimental result showing the estimated value of the grid angle θ as obtained from the PLL, that too in less than half a cycle of the grid voltage is shown in fig 2.11.

2.6.2 Front End Converter

Normally a diode bride rectifier is used to rectify the AC voltage into DC voltage. However, the rectifier will draw peaky currents from the grid which will disturb the grid. Front end converter is a controlled rectifier [73], developed using fully controlled semiconductor switches, which are modulated in such a way that it will draw sinusoidal currents at any required power factor. A detailed discussion on FEC is given in section 1.10.6.

In the proposed IBC, the three-legged inverter works as a front-end converter (FEC) while charging the battery. The real and reactive power can be controlled independently. Consider the real and reactive power equation in (2.32) and (2.33) respectively. For the proposed grid connected charger, the PLL ensures the voltage component along the $d-axis$ to be zero. Now substituting the condition that V_{sd} is zero in (2.32) and (2.33), it can be seen that the real and reactive power depends on I_{sq} and I_{sd} respectively. Thus,there is a decoupled control on the real and reactive

power.

$$p = V_{sq}I_{sq} + V_{sd}I_{sd} = V_{sq}I_{sq} \tag{2.32}$$

$$q = V_{sq}I_{sd} - V_{sd}I_{sq} = V_{sq}I_{sd} \tag{2.33}$$

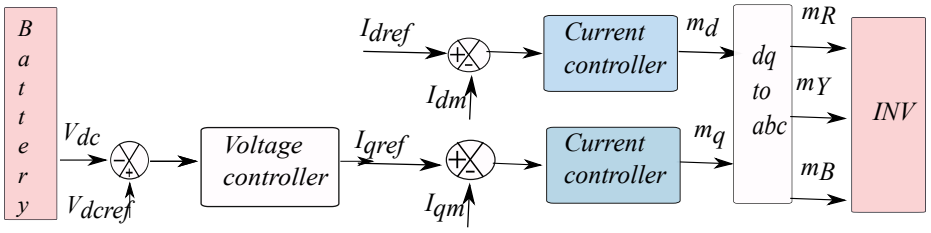

Fig. 2.12. Control structure of IBC with current controller in $d-q$ axis being replaced by different controllers.

The control block consists of an outer voltage control loop and an inner current control loop as shown in fig 2.12. The outer voltage control loop should ensure that the DC link voltage of the converter is maintained constant to the reference value. The required real power component of current to maintain the DC link voltage to the required level is the reference to the inner current controller.

The inner current controllers ($d-axis$ (reactive) and $q-axis$ (real)), ensures that the reference real and reactive power flows to the system by providing the corresponding pulse width modulated gating pulses to the three-legged converter. For unity power factor operation, the reference for d-axis current controller will be zero. Thus the three-phase inverter, acts as a front-end converter and maintains a constant DC link voltage by drawing the grid currents at unity power factor.

In actual EVs, the battery management system provides the reference current for the current controller based on the battery voltage, SoC and its temperature.

2.7 Current controllers for balancing the grid currents

As explained in earlier sections, due to the presence of pulsating magnetic field on the unsymmetrical motor windings, the current drawn from the grid will be unbalanced. As seen from the mathematical model, the result of unbalance is the presence of even harmonics in the $d-q$ components of the grid current ((2.29) and (2.30)). So the objective of the controllers is to limit the even harmonics in the $d-q$ components of

the grid current and to make the DC component of the grid current to be predominant and make the grid currents balanced. Hence in this chapter, three new current control schemes are implemented and compared to make the system balanced.

Case I: PI controller as the current controller

The most commonly used controller in $d-q$ reference frame for electric drive application is the PI controller. For a balanced system, when the variables in the grid reference frame ($a-b-c$ reference frame) are transformed into the synchronously rotating reference frame with respect to the grid ($d-q$ reference frame), the transformed variables will have only DC terms at steady state. And a proper controller that will provide zero steady state error for DC reference is the PI controller. Hence they are widely used as controller in electric drive applications. In the proposed work of IBC using split-phase machine, first control method is implemented using the PI controller as seen in fig 2.13, where K_P is the proportional gain, and K_I is the integral gain. Loop shaping method is used to design the gains of the controller. But as derived in the mathematical model, the $d-q$ component of grid currents, ie, I_{dg} and I_{qg}, ((2.29) and (2.30)) contains not only the DC terms, but also varying even harmonic terms that cannot be controlled effectively by the PI controllers.

Thus the resulting IBC with PI controller can maintain the DC link voltage at the reference value by drawing grid currents at upf. But the grid currents will be unbalanced in nature.

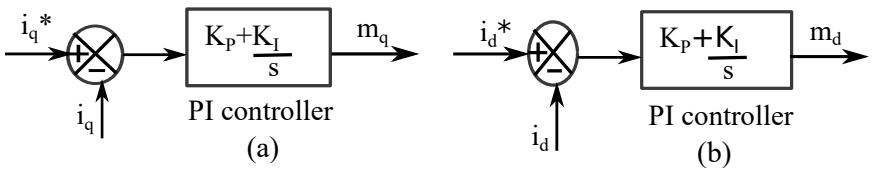

Fig. 2.13. Current control using PI controllers in (a) q - axis (b) d - axis [76].

Case II: PI as the current controller with feed-forward terms

By utilizing PI controller as current controller for both d and q axis current controllers, the even harmonic terms in the grid current were not properly controlled. But from the mathematical model of IBC, the terms in the machine voltages that contribute to the even harmonics are derived. These terms are utilized in the control loop as feed forward terms to nullify the even harmonics present in the system. The mathematical

model of the IBC ((2.29) and (2.30)), voltage terms contributing to the harmonics in the $d-q$ reference frame grid voltages are given. From this model the appropriate feed forward terms, V_{dff} and V_{qff} are derived ((2.34) and (2.35)) and given as feed-forward terms as shown in fig 2.14. Hence the PI current controller needs to correct only the static DC terms in the $d-q$ components of grid current for which it provides zero steady state error, and the feed forward terms will limit the even harmonic components. In the experimental set up, the stator current terms were only introduced as the feed forward terms.

$$\begin{aligned} V_{dff} = -\omega L'_{ss} I_{q_g} - \omega L'_{ss}(1-\sigma_{12})(I_{q_g}\cos(2\theta) + I_{d_g}\sin(2\theta)) \\ -\omega L'_{sr}(I_{rd_g}\sin(2\theta) + I_{rq_g}\cos(2\theta)) \end{aligned} \tag{2.34}$$

$$\begin{aligned} V_{qff} = \omega L'_{ss} I_{d_g} + \omega L'_{ss}(1-\sigma_{12})(-I_{d_g}\cos(2\theta) + I_{q_g}\sin(2\theta)) \\ +\omega L'_{sr}(-I_{rd_g}\cos(2\theta) + I_{rq_g}\sin(2\theta)) \end{aligned} \tag{2.35}$$

To implement the feed forward control all the machine parameter terms need to be

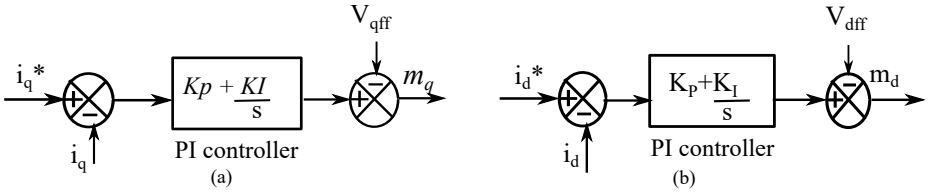

Fig. 2.14. Current control using PI controller and feed forward terms in (a) q- axis (b) d - axis.

calculated. Hence, open circuit and short circuit tests were conducted on the split-phase induction machine [44] and the winding self, mutual and leakage inductances were obtained that is given below. $L_{ss} = 80.13$mH; $\sigma_{12}L_{ss} = 1.05$mH; $L_{sr} = 76.8$mH; $L_{lr} = 2.28$mH;
$R_s = 1.05\Omega$; $R_r = 1.97\ \Omega$.
It can be seen from the results in section 2.9 that there is a significant reduction in the even harmonic components in I_{dg} and I_{qg} waveforms using feed forward control and the grid currents have been balanced to some extent.

Case III: PR controller for harmonic rejection with PI controller and feed-forward terms

With the use of feed forward terms, even harmonic terms were reduced to a large extent. The even harmonic terms in I_{dg} and I_{qg} mainly consists of 100 Hz component. To completely nullify the 100 Hz component, a PR controller is connected parallel with the PI controller as shown in fig 2.15. PR controllers provide zero steady state

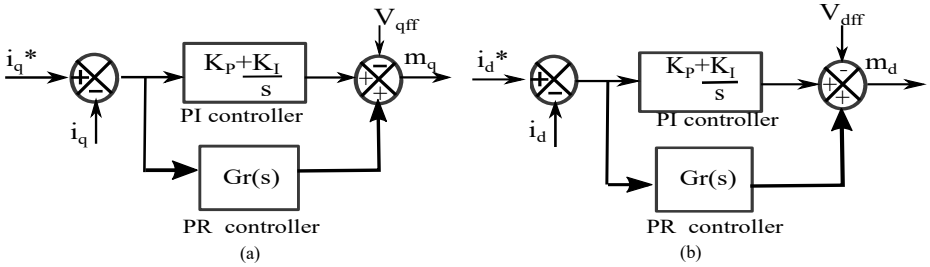

Fig. 2.15. Current control with second harmonic rejection using PR controller in (a) q-axis (b) d-axis.

error at a specified frequency of the reference signal [121], [122]. The transfer function of the PR controller is given in (2.36) [122].

$$G_r(s) = K_P + \frac{2K_i w_c s}{s^2 + 2w_c s + w_o^2} \tag{2.36}$$

The harmonic frequency for which the steady state error should be zero is given by w_o and the lower cut-off frequency is given by w_c. Here the PR controller gain values K_P and K_i are designed to provide complete rejection of 100 Hz component in the $d-q$ component of the grid current as referred in [76]. The experimental results provided in Section 2.9 shows that the 100 Hz component in I_{dg} and I_{qg} current waveforms have been nullified and the grid currents are almost balanced.

For actual electric vehicles, the battery management system continuously monitors the state of charge, state of health and the temperature of the battery cells using algorithms and provide the required current reference to the current controllers. Thus, there will not be an outer voltage control loop for the system.

2.8 Simulation Results

The proposed IBC with the derived model was simulated in MATLAB Simulink Version R2017b. A three-phase IBC using a split-phase machine of power capability up to

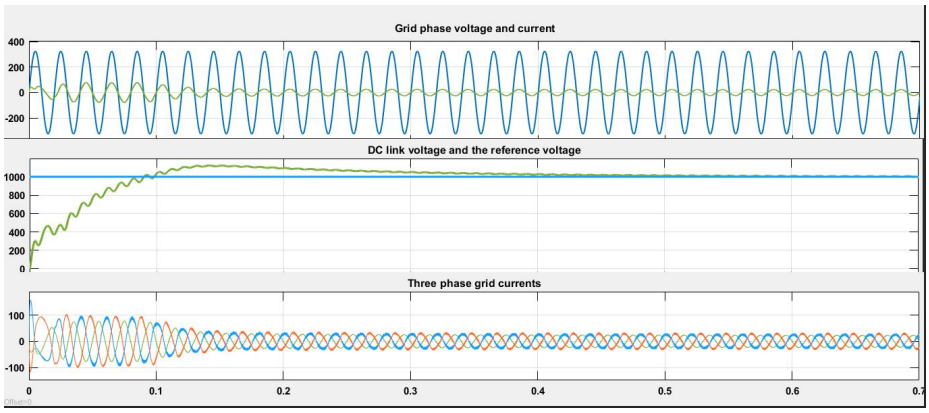

Fig. 2.16. Transient result at starting: The phase voltage and phase current, the DC link reference and actual voltage and the three-phase grid currents

20 kW was simulated. The machine parameters used for simulation are given below in table 2.2.

Table 2.2. Simulation - IBC parameters

DC link Voltage	1000 V
Stator self inductance L_{ss}	0.1627 H
Leakage inductance $\sigma_{12}L_{ss}$	9.635 mH
Mutual inductance between stator and rotor windings L_{sr}	0.1508 H
Stator resistance R_s	5 Ω
Rotor resistance R_r	3.4 Ω
Moment of inertia J	0.0165 kgm^2

The transient waveforms of the IBC at starting is shown in fig 2.16.It can be seen that the capacitor voltage settles at the reference value and the grid currents are drawn at unity power factor. From the steady state results shown in fig 2.17, it can be seen that the grid currents are not balanced as the three current waveforms are having different peak values and they are not pure sinusoidal in shape. The DC link currents and the DC link voltage along with the ripples can also be seen from the figure.

2.9 Experimental Results

A 11 kW, 415 V, 4-pole, three-phase induction machine rewound as a split-phase induction machine was used for the experiment. A three-phase inverter using 75 A,

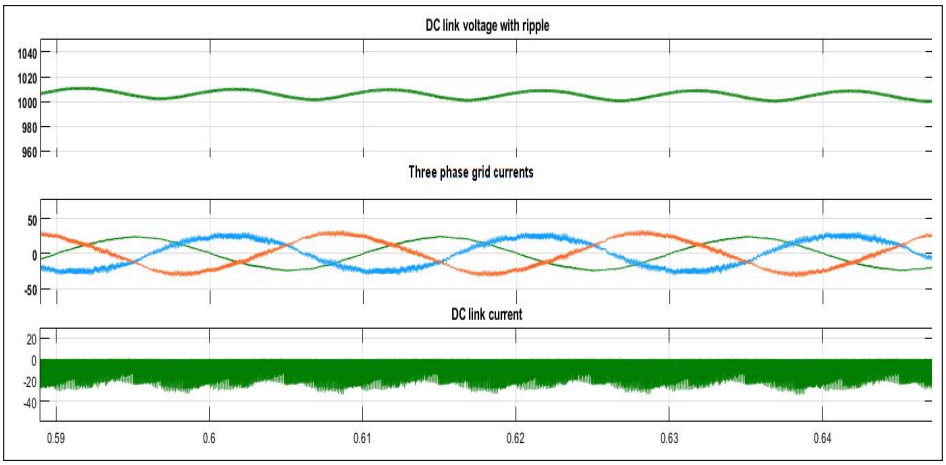

Fig. 2.17. Steady state results: The phase voltage and phase current, the three-phase grid currents, and the DC link currents.

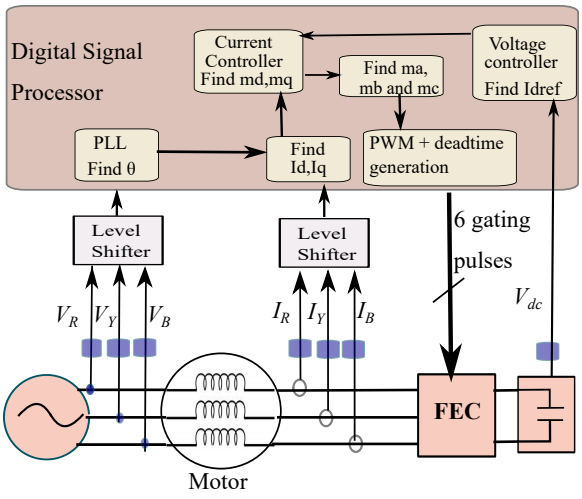

(a) Block diagram of various components in the experimental setup

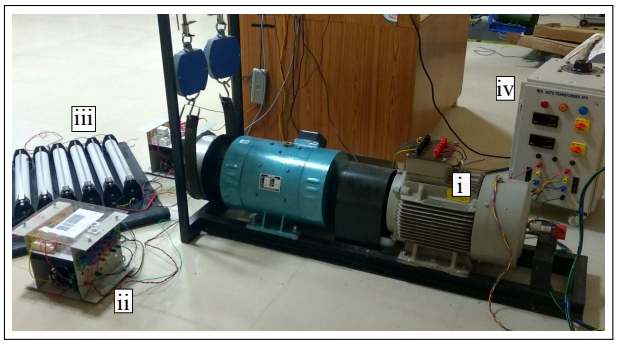

(b) Photograph of Experimental setup (i) Split-phase machine (ii) Inverter (iii) Load (iv) Autotransformer.

Fig. 2.18. Block diagram and photograph of the experimental set-up

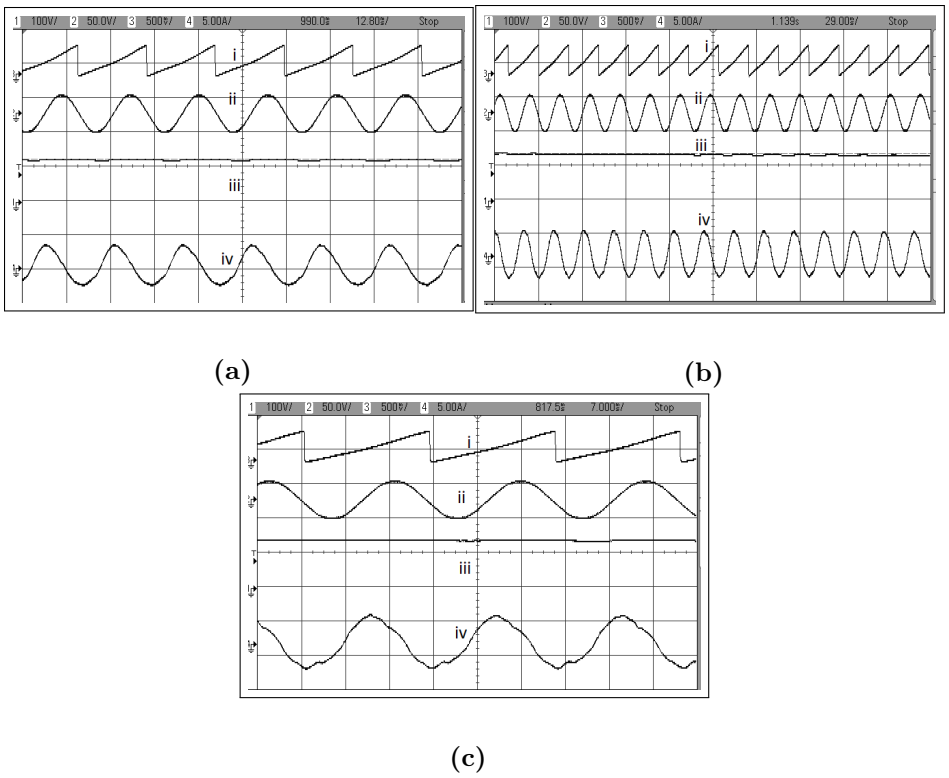

Fig. 2.19. Steady State results (phase voltage, phase current, DC-link voltage) of IBC during charging for a DC link voltage of 130 V for three control methods (a) PI controller (b) PI controller with feed forward (c) PI controller, feed forward and PR controller (i)Grid angle θ (6.28 rad/div) (ii) R Phase voltage (50V/div) (iii) DC link voltage (100V/div) (iv) Phase current (5A/div.)

1200 V IGBT half bridge modules (SKM75GB12T4) were used to work as front-end converter. The gate driver M57962L is used for driving the IGBT modules. The control part is implemented using TMS320F28377S 32-bit floating point microcontroller. LA55P current sensors were used to sense the three-phase grid currents. The block diagram of the components used for the experimental set-up is shown in fig 2.18a. There are three voltage sensors to sense the grid voltages, three current sensors to sense the grid currents, one voltage sensor to sense the DC link voltage, and level shifter and filter circuit to shift these signal and feed to the digital signal processor. The switching frequency was 5 kHz. The experimental set up is shown in fig 2.18b.

2.9.1 Steady State and Transient Results

fig 2.19 shows the steady state waveforms of IBCs while in charging mode for the three types of control methods. The DC voltage has settled at the reference value of 130 V while consuming grid currents at unity power factor. The transient waveforms

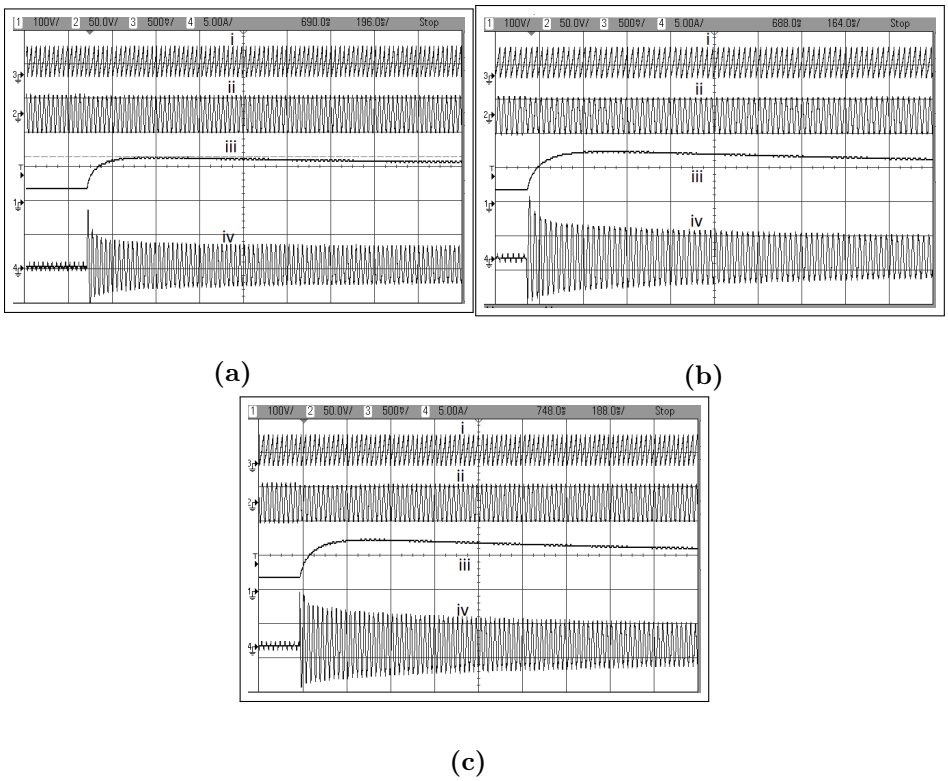

Fig. 2.20. Comparison of transient results (starting) for the three control methods (a) PI controller (b) PI controller with feed forward terms (c) PI controller, feed forward and PR controller (i)Grid angle θ (6.28 rad/div) (ii) R phase voltage (50 V/div) (iii) DC link voltage (100 V/div) (iv) Y phase current (5A/div.)

during the starting of charging of IBC is shown for the three control methods in fig 2.20.

2.9.2 Performance Analysis

Fig 2.21 shows the three-phase grid currents at steady state using all the three controllers for a DC link voltage of 182 V at 0.5 kW. The shape of grid currents gets better and balanced as we move from PI controller to PI controller with feed forward to PI controller with feed forward and PR controller. The fig 2.22 compares the harmonics in q-axis current. It can be seen from fig 2.22(a) that the q-axis current contains even harmonics especially the 100 Hz component. Using voltage feed forward along with PI controller the even harmonics, especially the 100 Hz component have been limited to a large extent as seen from fig 2.22(b). From fig 2.22(c) it is seen that the 100 Hz component has been completely eliminated using the PR controller along with the PI controller and voltage feed-forward terms.

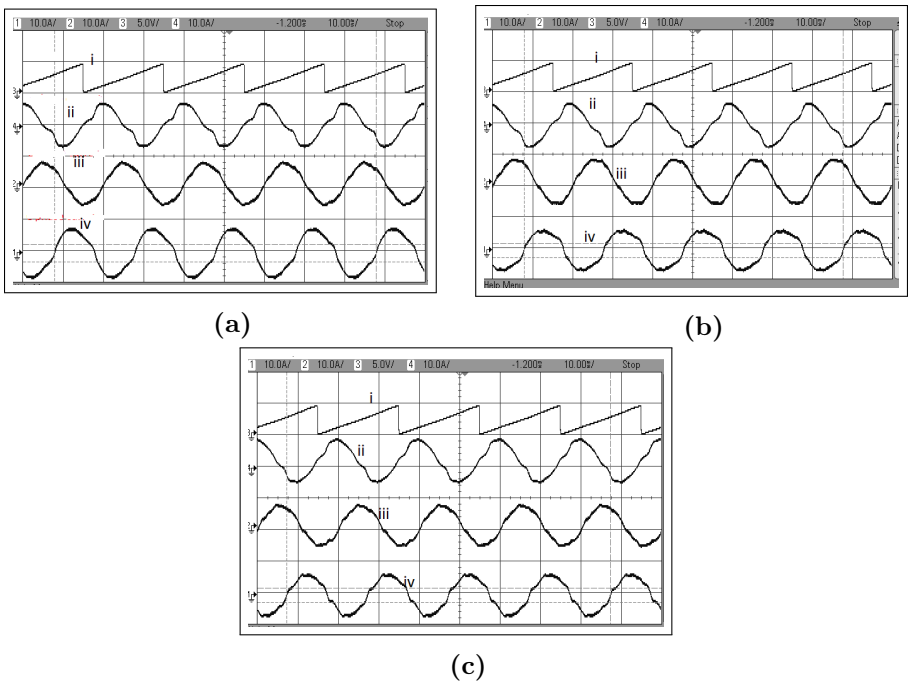

Fig. 2.21. Comparison of three-phase grid currents at steady state for the three control methods for a DC link voltage of 182V and load of 552W (a) PI controller (b) PI controller with feed forward terms (c) PI controller, feed forward and PR controller (i) Grid angle θ (6.28 rad/div) (ii) R phase current(10A/div) (iii) Y phase current (10A/div) (iv) B phase current (10A/div.)

The rms value of the three-phase currents using three different control methods are compared in Table. 2.3 for load of 330 W (Experimental result) and 20 kW (simulation). It can be seen from the table that by using voltage feed-forward and PR controller, the rms values of all the three-phase currents have become almost equal. Similarly Table. 2.4 gives the THD of grid currents for a load of 330 W (experimental result) and load of 20 kW (simulation result). Also the THD has improved with increase in load. Fig 2.23 provides the harmonic spectrum of a phase current for three different control methods for a load of 330 W.

Table 2.3. Comparison of rms value of three-phase currents for different controllers for load of 330 W and 20 kW.

Controller	330 W			20 kW		
	$I_R(A)$	I_Y(A)	I_B(A)	I_R(A)	I_Y(A)	I_B(A)
Case I PI controller	4.49	4.64	5.57	46.18	54.07	47.56
Case II PI with feed forward	4.54	5	4.7	49.68	51.39	51.79
Case III PI, PR, with feed forward	4.63	4.52	4.67	52.66	51.39	50.21

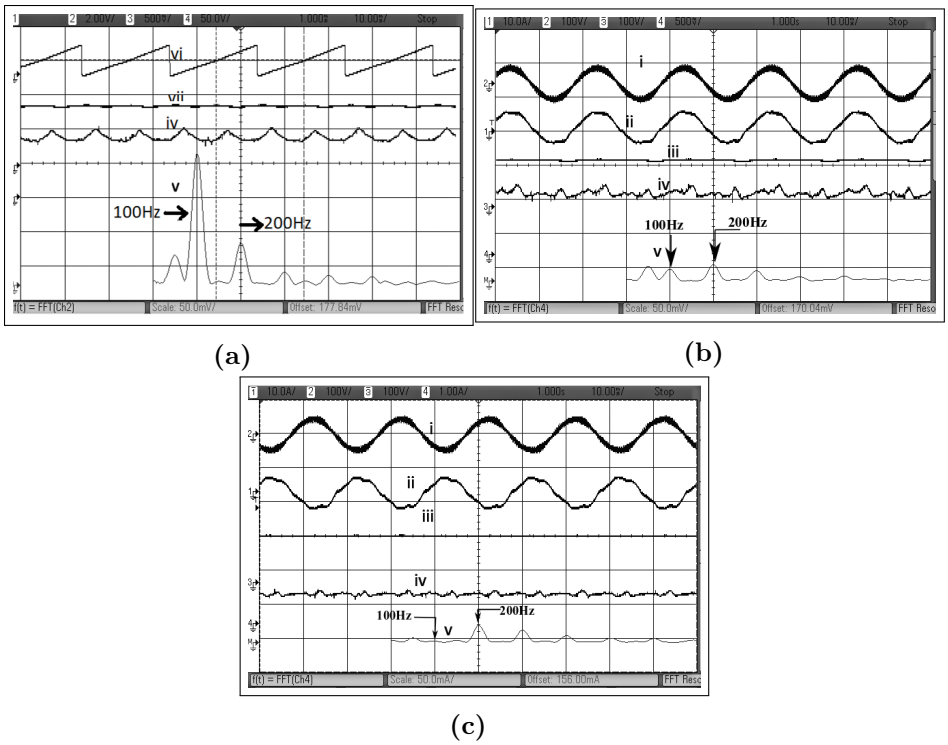

Fig. 2.22. Comparison of $q-axis$ component of grid current and its FFT analysis for the three control methods for a DC link voltage of 125V (a) PI controller (b) PI controller with feed forward terms (c) PI controller, feed forward and PR controller (i) Y phase voltage (100V/div) (ii) Y phase current (10A/div) (iii) DC link Voltage (100V/div) (iv) iq (40A/div) (v) FFT of (iv) with center at 200Hz (1V/div) (vi) Grid angle θ (6.28 rad/div) (vii) DC link voltage (50V/div.)

2.9.3 Calculation of Efficiency of IBC during charging

Efficiency is calculated for two power levels. A 500 W load using experimental setup and a 10 kW load from simulation results. The break-up for various losses for the two loads are shown in Table-III. For 500 W load, a DC link voltage of 300 V is considered. The inverter used for the experimental setup includes IGBT SKM75GB12T4. Inverter losses (switching and conduction losses) are calculated [123]. Following assumptions are made for calculating the power loss and efficiency. Switching frequency is 5 kHz, maximum current is 4.5 A per switch during charging for a load of 500 W, modulation index is assumed to be 0.8 at steady state. The rise time (39 ns), fall time (66 ns), and rated collector current (75 A) are provided in the data-sheet of the IGBT module. Short-circuit and open-circuit tests are conducted on the split-phase machine to measure the stator and rotor resistances [44]. The rms value of stator current was found to be 3.2 A for a load of 500 W. The efficiency was found to be 91.9%. For 10 kW load and maximum current of 15 A per switch, the efficiency was found to be

Table 2.4. Comparison of THD of three-phase currents for different controllers for a light load of 330 W and a high power load of 20 kW

Controller	330 W			20 kW		
	$I_{\text{R rms}}$	$I_{\text{Y rms}}$	$I_{\text{B rms}}$	$I_{\text{R rms}}$	$I_{\text{Y rms}}$	$I_{\text{B rms}}$
Case I PI controller	16.52%	7.5 %	14%	2.35%	4.75 %	5.74%
Case II PI with feed forward	13%	8.3%	11.5%	3.43%	4.43%	6.07%
Case III PI, PR, with feed forward	9.29%	8.96%	9.16%	3.25%	3.32%	5.1%

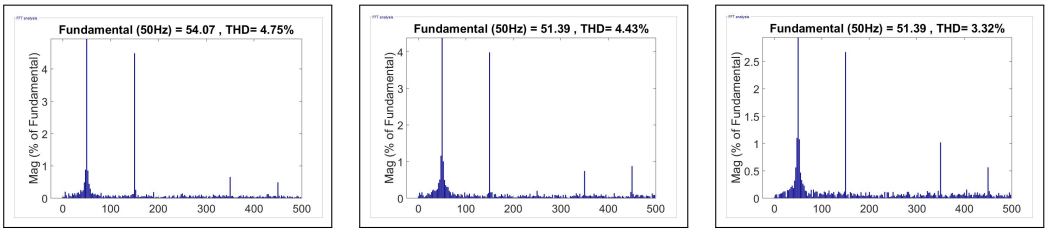

(a) **(b)** **(c)**

Fig. 2.23. Comparison of the FFT of Y phase grid current for the three control methods for a load of 20 kW (a) PI controller (b) PI controller with feed forward terms (c) PI controller, feed forward and PR controller (x-axis) Frequency(Hz).

93.5% as shown in Table. 2.5.

2.10 Conclusion

In this chapter, an integrated battery charger using a split-phase machine is discussed in detail, along with the mathematical model, simulation and experimental results. The working of the IBC using the existing three-phase machine with its reconfiguration into a split-phase machine is explained along with the windings diagrams. The usage of the existing three-legged inverter for driving mode and charging mode is also discussed. The connection to the windings in charging mode so as to generate

Table 2.5. Efficiency of the IBC

Power Component	Data 1	Data 2
Load	500 W	10 kW
Inverter Loss	7.2 W	48.537 W
Rotor copper loss (Rr = 1.97Ω)	20.17 W	283 W
Stator copper loss (Rs= 1.05Ω)	16.12 W	354.3 W
Efficiency	91.9%	93.5%

zero instantaneous torque is also discussed and proven mathematically. The issue of unbalance in grid currents due to the presence of pulsating flux on the asymmetrical winding arrangement of split-phase machine understood and the mathematical model of the system in stationary and synchronous reference frame is developed. The presence of even harmonics in the $d-q$ component of grid currents is found out. Different current control methods using the feed forward control and PR controllers is implemented and the grid current unbalance is limited to a large extent with the harmonic content in it limited to the IEEE standards. The advantages of the proposed topology are summarized below.

1. An IBC is developed using the existing three-phase machine and three-legged inverter inside the electric vehicle.

2. The power capability of IBC can be up to twice the motor power rating, and the maximum capability of the existing three-legged inverter. Thus a level-3 fast charging IBC is developed (It may be noted that the thermal aspects of the battery system should support the higher charging rate).

3. The proposed reconfiguration develops zero instantaneous torque inside the machine without any external blocking mechanisms while charging the battery and passing currents through the machine windings.

4. The proposed IBC is bidirectional in nature and hence can be used for vehicle to grid (V2G) operations and vehicle to load (V2L) as well.

5. There are minimal requirement of external components. Mainly, relay based contactors are used only for changeover of winding configuration of the machine from charging mode to driving mode.

6. The currents are drawn at unity power factor.

7. The THD of the grid currents are within the IEEE-519 standards.

8. This IBC can be charged from any location were the power supply is available. Also in fast charging stations if the DC chargers are not available, by providing high power AC outlets (minimal investment cost) and using the proposed level-3 IBC inside the EV, fast charging can be accomplished.

Simulation and experimental results are included to prove the concepts. Also, a high power IBC can be developed in all-wheel drive EVs, where two power drives

exists. Hence by utilizing the two power drives in parallel a fast charging IBC can be developed which will be discussed in detail in the next chapter.

Chapter 3

Parallel Operation of IBC using Split-Phase Machines for All-Wheel Drive Electric Vehicles

3.1 Introduction

In Chapter 2, the concept of IBC using a split-phase machine is discussed in detail. This proposed IBC has the advantage of utilizing the existing three-phase machine and three-legged inverter that is already present in the electric vehicle. Hence compared to other IBCs, there is no need to replace the existing system with multiphase machines and multi-legged inverters. Also while charging, it is mathematically proven that the instantaneous torque is zero, which implies that the motor won't vibrate while charging the battery [79]. The mathematical model of the IBC was developed and new control schemes were implemented to make the system balanced.

In the present chapter, a parallel combination of IBCs using the split-phase machine is discussed in detail [124], [125] which can be utilized in EVs have more than one motor in its powertrain and having a higher battery capacity, especially all-wheel drive EVs and heavy duty trucks. By connecting two IBCs in parallel, the power rating of the system is doubled, compared to a single IBC, and faster charging for the EV can be achieved from the existing system.

AWD EVs consist of two sets of inverters and motors that are capable of continuously providing power to all four wheels. They have independent control of the front wheel and back wheel torque, prevent wheel lock and slip, and hence have smooth driving ability on off-roads, snowy roads, and wet roads.

In chapter 2, the proposed IBC using a split-phase machine was found to have unbalanced grid currents, due to the asymmetrically placed machine windings in the presence of a pulsating magnetic field. The mathematical model of the IBC was derived and the inductance matrix was derived in the synchronously rotating reference frame. The grid current components in the $d-q$ axis were found to have even harmonic components along with the DC terms and feed-forward control was implemented to limit the unbalance. However, in the parallel IBC topology which is discussed in this chapter, the two motor windings are energized in such a way that the grid current unbalance is inherently canceled without any control effort. Each of the split-phase machines can be connected in six different configurations namely, $R-Y-B, R-B-Y, Y-B-R, Y-R-B, B-R-Y, B-Y-R$, with the grid. It is proposed in this work that when the first split-phase machine is connected in the $R-Y-B$configuration and the second split-phase machine is connected in $R-B-Y$ configuration, the unbalance that occurs in each of the single phase IBCs is canceled when connected in parallel. It will be seen that the individual IBC currents is unbalanced, but the grid currents are balanced. Mathematical proof for the same is included in this Chapter.

Also when two IBCs are connected in parallel with a common DC-link, there is a possibility of circulating current flowing within the two converters. In this chapter, the issue of circulating current, the factors affecting the flow of circulating current, and the control effort required to eliminate the circulating currents are discussed in detail. Circulating currents are inherent to parallel converter systems, and are mitigated by adopting a zero-sequence current-based modulation technique in this chapter. Mathematical derivations, simulation, and experimental results are included to verify the proposed concepts.

Section 3.2 gives the basic hardware layout of AWD vehicles. Section 3.3 explains the proposed topology on a parallel combination of IBCs, along with the mathematical derivations to prove that the grid currents are balanced. Section 3.4 discusses the issue of circulating currents, the factors on which it depends, and the control efforts required to reduce it. Section 3.5 discusses the control structure of the proposed system. Section 3.6 provides the simulation results to prove that the proposed parallel configuration cancels the grid current unbalance when compared to other possible configurations for parallel connection. Section 3.7 provides the experimental results in detail for various conditions. Section 3.8 concludes the chapter by summarizing the various features of the proposed system.

3.2 All Wheel Drive Electric Vehicles

Fig 3.1 shows the power train diagram for an AWD EV. It consists of two independent power trains on both the rear axle and front axle of the motor. The two powertrains provide higher torque when required, especially while driving through slippery, snowy, and wet road conditions by providing the required torque to the front and rear axle independently.

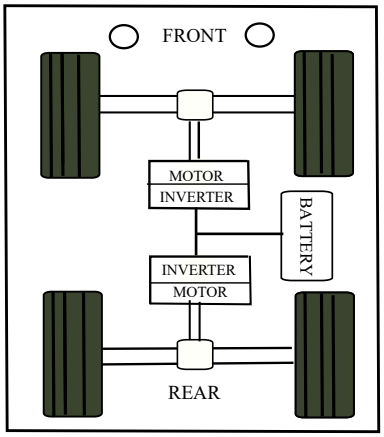

Fig. 3.1. Power train of an All Wheel Drive (AWD) Electric Vehicle

Different models of AWDs that are popular in the Indian and global markets are discussed in section. 1.3 and section. 1.4. From these market analysis, it has been found that both the front wheel and rear wheel axle power drives can have the same or different types of motor, with equal or unequal power rating, for example, Audi-e-tron has a permanent magnet synchronous machine of power rating 150 kW in its rear axle and an 80 kW induction motor in its front axle. But Tesla models had 2 induction motors of different power ratings in their front and rear axles. Jaguar-i-pace had two permanent magnet synchronous motors of the same power rating of 150 kW each on the front and rear axle.

Thus the motors can be of the same power rating or different power ratings. In this chapter, a parallel combination of the two power trains is utilized to charge the battery of the AWD at a higher power rating. Also, a new configuration for the two motor windings is proposed so that there is a natural cancellation of the grid current unbalance if the two motors are rated for the same power as in Jaguar-i-pace. If the motors are of different power ratings, there will be cancellation of unbalance in grid currents, as will be detailed in the next section.

Table 3.1. Pulsating Flux linkage in each phase for different configurations

Winding arrangement	Flux linkage in each phase winding		
	R- phase	Y- phase	B-phase
$R-Y-B$	Maximum	Minimum	Medium
$Y-R-B$	Minimum	Maximum	Medium
$R-B-Y$	Maximum	Medium	Minimum
$B-R-Y$	Minimum	Medium	Maximum
$B-Y-R$	Medium	Minimum	Maximum
$Y-B-R$	Medium	Maximum	Minimum

3.3 Parallel Operation of IBCs Using Split-Phase Machines

In all-wheel drives, there will be two sets of three-phase motors and a three-legged inverter, one on the front axis and the other on the rear axis for independent control of all four wheels. The two three-phase motors can be rewound as split-phase motors. As discussed in section 2.5.2, while in charging mode these split-phase motor windings can be connected in a proper way to pass grid currents through them without developing any instantaneous torque inside the motor.

Now there can be six different ways of connecting the split-phase windings between the grid and the FEC, which produces a pulsating magnetic field as shown in fig 3.2. Thus there can be a total of 36 possible combinations for two IBCs in parallel. Consider $R-Y-B$ configuration of winding arrangement for IBC, geometrically it can be found that the flux that links $a1, a2$ windings is maximum, the flux that links the windings $b1, c2$ is minimum, while the flux that links the windings $b2, c1$ is in between the two. Similarly, the flux linkage for different configurations on the three-phase windings is listed in Table. 3.1. From this table, it can be seen that for $R-Y-B$ winding configuration, the corresponding R-phase windings $a1, a2$ has maximum flux linkages, while for $Y-R-B$ configuration, the R-phase windings $b1, c2$ has minimum flux linkage. Thus the R-phase current in IBC using $R-Y-B$ configuration will have a maximum self-inductance effect and the R-phase current in $Y-R-B$ configuration will have a minimum inductance effect. Thus if these two configurations are connected in parallel, the R-phase current of the grid, which will be the sum of R-phase current of IBC-1 $(R-Y-B)$ and IBC-2 $(Y-R-B)$ will

have a natural cancellation of the effects of varying inductances. Similarly, the effect of flux linkage on the windings in each phase for different winding configurations is listed in Table. 3.1. of winding arrangement for IBC, geometrically it can be found that the flux that links $a1, a2$ windings is maximum, the flux that links the windings $b1, c2$ is minimum, while the flux that links the windings $b2, c1$ is in between the two. Similarly, the flux linkage for different configurations on the three-phase windings is listed in Table. 3.1.

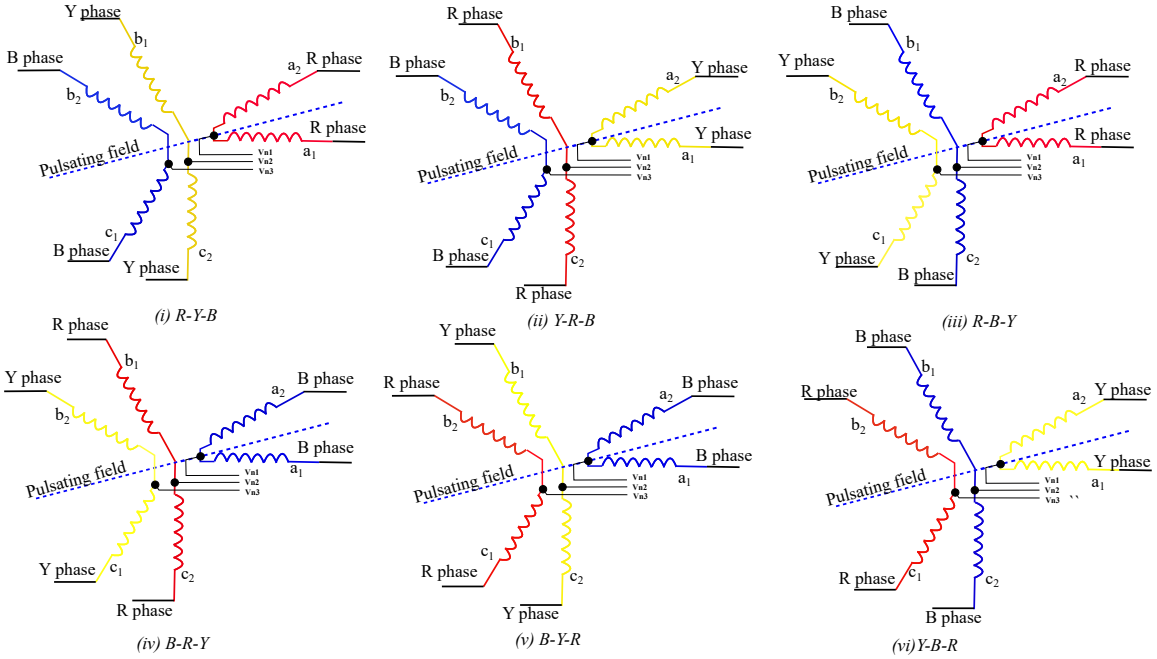

Fig. 3.2. Various configuration of split-phase windings that produce zero instantaneous torque

This assumption of balancing the effect of varying inductances based on geometry will be proved mathematically in the later sections. It will be proved later on that among the 36 possible combinations of parallel connection of motor windings, when the motor windings for the first IBC, i.e., IBC-1, are energized in $R-Y-B$ configuration and the windings of the second motor, i.e, IBC-2, are energized in $Y-R-B$ configuration, the unbalance was minimum and the grid currents were found to be balanced. Similarly, the other options where the system becomes balanced include the following.
IBC-1 /IBC-2: $(R-B-Y)$ and IBC-2 /IBC-1: $(B-R-Y)$
IBC-1 /IBC-2: $(B-Y-R)$ and IBC-2 /IBC-1: $(Y-B-R)$.

Fig 3.3 shows the block diagram of the parallel combination of IBCs using the split-phase machine. The rear axle and front axle motors can be reconfigured as split-phase machines. Along with their corresponding three-legged inverter, these two

power drives can be considered as two IBCs, namely IBC-1 and IBC-2, and can be connected in parallel as shown in fig 3.3. Here IBC-1 is given $R-Y-B$ configuration and IBC-2 is given $Y-R-B$ configuration. The windings $a1$ and $a2$ are connected in parallel between the grid R-phase and the inverter point V_{n1}, the windings $b1$ and $c2$ are connected in parallel between the grid Y-phase and the inverter point V_{n2}, the windings $b2$ and $c1$ are connected in parallel between the grid B-phase and the inverter point V_{n3}. The current through the motor windings of IBC-1, $a1, a2, b1, b2, c1$ and $c2$ are $I_{a1}, I_{a2}, I_{b1}, I_{b2}, I_{c1}$ and I_{c2} respectively. The input currents of IBC-1 are defined as follows.

$$\begin{aligned} I_R &= I_{a1} + I_{a2} \\ I_Y &= I_{b1} + I_{c2} \\ I_B &= I_{c1} + I_{b2} \end{aligned} \tag{3.1}$$

Similarly for IBC-2, the windings $a1'$ and $a2'$ are connected in parallel between the grid Y-phase and the inverter point $V_{n1'}$, the windings $b1$ and $c2$ are connected in parallel between the grid R-phase and the inverter point $V_{n2'}$, the windings $b2$ and $c1$ are connected in parallel between the grid B-phase and the inverter point $V_{n3'}$. The current through the motor windings, $a1', a2', b1', b2', c1'$ and $c2'$ are $I_{a1'}, I_{a2'}, I_{b1'}, I_{b2'}, I_{c1'}$ and $I_{c2'}$ respectively. The input currents of IBC-2 are defined as follows.

$$\begin{aligned} I_{Y'} &= I_{a1'} + I_{a2'} \\ I_{R'} &= I_{b1'} + I_{c2'} \\ I_{B'} &= I_{c1'} + I_{b2'} \end{aligned} \tag{3.2}$$

The grid currents, which are the sum of the currents of IBC-1 and IBC-2 are defined as follows.

$$\begin{aligned} I_{Rg} &= I_R + I_{R'} \\ I_{Yg} &= I_Y + I_{Y'} \\ I_{Bg} &= I_B + I_{B'} \end{aligned} \tag{3.3}$$

A mathematical model of the system is derived in the following section to prove that the proposed $R-Y-B$ / $Y-R-B$ configuration will minimize the unbalance in grid currents to minimum.

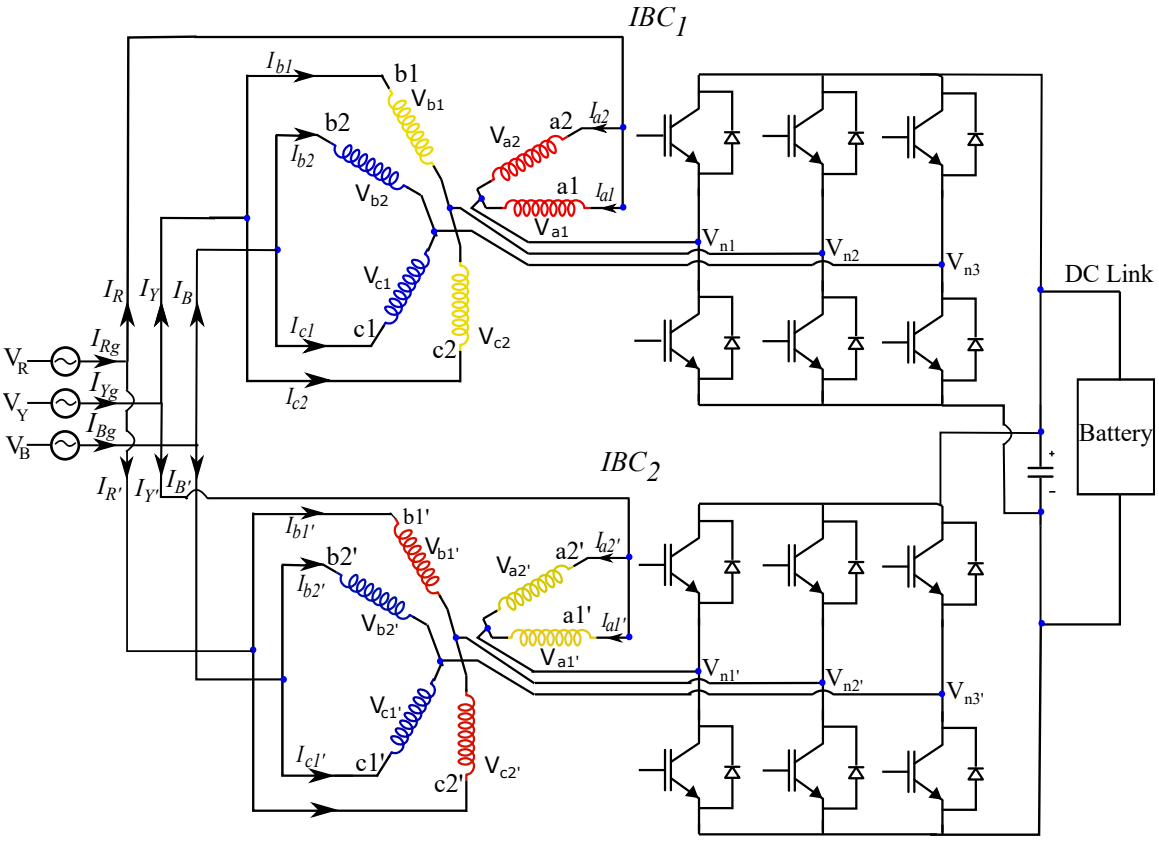

Fig. 3.3. Proposed Configuration of Parallel IBCs - ($R-Y-B$ and $Y-R-B$ phase sequences for IBC-1 and IBC-2 respectively.)

3.3.1 Model and Analysis of IBC-1

The winding arrangement of the split-phase machine for IBC-1 is shown in fig 3.4a. The IBC-1 motor windings are supplied with $R-Y-B$ phase sequence which is the same as that proposed in Chapter. 2. Hence the same model used for IBC-1 is used as shown below [79].

The stationary and synchronous rotating frames for modeling IBC-1 are shown in fig 3.4b. $\alpha-\beta$ is the stationary reference frame, and d_m-q_m is the synchronously rotating frame that rotates with the grid frequency ω. The α axis is aligned along the direction of pulsating magnetic field. The motor phase voltages are transformed into the defined reference frames using following equations.

$$\begin{bmatrix} V_{\alpha 1} \\ V_{\beta 1} \end{bmatrix} = \begin{bmatrix} \cos(15^\circ) & \cos(105^\circ) & \cos(225^\circ) \\ \cos(105^\circ) & \cos(15^\circ) & \cos(135^\circ) \end{bmatrix} \begin{bmatrix} V_{a_1} \\ V_{b_1} \\ V_{c_1} \end{bmatrix} \tag{3.4}$$

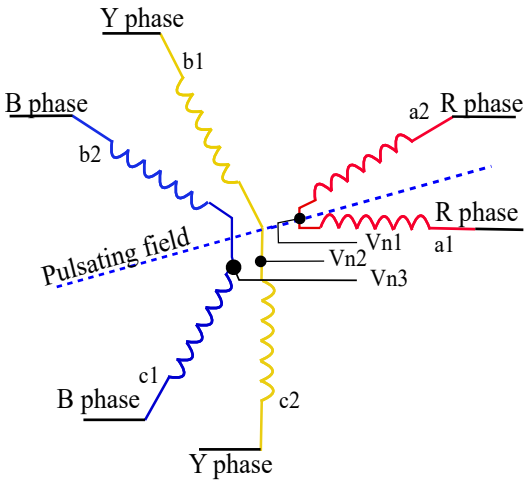

(a) $R-Y-B$ Winding configuration of split-phase machine

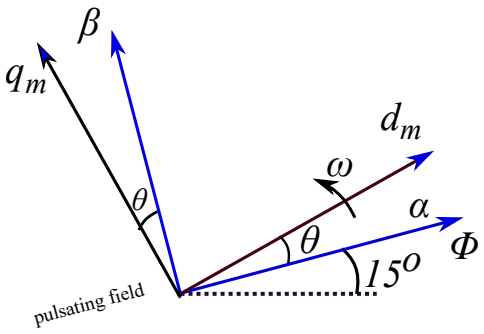

(b) Reference frame definition: Stationary and Synchronous reference frame

Fig. 3.4. IBC-1: $R-Y-B$ configuration and its reference frame

$$\begin{bmatrix} V_{\alpha 2} \\ V_{\beta 2} \end{bmatrix} = \begin{bmatrix} \cos(15^\circ) & \cos(135^\circ) & \cos(255^\circ) \\ \cos(75^\circ) & \cos(45^\circ) & \cos(165^\circ) \end{bmatrix} \begin{bmatrix} V_{a_2} \\ V_{b_2} \\ V_{c_2} \end{bmatrix} \tag{3.5}$$

Here, $V_{\alpha 1}, V_{\beta 1}$ are voltages corresponding to windings a_1, b_1, c_1 represented in the stationary reference frame and $V_{\alpha 2}, V_{\beta 2}$ are voltages corresponding to windings a_2, b_2, c_2. Since the windings are connected in parallel between the grid and inverter legs, the voltage across the phase windings are given by (3.6)-(3.8).

$$V_{a_1} = V_{a_2} \tag{3.6}$$

$$V_{b_1} = V_{c_2} \tag{3.7}$$

$$V_{c_1} = V_{b_2} \tag{3.8}$$

Similarly, the currents through the windings a_1, b_1, c_1 and a_2, b_2, c_2 can be transformed into the stationary reference frame as $I_{\alpha 1}, I_{\beta 1}$ and $I_{\alpha 2}, I_{\beta 2}$ respectively as shown below.

$$\begin{bmatrix} I_{\alpha 1} \\ I_{\beta 1} \end{bmatrix} = \begin{bmatrix} \cos(15^\circ) & \cos(105^\circ) & \cos(225^\circ) \\ \cos(105^\circ) & \cos(15^\circ) & \cos(135^\circ) \end{bmatrix} \begin{bmatrix} I_{a_1} \\ I_{b_1} \\ I_{c_1} \end{bmatrix} \tag{3.9}$$

$$\begin{bmatrix} I_{\alpha 2} \\ I_{\beta 2} \end{bmatrix} = \begin{bmatrix} \cos(15^\circ) & \cos(135^\circ) & \cos(255^\circ) \\ \cos(75^\circ) & \cos(45^\circ) & \cos(165^\circ) \end{bmatrix} \begin{bmatrix} I_{a_2} \\ I_{b_2} \\ I_{c_2} \end{bmatrix} \tag{3.10}$$

The equations to transform stationary reference frame into synchronous reference frame [76] is given in (3.11)-(3.13).

$$I_{dg1} + jI_{qg1} = (I_{\alpha 1} + jI_{\beta 1})\, e^{-j\omega t} \tag{3.11}$$

$$I_{dg2} + jI_{qg2} = (I_{\alpha 2} + jI_{\beta 2})\, e^{j\omega t} \tag{3.12}$$

$$I_{rdg} + jI_{rqg} = (I_{r\alpha} + jI_{r\beta})\, e^{-j\omega t} \tag{3.13}$$

where, $I_{d_{g1}}, I_{q_{g1}}$ and $I_{d_{g2}}, I_{q_{g2}}$ are the stator currents in rotating reference frame corresponding to the currents flowing through a_1, b_1, c_1 and a_2, b_2, c_2 windings respectively. Similarly I_{rd_g}, I_{rq_g} represent rotor current vectors in the rotating reference frame. The input phase currents to IBC-1, namely I_R, I_Y and I_B are transformed into I_{dm} and I_{qm} as shown in (3.14)-(3.15).

$$I_{dm} = I_{d_{g1}} + I_{d_{g2}} \tag{3.14}$$

$$I_{qm} = I_{q_{g1}} - I_{q_{g2}} \tag{3.15}$$

3.3.1.1 Inductance model and unbalance in IBC-1

The mathematical model of IBC using the split-phase machine in a rotating reference frame was derived in [79]. An inductance matrix was derived for stator voltages considering only the stator currents as is given in (3.16).

$$\begin{bmatrix} V_{d_m} \\ V_{q_m} \end{bmatrix} = \begin{bmatrix} L_d \frac{d}{dt} - \omega M_1 & -\omega L'_{ss} - \omega M_2 - L_{dq} \frac{d}{dt} \\ \omega L'_{ss} - \omega M_2 - L_{dq} \frac{d}{dt} & L_q \frac{d}{dt} + \omega M_1 \end{bmatrix} \begin{bmatrix} I_{d_m} \\ I_{q_m} \end{bmatrix} \tag{3.16}$$

where, ω = grid frequency
L_{ss} = stator inductance per phase of split-phase motor
$L'_{ss} = \frac{L_{ss}}{2}$
L_d (inductance in d-axis) $= L'_{ss} + L'_{ss}(1 - \sigma_{12})\cos(2\omega t)$
L_q (inductance in q-axis) $= L'_{ss} - L'_{ss}(1 - \sigma_{12})\cos(2\omega t)$
$M_1 = L'_{ss}(1 - \sigma_{12})\sin(2\omega t)$
$M_2 = L'_{ss}(1 - \sigma_{12})\cos(2\omega t)$ and

L_{dq} (Inductance between $d-q$ axis) $= L'_{ss}(1-\sigma_{12})\sin(2\omega t)$
$(1-\sigma_{12})L_{ss}$ = stator mutual inductance (coupling coefficient) between split-phase stator groups

From the inductance matrix of the IBC, the inductance terms are found to vary with the grid frequency. There exists a mutual inductance term L_{dq}, between the orthogonal rotating d and q axis which will be absent for a balanced system. Also, the d axis inductance term and q axis inductance terms are different, whereas, for a balanced system, they are equal. Hence from the above matrix, it can be seen that the presence of a pulsating field on the unsymmetrical windings of the split-phase machine makes the system unbalanced.

3.3.2 Modeling and Analysis of IBC-2

Similar to the modeling of IBC-1, the IBC-2 model is developed by considering the split-phase machine as two sets of three-phase windings. The first set of windings a'_1, b'_1, c'_1 is excited with the V_Y, V_R, V_B of the grid voltage, while the second set of windings a'_2, b'_2, c'_2 is excited with the opposite phase sequence, V_Y, V_B, V_R of the grid voltage. Thus both sets of three-phase windings produce rotating flux in opposite directions resulting in a net pulsating flux to be generated inside the motor and the machine will not rotate while charging the battery. Fig 3.5a shows the winding configuration of split-phase windings of IBC-2 when in charging mode.

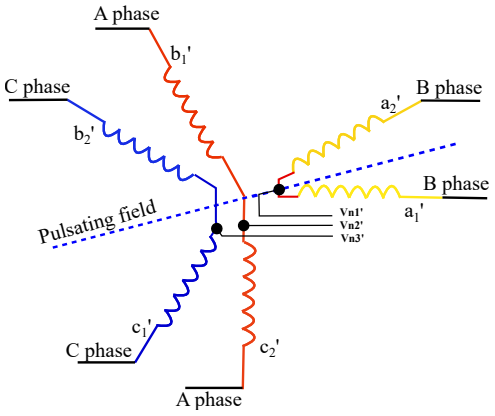

(a) $Y-R-B$ winding configuration of split-phase machine

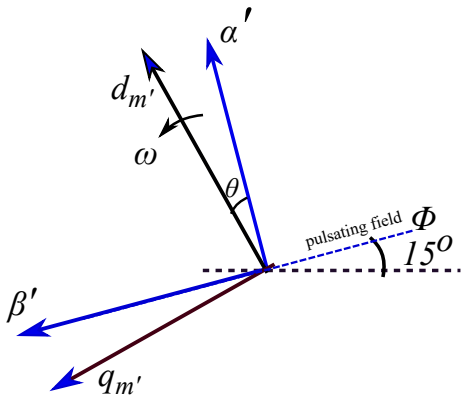

(b) d-q reference frame for IBC-2

Fig. 3.5. IBC-2: $Y-R-B$ Winding configuration and reference frame

The voltage and current variables are converted to stationary reference frame in

(3.17) and (3.18) similar to IBC-1 model.

$$\begin{bmatrix} V_{\alpha 1'} \\ V_{\beta 1'} \end{bmatrix} = \begin{bmatrix} \cos(15^\circ) & \cos(105^\circ) & \cos(225^\circ) \\ \cos(105^\circ) & \cos(15^\circ) & \cos(135^\circ) \end{bmatrix} \begin{bmatrix} V_{a'_1} \\ V_{b'_1} \\ V_{c'_1} \end{bmatrix} \tag{3.17}$$

$$\begin{bmatrix} V_{\alpha 2'} \\ V_{\beta 2'} \end{bmatrix} = \begin{bmatrix} \cos(15^\circ) & \cos(135^\circ) & \cos(255^\circ) \\ \cos(75^\circ) & \cos(45^\circ) & \cos(165^\circ) \end{bmatrix} \begin{bmatrix} V_{a'_2} \\ V_{b'_2} \\ V_{c'_2} \end{bmatrix} \tag{3.18}$$

Here, $V_{\alpha 1'}$, $V_{\beta 1'}$ and $V_{\alpha 2'}$, $V_{\beta 2'}$ are the voltages transformed to stationary reference frames corresponding to voltages across windings a'_1, b'_1, c'_1 and a'_2, b'_2, c'_2 respectively. As seen in fig 3.5a the voltage across the windings for $Y - R - B$ phase sequence is given by (3.19).

$$V_{a'_1} = V_{a'_2} \tag{3.19}$$

$$V_{b'_1} = V_{c'_2} \tag{3.20}$$

$$V_{c'_1} = V_{b'_2}; \tag{3.21}$$

Hence it can be proved that,

$$V_{\alpha 1'} = V_{\alpha 2'}; \quad V_{\beta 1'} = -V_{\beta 2'} \tag{3.22}$$

Similarly, the currents through the windings a'_1, b'_1, c'_1 and a'_2, b'_2, c'_2 can be transformed into the stationary reference frame as $I_{\alpha 1'}, I_{\beta 1'}$ and $I_{\alpha 2'}, I_{\beta 2'}$ respectively as shown below.

$$\begin{bmatrix} I_{\alpha 1'} \\ I_{\beta 1'} \end{bmatrix} = \begin{bmatrix} \cos(15^\circ) & \cos(105^\circ) & \cos(225^\circ) \\ \cos(105^\circ) & \cos(15^\circ) & \cos(135^\circ) \end{bmatrix} \begin{bmatrix} I_{a'_1} \\ I_{b'_1} \\ I_{c'_1} \end{bmatrix} \tag{3.23}$$

$$\begin{bmatrix} I_{\alpha 2'} \\ I_{\beta 2'} \end{bmatrix} = \begin{bmatrix} \cos(15^\circ) & \cos(135^\circ) & \cos(255^\circ) \\ \cos(75^\circ) & \cos(45^\circ) & \cos(165^\circ) \end{bmatrix} \begin{bmatrix} I_{a'_2} \\ I_{b'_2} \\ I_{c'_2} \end{bmatrix} \tag{3.24}$$

When the mathematical model of IBC-1 and IBC-2 are compared using (3.4), (3.5), (3.6), (3.17), (3.18) and (3.41), it can be seen that the variables in α' axis of IBC-2 corresponds to the voltages in β axis of IBC-1. Similarly, the variables in the β' axis of

IBC-2 correspond to variables in the $-\alpha$ axis of IBC-1. In other words, the stationary reference frame $\alpha' - \beta'$ of IBC-2 is shifted by 90° from stationary frame $\alpha - \beta$ of IBC-1. The reference frames of IBC-2 are shown in fig 3.5b. The equations to transform from stationary reference frame to synchronous reference frame for IBC-2 are given by (3.25).

$$I_{dg1'} + jI_{qg1'} = (I_{\alpha 1'} + jI_{\beta 1'})\, e^{j\omega t} \tag{3.25}$$

$$I_{dg2'} + jI_{qg2'} = (I_{\alpha 2'} + jI_{\beta 2'})\, e^{-j\omega t} \tag{3.26}$$

$$I_{rdg'} + jI_{rqg'} = (I_{r\alpha'} + jI_{r\beta'})\, e^{-j\omega t} \tag{3.27}$$

where, $I_{d'_{g1}}, I_{q'_{g1}}$ and $I_{d'_{g2}}, I_{q'_{g2}}$ are the stator currents in rotating reference frames corresponding to the currents through a'_1, b'_1, c'_1 and a'_2, b'_2, c'_2 windings respectively. Similarly I'_{rd_g}, I'_{rq_g} represent rotor current vectors in rotating reference frame. The input phase currents to IBC-2, namely I'_R, I'_Y and I'_B are transformed into I'_{dm} and I'_{qm} as shown in (3.28) and (3.29).

$$I'_{dm} = I_{d'_{g1}} + I_{d'_{g2}} \tag{3.28}$$

$$I'_{qm} = I_{q'_{g2}} - I_{q'_{g1}} \tag{3.29}$$

3.3.2.1 Inductance and unbalance in IBC-2

Inductance matrix of IBC-2 is derived in (3.30) similar to IBC-1.

$$\begin{bmatrix} -V_{q'_m} \\ V_{d'_m} \end{bmatrix} = \begin{bmatrix} L_d \frac{d}{dt} - \omega M_1 & -\omega L'_{ss} - \omega M_2 - L_{dq} \frac{d}{dt} \\ \omega L'_{ss} - \omega M_2 - L_{dq} \frac{d}{dt} & L_q \frac{d}{dt} + \omega M_1 \end{bmatrix} \begin{bmatrix} -I_{q'_m} \\ I_{d'_m} \end{bmatrix} \tag{3.30}$$

Similar to IBC-1, IBC-2 is also an unbalanced system and the motor input currents, I'_R, I'_Y and I'_B are not purely sinusoidal. Inductance terms are time-varying functions of the grid angle. Also, mutual inductance exists between the two orthogonal rotating d and q axes similar to IBC-1.

3.3.3 Proposed IBC System for AWD EVs - Parallel configuration of IBC-1 and IBC-2

From the previous section on the modeling, it is seen that both IBC-1, with $R-Y-B$ winding configuration, and IBC-2 with $Y-R-B$ winding configuration are unbalanced

systems. Now for AWD EVs, having two drive trains, it is proposed to connect IBC-1 and IBC-2 in parallel with the new configuration, namely $R-Y-B$ / $Y-R-B$ configuration. It was described geometrically in the previous section that this proposed configuration will reduce the unbalance. In this section, the mathematical model of the parallel system using the mathematical model of IBC-1 and IBC-2 is derived.

The grid currents I_{R_g}, I_{Y_g} and I_{B_g} is the sum of the phase currents to IBC-1 and IBC-2 as given in (3.31).

$$\begin{aligned} I_{R_g} &= I_R + I_{R'}; \\ I_{Y_g} &= I_Y + I_{Y'}; \\ I_{B_g} &= I_B + I_{B'}; \end{aligned} \tag{3.31}$$

The grid currents in synchronous reference frame, I_{dg} and I_{qg} is the sum of the currents in IBC-1 and IBC-2 as shown in (3.32).

$$\begin{aligned} I_{dg} &= I_{d_m} + I_{d'_m}; \\ I_{qg} &= I_{q_m} + I_{q'_m} \end{aligned} \tag{3.32}$$

3.3.3.1 Inductance matrix of the parallel system

The two IBCs are connected in parallel. Hence the equations (3.16) and (3.30) are added up to form (3.33) as shown below.

$$\begin{aligned} \begin{bmatrix} V_{d_m} \\ V_{q_m} \end{bmatrix} + \begin{bmatrix} V_{d'_m} \\ V_{q'_m} \end{bmatrix} = &\begin{bmatrix} L_d\frac{d}{dt} - \omega M_1 & -\omega L'_{ss} - \omega M_2 - L_{dq}\frac{d}{dt} \\ \omega L'_{ss} - \omega M_2 - L_{dq}\frac{d}{dt} & L_q\frac{d}{dt} + \omega M_1 \end{bmatrix} \begin{bmatrix} I_{d_m} \\ I_{q_m} \end{bmatrix} \\ &+ \begin{bmatrix} L_q\frac{d}{dt} + \omega M_1 & -\omega L'_{ss} + \omega M_2 + L_{dq}\frac{d}{dt} \\ \omega L'_{ss} + \omega M_2 + L_{dq}\frac{d}{dt} & L_d\frac{d}{dt} - \omega M_1 \end{bmatrix} \begin{bmatrix} I_{d'_m} \\ I_{q'_m} \end{bmatrix} \end{aligned} \tag{3.33}$$

It can be seen from (3.33) that the variable inductance terms that depend upon the angular frequency ω and the grid angle θ of IBC-1 is opposite to the corresponding terms in IBC-2. Thus the unbalance in IBC-1 is canceled by unbalance in IBC-2. Assuming an ideal case, where the load is equally shared between the two IBCs, and the input currents of IBC-1 and IBC-2 are equal, i.e., $I_{d_m} = I_{d'_m}$ and $I_{q_m} = I_{q'_m}$, then (3.33) reduces to (3.34).

$$\begin{bmatrix} V_{d_m} \\ V_{q_m} \end{bmatrix} + \begin{bmatrix} V_{d'_m} \\ V_{q'_m} \end{bmatrix} = \begin{bmatrix} L'_{ss} & -\omega L'_{ss} \\ \omega L'_{ss} & L'_{ss} \end{bmatrix} \begin{bmatrix} I_{d_g} \\ I_{q_g} \end{bmatrix} \tag{3.34}$$

(3.34) represents the inductance matrix of a balanced system. From the model of the system, the following things can be observed.

1. There is a natural cancellation of variable terms in the inductance matrix of IBC-1 and IBC-2, using the proposed $R-Y-B$ / $Y-R-B$ configuration.

2. There is complete cancellation of the variable terms and mutual inductance terms of IBC-1 and IBC-2 if both the systems have the same power level and have having same machine parameters. The inductance in the d axis and q axis are equal, they are not a function of the grid angle θ and there is no mutual inductance between the d and q axis, and the proposed topology behaves like a balanced system.

3. There will still be a reduction in unbalance but not complete cancellation if the IBC-1 and IBC-2 have different machine parameters.

Similarly two more configurations for parallel IBCs are possible which can reduce the unbalance. These are
(i) IBC-1 /IBC-2: $R-B-Y$, IBC-2 /IBC-1: $B-R-Y$
(ii) IBC-1 /IBC-2: $Y-B-R$, IBC-2 /IBC-1: $B-Y-R$

3.4 Circulating Current in the proposed parallel configuration

When two converters are connected in parallel, there can be a path for a current to circulate between the two converters producing losses and reducing the lifetime of the semiconductor devices. The circulating current may flow when there is a difference in the pole voltage of the same phase between the parallel connected converters. This can happen in the following cases.

1. Whenever an interleaving of carriers between the two parallel converters is implemented to remove the switching frequency ripple component in the load current. Due to interleaving in carriers, there will be a difference in pole voltage between the same phase in both the converters, which creates a difference in voltages and causes a current to circulate through the parallel system. The interleaving of carriers causes a high-frequency circulating current.

2. Whenever there is a difference in pole voltage of two converters because of the difference in interface inductance or impedance between the two converters and the input pole voltage of the two converters are different. This difference causes the flow of a low-frequency circulating current through the system.

In the proposed topology, there is a difference in interface inductance between each phase of inverter-1 and inverter-2. Hence the input voltage that comes across each phase of inverter-1 will be different from that of inverter-2. Hence there will be a presence of low-frequency circulating current through the system.

Also, in the proposed parallel system, the interleaving of carriers is not implemented between the inverters of IBC-1 and IBC-2. This is because IBC-1 has an $R-Y-B$ configuration and IBC-2 has $Y-R-B$ configuration. Hence the pole voltage of each phase of the front-end converter of IBC-1 will not be the same as that of the pole voltage of the front-end converter of IBC-2. Hence there won't be any harmonic suppression for the parallel combination of the two converters by interleaving the carriers. Hence, as the two converters are modulated with same carriers without any interleaving, there won't be much high-frequency circulating current in the system. Thus in the proposed system, the following points can be summarized about the circulating current.

1. There will be a presence of a low-frequency circulating current due to the difference in interface inductance between the same phases of IBC-1 and IBC-2.

2. There won't be any high-frequency circulating current as there is no interleaving of carriers being implemented in this proposed topology.

The circulating current flowing through the system will be due to the zero sequence terms [126]. Here, the zero sequence model of the system is derived to find the behavior of the zero sequence circulating current. It should be known what factors the low frequency circulating current is created, to limit the current. Thus the zero sequence model of the system needs to be derived.

3.4.1 Zero Sequence Current of IBC-1

The instantaneous voltage across winding each winding of the split-phase machine of IBC-1 can be written as in (3.35) to (3.40).

$$\begin{aligned} V_{a1} =& RI_{a1} + p(L_{ms}I_{a1} + L_{ls}I_{a1} + L_{ms}\cos(30^\circ)I_{a2} + L_{ms}\cos(120^\circ)I_{b1} + L_{ms}\cos(150^\circ)I_{b2} \\ &+ L_{ms}\cos(240^\circ)I_{c1} + L_{ms}\cos(270^\circ)I_{c2}) \end{aligned} \tag{3.35}$$

$$\begin{aligned} V_{a2} =& RI_{a2} + p(L_{ms}\cos(30^\circ)I_{a1} + L_{ms}I_{a2} + L_{ls}I_{a2} + L_{ms}\cos(90^\circ)I_{b1} + L_{ms}\cos(120^\circ)I_{b2} \\ &+ L_{ms}\cos(210^\circ)I_{c1} + L_{ms}\cos(240^\circ)I_{c2}) \end{aligned} \tag{3.36}$$

$$\begin{aligned} V_{b1} =& RI_{b1} + p(L_{ms}\cos(240^\circ)I_{a1} + L_{ms}\cos(270^\circ)I_{a2} + L_{ms}I_{b1} + L_{ls}I_{b1} + L_{ms}\cos(30^\circ)I_{b2} \\ &+ L_{ms}\cos(120^\circ)I_{c1} + L_{ms}\cos(150^\circ)I_{c2}) \end{aligned} \tag{3.37}$$

$$\begin{aligned} V_{b2} =& RI_{b2} + p(L_{ms}\cos(210^\circ)I_{a1} + L_{ms}\cos(240^\circ)I_{a2} + L_{ms}\cos(30^\circ)I_{b1} + L_{ms}I_{b2} + L_{ls}I_{b2} \\ &+ L_{ms}\cos(90^\circ)I_{c1} + L_{ms}\cos(120^\circ)I_{c2}) \end{aligned} \tag{3.38}$$

$$\begin{aligned} V_{c1} =& Ri_{c1} + p(L_{ms}\cos(120^\circ)I_{a1} + L_{ms}\cos(150^\circ)I_{a2} + L_{ms}\cos(240^\circ)I_{b1} + L_{ms}\cos(270^\circ)I_{b2} \\ &+ L_{ms}I_{c1} + L_{ls}I_{c1} + L_{ms}\cos(30^\circ)I_{c2}) \end{aligned} \tag{3.39}$$

$$\begin{aligned} V_{c2} =& RI_{c2} + p(L_{ms}\cos(90^\circ)I_{a1} + L_{ms}\cos(120^\circ)I_{a2} + L_{ms}\cos(210^\circ)I_{b1} + L_{ms}\cos(240^\circ)I_{b2} \\ &+ L_{ms}\cos(30^\circ)I_{c1} + L_{ms}I_{c2} + L_{ls}I_{c2}) \end{aligned} \tag{3.40}$$

where, L_{ls} = Leakage inductance of each winding,
L_{ms} = Mutual inductance between two windings,
R = Resistance of each winding, $p = \frac{d}{dt}$
V_{a1}= Voltage across a1 winding,
V_{a2}= Voltage across a2 winding,
V_{b1}= Voltage across b1 winding,
V_{b2}= Voltage across b2 winding,
V_{c1}= Voltage across c1 winding,
V_{c2}= Voltage across c2 winding.

It was already proven in [79], that the currents through the parallel windings of the split-phase machine in an IBC are equally divided using (3.41).

$$I_{a1} = I_{a2} = \frac{I_R}{2}; I_{b1} = I_{c2} = \frac{I_Y}{2}; \text{and} \;\; I_{b2} = I_{c1} = \frac{I_B}{2}; \tag{3.41}$$

Substituting (3.41) in (3.35) to (3.40), the equations can be simplified and written in matrix form as shown in (3.42).

$$\begin{bmatrix} V_{a1} \\ V_{b1} \\ V_{c1} \end{bmatrix} = \begin{bmatrix} L'_{ls} + L'_{ms} + L'_{ms}\cos(30°) & L'_{ms}\cos(120°) & L'_{ms}\cos(150°) + L'_{ms}\cos(240°) \\ L'_{ms}\cos(120°) & L'_{ls} + L_{ms} - L'_{ms}\cos(30°) & L'_{ms}\cos(240°) + L'_{ms}\cos(330°) \\ L'_{ms}\cos(120°) + L'_{ms}\cos(150°) & L'_{ms}\cos(120°) + L'_{ms}\cos(30°) & L'_{ls} + L'_{ms} \end{bmatrix} \begin{bmatrix} \frac{d}{dt}\frac{I_R}{2} \\ \frac{d}{dt}\frac{I_Y}{2} \\ \frac{d}{dt}\frac{I_B}{2} \end{bmatrix} + \begin{bmatrix} R' & 0 & 0 \\ 0 & R' & 0 \\ 0 & 0 & R' \end{bmatrix} \begin{bmatrix} \frac{I_R}{2} \\ \frac{I_Y}{2} \\ \frac{I_B}{2} \end{bmatrix} \tag{3.42}$$

From this a-b-c model of the IBC, the following conclusions can be listed.

1. The self-inductance terms of each phase (diagonal terms of the inductance matrix) are different from each other, making the system unbalanced.

2. The mutual inductance terms of R-phase to Y-phase is different from the mutual inductance terms of R-phase to B- phase making the system unbalanced.

3. The self inductance term of R-phase is largest, of Y-phase is smallest and of B-phase is in between that of R-phase or Y-phase in $R-Y-B$ configuration of machine windings in IBC.

By rearranging the terms, the following equations are derived for IBC-1.

$$pI_R = \frac{1}{Z/2}[(L_{ls} + 1.133L_{ms})(V_{a1} - \frac{R}{2}I_R) + (0.5L_{ms})(V_{b1} - \frac{R}{2}I_Y) + (1.366L_{ms})(V_{c1} - \frac{R}{2}I_B)] \tag{3.43}$$

$$pI_Y = \frac{1}{Z/2}[(0.5L_{ms})(V_{a1} - \frac{R}{2}I_R) + (L_{ls} + 2.866L_{ms})(V_{b1} - \frac{R}{2}I_Y) - (0.366L_{ms})(V_{c1} - \frac{R}{2}I_B)] \tag{3.44}$$

$$pI_C = \frac{1}{Z/2}[(1.366L_{ms})(V_{a1} - \frac{R}{2}I_R) - (0.366L_{ms})(V_{b1} - \frac{R}{2}I_Y) + (L_{ls} + 2L_{ms})(V_{c1} - \frac{R}{2}I_B)] \tag{3.45}$$

where, $Z = L_{ls} + 3L_{ms}$
This can be simplified and written as shown in (3.46).

$$\begin{bmatrix} \frac{d}{dt}I_R \\ \frac{d}{dt}I_Y \\ \frac{d}{dt}I_B \end{bmatrix} = \frac{1}{Z}\begin{bmatrix} L'_{ls} + 1.133L'_{ms} & 0.5L'_{ms} & 1.366L'_{ms} \\ 0.5L'_{ms} & L'_{ls} + 2.866L'_{ms} & -0.366L'_{ms} \\ 1.366L'_{ms} & -0.366L'_{ms} & L'_{ls} + 2L'_{ms} \end{bmatrix}\begin{bmatrix} V_{a1} - R'I_R \\ V_{b1} - R'I_Y \\ V_{c1} - R'I_B \end{bmatrix} \tag{3.46}$$

The voltage across the motor windings can be written in terms of inverter pole voltages, common mode voltage and the grid voltage as shown below.

$$V_{a1} = (V_{a1o} - V_{no}) - V_{an} = (V_{a1o} - \frac{1}{2}(V_{o1} + V_{o2})) - V_{an} \tag{3.47}$$

$$V_{b1} = (V_{b1o} - V_{no}) - V_{bn} = (V_{b1o} - \frac{1}{2}(V_{o1} + V_{o2})) - V_{bn} \tag{3.48}$$

$$V_{c1} = (V_{c1o} - V_{no}) - V_{cn} = (V_{c1o} - \frac{1}{2}(V_{o1} + V_{o2})) - V_{cn} \tag{3.49}$$

where V_{an} = 'a' phase to neutral voltage of the grid.
V_{a1o} = Voltage of 'a' phase leg of inverter with respect to the common point 'o'
V_{bn} = 'b' phase to neutral voltage of the grid.
V_{b1o} = Voltage of 'b' phase leg of inverter with respect to the common point 'o'
V_{cn} = 'c' phase to neutral voltage of the grid.

V_{c1o} = Voltage of 'c' phase leg of inverter with respect to the common point 'o'
V_{o1} = common mode voltage of IBC-1 and is defined below

$$V_{o1} = \frac{V_{a1o} + V_{b1o} + V_{c1o}}{3} \tag{3.50}$$

V_{o2} = common mode voltage of IBC-2
V_{no} = Voltage of the common point 'o' with respect to the neutral.
The definition of zero sequence current for IBC-1, I_{o1} is given by (3.51).

$$I_{o1} = \frac{I_R + I_Y + I_B}{3} \tag{3.51}$$

Substituting (3.47) to (3.49) and (3.46) in (3.51) we get the expression for the zero sequence current in IBC-1 as in (3.52).

$$pI_{o1} = \frac{\frac{1}{2}(V_{o1} - V_{o2}) - \frac{R}{2}I_{o1}}{\frac{L_{ls}}{2}} \tag{3.52}$$

3.4.2 Zero Sequence Current of IBC-2

For IBC-2, the voltage across windings can be derived similar to IBC-1 and is given in (3.53).

$$\begin{bmatrix} V_{b1'} \\ V_{a1'} \\ V_{c1'} \end{bmatrix} = \begin{bmatrix} L'_{ls} + L_{ms} - L'_{ms}\cos(30^\circ) & L'_{ms}\cos(120^\circ) & L'_{ms}\cos(240^\circ) + L'_{ms}\cos(330^\circ) \\ L'_{ms}\cos(120^\circ) & L'_{ls} + L'_{ms} + L'_{ms}\cos(30^\circ) & L'_{ms}\cos(150^\circ) + L'_{ms}\cos(240^\circ) \\ L'_{ms}\cos(120^\circ) + L'_{ms}\cos(30^\circ) & L'_{ms}\cos(120^\circ) + L'_{ms}\cos(150^\circ) & L'_{ls} + L'_{ms} \end{bmatrix} \begin{bmatrix} \frac{d}{dt}\frac{I_{R'}}{2} \\ \frac{d}{dt}\frac{I_{Y'}}{2} \\ \frac{d}{dt}\frac{I_{B'}}{2} \end{bmatrix} + \begin{bmatrix} R' & 0 & 0 \\ 0 & R' & 0 \\ 0 & 0 & R' \end{bmatrix} \begin{bmatrix} \frac{I_{R'}}{2} \\ \frac{I_{Y'}}{2} \\ \frac{I_{B'}}{2} \end{bmatrix} \tag{3.53}$$

where, $V_{a1'}$= Voltage across a1' winding
$V_{b1'}$= Voltage across b1' winding
$V_{c1'}$= Voltage across c1' winding
Similar to the phase currents in IBC-1, the phase currents $I_{R'}$, $I_{Y'}$ and $I_{B'}$ can be derived and is given in (3.54) to (3.56).

$$pi_{R'} = \frac{1}{Z/2}[(0.5L_{ms})(V_{a1'} - \frac{R}{2}i_{Y'}) + (L_{ls} + 2.866L_{ms})(V_{b1'} - \frac{R}{2}i_{R'}) - (0.366L_{ms})(V_{c1'} - \frac{R}{2}i_{B'})] \tag{3.54}$$

$$pi_{Y'} = \frac{1}{Z/2}[(L_{ls} + 1.133L_{ms})(V_{a1'} - \frac{R}{2}i_{Y'}) + (0.5L_{ms})(V_{b1'} - \frac{R}{2}i_{R'}) + (1.366L_{ms})(V_{c1'} - \frac{R}{2}i_{B'})] \tag{3.55}$$

$$pi_{B'} = \frac{1}{Z/2}[(1.366L_{ms})(V_{a1'} - \frac{R}{2}i_{Y'}) - (0.366L_{ms})(V_{b1'} - \frac{R}{2}i_{R'}) + (L_{ls} + 2L_{ms})(V_{c1'} - \frac{R}{2}i_{B'})] \tag{3.56}$$

These equations can be simplified and written in matrix form as given in (3.57) shown below.

$$\begin{bmatrix} \frac{d}{dt}I_{R'} \\ \frac{d}{dt}I_{Y'} \\ \frac{d}{dt}I_{B'} \end{bmatrix} = \frac{1}{Z}\begin{bmatrix} L'_{ls} + 2.866L'_{ms} & 0.5L'_{ms} & -0.366L'_{ms} \\ 0.5L'_{ms} & L'_{ls} + 1.133L'_{ms} & 1.366L'_{ms} \\ -0.366L'_{ms} & 1.366L'_{ms} & L'_{ls} + 2L'_{ms} \end{bmatrix}\begin{bmatrix} V_{b1'} - R'I'_R \\ V_{a1'} - R'I'_Y \\ V_{c1'} - R'I'_B \end{bmatrix} \tag{3.57}$$

The voltage across the motor windings can be written in terms of inverter pole voltages, common mode voltage and the grid voltage as shown below.

$$V_{a1'} = (V_{a1'o} - V_{no}) - V_{an} = (V_{a1'o} - \frac{1}{2}(V_{o1} + V_{o2})) - V_{an} \tag{3.58}$$

$$V_{b1'} = (V_{b1'o} - V_{no}) - V_{bn} = (V_{b1'o} - \frac{1}{2}(V_{o1} + V_{o2})) - V_{bn} \tag{3.59}$$

$$V_{c1'} = (V_{c1'o} - V_{no}) - V_{cn} = (V_{c1'o} - \frac{1}{2}(V_{o1} + V_{o2})) - V_{cn} \tag{3.60}$$

where
$V_{a1'o}$ = Voltage of 'a' phase leg of inverter with respect to the common point 'o',
$V_{b1'o}$ = Voltage of 'b' phase leg of inverter with respect to the common point 'o',
$V_{c1'o}$ = Voltage of 'c' phase leg of inverter with respect to the common point 'o',
V_{o2} = common mode voltage of IBC-2 and is given below.

$$V_{o2} = \frac{V_{a1'o} + V_{b1'o} + V_{c1'o}}{3} \tag{3.61}$$

V_{no} = Voltage of the common point 'o' with respect to the neutral.
The definition of zero sequence current for IBC-2, I_{o2} is given by (3.62).

$$I_{o2} = \frac{I_{R'} + I_{Y'} + I_{B'}}{3} \tag{3.62}$$

Substituting the equations for phase currents and winding voltages in (3.62), the common mode current of IBC-2 is given by (3.63).

$$pI_{o2} = \frac{\frac{1}{2}(V_{o2} - V_{o1}) - \frac{R}{2}i_{o2}}{\frac{L_{ls}}{2}} \tag{3.63}$$

From the derived equations for the common mode current in IBC-1 and IBC-2, it can be seen that the common mode current of IBC-1 is equal and opposite to the common mode current of IBC-2. Now it should also be verified that the common mode component of current to the grid is zero to ensure that it circulates only between IBC-1 and IBC-2 will is derived in the following section.

3.4.3 Common mode component in the Grid Currents

The grid currents I_{Rg}, I_{Yg} and I_{Bg} can be written as the sum of phase currents of IBC-1 and IBC-2 as mentioned below.

$$i_{Rg} = i_R + i_{R'} \tag{3.64}$$

$$i_{Yg} = i_Y + i_{Y'} \tag{3.65}$$

$$i_{Bg} = i_B + i_{B'} \tag{3.66}$$

Substituting the equations of phase currents of IBC-1 and IBC-2 which were derived in the previous sections, the equations for grid currents are derived below.

$$\begin{aligned}
pi_{Rg} =& \frac{1}{\frac{Z}{2}}[(L_{ls} + 1.133L_{ms})V_A + 0.5L_{ms}V_B + 1.366L_{ms}V_C + 1.732L_{ms}(V_{an} + V_{no} - V_{a1'o} \\
& - \frac{R}{2}i_{R'}) - 1.732L_{ms}(V_{cn} + V_{no} - V_{c1'o} - \frac{R}{2}i_{B'})] \\
pi_{Yg} =& \frac{1}{\frac{Z}{2}}[0.5L_{ms}V_A + (L_{ls} + 1.133L_{ms})V_B - 0.366L_{ms}V_C + 1.732L_{ms}(V_{bn} + V_{no} - V_{b1o} \\
& - \frac{R}{2}i_Y) + 1.732L_{ms}(V_{cn} + V_{no} - V_{c2o} - \frac{R}{2}i_{B'})] \\
pi_{Bg} =& \frac{1}{\frac{Z}{2}}[1.366L_{ms}V_A + 1.366L_{ms}V_B + (L_{ls} + 2L_{ms})V_C - 1.732L_{ms}(V_{an} + V_{no} - V_{a2o} \\
& - \frac{R}{2}i_{R'}) - 1.732L_{ms}(V_{bn} + V_{no} - V_{b1o} - \frac{R}{2}i_Y)]
\end{aligned} \tag{3.67}$$

where,

$$V_A = (2V_{an} + 2V_{no} - V_{a1o} - V_{a1'o} - \frac{R}{2} i_{Rg}) \tag{3.68}$$

$$V_B = (2V_{bn} + 2V_{no} - V_{b1o} - V_{b1'o} - \frac{R}{2} i_{Yg}) \tag{3.69}$$

$$V_C = (2V_{cn} + 2V_{no} - V_{c1o} - V_{c1'o} - \frac{R}{2} i_{Bg}) \tag{3.70}$$

Substituting these equations to derive the common mode component of grid current defined as

$$i_{og} = \frac{i_{Rg} + i_{Yg} + i_{Bg}}{3} = 0 \tag{3.71}$$

The common mode component of grid current is found to be zero. Thus the common mode current is present in IBC-1 and IBC-2, but it is zero in the grid side. The following can be commented about the common mode current.

1. The common mode current of IBC-1 is equal and opposite to the common mode current of IBC-2.
2. Also the common mode component of current in the grid is zero.
3. Thus the common mode current will be the circulating between IBC-1 and IBC-2.
4. The common mode current depends only on the difference in the common mode voltage between IBC-1 and IBC-2, and on the leakage inductance of the two machines.
5. The common mode current is not affected by the asymmetrical nature of the split-phase machine and hence does not depend on the unbalanced mutual and self-inductance terms.
6. The common mode current is common between IBC-1 and IBC-2. Hence only one current controller is needed to limit the common mode current.

3.5 Control Structure for the proposed $R-Y-B$ / $Y-R-B$ parallel configuration of IBCs

The proposed $R-Y-B$ / $Y-R-B$ parallel configuration of IBCs naturally cancels the unbalance in grid current. Hence additional control efforts are not needed as those

implemented in chapter 2. The control block for the parallel combination of IBC-1 and IBC-2 with a common DC link is shown in fig 3.6. The two IBCs work as front-end converters to maintain the required voltage across the common DC link. The grid voltages, motor currents, and the DC link voltage are the sensed quantities. These sensed quantities are transformed into $d-q$ reference frames using Clarke and Park transformation. As in a single IBC using a split-phase machine, the angle and phase information are obtained from the sensed voltages using a Phase Locked Loop (PLL). The d-component of grid voltage is made zero using the PI controller and the grid reference voltage is aligned along the q- axis. Thus a decoupled control of real and reactive power is achieved by controlling the q-axis and d-axis currents.

The outer voltage control loop tries to maintain the DC link voltage to the reference voltage. The voltage controller provides the reference (corresponding to the real power) for the inner current loop. The load sharing factor k_{lf} determines how the real power should be shared between IBC-1 and IBC-2. If the real power is equally divided k_{lf} will be equal to 0.5. For practical battery charging applications in electric vehicles, the load sharing factor k_{lf} and battery currents are determined by the battery management system. Separate PI controllers are used to control the real power component (I_{qm} and I'_{qm}) and reactive power component (I_{dm} and I'_{dm}) of IBC-1 and IBC-2 respectively.

There is a presence of low frequency circulating current of very low magnitude which is circulating between IBC-1 and IBC-2 as discussed in the previous section. A single PI controller is used to control and reduce the zero sequence circulating current flowing through both the IBCs.

For actual electric vehicles, the battery management system continuously monitors the state of charge, state of health and the temperature of the battery cells using algorithms and provide the required current reference to the current controllers. Thus, there will not be an outer voltage control loop for the system.

3.6 Simulation Results

The proposed parallel combination of IBCs using a Split Phase machine was simulated in MATLAB for a 10 kW system with a DC link voltage of 1000 V for a switching frequency of 10 kHz. The machine parameters used for the simulation are given below in table 3.2. In this chapter, both machines are assumed to have the same parameters.

The parallel system was simulated for two different winding configurations. In the first one, the motor windings of IBC-1 and IBC-2 are having the same connection,

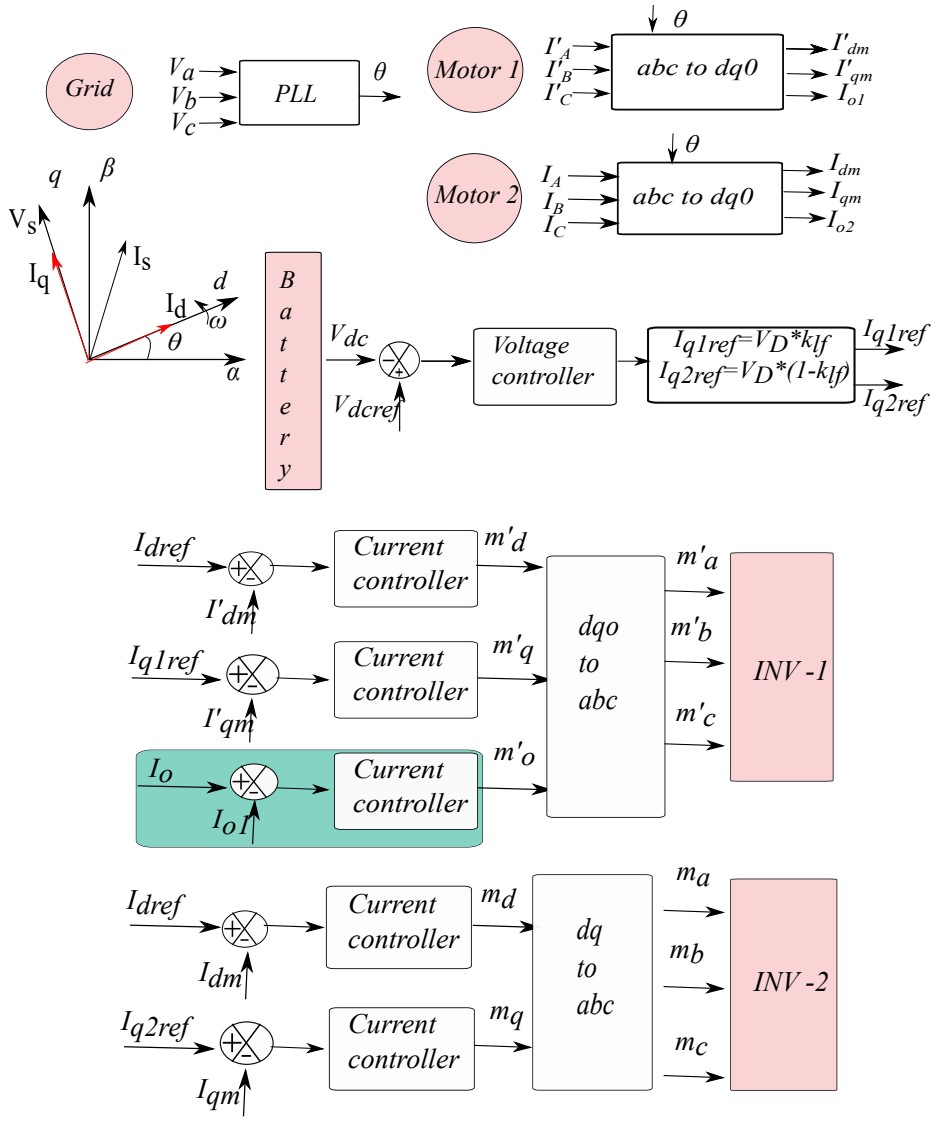

Fig. 3.6. Control block diagram for parallel IBC

that is $R-Y-B/\ R-Y-B$. In the second simulation model, the motor windings of IBC-1 and IBC-2 are given the proposed winding connections, i.e. the $R-Y-B/\ Y-R-B$ connections. It will be seen from the simulation results that the proposed $R-Y-B/\ Y-R-B$ configuration will effectively minimize the unbalance in grid current which was present in a single IBC with split-phase machine.

The steady-state current waveforms of IBC-1, IBC-2, and the grid for $R-Y-B/\ R-Y-B$ configuration are shown in fig 3.7. It can be seen that the three-phase currents of IBC-1 and IBC-2 are not balanced. Also, the grid currents which is the sum of phase currents of IBC-1 and IBC-2 are not balanced.

Table 3.2. Simulation - Machine parameters

DC link Voltage	1000 V
Stator self inductance L_{ss}	0.1627 H
Leakage inductance $\sigma_{12}L_{ss}$	9.635 mH
Mutual inductance between stator and rotor windings L_{sr}	0.1508 H
Stator resistance R_s	5 Ω
Rotor resistance R_r	3.4 Ω
Moment of inertia J	0.0165 kgm^2

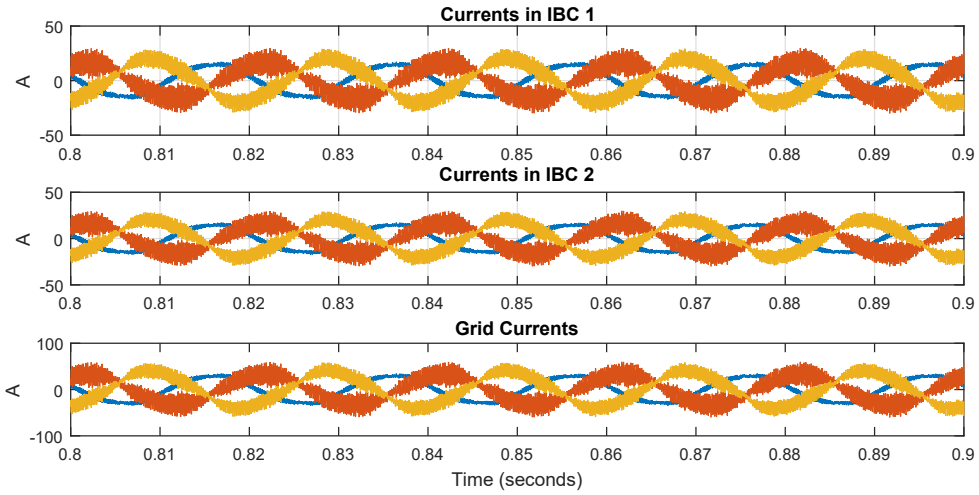

Fig. 3.7. Steady state current waveforms: $R-Y-B/R-Y-B$ configuration: (1) IBC 1 motor phase currents (2) IBC 2 motor phase currents (3) Three phase grid currents

However, the steady state simulation results of $R-Y-B/\ Y-R-B$ configuration shown in fig 3.8 give a positive result as proved in the theoretical analysis. The phase currents of IBC-1 and IBC-2 are unbalanced, however, the grid currents, which is the sum of phase currents are found to be balanced. This validates the mathematical proof that has been derived in [125].

3.6.1 Negative Sequence terms in grid current and cancellation of unbalance

To check the cancellation of unbalance in grid currents quantitatively, the negative sequence terms of phase currents of IBC-1 and IBC-2, and the three-phase grid currents were calculated for both $R-Y-B/\ R-Y-B$ and $R-Y-B/\ Y-R-B$ configuration. This is done by converting the three-phase quantities to the d-q domain but with an

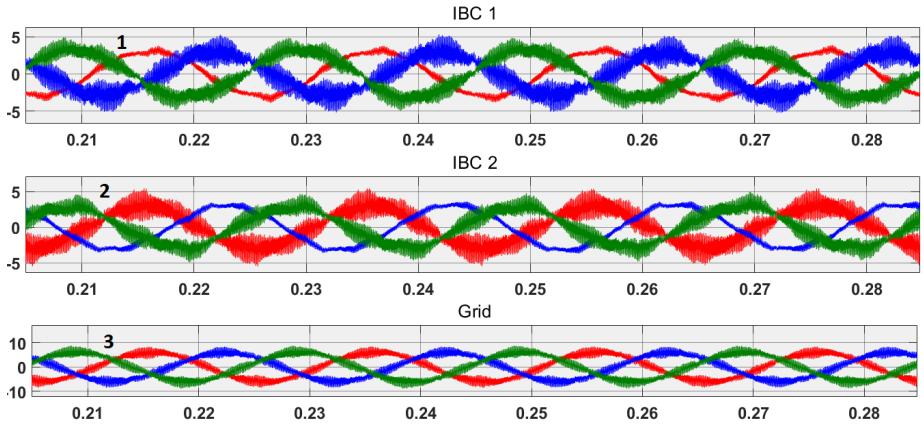

Fig. 3.8. Steady state current waveforms: Proposed $R-Y-B/Y-R-B$ configuration: (1) IBC 1 motor phase currents (2) IBC 2 motor phase currents (3) Three phase grid currents

angular frequency equal to the negative of the grid frequency. The DC terms in that transformation give the negative sequence terms of the phase currents and the grid currents.

The comparison of the negative sequence current terms for both configurations is written in Table. 3.3. For the $R-Y-B/\ R-Y-B$ configuration, there are negative sequence terms in the phase currents of IBC-1 and IBC-2, which should be present since they are unbalanced systems. But in the grid current also a high value of negative sequence component is seen, which can be approximated as the sum of negative sequence components of IBC-1 and IBC-2. This clearly shows that the parallel combination of IBCs using $R-Y-B/\ R-Y-B$ configuration makes the system more unbalanced.

Now consider the negative sequence current components in the proposed $R-Y-B/\ Y-R-B$ configuration as given in Table.3.3. It can be seen that there are negative sequence terms in the phase currents of IBC-1 and IBC-2, as they are unbalanced systems. However, the negative sequence component of the grid current is found to be very low, which can be approximated as the difference in the negative sequence components of phase currents of IBC-1 and IBC-2. Thus from this result, it can be verified that the proposed $R-Y-B/\ Y-R-B$ configuration of parallel combination of IBCs makes the system balanced by canceling out the unbalance in each IBC to it maximum extent.

Table 3.3. Negative sequence in $R-Y-B/R-Y-B$ configuration and $R-Y-B/Y-R-B$ configuration

System	$R-Y-B \sim/\sim R-Y-B$				***Proposed*** $R-Y-B\sim/\sim Y-R-B$			
	Id		Iq		Id		Iq	
	mag	phase	mag	phase	mag	phase	mag	phase
IBC-1	3.87	270	3.06	270	3.14	270	3.21	270
IBC-2	3.87	270	3.06	270	2.14	90	2.37	90
Grid	7.73	270	6.13	270	0.99	270	0.84	270

3.7 Experimental Results

3.7.1 Experimental Setup

Two 4-pole, 11 kW, 415 V three-phase induction machines which are rewound as a split-phase induction machine were used for the experiment. Two three-phase inverters using 75 A, 1200 V IGBT half bridge modules (SKM75GB12T4) were used to work as front-end converters. The gate driver M57962L is used for driving the IGBT modules. The control part is implemented using TMS320F28377S digital signal processor. The DSP was used to implement the voltage and current control loop and get the modulating signals. The modulating signals are then compared with triangular carrier waveforms at 5 kHz along with providing a dead time to generate the gating pulses for both the converters of both IBC-1 and IBC-2. LA55P current sensors were used to sense the three-phase grid currents and phase currents of IBC-1 and IBC-2.

Table 3.4. Rms Value of grid currents for $R-Y-B/R-Y-B$ Configuration

System	$I_{\text{a, rms}}$	$I_{\text{b, rms}}$	$I_{\text{c, rms}}$
Grid	2.6A	3.1 A	3.9 A

3.7.2 Steady State Results

A comparison using two different topologies is implemented to understand the effect of the unbalance in grid currents and how it is getting reduced using the proposed topology. Hence the proposed $R-Y-B$ / $Y-R-B$ topology is compared with $R-Y-B$ / $R-Y-B$ topology for different steady state conditions.

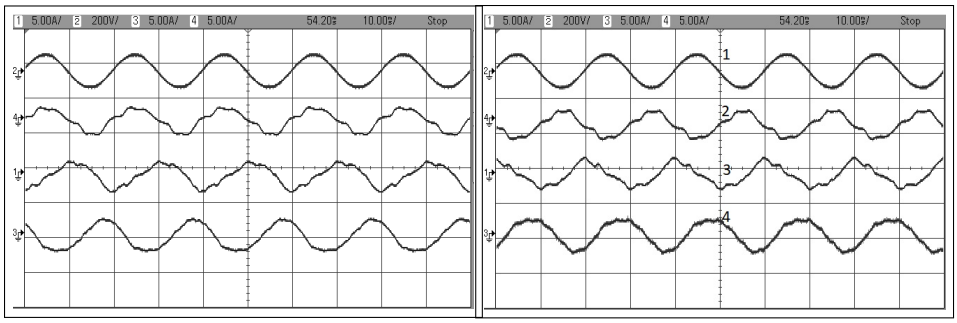

(a) IBC-1 currents ($R-Y-B$ configuration)

(b) IBC-2 currents ($R-Y-B$ configuration)

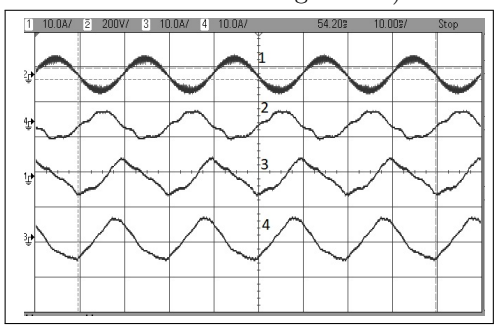

(c) grid currents

Fig. 3.9. Steady state current waveforms: $R-Y-B/R-Y-B$ configuration: (1) Grid A Phase voltage (200 V/div) (2) Phase A current (5 A/div) (3) Phase B current (5 A/div) (4) Phase C current (5 A/div)

3.7.2.1 $R-Y-B$ / $R-Y-B$ Configuration

Fig 3.9 shows the steady state current waveforms for a power level of 500 W for $R-Y-B$ / $R-Y-B$ configuration. Here the IBC-1 and IBC-2 are connected in the same configuration, namely $R-Y-B$. From the results, it can be seen that the input currents of IBC-1 are unbalanced. The input currents of IBC-2 are unbalanced. And the grid currents are also unbalanced. The RMS values of grid currents are given in Table. 3.4. The values of all the three-phase currents are different.

3.7.2.2 $R-Y-B$ /$Y-R-B$ Configuration

Fig 3.10 shows the steady state current waveforms for a power level of 1 kW and 300 V for $R-Y-B/Y-R-B$ configuration. From the results, it can be seen that the currents in IBC-1 and IBC-2 are unbalanced, but the grid current is found to be balanced and sinusoidal in shape. Fig 3.11 shows the steady state current waveforms for 600 W power level for the same configuration. It can be seen from these results that the current waveforms have better waveform as the system carries higher power.

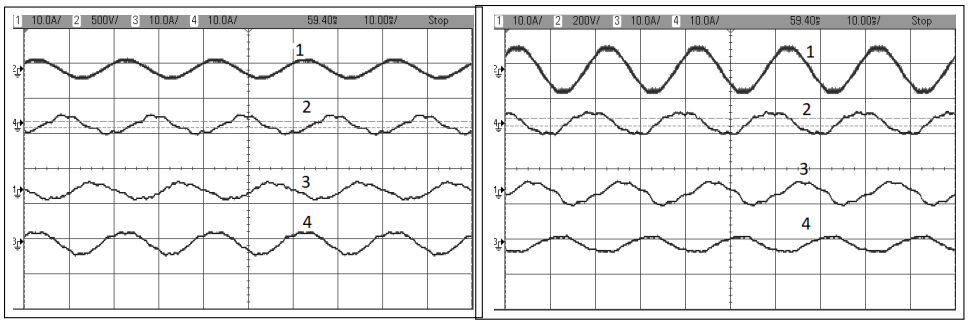

(a) IBC 1 currents $(R-Y-B$ Configuration)

(b) IBC 2 currents $(Y-R-B$ Configuration)

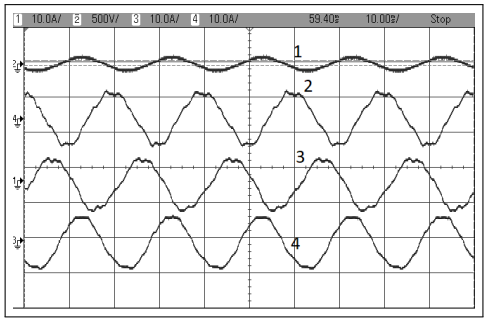

(c) Grid currents

Fig. 3.10. Steady State Results at 300 V and 1 kW: (1) Grid B phase voltage (500 V/div) (2) R phase current (10 A/div) (3) Y Phase Current (10 A/div) (4) B phase current (10 A/div)

Table. 3.5 gives the rms values of currents for 600 W and 1 kW power level. The rms values of the IBC-1 and IBC-2 currents are different, but the rms values of the three-phase grid currents are almost the same. Among the two power levels, the currents are more balanced as the power level increases.

In fig 3.12, the q- component of IBC-1, IBC-2, and grid is shown along with its harmonic spectrum. Since IBC-1 and IBC-2 are unbalanced, and as seen previously from the mathematical model, the i_q current has a high 100 Hz component in its spectrum. But as seen from the figure, the harmonic component of the i_q current of the grid has a very low 100 Hz component, proving that the unbalance is minimized with the proposed configuration.

Fig 3.13 gives the THD of the grid currents in all three three-phases. As discussed before, there is no high frequency zero sequence current in the system as there is no interleaving of carriers between IBC-1 and IBC-2. However, due to the difference in inductance for each phase of IBC-1 and IBC-2, there will be a difference in pole voltage between each phase of IBC-1 and IBC-2. This can lead to the flow of a low harmonic low magnitude circulating current, limited using a single zero sequence controller.

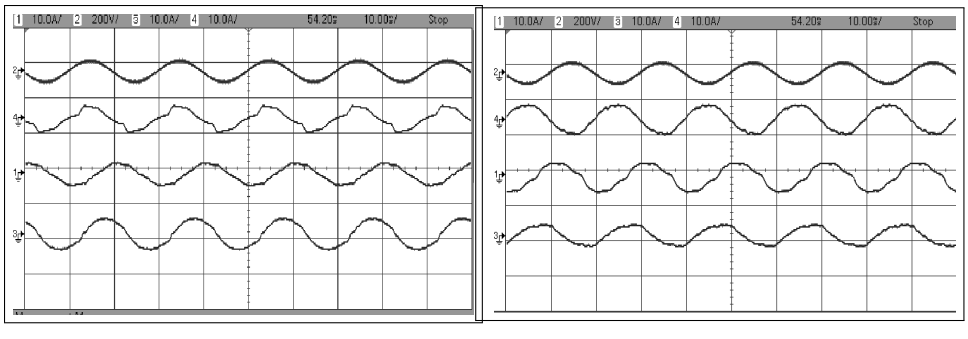

(a) IBC-1 currents **(b)** IBC-2 currents

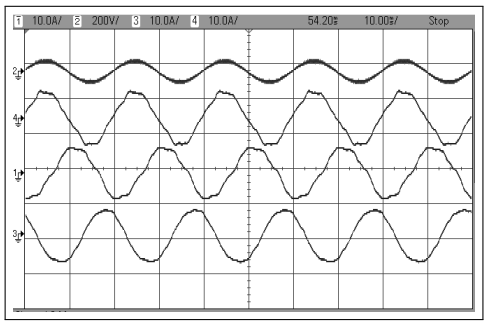

(c) grid currents

Fig. 3.11. Steady State Current Waveforms: $R-Y-B/Y-R-B$ configuration: 600 W, 230 V (1) Grid R-Phase voltage (200 V/div) (2) Phase R-current (10 A/div) (3) Y-phase current (10 A/div) (4) B-phase current (10 A/div)

Only one zero sequence controller is sufficient as the circulating current in IBC-1 and IBC-2 are equal and opposite. Using the zero sequence controller, the circulating current in the system is minimized. This is seen in fig 3.14. The results show the sum of all the three grid currents. The actual circulating current will be one-third of the shown waveform.

3.7.3 Transient Results

The results are shown in fig 3.15 for a sudden change in load current and a sudden change in dc-link voltage for the proposed configuration. When there is a sudden increase in load current, the DC link voltage will change but finally come back to the steady state value. The grid current increases but will be still at the unity power factor.

Fig 3.16 shows the results of current waveforms when there is a sudden change in load sharing between two IBCs. There is a change from equal power sharing to unequal power sharing. With unequal power sharing the grid currents will have a

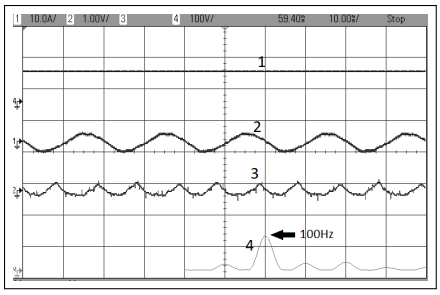

(a) IBC 1 - iq current and its harmonic Spectrum

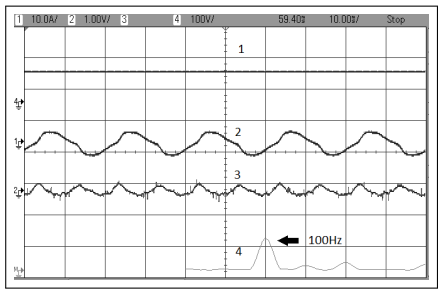

(b) IBC 2 - iq current and its harmonic Spectrum

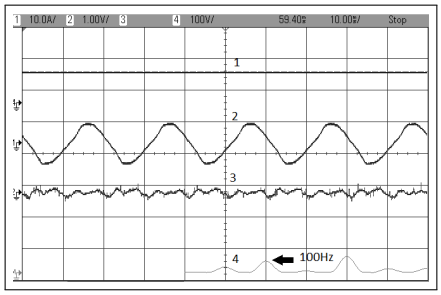

(c) Grid - iq current and its harmonic Spectrum

Fig. 3.12. Reduction in Unbalance: (1) DC link voltage (100 V/div) (2) Y phase current (10 A/-div) (3) Iq current (1V/div) (4) Harmonic spectrum centered around 50Hz (100 mV/div).

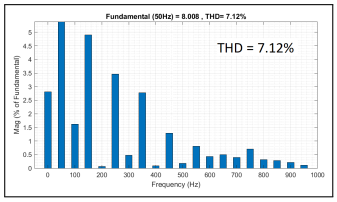

(a) Grid R-phase current

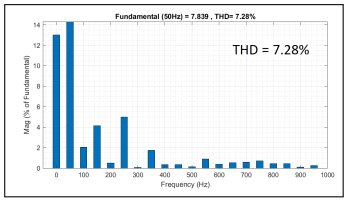

(b) Grid Y-phase current

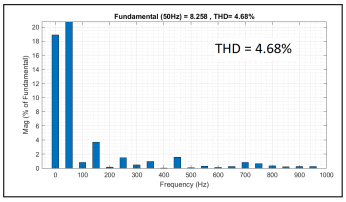

(c) Grid B-phase current

Fig. 3.13. Harmonic Spectrum of grid currents for a 600 W load for DC link voltage of 232 V

small unbalance and the grid current will not be pure sinusoidal in shape as was with balanced power sharing mode.

3.7.4 V2G Operation Results

Sometimes when there is an emergency, the battery can supply power to the grid as it is a bidirectional IBC. This mode of operation is called the Vehicle to Grid mode of operation. In fig 3.17, a change in the mode of operation from grid to vehicle (G2V) to Vehicle to grid (V2G) is shown. The current waveform changes its phase when the operation changes from G2V to V2G as seen from the result. This result proves that

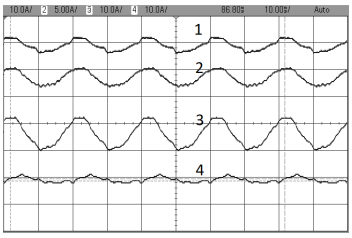

Fig. 3.14.
Circulating Current at 320 V: (1) IBC-1 phase R-phase current (10A/division) (2) IBC-2 phase R-phase current (10A/div) (3) Grid R-phase current (10A/div) (4) Zero sequence current (1.67 A/div)

Table 3.5. RMS value of currents through IBC-1, IBC-2 and GRID for $R-Y-B$ /$Y-R-B$ configuration

System	600 W and 232 V			1 kW and 300 V		
	$I_R(A)$	I_Y (A)	I_B (A)	$I_R(A)$	I_Y(A)	I_B(A)
IBC-1	2.36	2.21	3.24	1.73	1.61	2.25
IBC-2	2.96	2.97	2.17	2.21	2.19	1.55
GRID	5.31	5.20	5.41	5.28	5.12	5.28

this system can be well utilized for V2G mode of operation if required.

3.8 Conclusion

In this chapter, a parallel combination of two IBCs using a split-phase machine is proposed using the existing components of an all-wheel drive electric vehicle. Two IBCs using split-phase machines are connected in parallel to enhance the power handling capacity of the integrated battery charger. This proposed topology can naturally minimize the unbalance in grid currents that existed in a single IBC using a split-phase machine. The advantages of the proposed topology are listed below.

1. The system utilizes the existing components inside the all-wheel drive EV to make a fast on-board charger.

2. The proposed $R-Y-B$ / $Y-R-B$ configuration cancels the unbalance in the grid currents naturally without any extra control effort that was needed for the case of an IBC using a split-phase machine. The mathematical proof is also included in this chapter.

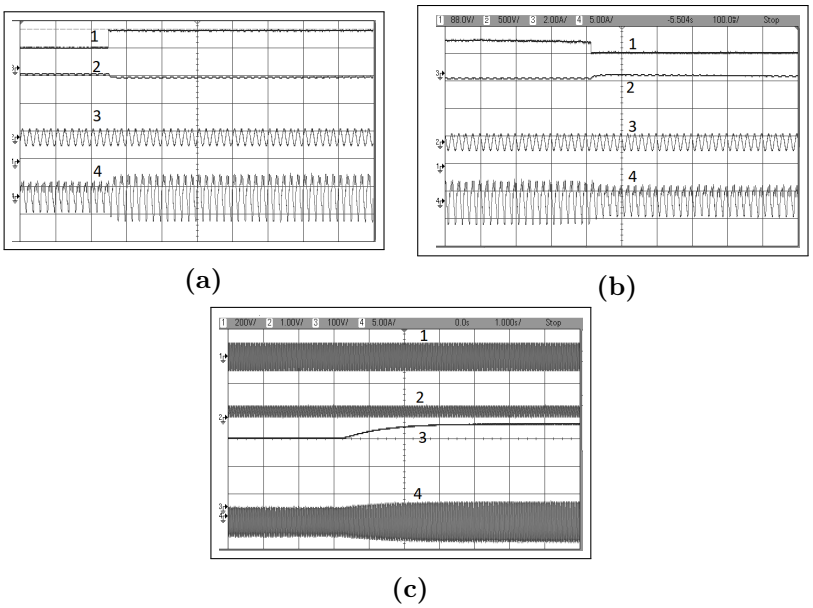

Fig. 3.15. Transient Results: For sudden change in load (a) From 400 W to 800 W (b) From 800 W to 400 W: (1) Load current (2A/div) (2) DC link voltage (88V/div) (3) Grid Voltage (500V/div) (4) Grid Current (5A/div) (c) Sudden change in DC link Voltage from 250 V to 300 V: (1) Grid angle θ (2) Grid Voltage (200V/div) (3) DC link Voltage (100v/div) (4) Grid Current (5A/div)

3. During charging, the torque developed inside both the machines is zero instantaneously, and hence both the motors will not rotate while charging the battery.

4. The low-frequency circulating current is only present in the system as there is no interleaving of carriers. This current is minimized using a single zero sequence current controller.

5. The power rating is the sum of individual powers of IBCs.

6. This proposed system can work with two equal power-rated motors or two unequal power-rated motors which can be found in different models of all-wheel drive EVs.

7. The proposed IBC is bidirectional and can be used if needed to supply power to the grid.

A high power unity power factor on-board charger with zero instantaneous torque and balanced currents is developed in this thesis. Experimental results verify the theoretical analysis done for this work. The results prove that the proposed configuration of

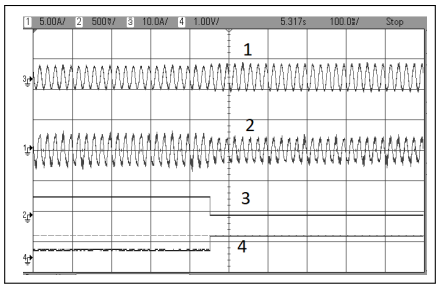

Fig. 3.16. From balanced power sharing to Unbalanced power sharing (1) IBC-1 phase current (10A/div) (2) IBC-2 phase current (5A/div) (3) IQ ref for IBC-1 from dsp (1V/div) (4) IQ ref for IBC-2 from dsp (500 mV/div)

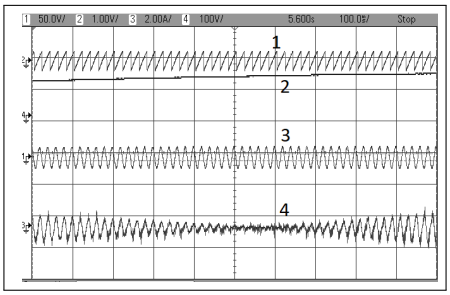

(a) Change in mode from G2V to V2G

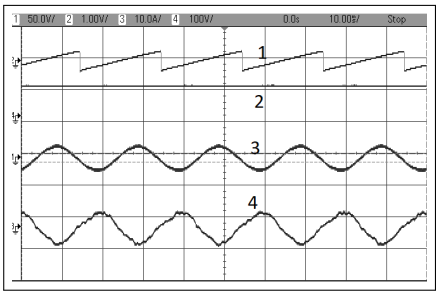

(b) V2G mode of operation

Fig. 3.17. Vehicle to grid operation operation: (1) Grid angle θ from PLL (2) Dc link voltage (100 V/div) (3) Grid phase voltage (50 V/div) (4) Grid phase current (2A/div)

parallel IBCs and the proposed control technique can be used as a viable on-board charging scheme for all-wheel drive vehicles.

In the present chapter, a charging scheme utilizing both the drives inside the all-wheel drive EV is discussed in detail. In the next chapter, an efficient driving scheme utilizing both the inverters to drive the vehicle is discussed in detail. Usually for an AWD EV, only one drive is energized during its normal driving condition, and the other drive is only utilized when in need of extra traction like on slippery roads or while driving off roads. Thus the other drive is mostly not energized.

A driving scheme utilizing the two inverters and running the motor as an open-end winding motor is discussed in detail which has several advantages compared to the existing drive using a star-connected motor, in the following chapter.

Chapter 4

An Efficient Driving Scheme for All-Wheel Drive EVs with Advanced Voltage Space Vectors

4.1 Introduction

In chapter 2 and chapter 3, a new charging scheme based on IBCs for EVs, especially AWD EVs was discussed in detail. In the present chapter, an efficient driving mechanism that can be implemented in EVs, especially AWDs is dealt with in detail. In AWDs, there are two motor drive systems in which only one motor is engaged all the time. The other system is used only during certain road conditions, which requires extra traction for some of the wheels. In this chapter, a driving scheme is proposed, wherein the main motor (which is always engaged) is driven using the two inverters (present in both the rear axle and front axle) as an open-end winding scheme and thus improving the performance of the system.

A brief introduction of the open-end winding machine and its space vector PWM schemes is discussed in section 1.10.4. In this chapter, the main motor drive is configured as an OEW motor with two, two-level inverters. The first inverter is connected to a DC source, while the second inverter is connected to a DC link capacitor. The second inverter mainly acts as a switched capacitor converter and a new switching scheme is implemented wherein the voltage of the capacitor is always regulated irrespective of the load conditions without needing closed loop controllers. A mathematical proof is also provided as to how the capacitor voltage is maintained constant without any closed loop control, by using the proposed switching scheme. In

this chapter, using the existing two two-level inverters, 12-sided, 18-sided, and 24-sided OEW voltage space vector schemes using a single DC source are discussed in detail.

Also, an over-modulation scheme is implemented to get a linear relationship between the fundamental voltage across the motor and the DC link voltage for the region above the linear region of operation in the space vector modulation scheme. Thus with the same DC voltage source, higher fundamental phase voltages across the motor windings can be achieved, which leads to better utilization of the battery especially for high-speed application of EVs. The linearization of the over-modulation region is implemented for 12-sided,18-sided, and 24-sided space vector modulation schemes for the OEW IM.

The advantages of using open-end winding motors using two two-level inverters for AWDs are the following.

1. For the same machine, by implementing multi-sided space vector modulation schemes using OEW configuration, the lower order harmonics in the motor phase voltages are eliminated.

2. The second inverter acts as a switched capacitive filter. The voltage of the capacitor is naturally maintained constant at a lower value compared to the DC source, without any closed loop voltage controller.

3. The harmonics in the motor phase voltage in the square wave mode of operation is reduced as the number of sides in the space vector polygon is increased.

4. The second inverter has a lower DC link voltage in this proposed driving scheme, thus it has lower switching losses.

5. Linearisation of the over-modulation region is also implemented to utilize the battery to its maximum capacity.

Section 4.3 discusses about open-end winding machines. Section 4.4, section 4.5 and section 4.6 discusses in detail along with mathematical proofs, the open-end winding space vector schemes for 12-sided, 24-sided, and 18-sided voltage polygons with a single DC source. Section 4.7 discusses in detail the linearisation of over-modulation region in any space vector scheme. Section 4.7, section 4.8 and section 4.9 discusses the implementation of linearisation of over-modulation region in the multi-sided space vector schemes for 12-sided, 24-sided, and 18-sided voltage polygons. Section 4.10 shows the simulation and experimental results for the three multi-sided space vector schemes.

4.2 All-Wheel Drive Electric Vehicles

Electric Vehicles can be classified mainly into 4 different types based on their electric drive train. They are front-wheel drive, rear-wheel drive, both front and rear-wheel independent driven (AWD), and four in-wheel motor drive vehicles [127–133]. Among these, AWD has the advantage of fail-safe operation, that is whenever there is a failure in any part of one motor drive, the vehicle will still run with the other motor drive, which is not the case with all other configurations. The last one, which is a four-in-wheel motor drive, may cause the spinning of wheels when any of the motor drive fails. The front and rear wheel drive of AWDs are independently controlled. The rotors of the motors are connected to the wheels through the differential gear and they transmit the generated torque to the wheels according to the gear ratio. Also, AWDs are of two types. In some AWD vehicles, both the drives are powered continuously, whereas, in the second type, the vehicle usually is driven with one motor drive, either as front wheel drive or back wheel drive depending on the model of the vehicle, but when needed, it automatically powers both axles. The states of the front and rear wheels are continuously fed back to the vehicle management system and proper action is taken. Variable torque distribution control can be implemented under various running conditions. For example, when the vehicle is taking a sharp turn, the outer wheels need more traction than the inner wheels. The AWDs automatically power both drives and split the torque distribution accordingly. Similarly when driving on slippery roads, if the front wheels try to slip, sudden action is taken to reduce the torque reference to the front wheels and provide higher torque to the back wheels. But when driving on normal roads, only one drive train is powered on. The other drive train is not utilized.

In this chapter, a new open-end space vector scheme is introduced, especially when the AWDs are running with only one drive train being powered on. This scheme, called Open End winding Space vector control of the motor, utilizes the inverter of the two drive trains to rotate a single motor, which can reduce the switching frequency of the system, and hence increase the efficiency of the system to a better value. However, additional isolation between the two different DC link needs to be implemented.

4.3 Multi-sided voltage space vector schemes using two, two-level inverters with a single DC source for open-end wound IM

In the introduction, the multi-sided voltage space vector modulation scheme has been discussed where two inverters drive a single OEW motor. The neutral of the motor winding is disconnected and there will be six terminals from the stator of the motor. It has been discussed that multi-sided space vector modulation has the advantage of reducing the switching frequency and hence the switching losses of inverters compared to three-level inverters. When the AWDs have only one drive being powered on, the other drive is not utilized. Hence the two driving inverters can be connected to the OEW motor and improve the performance of the powertrain. In this chapter different OEW space vector schemes using a single DC source which can be implemented in AWDs while driving in single axes mode are discussed in detail. In all these schemes only one inverter has a DC source and the other inverter only has a DC link capacitor. The main highlight of this scheme is that the capacitor voltage is inherently regulated without any voltage controller. Also, there is a reduction in switching losses.

4.4 12-sided voltage space vector modulation scheme using single DC source without any voltage controller

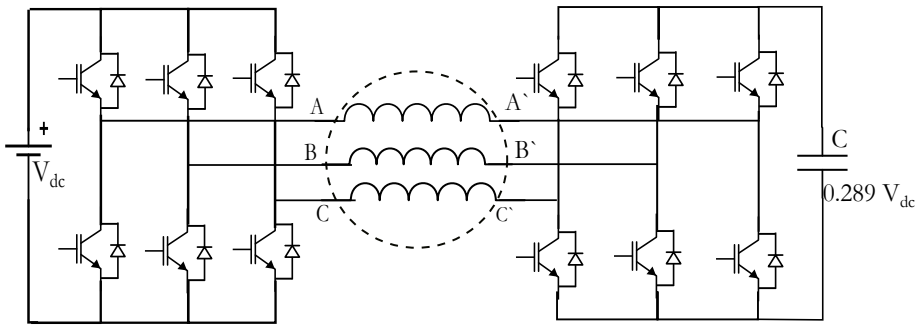

Fig. 4.1. Schematic for Dodecagonal Space vector scheme using one DC source

The circuit for the scheme is shown in fig 4.1. The circuit uses two two-level

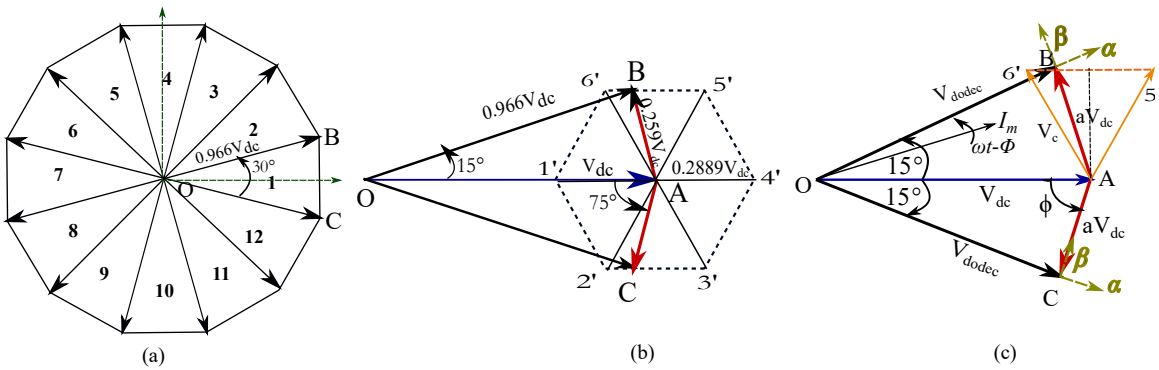

Fig. 4.2. (a) Dodecagonal Voltage Space Vector (b) Sector 1 formed as a vector combination of voltage vectors of Inverter 1 and Inverter 2 (c) Inverter 1 and Inverter 2 voltage vectors and motor current in sector 1

inverters, Inverter 1 and Inverter 2. Inverter 1 is provided with a DC source of magnitude V_{dc} and Inverter 2 is connected with a capacitor. The capacitor voltage is maintained constant without any voltage controller irrespective of different load conditions, using the proper modulation method.

The combination of proper vectors of inverter-1 and inverter-2 develops a 12-sided voltage vector space with a difference of 30° between each vector across the windings of the motor. For the capacitor voltage to be maintained automatically, the voltage vectors switched by inverter-2 at every instant should be such that the average active power absorbed by the capacitor is zero, irrespective of the load conditions. The next section describes the mathematical proof for selecting the proper amplitude and angle of the voltage vector of inverter-2 to create a dodecagonal voltage vector across the open-end winding by maintaining constant capacitor voltage.

4.4.1 Mathematical Proof - The voltage vector which will make inverter-2 absorb zero real power in average sense

A 12-sided Voltage vector space is shown in fig 4.2(a). A 12-sided voltage vector is formed as a vector sum of the voltage vector of inverter one and inverter two as shown for sector 1 in fig 4.2(b). In sector 1, a voltage vector $\overrightarrow{OA}$ of inverter-1 and voltage vector $\overrightarrow{AB}$ of inverter-2 generates one of the 12-sided voltage vector $\overrightarrow{OB}$. Similarly, voltage vector $\overrightarrow{OA}$ of inverter-1 and voltage vector $\overrightarrow{AC}$ of inverter-2 generates one of the 12-sided voltage vector $\overrightarrow{OC}$. The vectors $\overrightarrow{AB}$ and $\overrightarrow{AC}$ are the vectors generated by inverter two, such that the average active power consumed by inverter two is zero. Assume the magnitude and angle of AB and AC to be aV_{dc} and ϕ respectively to

maintain the capacitor voltage at a constant value irrespective of the load variations. Let the load current be $I_m \sin(\omega t - \phi)$.

Consider square wave mode of operation, where each of the dodecagonal vectors will be switched for 30° duration, that is in sector 1, $\overrightarrow{OC}$ will be applied from $-30° \leq \omega t \leq 0°$ and $\overrightarrow{OB}$ will be applied from $0° \leq \omega t \leq 30°$.

Inverter one vector will be switched for an entire period of 60° from $-30° \leq \omega t \leq 0°$ (name as region-1) and from $0° \leq \omega t \leq 30°$ (named as region-2). For this entire period the average real power consumed by inverter-2 should be zero. From instantaneous PQ theory [134], the instantaneous real load power can be written as

$$p_{real} = V_\alpha . I_\alpha + V_\beta . I_\beta \tag{4.1}$$

where V_α , V_β and I_α , I_β are the stationary reference frame components of load voltage and load current respectively.

4.4.1.1 Real power calculation for region-1

Region-1 is defined from $-30° \leq \omega t \leq 0°$. For square wave operation during this entire region, $\overrightarrow{OC}$ will be switched on, which is obtained as a vector sum of $\overrightarrow{OA}$ of inverter-1 and $\overrightarrow{AC}$ of inverter-2. To obtain the real power equation using instantaneous p-q theory, a stationary reference frame needs to be defined. For this region, the stationary reference frame α axis is defined along $\overrightarrow{OC}$ as shown in fig 4.2(c). The inverter-2 voltage vector $\overrightarrow{AC}$, assumed to have a magnitude of aV_{dc} and phase ϕ needs to be converted to stationary reference frame components $V_{2\alpha}$ and $V_{2\beta}$ components as defined in (4.2) below.

$$V_{2\alpha} = -aV_{dc}\cos(\phi + 15°) \text{and} \quad V_{2\beta} = -aV_{dc}\sin(\phi + 15°) \tag{4.2}$$

The motor current also needs to be converted to the stationary reference frame components $I_{m\alpha}$ and $I_{m\beta}$ as defined in (4.3) and (4.4) as shown below. The current is defined for two cases. One from $-30° \leq \omega t \leq -15°$ ((4.3)) and the other for $-15° \leq \omega t \leq 0°$ ((4.4)). For $-30° \leq \omega t \leq -15°$

$$\begin{aligned} I_{m\alpha} &= I_m \cos(\omega t + 15° - \Phi) \\ I_{m\beta} &= -I_m \sin(\omega t + 15° - \Phi) \end{aligned} \tag{4.3}$$

For $-15^\circ \leq \omega t \leq 0^\circ$

$$\begin{aligned} I_{m\alpha} &= I_m \cos(\omega t + 15^\circ - \Phi) \\ I_{m\beta} &= I_m \sin(\omega t + 15^\circ - \Phi) \end{aligned} \tag{4.4}$$

Substituting (4.2), (4.3) and (4.4) in the instantaneous real power equation given in (4.1), and integrating for the entire switching time of 30° to get the average real power P_{21real} absorbed by inverter-2, (4.5) is derived as shown below.

$$P_{21real} = aV_{dc}.I_m \Bigg[- cos(\phi + 15^\circ) \int_{-30^\circ}^{0^\circ} \cos(\omega t + 15^\circ - \Phi) d\omega t - \sin(\phi + 15^\circ) \int_{-15^\circ}^{0^\circ} \sin(\omega t + 15^\circ - \Phi) d\omega t + \sin(\phi + 15^\circ) \int_{-30^\circ}^{-15^\circ} \sin(\omega t + 15^\circ - \Phi) d\omega t \Bigg] \tag{4.5}$$

This can be simplified as

$$P_{21real} = aV_{dc}.I_m(2.\sin(\phi)\cos(\Phi) - 2\sin(\phi + 15^\circ)\cos(\Phi)) \tag{4.6}$$

4.4.1.2 Real power calculation for region-2

Similar to region-1, the average real power for inverter-2 during region-2, P_{22real} for $0^\circ \leq \omega t \leq 30^\circ$ has to be calculated. To calculate the power using the instantaneous p-q theory [134], the stationary reference frame needs to be defined. For region-2 the α axis of the stationary reference frame is defined along the dodecagonal vector $\overrightarrow{OB}$ as shown in fig 4.2(c). Similar to region-1, the stationary reference frame components of the inverter-2 voltage vector $\overrightarrow{AB}$, that generates the dodecagonal vector $\overrightarrow{OB}$ is derived as shown in (4.7) below.

$$V_{2\alpha} = -aV_{dc}\cos(\phi + 15^\circ) \text{and} \quad V_{2\beta} = aV_{dc}\sin(\phi + 15^\circ) \tag{4.7}$$

The stationary components of the load current are calculated for two areas similar to region one as derived in (4.8) and (4.9). For $0^\circ \leq \omega t \leq 15^\circ$

$$I_{m\alpha} = I_m \cos(\omega t - 15^\circ - \Phi) \text{and} \quad I_{m\beta} = -I_m \sin(\omega t - 15^\circ - \Phi) \tag{4.8}$$

For $15^\circ \leq \omega t \leq 30^\circ$

$$I_{m\alpha} = I_m \cos(\omega t - 15^\circ - \Phi) \text{ and } I_{m\beta} = I_m \sin(\omega t - 15^\circ - \Phi) \tag{4.9}$$

Substituting (4.7),(4.8) and (4.9) in (4.1), and integrating for the entire switching time of 30°, the average real power for region-2 P_{22real} can be derived as shown in (4.10) below.

$$P_{22real} = aV_{dc}.I_m\Bigg[- cos(\phi + 15^\circ)\int_{0^\circ}^{30^\circ} \cos(\omega t - 15^\circ - \Phi)d\omega t - \sin(\phi + 15^\circ)\int_{0^\circ}^{15^\circ} \sin(\omega t - 15^\circ - \Phi)d\omega t + \sin(\phi + 15^\circ)\int_{15^\circ}^{30^\circ} \sin(\omega t - 15^\circ - \Phi)d\omega t\Bigg] \tag{4.10}$$

This can be simplified as

$$P_{22real} = aV_{dc}.I_m(-2.\sin(30^\circ + \phi)\cos(\Phi) + 2\sin(\phi + 15^\circ)\cos(\Phi)) \tag{4.11}$$

4.4.1.3 Average real power of inverter-2 for a duration of 60°

The voltage vector $\overrightarrow{OA}$ of inverter-1 is switched on for a duration of 60°. Hence over that period of 60°, the average real power absorbed by inverter-2 should be zero to maintain the capacitor voltage constant. Thus the magnitude and phase of inverter-2 vector should be such that the sum of average real power for inverter-2 over region-1 and region-2 should be zero.

$$P_{21real} + P_{22real} = 0; \tag{4.12}$$

Substituting and simplifying, the equation reduces to

$$aV_{dc}.I_m.2.\cos(\Phi).\cos(\phi + 15^\circ)\sin(-15^\circ) = 0 \tag{4.13}$$

$$\implies \phi + 15^\circ = 90^\circ \tag{4.14}$$

Solving the equation, magnitude and angle of voltage vector of inverter-2 is given by

$$\phi = 75^\circ \quad \text{and} \quad a = 0.2588; \tag{4.15}$$

This shows that when the inverter-2 vector becomes perpendicular to the dodecagonal vector, inverter-2 does not absorb any average real power from the DC source of inverter-1. Now consider the triangle OAB or triangle OAC which will not be right angled triangle , right angled at B and C respectively. The magnitude of $\overrightarrow{AB}$ or $\overrightarrow{AC}$ can be found out to be

$$a.V_{dc} = V_{dc}.\tan 15^\circ = \overrightarrow{AB} = \overrightarrow{AC} \tag{4.16}$$

Thus the magnitude of inverter-2 vector is

$$a = 0.2588 \quad \text{and} \quad \overrightarrow{AB} = \overrightarrow{AC} = 0.2588.V_{dc} \tag{4.17}$$

Hence a voltage vector of magnitude 0.2588 $V_{dc}\angle 75^\circ$ should be generated by inverter-2.

4.4.1.4 Switching scheme to generate the voltage vector $0.2588V_{dc}\angle 75^\circ$

As seen from fig 4.2(b,c), the inverter-2 has to generate a voltage vector $0.2588V_{dc}\angle 75^\circ$, during each sector in square wave mode of operation. Consider sector 1, where the inverter has to generate the vectors $\overrightarrow{AB}$ for a duration of $0^\circ \leq \omega t \leq 30^\circ$. This can be obtained by switching vectors 6' and 5' in an average sense. For that first the magnitude of vectors (1' to 6') should be fixed. In another way, the magnitude of Capacitor voltage V_c of inverter-2 to generate a vector of $0.2588V_{dc}\angle 75^\circ$ needs to be calculated. From fig 4.2(c), the following equation can be derived.

$$V_c \cos(30^\circ) = 0.2588.V_{dc} \cos(25^\circ) \tag{4.18}$$

Thus, the magnitude of capacitor voltage is found to be as shown in (4.19).

$$V_c = 0.2889.V_{dc} \tag{4.19}$$

To calculate the time duration for which vectors 6' and 5' need to be applied, let the time for which inverter-2 applies $\overrightarrow{AB}$ be assumed as T1 sec. Let vectors 6' and 5' be applied in the ratio of k: (1-k) among the total T1 time duration. At steady state the volt - second applied by $\overrightarrow{AB}$ for time TI should be the same as the sum of volt-sec of vector 6' for k.T1 time and vector 5' for (1-k).T1. The volt-sec balance along an axis perpendicular to 5' is shown in (4.20).

$$0.2588V_{dc}.T1.\sin 45^\circ = 0.2889V_{dc}.k.T1.\sin 60^\circ + 0.2889V_{dc}.(1-k).T1.\sin(0^\circ) \tag{4.20}$$

Solving this equation, the value of k is found to be 0.732. Thus to apply a vector $\overrightarrow{AB}$, vector 6' needs to be applied for 0.732.T1, and vector 5' needs to be applied for (1-0.732)T1 seconds. Similarly to apply a vector $\overrightarrow{AC}$, vector 2' needs to be applied for 0.732.T1 and vector 3' needs to be applied for (1-0.732)T1 seconds.

4.4.1.5 Average real power from inverter-1 for region-1 and region-2

Similar to inverter-2, the average real power of inverter-1 is calculated for region-1 and region-2. For both regions inverter-1 switched vector 1 in square wave mode of operation.

The stationary reference frame component of vector 1, is calculated as shown in (4.21) below for region-1.

$$V_{1\alpha} = V_{dc}\cos\,(15^\circ)\text{and}\quad V_{1\beta} = V_{dc}\sin\,(15^\circ) \tag{4.21}$$

The stationary components of the load current for two areas in region one are already derived in (4.3) and (4.4). Substituting (4.21),(4.3) and (4.4) in (4.1), and integrating for the entire switching time of 30°, the average real power for region-1 P_{11real} can be derived as shown in (4.22) below.

$$\begin{aligned} P_{11real} =& V_{dc}.I_m\Bigg[\cos(15^\circ)\int_{-30^\circ}^{0^\circ}\cos(\omega t+15^\circ-\Phi)d\omega t-\sin(15^\circ)\int_{-15^\circ}^{0^\circ}\sin(\omega t+15^\circ-\Phi)d\omega t \\ &+\sin(15^\circ)\int_{-30^\circ}^{-15^\circ}\sin(\omega t+15^\circ-\Phi)d\omega t\Bigg] \end{aligned} \tag{4.22}$$

Similarly for region-2, the voltage vector components of inverter-1 in stationary reference frame are defined in (4.23).

$$V_{2\alpha} = V_{dc}\cos(15^\circ)\text{and}\quad V_{2\beta} = -V_{dc}\sin(15^\circ) \tag{4.23}$$

The motor current components are already derived in (4.8) and (4.9). Hence the average real power P_{12real} for region-2 for inverter-1 is derived in (4.24) below.

$$\begin{aligned} P_{12real} =& V_{dc}.I_m\Bigg[cos(15^\circ)\int_{0^\circ}^{30^\circ}\cos(\omega t-15^\circ-\Phi)d\omega t+\sin(15^\circ)\int_{0^\circ}^{15^\circ}\sin(\omega t-15^\circ-\Phi)d\omega t \\ &-\sin(15^\circ)\int_{15^\circ}^{30^\circ}\sin(\omega t-15^\circ-\Phi)d\omega t\Bigg] \end{aligned} \tag{4.24}$$

Hence the total average power of inverter-1 for a duration of 60° P_{1real}, can be calculated by adding (4.22) and (4.24) and can be simplified to get (4.25) as shown below.

$$P_{1real} = 4.V_{dc}.I_m.\sin 15^\circ\cos 15^\circ.\cos\Phi \tag{4.25}$$

This is the power that will be transferred to the motor windings from the dc source of inverter-1.

4.4.1.6 Average real power across the motor for a duration of 60°

Consider the dodecagonal vector to be of magnitude V_{dodec}. The stationary reference frame components of this vector for region-1 and region-2 are given in (4.26) and (4.27).

$$V_{dod1\alpha} = V_{dodec} \quad \text{and} \quad V_{dod1\beta} = 0 \tag{4.26}$$

$$V_{dod2\alpha} = V_{dodec} \quad \text{and} \quad V_{dod2\beta} = 0 \tag{4.27}$$

The average real power for whole 60°, P_{dodec} can be derived as in (4.28)

$$P_{dodec} = V_{dodec}.I_m \left[\int_{-30^\circ}^{0^\circ} \cos(\omega t + 15^\circ - \Phi) d\omega t + \int_{0^\circ}^{30^\circ} \cos(\omega t - 15^\circ - \Phi) d\omega t \right] \tag{4.28}$$

This can be simplified as

$$P_{dodec} = 4.V_{dodec}.I_m.\sin(15^\circ).\cos(\Phi) \tag{4.29}$$

Since average real power of inverter-2 is zero, the average real power of inverter-1 should be equal to the real power drawn by the motor windings.

$$P_{1real} = P_{dodec} \tag{4.30}$$

$$\begin{aligned} 4.V_{dc}.I_m.\sin 15^\circ \cos 15^\circ.\cos\Phi &= 4.V_{dodec}.I_m.\sin(15^\circ).\cos(\Phi) \\ 4.V_{dc}.\sin 15^\circ \cos 15^\circ &= 4.V_{dodec}.\sin(15^\circ) \end{aligned} \tag{4.31}$$

multiplying both sides by $\frac{3}{\pi}$

$$\frac{4}{\pi} V_{dc}.\frac{3}{2}.\sin 30^\circ = \frac{4}{\pi} V_{dodec}.3.\sin 15^\circ \tag{4.32}$$

This can be simplified as

$$V_{6fund} = V_{12fund} \tag{4.33}$$

Thus (4.33) proves that inverter-2 will draw zero active power if the dodecagonal vector magnitude is such that the fundamental voltage component of inverter-1 is same as the fundamental voltage component of dodecagon. Thus

$$V_{dodec} = 0.9659.V_{dc} \tag{4.34}$$

Now the steady state vector position of inverter-2 at which it absorbs zero real power is determined and if proper switching is selected, the capacitor voltage will be maintained at that constant voltage of $0.288V_{dc}$. Now it has to be proved that the capacitor voltage is a stable point, which is discussed in the next section.

4.4.2 Capacitor voltage and real power of inverter-2 during transient conditions

It is proved in the previous section that at the derived value of capacitor voltage and the corresponding voltage vector generated by inverter-2, the power absorbed in an average sense by inverter-2 is zero. Hence the capacitor voltage will remain constant under a steady state. Now, it has to be analyzed what will happen if there is a sudden change in capacitor voltage due to some transients. Also, at starting, how will the capacitor voltage build up and remain constant at 0.2889 V_{dc}? Under any transient condition let the capacitor voltage be assumed to be at a voltage higher than 0.2889 V_{dc} and let the inverter voltage be at a' V_{dc}, which makes the dodecagonal vector magnitude be V'_{doded}. But the switching scheme for inverter-2 is fixed, hence the inverter-2 vector is still at an angle of $\angle 75°$. The angle of dodecagonal voltage is assumed to change from 15° to $(15° + \delta)$ as shown in fig 4.3.

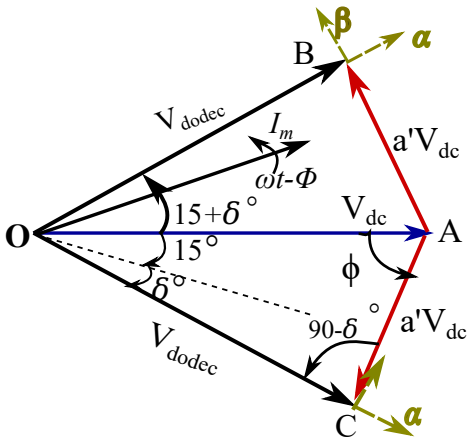

Fig. 4.3. (a) Inverter 1 and Inverter 2 voltage vectors and motor current in sector 1 of dodecagon under a transient condition

For this condition, the real power absorbed by inverter-2 for a period of 60° is calculated in the following section. For region-1, the average real power of inverter-2, P'_{21real} is given by

(4.38), where the stationary frame reference axis is taken along the dodecagonal vector $\overrightarrow{OC}$.

$$\begin{aligned} p_{2real} &= V'_{2\alpha}.I_{m\alpha} + V'_{2\beta}.I_{m\beta} \\ V'_{2\alpha} &= a'V_{dc}\cos(90^\circ - \delta) \\ V'_{2\beta} &= -a'V_{dc}\sin(90^\circ - \delta) \end{aligned} \tag{4.35}$$

For $-30^\circ \leq \omega t \leq -15^\circ$

$$\begin{aligned} I_{m\alpha} &= I_m\cos(\omega t + 15^\circ + \delta - \Phi) \\ I_{m\beta} &= -I_m\sin(\omega t + 15^\circ + \delta - \Phi) \end{aligned} \tag{4.36}$$

For $-15^\circ \leq \omega t \leq 0^\circ$

$$\begin{aligned} I_{m\alpha} &= I_m\cos(\omega t + 15^\circ + \delta - \Phi) \\ I_{m\beta} &= I_m\sin(\omega t + 15^\circ + \delta - \Phi) \end{aligned} \tag{4.37}$$

Substituting (4.37) and (4.36) in (4.35), expanding the dot product and integrating for the entire switching time of 30°,

$$\begin{aligned} P'_{21real} = a'V_{dc}.I_m \Bigg[&\sin(\delta)\int_{-30^\circ}^{0^\circ}\cos(\omega t + 15^\circ + \delta - \Phi)\cos(0^\circ)d\omega t + \\ &\cos(\delta)\int_{-15^\circ}^{0^\circ}\sin(\omega t + 15^\circ + \delta - \Phi)\cos(180^\circ)d\omega t \\ &+ \cos(\delta)\int_{-30^\circ}^{-15^\circ}\sin(\omega t + 15^\circ + \delta - \Phi)\cos(0^\circ)d\omega t \Bigg] \end{aligned} \tag{4.38}$$

This further reduced to

$$P'_{21real} = a'V_{dc}I_m[\cos(15^\circ - \Phi) + \cos(-15^\circ + 2\delta - \Phi) - 2\cos(\delta)\cos(\Phi)] \tag{4.39}$$

Similarly, the average real power for inverter-2 during region-2, P'_{22real} is given by (4.10), where the stationary reference frame is taken along the dodecagonal vector OB.

$$\begin{aligned} V'_{2\alpha} &= a'V_{dc}\sin(\delta) \\ V'_{2\beta} &= a'V_{dc}\cos(\delta) \end{aligned} \tag{4.40}$$

For $0^\circ \leq \omega t \leq 15^\circ$

$$\begin{aligned} I_{m\alpha} &= I_m\cos(\omega t - 15^\circ - \delta - \Phi) \\ I_{m\beta} &= -I_m\sin(\omega t - 15^\circ - \delta - \Phi) \end{aligned} \tag{4.41}$$

For $15^\circ \leq \omega t \leq 30^\circ$

$$\begin{aligned} I_{m\alpha} &= I_m \cos(\omega t - 15^\circ - \delta - \Phi) \\ I_{m\beta} &= I_m \sin(\omega t - 15^\circ - \delta - \Phi) \end{aligned} \tag{4.42}$$

Substituting (4.40),(4.41) and (4.42) in (4.35), and integrating for the entire switching time of 30°,

$$\begin{aligned} P_{22real} =& a' V_{dc}.I_m \Bigg[\sin(\delta) \int_{0^\circ}^{30^\circ} \cos(\omega t - 15^\circ - \delta - \Phi) \cos(0^\circ) d\omega t + \\ & \cos(\delta) \int_{0^\circ}^{15^\circ} \sin(\omega t - 15^\circ - \delta - \Phi) \cos(180^\circ) d\omega t + \\ & \cos(\delta) \int_{15^\circ}^{30^\circ} \sin(\omega t - 15^\circ - \delta - \Phi) \cos(0^\circ) d\omega t \Bigg] \end{aligned} \tag{4.43}$$

This can be further reduced as

$$P'_{22real} = a' V_{dc} I_m [-\cos(15^\circ - \Phi) + \cos(15^\circ + 2\delta + \Phi) + 2\cos(\delta)\cos(\Phi)] \tag{4.44}$$

The average real power over 60° can be derived as (4.45).

$$P_{21real} + P_{22real} = 2\sin(15^\circ + \Phi)\sin(\delta); \tag{4.45}$$

The real power delivered by inverter two is positive. This shows that the capacitor will keep on discharging until $\delta = 0^\circ$, where the real power delivered by inverter-2 will become zero and the capacitor voltage will be maintained at $0.2889 V_{dc}$. Thus it can be concluded that the capacitor voltage will keep on discharging/ charging until it reaches the steady state value of $0.288 V_{dc}$ for any initial conditions in the system and the voltage is a stable equilibrium point. Hence there is no need for any voltage controller. The capacitor voltage will automatically stabilize to the steady state stable voltage of 0.288 V_{dc}.

4.4.2.1 Switching Combinations of Inverter 1 and Inverter 2 voltage vectors for different Sectors

For any sampling time Ts, the vectors in a sector will be switched for T1, T2, and T0 time duration such that T1+T2+T0=Ts. To generate a dodecagonal vector in each sector, Table. 4.1 shows which and all vectors of Inverter 1 and Inverter 2 need to be switched on at each instant. It has to be noted that the switchings for every time duration should be in a symmetric manner.

Table 4.1. Voltage Vectors of Inverter-1 and Inverter-2 to generate the Dodecagonal Voltage Polygon

Sector	Inv-1		Inv-2			
	T1	T2	kT1	(1-k)T1	kT2	(1-k)T2
1	1	1	2’	3’	6’	5’
2	1	2	6’	5’	3’	4’
3	2	2	3’	4’	1’	6’
4	2	3	1’	6’	4’	5’
5	3	3	4’	5’	2’	1’
6	3	4	2’	1’	5’	6’
7	4	4	5’	6’	3’	2’
8	4	5	3’	2’	6’	1’
9	5	5	6’	1’	4’	3’
10	5	6	4’	3’	1’	2’
11	6	6	1’	2’	5’	4’
12	6	1	5’	4’	2’	3’

4.5 24-sided Voltage Space Vector Modulation Scheme

A 24-sided Voltage space vector scheme using two two-level inverter with a single DC source and a DC link capacitor without any voltage controller is discussed in this section. The schematic is shown in fig 4.4.

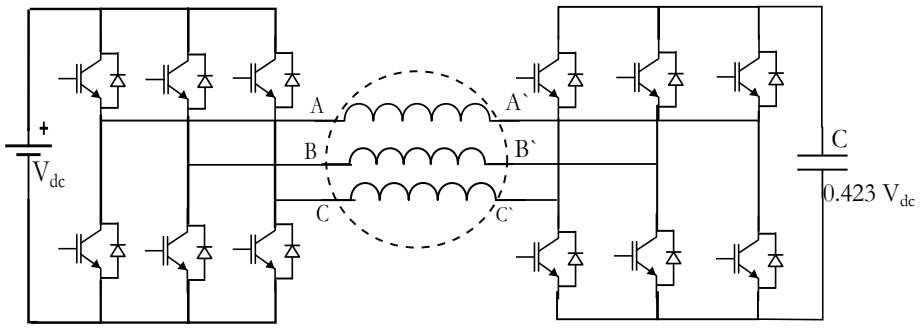

Fig. 4.4. Schematic for a 24-sided Voltage Space vector scheme using one DC source

Each sector of the 24-sided voltage space vector is at an angle of 15° as shown in fig 4.5(a). Similar to the dodecagonal voltage space vector scheme, the inverter-2 should generate voltage vectors such that the average power absorbed by inverter-2 throughout 60° should be zero. Thus a 24-sided voltage space vector is constructed similarly to a 12-sided voltage

space vector by generating vectors from a dodecagon which will be perpendicular to the 24-sided voltage vectors. This is explained in detail in the below section.

4.5.1 Construction of 24-sided voltage space vector using two two-level inverters

Consider fig 4.5(b). $\overrightarrow{OA}$ is the inverter-1 vector. $\overrightarrow{OB}$ and $\overrightarrow{OC}$ are the dodecagonal vectors. Vectors $\overrightarrow{CA_{24}}$ is generated by inverter-2 perpendicular to $\overrightarrow{OA_{24}}$, such that the angle between $\overrightarrow{OC}$ and $\overrightarrow{OA_{24}}$ is 7.5°.

Since the vector $\overrightarrow{CA_{24}}$ is perpendicular to the 24-sided voltage vector $\overrightarrow{OA_{24}}$, inverter-2 does not consume any real power in average sense to generate this vector. Already inverter-2 draws zero average power for generating vector $\overrightarrow{AC}$ to generate the dodecagonal vector $\overrightarrow{OC}$. Now instead of generating a 24-sided voltage vector from a dodecagon, 24 sides can be directly by inverter-1 and inverter-2 vectors. Thus instead of generating vectors $\overrightarrow{OC}$ and $\overrightarrow{CA_{24}}$, inverter-2 can directly generate the vector $\overrightarrow{AA_{24}}$ ($\overrightarrow{OC}$+$\overrightarrow{CA_{24}}$). The inverter-2 will draw zero average real power from the DC source to generate $\overrightarrow{CA_{24}}$, as it is the sum of vectors for which inverter-2 draws zero power. Similarly, some of the other 24-sided vectors

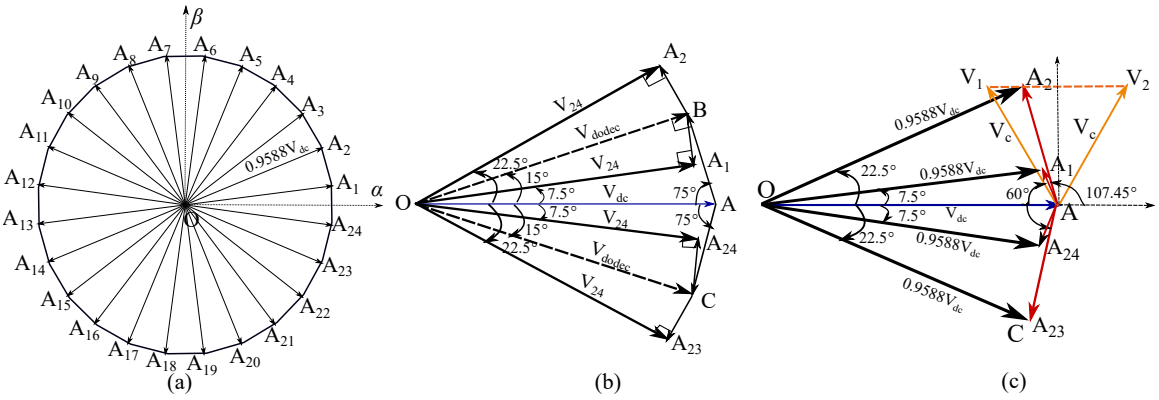

Fig. 4.5. (a) 24-sided voltage space vector (b) 24-sided vectors as a combination of Dodecagonal vectors and inverter-2 vectors (c) 24-sided vectors as a combination of inverter-1 and inverter-2 vectors.

are generated as shown below.

$$\overrightarrow{OA_{23}} = \overrightarrow{OA} + \overrightarrow{AA_{23}}, \quad \text{where} \quad \overrightarrow{AA_{23}} = \overrightarrow{AC} + \overrightarrow{CA_{23}} \tag{4.46}$$

$$\overrightarrow{OA_1} = \overrightarrow{OA} + \overrightarrow{AA_1}, \quad \text{where} \quad \overrightarrow{AA_1} = \overrightarrow{AB} + \overrightarrow{BA_1} \tag{4.47}$$

$$\overrightarrow{OA_2} = \overrightarrow{OA} + \overrightarrow{AA_2}, \quad \text{where} \quad \overrightarrow{AA_2} = \overrightarrow{AB} + \overrightarrow{BA_2} \tag{4.48}$$

Similarly, all other 24 sides can be generated. The magnitude and angle of all these vectors are calculated in (4.49) using fig 4.5(b).

$$\begin{aligned}
V_{dodec} &= V_{dc}\cos(15^\circ) = 0.966V_{dc}\angle 15^\circ = \overrightarrow{OB} \\
\overrightarrow{OA_1} &= V_{dc}\cos(15^\circ)\cos(7.5^\circ) = 0.958V_{dc}\angle 7.5^\circ \\
\overrightarrow{OA_2} &= V_{dc}\cos(15^\circ)\cos(7.5^\circ) = 0.958V_{dc}\angle 22.5^\circ \\
\overrightarrow{BA_1} &= V_{dodec} - \overrightarrow{0A_1} = 0.126V_{dc}\angle -82.5^\circ \\
\overrightarrow{AA_1} &= \overrightarrow{AB} + \overrightarrow{BA_1} = 0.134V_{dc}\angle 112^\circ \\
\overrightarrow{BA_2} &= V_{dodec} - \overrightarrow{0A_2} = 0.126V_{dc}\angle 112.5^\circ \\
\overrightarrow{AA_2} &= \overrightarrow{AB} + \overrightarrow{BA_2} = 0.3847V_{dc}\angle 107.45^\circ
\end{aligned} \tag{4.49}$$

Fig 4.5(c) shows the actual vectors of inverter-2 that need to be generated in an average sense to generate the 24-sided voltage space vector across the OEW induction motor.

4.5.2 Mathematical Proof to show that zero average real power is absorbed by inverter-2

Similar to the proof derived for the dodecagonal voltage space vector scheme, instantaneous p-q theory is used to derive the real power absorbed by inverter-2 to generate different vectors over a range of 60°. The stationary reference frames are defined along the 4, 24-sided vectors (for an entire angle duration of 60°) as shown in fig 4.6.

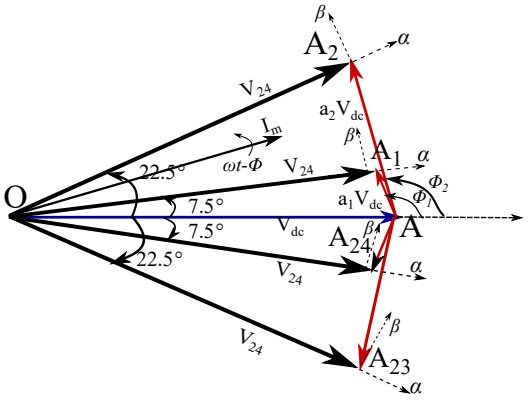

Fig. 4.6. (a) 24-sided vectors as a combination of inverter-1 and inverter-2 vectors along with the stationary reference frames and motor current

Let $\overrightarrow{AA_1}$ be a vector of magnitude and angle $a1V_{dc}\angle(\phi_1)$ and let $\overrightarrow{AA_2}$ be a vector of

magnitude and angle $a2V_{dc}\angle(\phi_2)$. The voltage components along the stationary reference frame for different regions are given below.

$$\begin{aligned}
\text{For} \quad -30^\circ \leq \omega t \leq -15^\circ, \quad V_\alpha &= -a2V_{dc}\cos 22.5^\circ + \phi_2 \quad \text{and} \quad V_\beta = -a2V_{dc}\sin 22.5^\circ + \phi_2 \\
\text{For} \quad -15^\circ \leq \omega t \leq 0^\circ, \quad V_\alpha &= -a1V_{dc}\cos 7.5^\circ + \phi_1 \quad \text{and} \quad V_\beta = -a1V_{dc}\sin 7.5^\circ + \phi_1 \\
\text{For} \quad 0^\circ \leq \omega t \leq -15^\circ, \quad V_\alpha &= -a1V_{dc}\cos 7.5^\circ + \phi_1 \quad \text{and} \quad V_\beta = a1V_{dc}\sin 7.5^\circ + \phi_1 \\
\text{For} \quad 0^\circ \leq \omega t \leq 30^\circ, \quad V_\alpha &= -a2V_{dc}\cos 22.5^\circ + \phi_2 \quad \text{and} \quad V_\beta = a2V_{dc}\sin 22.5^\circ + \phi_2
\end{aligned} \tag{4.50}$$

Similarly the current components in different regions are given by the following equation.

$$\begin{aligned}
\text{For} \quad -30^\circ \leq \omega t \leq -22.5^\circ, \quad I_\alpha &= I_m\cos(\omega t + 22.5^\circ - \Phi) \quad \text{and} \quad I_\beta = -I_m\sin(\omega t + 22.5^\circ - \Phi) \\
\text{For} \quad -22.5^\circ \leq \omega t \leq -15^\circ, \quad I_\alpha &= I_m\cos(\omega t + 22.5^\circ - \Phi) \quad \text{and} \quad I_\beta = I_m\sin(\omega t + 22.5^\circ - \Phi) \\
\text{For} \quad -15^\circ \leq \omega t \leq -7.5^\circ, \quad I_\alpha &= I_m\cos(\omega t + 7.5^\circ - \Phi) \quad \text{and} \quad I_\beta = -I_m\sin(\omega t + 7.5^\circ - \Phi) \\
\text{For} \quad -7.5^\circ \leq \omega t \leq 0^\circ, \quad I_\alpha &= I_m\cos(\omega t + 7.5^\circ - \Phi) \quad \text{and} \quad I_\beta = I_m\sin(\omega t + 7.5^\circ - \Phi) \\
\text{For} \quad 0^\circ \leq \omega t \leq 7.5^\circ, \quad I_\alpha &= I_m\cos(\omega t - 7.5^\circ - \Phi) \quad \text{and} \quad I_\beta = -I_m\sin(\omega t - 7.5^\circ - \Phi) \\
\text{For} \quad 7.5^\circ \leq \omega t \leq 15^\circ, \quad I_\alpha &= I_m\cos(\omega t - 7.5^\circ - \Phi) \quad \text{and} \quad I_\beta = I_m\sin(\omega t - 7.5^\circ - \Phi) \\
\text{For} \quad 15^\circ \leq \omega t \leq 22.5^\circ, \quad I_\alpha &= I_m\cos(\omega t - 22.5^\circ - \Phi) \quad \text{and} \quad I_\beta = -I_m\sin(\omega t - 22.5^\circ - \Phi) \\
\text{For} \quad 22.5^\circ \leq \omega t \leq 30^\circ, \quad I_\alpha &= I_m\cos(\omega t - 22.5^\circ - \Phi) \quad \text{and} \quad I_\beta = I_m\sin(\omega t - 22.5^\circ - \Phi)
\end{aligned} \tag{4.51}$$

The average real power for inverter-2 over 60° can be derived

$$P_{2real} = \int_{-30^\circ}^{30^\circ} (V_\alpha . I_\alpha + V_\beta . I_\beta) d\omega t \tag{4.52}$$

Substituting all the voltage and current components in the above equation and simplifying the following condition is derived for inverter-2 to absorb zero average real power.

$$a1\cos(7.5^\circ + \phi_1) + a_2\cos(22.5^\circ + \phi_2) = 0 \tag{4.53}$$

The derived values of AA_1 and AA_2 in (4.49) satisfy these equations which verify mathematically that the real power drawn by inverter-2 to generate the 24-sided voltage vectors across the OEW motor is zero.

4.5.3 Average Real power for inverter 1

For inverter-1 the average real power of 60° is calculated in this section. The voltage component of the inverter-1 vector over different regions is given below.

$$\begin{aligned}
\text{For} \quad -30^\circ \leq \omega t \leq -15^\circ, \quad V_{1\alpha} &= V_{dc}\cos 22.5^\circ \quad \text{and} \quad V_{1\beta} = V_{dc}\sin 22.5^\circ \\
\text{For} \quad -15^\circ \leq \omega t \leq 0^\circ, \quad V_{1\alpha} &= V_{dc}\cos 7.5^\circ \quad \text{and} \quad V_{1\beta} = V_{dc}\sin 7.5^\circ \\
\text{For} \quad 0^\circ \leq \omega t \leq -15^\circ, \quad V_{1\alpha} &= V_{dc}\cos 7.5^\circ \quad \text{and} \quad V_{1\beta} = -V_{dc}\sin 7.5^\circ \\
\text{For} \quad 0^\circ \leq \omega t \leq 30^\circ, \quad V_{\alpha} &= V_{dc}\cos 22.5^\circ \quad \text{and} \quad V_{1\beta} = -V_{dc}\sin 22.5^\circ
\end{aligned} \tag{4.54}$$

The current components are already derived in (4.51). Substituting these equations of voltage and current components in the real power equation and taking the average for a period of 60° as in (4.52) and simplifying, the average real power of inverter-1, P_{1real} is shown below.

$$P_{1real} = 2.V_{dc}.I_m.\sin 30^\circ.\cos\Phi \tag{4.55}$$

4.5.4 Average real power across the motor windings of OEW IM for a period of 60°

The voltage component of the 24-sided vectors along the stationary reference frame is given below where V_{24} is the length of each of the 24-sided voltage vector.

$$\begin{aligned}
\text{For} \quad -30^\circ \leq \omega t \leq -15^\circ, \quad V_{24\alpha} &= V_{24} \quad \text{and} \quad V_{24\beta} = 0 \\
\text{For} \quad -15^\circ \leq \omega t \leq 0^\circ, \quad V_{24\alpha} &= V_{24} \quad \text{and} \quad V_{24\beta} = 0 \\
\text{For} \quad 0^\circ \leq \omega t \leq -15^\circ, \quad V_{24\alpha} &= V_{24} \quad \text{and} \quad V_{24\beta} = 0 \\
\text{For} \quad 0^\circ \leq \omega t \leq 30^\circ, \quad V_{24\alpha} &= V_{24} \quad \text{and} \quad V_{24\beta} = 0
\end{aligned} \tag{4.56}$$

Substituting these equations along with (4.51) in (4.52), and simplifying, the average real power across the OEW IM is given as shown below.

$$P_{24real} = 8.V_{24}.I_m.\sin 7.5^\circ.\cos\Phi \tag{4.57}$$

The average real power of inverter-1 should be equal to the average real power across the OEW IM, as inverter-2 absorbs zero power. Thus,

$$\begin{aligned}
P_{1real} &= P_{24real} \\
2.V_{dc}.I_m.\sin(30^\circ).\cos\Phi &= 8.V_{24}.I_m.\sin(7.5^\circ).\cos\Phi \\
2.V_{dc}.\sin(30^\circ) &= 8.V_{24}.\sin(7.5^\circ)
\end{aligned} \tag{4.58}$$

Multiplying both sides by $\frac{2}{\pi}.\frac{3}{2}$,

$$\begin{aligned} V_{6fund} &= V_{24fund} \\ V_{24} &= \frac{\sin(30^\circ)}{4.\sin(7.5^\circ)} \\ V_{24} &= 0.9576.V_{dc} \end{aligned} \tag{4.59}$$

Similar to the 12-sided voltage space vector, in the 24-sided vector scheme, the voltage magnitude should be such that the fundamental component of the 24-step voltage waveform is equal to the fundamental component of the six-step voltage waveform.

4.5.5 Sizing of the secondary inverter for 24-sided polygon

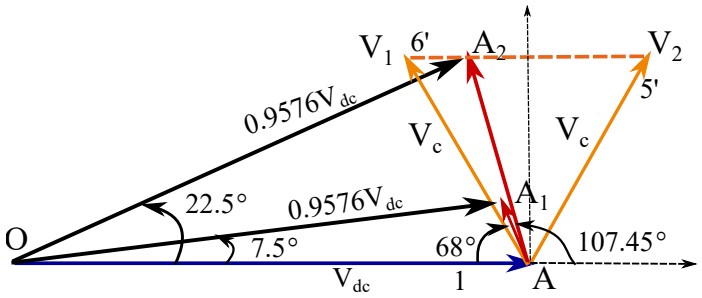

Fig. 4.7. 24-sided voltage vector generated as a vector sum of inverter-1 and inverter-2 vectors.

Consider the fig 4.7 where V_c is the capacitor voltage required to generate vectors $\overrightarrow{AA_1}$ and $\overrightarrow{AA_2}$. $\overrightarrow{AA_2}$ is the largest vector that needs to be generated by inverter two by switching 6' and 5'. The capacitor voltage required to generate the vector $\overrightarrow{AA_2}$ can be derived using (4.60)

$$V_c \cos(30^\circ) = 0.384 V_{dc} \cos(107.45^\circ - 90^\circ) \tag{4.60}$$

$$V_c = 0.423 V_{dc} \tag{4.61}$$

Thus the capacitor voltage will be maintained at a stable steady state value of 0.423 V_{dc}.

4.5.6 Timing Calculation for inverter-2 vectors to generate the voltage vector AA_1

Assume the voltage vector $\overrightarrow{AA_1}$ has to be applied for time T1. To generate this vector let the V1, V2, and zero vectors of inverter-2 be applied for k1TI, k2TI, and (1-k1-k2)T1 respectively.

The values of k1 and k2 are found by volt- sec balance as shown below.

$$\begin{aligned} k1 =& \frac{AA_1}{V_c} \frac{\sin(60^\circ - (120^\circ - 112^\circ))}{\sin(60^\circ)} \\ k1 =& 0.288 \end{aligned} \tag{4.62}$$

$$\begin{aligned} k2 =& \frac{AA_1}{V_c} \frac{\sin(120^\circ - 112^\circ)}{\sin(60^\circ)} \\ k2 =& 0.0509 \end{aligned} \tag{4.63}$$

4.5.7 Timing calculation for inverter-2 vectors to generate the voltage vector AA_2

Assume the pseudo vector $\overrightarrow{AA_2}$ has to be applied for time T1. To generate this vector let the V1 and V2 vectors of inverter-2 be applied for kT1 and (1-k)T1 respectively. The value of k is found by volt- sec balance as shown below.

$$\begin{aligned} k =& \frac{AA_2}{V_c} \frac{\sin(60^\circ - (120^\circ - 107.45^\circ))}{\sin(60^\circ)} \\ k =& 0.7722 \end{aligned} \tag{4.64}$$

The V2 vector will be applied for (1-k)T1, that is 0.2278 T1 duration.

4.5.8 Selection of switching states

Consider an instant where the reference voltage is in sector 2, where for T1 time duration vector $\overrightarrow{AA_2}$ will be generated and vector $\overrightarrow{AA_1}$ will be switched for T2 duration and zero vector will be switched for T0 duration. Among the T1 duration,inverter-1 will switch 1 vector for the entire duration. Inverter 2 will switch the 6' vector for 0.7722 T1 duration and the 5' vector for 0.2278 T1 duration. For T0 duration both inverters will be clamped and a zero voltage vector will be generated. For T2 duration, inverter-1 will switch vector 1 for the entire duration and inverter-2 will switch 6' vector for 0.288 T2 duration, 5' vector for 0.0509 T2 duration, and zero vector for the remaining time. In a similar war, the vectors are switched for inverter-1 and inverter-2 for other sectors as shown in Table. 4.2. All the vectors should be switched in a symmetric sequence for each time interval.

Table 4.2. Voltage Vector of Inverter-1 and Inverter-2 for different sectors of 24-sided Voltage Polygon

Sector	Inv-1		Inv-2		Sector	Inv-1		Inv-2	
	T1	T2	T1	T2		T1	T2	T1	T2
1	1	1	k1T1: 2' k2T1: 3' (1-k2-k2)T1: 7'/8'	k1T2: 6' k2T2: 5' (1-k1-k2)T2: 7'/8'	13	4	4	k1T1: 5' k2T1: 6' (1-k1-k2)T1: 7'/8'	k1T2: 3' k2T2: 2' (1-k1-k2)T2: 7'/8'
2	1	1	k1T1: 6' k2T1: 5' (1-k2-k2)T1: 7'/8'	kT2: 6' (1-k)T2: 5'	14	4	4	k1T1: 3' k2T1: 2' (1-k1-k2)T1: 7'/8'	kT2: 3' (1-k)T2: 2'
3	1	2	kT1: 6' (1-k)T1: 5'	kT2: 3' (1-k)T2: 4'	15	4	5	kT1: 3' (1-k)T1: 2'	kT2: 6' (1-k)T2 : 1'
4	2	2	kT1: 3' (1-k)T1: 4'	k1T2: 3' k2T2: 4' (1-k1-k2)T2: 7'/8'	16	5	5	kT1: 6' (1-k)T1: 1'	k1T2: 6' k2T2: 1' (1-k1-k2)T2: 7'/8'
5	2	2	k1T1: 3' k2T1: 4' (1-k1-k2)T2: 7'/8'	k1T2: 1' k2T2: 6' (1-k1-k2)T2: 7'/8'	17	5	5	k1T1: 6' k2T1: 1' (1-k1-k2)T2: 7'/8'	k1T2: 4' k2T2: 3' (1-k1-k2)T2: 7'/8'
6	2	2	k1T1: 1' k2T1: 6' (1-k1-k2)T2: 7'/8'	kT2: 1' (1-k)T2: 6'	18	5	5	k1T1: 4' k2T1: 3' (1-k1-k2)T2: 7'/8'	kT2: 4' (1-k)T2: 3'
7	2	3	kT1: 1' (1-k)T1: 6'	kT2: 4' (1-k)T2: 5'	19	5	6	kT1: 4' (1-k)T1: 3'	kT2: 1' (1-k)T2: 2'
8	3	3	kT1: 4' (1-k)T1: 5'	k1T2: 4' k2T2: 5' (1-k1-k2)T2: 7'/8'	20	6	6	kT1: 1' (1-k)T1 : 2'	k1T2: 1' k2T2: 2' (1-k1-k2)T2: 7'/8'
9	3	3	k1T1: 4' k2T1: 5' (1-k1-k2)T1: 7'/8'	k1T2: 2' k2T2: 1' (1-k1-k2)T2: 7'/8'	21	6	6	k1T1: 1' k2T1: 2' (1-k1-k2)T1: 7'/8'	k1T2: 5' k2T2: 4' (1-k1-k2)T2: 7'/8'
10	3	3	k1T1: 2' k2T1: 1' (1-k1-k2)T1: 7'/8'	kT2: 2' (1-k)T2: 1'	22	6	6	k1T1: 5' k2T1: 4' (1-k1-k2)T1: 7'/8'	kT2: 5' (1-k)T2: 4'
11	3	4	kT1: 2' (1-k)T1: 1'	kT2: 5' (1-k)T2: 6'	23	6	1	kT1: 5' (1-k)T1: 4'	kT2: 2' (1-k)T2: 3'
12	4	4	kT1: 5' (1-k)T1: 6'	k1T2: 5' k2T2: 6' (1-k1-k2)T2: 7'/8'	24	1	1	kT1: 2' (1-k)T1: 3'	k1T2: 2' k2T2: 3' (1-k1-k2)T2: 7'/8'

4.6 18-sided Voltage space vector structure and modulation scheme

The schematic for generating an 18-sided voltage space vector using two two-level inverters is shown in fig 4.8. Similar to the 12-sided and 24-sided voltage space vector scheme, the capacitor voltage of inverter-2 will be maintained at a steady value of $0.378V_{dc}$ without any voltage controller, and only by using a proper switching scheme. Each sector of the 18-sided voltage vector space is at an angle of 20°.

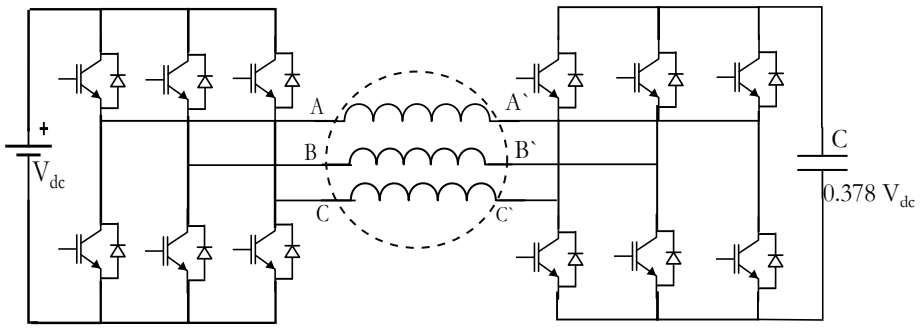

Fig. 4.8. Schematic for an 18-sided Voltage Space vector scheme using one DC source

4.6.1 Construction of 18-sided voltage space vector using two, two-level inverters

The 18-sided voltage vector space is shown in fig 4.9(a). The vector combination of voltage vectors of inverter-1 and inverter-2 to form the 18-sided voltage vectors for sector 18 and sector 1 are shown in fig 4.9(b). From fig 4.9(b), it can be seen that using inverter-1

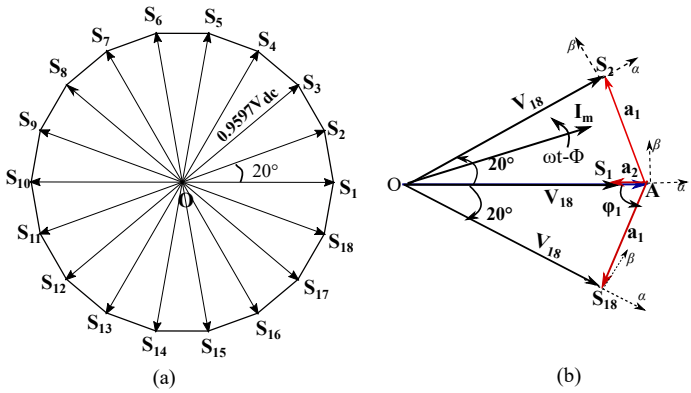

Fig. 4.9. (a) 18-sided voltage space vectors (b) vector combination of Voltage vectors of inverter-1 and inverter-2 to form 18-sided voltage space vectors.

voltage vector $\overrightarrow{OA}$, and three vectors of inverter-2, that is $\overrightarrow{AS_1}$, $\overrightarrow{AS_2}$ and $\overrightarrow{AS_{18}}$, three 18-sided voltage vectors $\overrightarrow{OS_1}$, $\overrightarrow{OS_2}$ and $\overrightarrow{OS_{18}}$ respectively are generated. Similar to dodecagonal and 24-sided vector space schemes, the average real power absorbed by inverter-2 over an angle of 60° should be zero. But it can be seen from fig 4.9(b) that $\overrightarrow{AS_1}$ will absorb real power from the dc source. Hence $\overrightarrow{AS_{18}}$ and $\overrightarrow{AS_2}$ generated should deliver real power such that over a period of 60°, the average real power of inverter-2 will be zero.

4.6.2 Average real Power of inverter-2 over a period of 60°

Assume that voltage vector $\overrightarrow{AS_2}$ has a magnitude of a_1V_{dc} and angle $\angle\phi_1$ and $\overrightarrow{AS_1}$ has a magnitude of a_2V_{dc}. The stationary reference frames are defined along the 18 voltage vector sides as shown in fig 4.9(b). The inverter-2 voltage components along the stationary reference frames are given below.

$$\begin{aligned}
\text{For} \quad & -30^\circ \leq \omega t \leq -10^\circ, \quad V_\alpha = -a_1V_{dc}\cos 20^\circ + \phi_1 \quad \text{and} \quad V_\beta = -a_1V_{dc}\sin 20^\circ + \phi_1 \\
\text{For} \quad & -10^\circ \leq \omega t \leq 10^\circ, \quad V_\alpha = -a_1V_{dc} \quad \text{and} \quad V_\beta = 0 \\
\text{For} \quad & 10^\circ \leq \omega t \leq 30^\circ, \quad V_\alpha = -a_1V_{dc}\cos 20^\circ + \phi_1 \quad \text{and} \quad V_\beta = a_1V_{dc}\sin 20^\circ + \phi_1
\end{aligned} \tag{4.65}$$

Similarly, the motor current components along stationary reference frames for different regions are given below.

$$\begin{aligned}
\text{For} \quad & -30^\circ \leq \omega t \leq -20^\circ, \quad I_\alpha = I_m\cos(\omega t + 20^\circ - \Phi) \quad \text{and} \quad I_\beta = -I_m\sin(\omega t + 20^\circ - \Phi) \\
\text{For} \quad & -20^\circ \leq \omega t \leq -10^\circ, \quad I_\alpha = I_m\cos(\omega t + 20^\circ - \Phi) \quad \text{and} \quad I_\beta = I_m\sin(\omega t + 20^\circ - \Phi) \\
\text{For} \quad & -10^\circ \leq \omega t \leq 0^\circ, \quad I_\alpha = I_m\cos(\omega t - \Phi) \quad \text{and} \quad I_\beta = -I_m\sin(\omega t - \Phi) \\
\text{For} \quad & 0^\circ \leq \omega t \leq 10^\circ, \quad I_\alpha = I_m\cos(\omega t - \Phi) \quad \text{and} \quad I_\beta = I_m\sin(\omega t - \Phi) \\
\text{For} \quad & 10^\circ \leq \omega t \leq 20^\circ, \quad I_\alpha = I_m\cos(\omega t - 20^\circ - \Phi) \quad \text{and} \quad I_\beta = -I_m\sin(\omega t - 20^\circ - \Phi) \\
\text{For} \quad & 20^\circ \leq \omega t \leq 30^\circ, \quad I_\alpha = I_m\cos(\omega t - 20^\circ - \Phi) \quad \text{and} \quad I_\beta = I_m\sin(\omega t - 20^\circ - \Phi)
\end{aligned} \tag{4.66}$$

Substituting these equations into the real power equation according to instantaneous p-q theory and taking the average along the 60°, the average real power for inverter-2, P_{2real} is given by the following equation.

$$P_{2real} = 2.V_{dc}.Im.\sin(10^\circ).(-2a_1\cos(20^\circ + \phi_1) - a_2).\cos(\Phi) \tag{4.67}$$

Thus the condition to get average real power for inverter-2 can be derived from the above equation as given below.

$$(-2a_1\cos(20^\circ + \phi_1) - a_2) = 0; \tag{4.68}$$

4.6.3 Average real power of inverter-1 and across the OEW IM for 60°

The stationary reference components of the inverter-1 vector are given below.

$$\begin{aligned} \text{For} \quad -30^\circ \leq \omega t \leq -10^\circ, \quad V_\alpha &= V_{dc}\cos 20^\circ \quad \text{and} \quad V_\beta = V_{dc}\sin 20^\circ \\ \text{For} \quad -10^\circ \leq \omega t \leq 10^\circ, \quad V_\alpha &= V_{dc} \quad \text{and} \quad V_\beta = 0 \\ \text{For} \quad 10^\circ \leq \omega t \leq 30^\circ, \quad V_\alpha &= V_{dc}\cos 20^\circ \quad \text{and} \quad V_\beta = -V_{dc}\sin 20^\circ \end{aligned} \tag{4.69}$$

Using these above equation, the average real power of inverter-1 , P_{1real} is found to be

$$\begin{aligned} P_{1real} &= V_{dc}.I_m.(2\cos(20^\circ)+1)(\sin(10^\circ+\Phi)+\sin(10^\circ-\Phi)) \\ P_{1real} &= V_{dc}.I_m.(2\cos(20^\circ)+1).2\sin(10^\circ).\cos(\Phi) \\ P_{1real} &= V_{dc}.I_m.\cos(\Phi) \end{aligned} \tag{4.70}$$

Similarly, the average real power for the 18-sided voltage vectors throughout 60° can be found. The voltage components along the stationary reference frames are given by the following equations.

$$\begin{aligned} \text{For} \quad -30^\circ \leq \omega t \leq -10^\circ, \quad V_\alpha &= V_{18} \quad \text{and} \quad V_\beta = 0 \\ \text{For} \quad -10^\circ \leq \omega t \leq 10^\circ, \quad V_\alpha &= V_{18} \quad \text{and} \quad V_\beta = 0 \\ \text{For} \quad 10^\circ \leq \omega t \leq 30^\circ, \quad V_\alpha &= V_{18} \quad \text{and} \quad V_\beta = 0 \end{aligned} \tag{4.71}$$

The real power across the motor windings for a duration of 60° can be found using the instantaneous p-q theory as shown below.

$$P_{real} = 6.V_{18}.I_m.\sin(10^\circ).\cos(\Phi) \tag{4.72}$$

Under steady state conditions, the average power absorbed by the motor should to equal to the power delivered by inverter-1.

$$\begin{aligned} P_{1real} &= P_{real} \\ V_{dc} &= 6.V_{18}.\sin(10^\circ) \end{aligned} \tag{4.73}$$

multiplying both sides by $\frac{4}{\pi}\frac{3}{2}\sin(30^\circ)$

$$\begin{aligned} V_{6fund} &= V_{18fund} \\ V_{18} &= 0.9597V_{dc} \end{aligned} \tag{4.74}$$

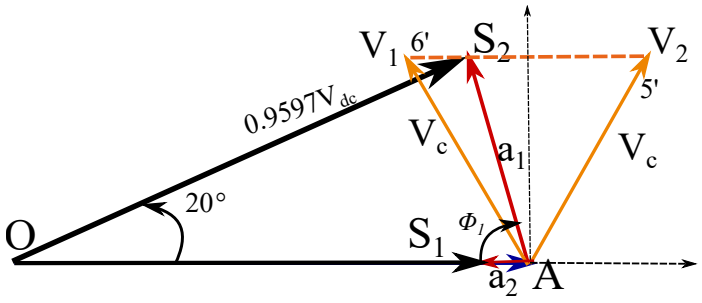

Fig. 4.10. Vector combination of Voltage vectors of inverter-1 and inverter-2 to form 18-sided voltage space vectors.

Consider fig 4.10. The magnitude of $\overrightarrow{AS_1}$,is given by

$$a_2 = V_{dc} - 0.9597V_{dc} = 0.0403V_{dc} \tag{4.75}$$

Also consider triangle OAS_2,

$$V_{dc}\sin(20^\circ) = a_1\sin(20^\circ + \phi_1) \tag{4.76}$$

Solving (4.68) and (4.76), the vector $\overrightarrow{AS_2}$ is found to be

$$a_1 = 0.3426 \quad \text{and} \quad \phi_1 = 73.37^\circ \tag{4.77}$$

Also consider the vectors $\overrightarrow{V_1}$ and $\overrightarrow{AS_2}$

$$\begin{aligned} V_c.\cos(30^\circ) &= 0.3426.V_{dc}.\cos(17^\circ) \\ V_c &= 0.3783.V_{dc} \end{aligned} \tag{4.78}$$

Thus for the proposed scheme, the capacitor voltage will be maintained at $0.3783V_{dc}$ at steady state without any voltage controller.

4.6.4 Timing Calculations of switching vectors to generate AS_1 and AS_2

To generate $\overrightarrow{AS_1}$ for time T1, let 4' be switched for k1 duration and 7'/8' be switched for (1-k1) duration. k1 can be found as follows.

$$\begin{aligned} 0.0403.V_{dc}T1 &= 0.3783.V_{dc}k1T1 \\ k1 &= 0.1052 \end{aligned} \tag{4.79}$$

Similarly to generate $\overrightarrow{AS_2}$ for time T2, let 6' be switched for k2T2 duration and 5' be switched for (1-k2)T2 duration. k2 can be found out as follows.

$$\begin{aligned} k2 =& \frac{0.3426V_{dc}}{0.378V_{dc}} \frac{\sin(46.8^\circ)}{\sin(60^\circ)} \\ k2 =& 0.7606 \end{aligned} \tag{4.80}$$

The voltage vectors to be switched for different sectors is shown in Table. 4.3. It should

Table 4.3. Voltage Vectors of Inverter-1 and Inverter-2 for different sector of 18-sided Voltage Polygon

Sector	**Inv-1**		**Inv-2**		**Sector**	**Inv-1**		**Inv-2**	
	T1	T2	T1	T2		T1	T2	T1	T2
1	1	1	k2T1: 6' (1-k2)T1: 5'	k1T2: 1' (1-k1)T2: 7'/8'	10	4	4	k2T1: 3' (1-k2)T1: 2'	k1T2: 4' (1-k1)T2: 7'/8'
2	2	1	k2T1: 3' (1-k2)T1: 4'	k2T2: 6' (1-k2)T2: 5'	11	5	4	k2T1: 6' (1-k2)T1: 1'	k2T2: 3' (1-k2)T2: 2'
3	2	2	k1T1: 2' (1-k1)T1: 7'/8'	k2T2: 3' (1-k2)T2: 4'	12	5	5	k1T1: 5' (1-k1)T1: 7'/8'	k2T2: 6' (1-k2)T2: 1'
4	2	2	k2T1: 1' (1-k2)T1: 6'	k1T2: 2' (1-k1)T2: 7'/8'	13	5	5	k2T1: 4' (1-k2)T1: 3'	k1T2: 5' (1-k1)T2: 7'/8'
5	3	2	k2T1: 4' (1-k2)T1: 5'	k2T2: 1' (1-k2)T2: 6'	14	6	5	k2T1: 1' (1-k2)T1: 2'	k2T2: 4' (1-k2)T2: 3'
6	3	3	k1T1 : 3' (1-k1)T1: 7'/8'	k2T2 : 4' (1-k2)T2 : 5'	15	6	6	k1T1 : 6' (1-k1)T1: 7'/8'	k2T2 : 1' (1-k2)T2 : 2'
7	3	3	k2T1: 2' (1-k2)T1: 1'	k1T2: 3' (1-k1)T2: 7'/8'	16	6	6	k2T1: 5' (1-k2)T1: 4'	k1T2: 6' (1-k1)T2: 7'/8'
8	4	3	k2T1: 5' (1-k2)T1: 6'	k2T2: 2' (1-k2)T2: 1'	17	1	6	k2T1: 2' (1-k2)T1: 3'	k2T2: 5' (1-k2)T2: 4'
9	4	4	k1T1: 4' (1-k1)T1: 7'/8'	k2T2: 5' (1-k2)T2: 6'	18	1	1	k1T1: 1' (1-k1)T1: 7'/8'	k2T2: 2' (1-k2)T2: 3'

be noted that each vector should be switched symmetrically for every time duration for the capacitor voltage to be maintained constant. In this section, a detailed discussion on the linearization of over-modulation regions for dodecagonal voltage space vector, 24-sided voltage space vector, and 18-sided voltage space vector is given.

4.7 Over-modulation region and linearization techniques for dodecagonal voltage space vectors

Linearization of the over-modulation region for a 6-sided voltage space vector has been discussed in detail in Section. 1.10.5. For the 12-sided voltage space vector, the linear region is until the inscribed circle inside the dodecagon as shown in fig 4.11 similar to hexagonal

space vectors discussed in Chapter 1.

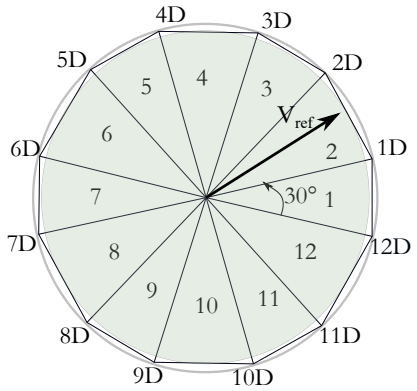

Fig. 4.11. Linear and over-modulation region of a 12-sided voltage vector space.

The modulation index m_{12} can be defined as given below.

$$\begin{aligned} m_{12} &= \frac{V_{m1}}{V_{12fund}} \\ V_{12fund} &= \frac{4}{\pi} 3 \sin 15^{\circ} V_{dodec} \\ V_{dodec} &= 0.9659 V_{dc} \\ V_{12fund} &= 0.9549 V_{dc} \end{aligned} \tag{4.81}$$

For maximum linear operation,

$$\begin{aligned} V_{m1} &= 0.9659 V_{dc} \cos(15^{\circ}) = 0.933 V_{dc} \\ m_{12} &= 0.977 \end{aligned}$$

Thus for a dodecagonal voltage space vector the fundamental voltage and the DC link voltage can be defined using the below equation.

$$V_{fund} = 0.9548.m_{12}.V_{dc} \tag{4.82}$$

where the region are defined as given below.
linear region —- $0 \leq m_{12} \leq 0.977$
over-modulation region-1 — $0.977 \leq m_{12} \leq 0.988$
over-modulation region-2 — $0.988 \leq m_{12} \leq 1$

4.7.1 Over modulation region-1

Over modulation region-1 for dodecagonal space vector is defined for a range of modulation index $0.977 \leq m_{12} \leq 0.988$. The reference waveform and the actual waveform are shown

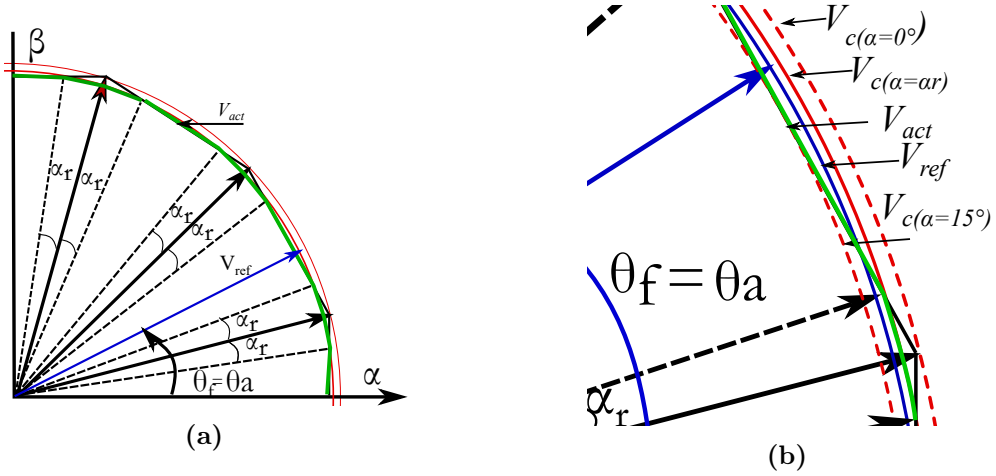

Fig. 4.12. (a) Reference voltage and actual voltage trajectory for region-1 (b) Zoomed part of region-1

in fig 4.12. The fundamental reference phase voltage is $V_{ref}\angle\theta_r$ and the actual voltage vector is $V_{act}\angle\theta_a$. In this region, the reference sinusoidal voltage vector and the actual non-sinusoidal voltage vector move together with the same angular frequency, which implies $\theta_f = \theta_a$. An angle α_r is measured from the vertices of the dodecagon, with its range varying from $0 \leq \alpha_r \leq 15°$. A voltage vector V_c is defined corresponding to each value of α_r. α_r is calculated for each value of the modulation index, which will be described in later in Table. 4.5. When modulation index $m = 0.977$, α_r corresponds to 15° and when $m = 0.988$, α_r corresponds to 0° as shown in fig 4.12(b).

When the fundamental reference voltage vector starts to move from $(\theta_r = 0°)$ to $(15° - \alpha_r)$, the actual vector V_{act} will follow the boundary of the dodecagon as seen from fig 4.12. When the fundamental reference voltage vector moves from $(15° - \alpha_r)$ to $(15° + \alpha_r)$, the actual vector V_{act} will follow the circular path produced by vector $V_c\angle\alpha_r$ as shown in fig 4.12a and fig 4.12b. Fig 4.13 shows the trajectory of the reference and actual voltage waveforms in region-1 of the dodecagonal voltage vector space. From this figure, it can be seen that the actual voltage vector can be divided into seven functions f_1 to f_7. The expression of voltage for each of these sections as a function of angle θ_a is given in Table. 4.4.

The fundamental component is calculated based on the Fourier series expression shown in (4.83).

$$V_{fund} = \frac{4}{\pi}\left[\int_{S1} f_1.\sin\theta.d\theta + \int_{S2} f_2.\sin\theta.d\theta + \int_{S3} f_3.\sin\theta.d\theta + \int_{S4} f_4.\sin\theta.d\theta + \int_{S5} f_5.\sin\theta.d\theta + \int_{S6} f_6.\sin\theta.d\theta + \int_{S7} f_7.\sin\theta.d\theta\right] \tag{4.83}$$

Equating the value obtained in (4.82) for different m values, with (4.83), a relationship

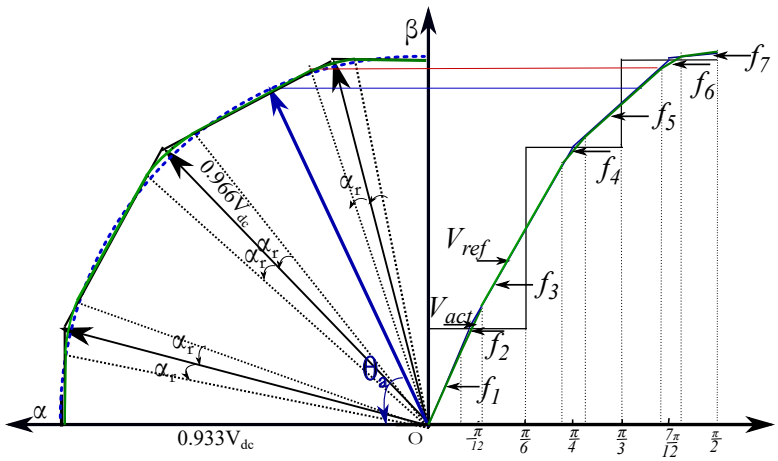

Fig. 4.13. Trajectory of reference and actual voltage in mode 1

Table 4.4. Phase Voltage Equations for Over modulation Region I

Section	Region-1
$0° \leq \theta_a \leq (15° - \alpha_r)$	$f_1 = \frac{0.933.V_{dc}}{\cos(\theta_a)}.\sin(\theta_a)$
$(15° - \alpha_r) \leq \theta_a \leq (15° + \alpha_r)$	$f_2 = \frac{0.933.V_{dc}}{\cos(15° - \alpha_r)}.\sin(\theta_a)$
$(15° + \alpha_r) \leq \theta_a \leq (45° - \alpha_r)$	$f_3 = \frac{0.933.V_{dc}}{\cos(30° - \theta_a)}.\sin(\theta_a)$
$(45° - \alpha_r) \leq \theta_a \leq (45° + \alpha_r)$	$f_4 = \frac{0.933.V_{dc}}{\cos(15° - \alpha_r)}.\sin(\theta_a)$
$(45° + \alpha_r) \leq \theta_a \leq (75° - \alpha_r)$	$f_5 = \frac{0.933.V_{dc}}{\cos(60° - \theta_a)}.\sin(\theta_a)$
$(75° - \alpha_r) \leq \theta_a \leq (75° + \alpha_r)$	$f_6 = \frac{0.933.V_{dc}}{\cos(15° - \alpha_r)}.\sin(\theta_a)$
$(75° + \alpha_r) \leq \theta_a \leq 90°$	$f_7 = \frac{0.933.V_{dc}\sin(\theta_a)}{\cos(90° - \theta_a)} = 0.933V_{dc}$

between modulation index m and angle α_r is obtained [135]. For example, consider α_r equal to 0°, then the value of $V_{fund} = \frac{4}{\pi}0.74129$ as per (4.83). Comparing with (4.11)

$$\begin{aligned} \frac{4}{\pi}0.74129 &= 0.9548 m_{12} V_{dc} \\ m_{12} &= 0.988 \end{aligned} \tag{4.84}$$

This is the maximum value of modulation index in the over-modulation region-1 where angle α_r has reached the limit. The different values of modulation index corresponding to different values of angle α_r is given below. The calculations were done using MAPLE software.

Table 4.5. Modulation index, Fundamental Voltage and angle α_r in over-modulation region-1

α_r	V_{fund}	m_{12}
15°	$0.73277V_{dc}\frac{4}{\pi}$	0.977
10°	$0.73495V_{dc}\frac{4}{\pi}$	0.9803
5°	$0.73904V_{dc}\frac{4}{\pi}$	0.985
0°	$0.74129V_{dc}\frac{4}{\pi}$	0.988

4.7.2 Over-modulation region-2

When the modulation index is higher than 0.988, the actual voltage vector cannot be produced using the modulation method of region-1 as the angle α_r has reached its limit of 0°. Now to generate higher voltage with the same DC input, the inverter has to remain on the dodecagonal vectors for a longer duration, the duration determined by a holding angle called α_h from the vertices of the dodecagon. Thus the actual voltage will not remain a continuous waveform, but will now become a discontinuous waveform that will rotate at a different speed from the reference fundamental voltage vector V_{ref}. Thus the angle of reference fundamental vector θ_r and angle of actual voltage vector θ_a will be different as shown in fig 4.14. When the reference fundamental vector starts

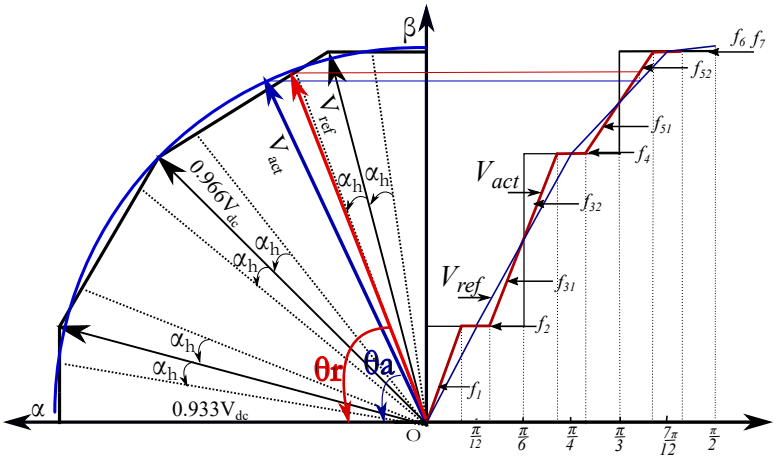

Fig. 4.14. Trajectory of reference and actual voltage in over-modulation region-2

to move from ($\theta_r = 0°$) to $15° - \alpha_h$ at a constant speed, the actual vector V_{act} will accelerate its speed from ($\theta_a = 0°$) to ($\theta_a = 15°$), by following the boundary of the dodecagon and reaches the dodecagonal vector as shown in fig 4.14. Then, when the reference fundamental voltage is moving from ($\theta_r = 15° - \alpha_h$) to $15° + \alpha_h$, the actual vector is held at the dodecagonal voltage vector. From ($15° + \alpha_h$) till 30°, the actual

vector is lagging the reference vector. At 30°, both the reference and actual vector coincide.
The actual voltage waveform is divided into different sections from f_1 to f_7 as shown in fig 4.14. For each region, a relationship between θ_a and θ_r is defined and the fundamental voltage for that region is derived.

4.7.3 Region f_1:

In region f_1, when the reference fundamental vector moves form 0° to $15 - \alpha_h$, the actual vector moves from 0° to 15° at a faster rate. Thus $\theta_a : 15^\circ = \theta_r : \ (15 - \alpha_h)$. Thus we can define the fundamental voltage and the relation between the actual angle and reference angle as given below.

$$\begin{aligned} \text{For} \quad & 0 \leq \theta_r \leq (15^\circ - \alpha_h) \ \text{ and } \ 0 \leq \theta_a \leq 15^\circ \\ & \theta_a = \frac{\theta_r}{1 - \frac{\alpha_h}{15^\circ}} \ \text{ and } \ f_1 = 0.933 V_{dc} \frac{\sin(\theta_a)}{\cos(\theta_a)} \end{aligned} \tag{4.85}$$

4.7.4 Region f_2:

For region f_2, the actual voltage is held constant, while the fundamental voltage is moving from $(15^\circ - \alpha_h)$ to $(15^\circ - \alpha_h)$.

$$\begin{aligned} \text{For} \quad & (15^\circ - \alpha_h) \leq \theta_r \leq (15^\circ + \alpha_h) \\ & f_2 = \frac{0.933 V_{dc} \sin(15^\circ)}{\cos(15^\circ)} \end{aligned} \tag{4.86}$$

4.7.5 Region f_{31}:

For region f_{31}, when the reference fundamental vector moves form $15^\circ + \alpha_h$ to 30°, the actual vector θ_a moves from 15° to 30°. New angles, local reference angle θ'_r and θ'_a are defined as given below.

$$\begin{aligned} 15^\circ + \alpha_h \leq \theta_r \leq 30^\circ \implies & \alpha_h \leq \theta'_r \leq 15^\circ, \text{where} \ \ \theta'_r = \theta_r - 15^\circ \\ & 0^\circ \leq \theta'_r - \alpha_h \leq 15^\circ - \alpha_h \\ \text{similarly}, 15^\circ \leq \theta_a \leq 30^\circ \implies & 0^\circ \leq \theta'_a \leq 15^\circ, \text{where} \ \ \theta'_a = \theta_a - 15^\circ \\ & \theta'_a : \ 15^\circ = \theta'_r - \alpha_h : \ (15 - \alpha_h) \end{aligned} \tag{4.87}$$

The actual voltage can be defined as follows.

$$\begin{aligned} \text{For} \quad & 15 + \alpha_h^\circ \leq \theta_r \leq (30^\circ) \ \text{ and } \ 0^\circ \leq \theta'_r - \alpha_h \leq (15^\circ - \alpha_h) \\ & \theta'_a = \frac{\theta'_r - \alpha_h}{1 - \frac{\alpha_h}{15^\circ}} \ \text{ and } \ f_{31} = 0.933 V_{dc} \frac{\sin(\theta'_a + 15^\circ)}{\cos(15^\circ - \theta'_a)} \end{aligned} \tag{4.88}$$

4.7.6 Region f_{32}:

For region f_{32}, when the reference fundamental vector moves form 30° to $45^\circ - \alpha_h$, local reference angle θ'_r and θ'_a are defined as given below.

$$\begin{aligned} 30^\circ \leq \theta_r \leq 45^\circ - \alpha_h \implies & 0^\circ \leq \theta'_r \leq 15^\circ - \alpha_h, \text{where } \ \theta'_r = \theta_r - 30^\circ \\ \text{similarly}, 30^\circ \leq \theta_a \leq 45^\circ \implies & 0^\circ \leq \theta'_a \leq 15^\circ, \text{where } \ \theta'_a = \theta_a - 30^\circ \\ & \theta'_a : \ 15^\circ = \theta'_r : (15 - \alpha_h) \end{aligned} \tag{4.89}$$

The actual voltage can be defined as follows.

$$\begin{aligned} \text{For} \quad & 30^\circ \leq \theta_r \leq 45^\circ - \alpha_h \ \text{ and } \ 0^\circ \leq \theta'_r \leq (15^\circ - \alpha_h) \\ & \theta'_a = \frac{\theta'_r}{1 - \frac{\alpha_h}{15^\circ}} \ \text{ and } \ f_{32} = 0.933 V_{dc} \frac{\sin(\theta'_a + 30^\circ)}{\cos(\theta'_a)} \end{aligned} \tag{4.90}$$

4.7.7 Region f_4:

For region f_4, the actual voltage is held constant, while the fundamental voltage is moving from $(45^\circ - \alpha_h)$ to $(45^\circ - \alpha_h)$.

$$\begin{aligned} \text{For} \quad & (45^\circ - \alpha_h) \leq \theta_r \leq (45^\circ + \alpha_h) \\ & f_4 = 0.933 V_{dc} \frac{\sin(45^\circ)}{\cos(15^\circ)} \end{aligned} \tag{4.91}$$

4.7.8 Region f_{51}:

For region f_{51}, local reference angle θ'_r and θ'_a are defined as given below.

$$\begin{aligned} 45^\circ + \alpha_h \leq \theta_r \leq 60^\circ \implies & 0^\circ \leq \theta'_r - \alpha_h \leq 15^\circ - \alpha_h, \text{where } \ \theta'_r = \theta_r - 45^\circ \\ \text{similarly}, 45^\circ \leq \theta_a \leq 60^\circ \implies & 0^\circ \leq \theta'_a \leq 15^\circ, \text{where } \ \theta'_a = \theta_a - 45^\circ \\ & \theta'_a : \ 15^\circ = \theta'_r - \alpha_h : \ (15 - \alpha_h) \end{aligned} \tag{4.92}$$

The actual voltage can be defined as follows.

$$\begin{aligned} \text{For} \quad & 45^\circ + \alpha_h \leq \theta_r \leq 60^\circ \ \text{ and } \ 0^\circ \leq \theta'_r \leq (15^\circ - \alpha_h) \\ & \theta'_a = \frac{\theta'_r - \alpha_h}{1 - \frac{\alpha_h}{15^\circ}} \ \text{ and } \ f_{51} = 0.933 V_{dc} \frac{\sin(\theta'_a + 45^\circ)}{\cos(15^\circ - \theta'_a)} \end{aligned} \tag{4.93}$$

4.7.9 Region f_{52}:

For region f_{52}, when the reference fundamental vector moves form 60° to $75^\circ - \alpha_h$, local reference angle θ'_r and θ'_a are defined as given below.

$$\begin{aligned} 60^\circ \leq \theta_r \leq 75^\circ - \alpha_h \implies & 0^\circ \leq \theta'_r \leq 15^\circ - \alpha_h, \text{where } \ \theta'_r = \theta_r - 60^\circ \\ \text{similarly}, 60^\circ \leq \theta_a \leq 75^\circ \implies & 0^\circ \leq \theta'_a \leq 15^\circ, \text{where } \ \theta'_a = \theta_a - 60^\circ \\ & \theta'_a : \ 15^\circ = \theta'_r : (15 - \alpha_h) \end{aligned} \tag{4.94}$$

The actual voltage can be defined as follows.

$$\begin{aligned} \text{For} \quad & 60^\circ \leq \theta_r \leq 75^\circ - \alpha_h \ \text{ and } \ 0^\circ \leq \theta'_r \leq (15^\circ - \alpha_h) \\ & \theta'_a = \frac{\theta'_r}{1 - \frac{\alpha_h}{15^\circ}} \ \text{ and } \ f_{52} = 0.933 V_{dc} \frac{\sin(\theta'_a + 60^\circ)}{\cos(\theta'_a)} \end{aligned} \tag{4.95}$$

4.7.10 Region f_6:

For region f_6, the actual voltage is held constant, while the fundamental voltage is moving from $(75^\circ - \alpha_h)$ to $(75^\circ - \alpha_h)$.

$$\begin{aligned} \text{For} \quad & (75^\circ - \alpha_h) \leq \theta_r \leq (75^\circ + \alpha_h) \\ & f_6 = 0.933 V_{dc} \frac{\sin(75^\circ)}{\cos(15^\circ)} = 0.933 V_{dc} \end{aligned} \tag{4.96}$$

4.7.11 Region f_7:

For region f_7, local reference angle θ'_r and θ'_a are defined as given below.

$$\begin{aligned} 75^\circ + \alpha_h \leq \theta_r \leq 90^\circ \implies & 0^\circ \leq \theta'_r - \alpha_h \leq 15^\circ - \alpha_h, \text{where } \ \theta'_r = \theta_r - 75^\circ \\ \text{similarly}, 75^\circ \leq \theta_a \leq 90^\circ \implies & 0^\circ \leq \theta'_a \leq 15^\circ, \text{where } \ \theta'_a = \theta_a - 75^\circ \\ & \theta'_a : \ 15^\circ = \theta'_r - \alpha_h : \ (15 - \alpha_h) \end{aligned} \tag{4.97}$$

The actual voltage can be defined as follows.

$$\begin{aligned} &\text{For} \quad 75^\circ + \alpha_h \leq \theta_r \leq 90^\circ \quad \text{and} \quad 0^\circ \leq \theta'_r \leq (15^\circ - \alpha_h) \\ &\theta'_a = \frac{\theta'_r - \alpha_h}{1 - \frac{\alpha_h}{15^\circ}} \quad \text{and} \quad f_7 = 0.933 V_{dc} \frac{\sin(\theta'_a + 75^\circ)}{\cos(15^\circ - \theta'_a)} = 0.933 V_{dc} \end{aligned} \tag{4.98}$$

The fundamental value of the phase voltage is obtained similar to that obtained in region-1 as shown below.

$$\begin{aligned} V_{fund} = \frac{4}{\pi} \Bigg[&\int_{S1} f_1 . \sin\theta . d\theta + \int_{S2} f_2 . \sin\theta . d\theta + \int_{S31} f_{31} . \sin\theta . d\theta + \int_{S32} f_{32} . \sin\theta . d\,\theta + \int_{S4} \\ &f_4 . \sin\theta \; d\theta + \int_{S51} f_{51} . \sin\theta . d\theta + \int_{S52} f_{52} . \sin\theta . d\theta + \int_{S6} f_6 . \sin\theta . d\theta + \int_{S7} f_7 . \sin\theta . d\theta \Bigg] \end{aligned} \tag{4.99}$$

Equating the value obtained in (4.82) for different m values, with (4.99), a relationship between modulation index m and angle α_h is obtained as shown in Table. 4.6. The mathematical calculation was done using the numerical analysis method (Simpson's Method) in MATLAB.

Table 4.6. Modulation index, Fundamental Voltage and holding angle α_h in over-modulation region-2

α_h	V_{fund}	m_{12}
2.5°	$0.743956 V_{dc} \frac{4}{\pi}$	0.9922
5°	$0.746140 V_{dc} \frac{4}{\pi}$	0.9951
7.5°	$0.747844 V_{dc} \frac{4}{\pi}$	0.9974
10°	$0.749066 V_{dc} \frac{4}{\pi}$	0.9990
12.5°	$0.749804 V_{dc} \frac{4}{\pi}$	0.9996
15°	$0.7500 V_{dc} \frac{4}{\pi}$	1

4.8 24-sided Voltage space vector - Linearization of over-modulation region

Similar to the linearization method in a 12-sided voltage space vector , the over-modulation region of a 24-sided voltage space vector can be linearized. The modulation

index m_{24} for a 24-sided voltage space vector can be defined as given below.

$$\begin{aligned} m_{24} &= \frac{V_{m1}}{V_{24fund}} \\ V_{24fund} &= \frac{4}{\pi} 6 \sin 7.5^{\circ} V_{24} \\ V_{24} &= 0.95766 V_{dc} \\ V_{24fund} &= 0.9548 V_{dc} \end{aligned} \tag{4.100}$$

Thus for a 24-sided voltage space vector the fundamental voltage and the DC link voltage can be defined using the below linear equation.

$$V_{fund} = 0.9548.m_{24}.V_{dc} \tag{4.101}$$

For maximum linear operation,

$$\begin{aligned} V_{m1} &= 0.9576 V_{dc} \cos(7.5^{\circ}) = 0.94946 V_{dc} \\ m_{24} &= 0.994 \end{aligned} \tag{4.102}$$

where the region is defined as given below.
linear region —- $0 \leq m_{24} \leq 0.994$
over-modulation region-1 — $0.994 \leq m_{24} \leq 0.996$
over-modulation region-2 — $0.996 \leq m_{24} \leq 1$
The linear region is defined from $0 \leq m \leq 0.9943$, where the normal space vector scheme is utilized and the nonlinear region is defined from $0.9943 \leq m \leq 1$.

4.8.0.1 Over modulation region-1 and region-2

Region 1 is defined for a range of modulation index between $0.9943 \leq m \leq 0.996$. In this region, the reference fundamental voltage and the actual voltage move together with the same speed, that is, $\theta_r = \theta_a$. A switching scheme similar to dodecagon is implemented for 24-sided SV, by calculating values of angles α_r for different values of modulation index, m_{24}. The limit of the region-1 is calculated by finding the fundamental voltage corresponding to $\alpha_r = 0^{\circ}$. The modulation index m_{24} corresponding to this operating point is found to be 0.996.
The over-modulation region-2 is defined for the remaining region, that is , from $m_{24} = 0.996$ to $m_{24} = 1$. The modulation technique similar to dodecagonal modula-

Table 4.7. Phase Voltage Equations for Over modulation Region I

section	Region I
$0° \leq \theta_a \leq (7.5° - \alpha_r)$	$f_1 = \frac{0.9494.V_{dc}}{\cos(\theta_a)}.\sin(\theta_a)$
$(7.5° - \alpha_r) \leq \theta_a \leq (7.5° + \alpha_r)$	$f_2 = \frac{0.9494.V_{dc}}{\cos(7.5° - \alpha_r)}.\sin(\theta_a)$
$(7.5° + \alpha_r) \leq \theta_a \leq (22.5° - \alpha_r)$	$f_3 = \frac{0.9494.V_{dc}}{\cos(15° - \theta_a)}.\sin(\theta_a)$
$(22.5° - \alpha_r) \leq \theta_a \leq (22.5° + \alpha_r)$	$f_4 = \frac{0.9494.V_{dc}}{\cos(7.5° - \alpha_r)}.\sin(\theta_a)$
$(22.5° + \alpha_r) \leq \theta_a \leq (37.5° - \alpha_r)$	$f_5 = \frac{0.9494.V_{dc}}{\cos(30° - \theta_a)}.\sin(\theta_a)$
$(37.5° - \alpha_r) \leq \theta_a \leq (37.5° + \alpha_r)$	$f_6 = \frac{0.9494.V_{dc}}{\cos(7.5° - \alpha_r)}.\sin(\theta_a)$
$(37.5° + \alpha_r) \leq \theta_a \leq (52.5° - \alpha_r)$	$f_7 = \frac{0.9494.V_{dc}}{\cos(45° - \theta_a)}.\sin(\theta_a)$
$(52.5° - \alpha_r) \leq \theta_a \leq (52.5° + \alpha_r)$	$f_8 = \frac{0.9494.V_{dc}}{\cos(7.5° - \alpha_r)}.\sin(\theta_a)$
$(52.5° + \alpha_r) \leq \theta_a \leq (67.5° - \alpha_r)$	$f_9 = \frac{0.9494.V_{dc}}{\cos(60° - \theta_a)}.\sin(\theta_a)$
$(67.5° - \alpha_r) \leq \theta_a \leq (67.5° + \alpha_r)$	$f_{10} = \frac{0.9494.V_{dc}}{\cos(7.5° - \alpha_r)}.\sin(\theta_a)$
$(67.5° + \alpha_r) \leq \theta_a \leq (82.5° - \alpha_r)$	$f_{11} = \frac{0.9494.V_{dc}}{\cos(75° - \theta_a)}.\sin(\theta_a)$
$(82.5° - \alpha_r) \leq \theta_a \leq (82.5° + \alpha_r)$	$f_{12} = \frac{0.9494.V_{dc}}{\cos(7.5° - \alpha_r)}.\sin(\theta_a)$
$(82.5° + \alpha_r) \leq \theta_a \leq 90°$	$f_{13} = \frac{0.9494.V_{dc}\sin(\theta_a)}{\cos(90° - \theta_a)} = 0.9494V_{dc}$

tion in over-modulation region-2 is followed by defining a holding angle, α_h, which can vary from $0 \leq \alpha_r \leq 7.5°$.

4.9 18-sided Voltage space vector - Linearization of over-modulation region

The modulation index m_{18} for an 18-sided voltage space vector can be defined as given below.

$$\begin{aligned} m_{18} &= \frac{V_{m1}}{V_{18fund}} \\ V_{18fund} &= \frac{4}{\pi}\frac{9}{2}\sin 10° V_{18} \\ V_{18} &= 0.9597V_{dc} \\ V_{18fund} &= 0.9548V_{dc} \end{aligned} \tag{4.103}$$

Thus for a 18-sided voltage space vector the fundamental voltage and the DC link voltage can be defined using the below linear equation.

$$V_{fund} = 0.9548.m_{18}.V_{dc} \tag{4.104}$$

For maximum linear operation,

$$\begin{aligned} V_{m1} &= 0.9597 V_{dc} \cos(10^\circ) = 0.9452 V_{dc} \\ m_{18} &= 0.9899 \end{aligned} \tag{4.105}$$

where the region is defined as given below.
linear region —- $0 \leq m_{18} \leq 0.9899$
over-modulation region-1 — $0.9899 \leq m_{18} \leq 0.995$
over-modulation region-2 — $0.995 \leq m_{24} \leq 1$

4.9.1 Over modulation region-1 and region-2

Region 1 is defined for a range of modulation index between $0.9899 \leq m \leq 0.995$. In this region, the reference fundamental voltage and the actual voltage move together with the same speed, that is, $\theta_r = \theta_a$. A switching scheme similar to dodecagon is implemented for 18-sided SV, by calculating values of angles α_r for different values of modulation index, m_{18}.

The limit of the region-1 is calculated by finding the fundamental voltage corresponding to $\alpha_r = 0^\circ$. The modulation index m_{18} corresponding to this operating point is found to be 0.995.
The over-modulation region-2 is defined for the remaining region, that is , from $m_{18} = 0.995$ to $m_{18} = 1$. The modulation technique similar to dodecagonal modulation in over-modulation region-2 is followed by defining a holding angle, α_h, which can vary from $0 \leq \alpha_r \leq 10^\circ$.

4.10 Simulation and Experimental Results

The proposed modulation scheme was implemented in MATLAB Simulink for a DC link voltage of 400 V. The inverter-2 voltage is maintained constant at different

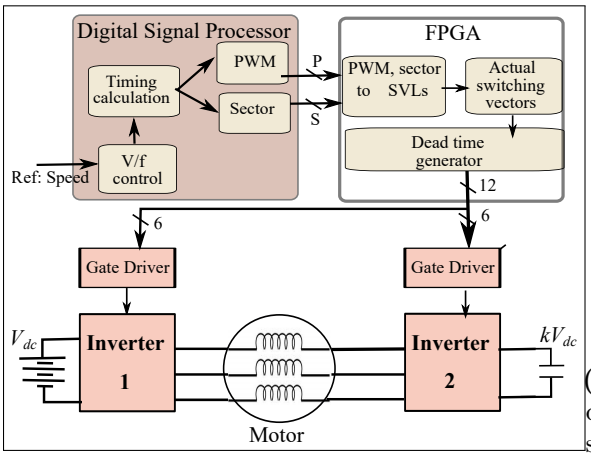

(a) Block diagram of the hardware components including the functions performed by DSP and FPGA

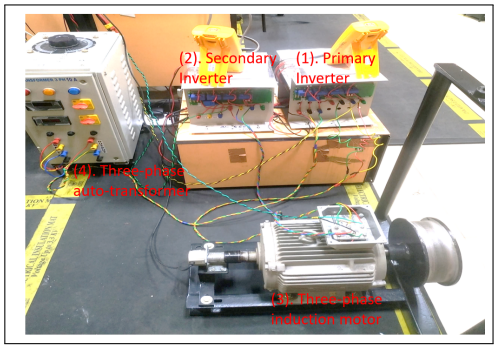

(b) Hardware set-up for the implementation of dodecagon space vector structure with single source: (1). Primary inverter (Inverter-1). **(2).** Secondary inverter (Inverter-2). **(3).** Three-phase induction motor. **(4).** Three-phase auto-transformer

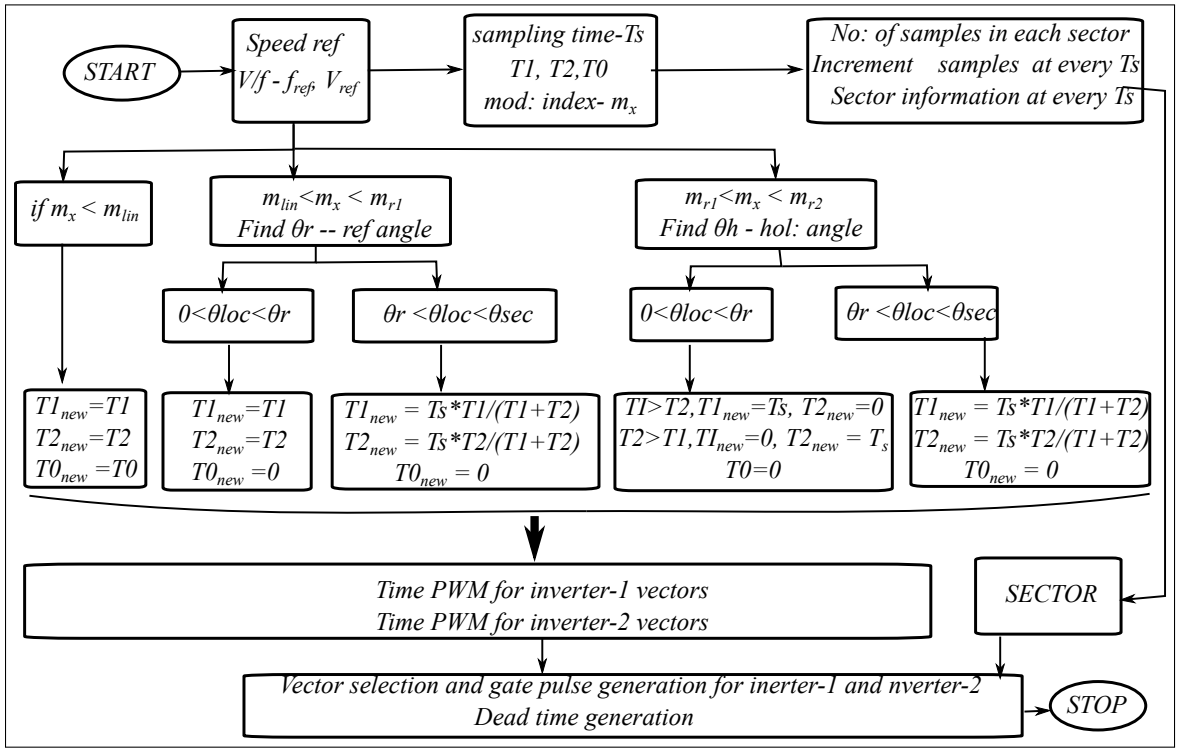

Fig. 4.16. Flowchart of the algorithm to generate the gating pulses for inverter-1 and inverter-2

Table 4.8. Phase Voltage Equations for Over modulation Region I

section	Region I
$0° \leq \theta_a \leq (10° - \alpha_r)$	$f_1 = \frac{0.9451.V_{dc}}{\cos(\theta_a)}.\sin(\theta_a)$
$(10° - \alpha_r) \leq \theta_a \leq (10° + \alpha_r)$	$f_2 = \frac{0.9451.V_{dc}}{\cos(10° - \alpha_r)}.\sin(\theta_a)$
$(10° + \alpha_r) \leq \theta_a \leq (30° - \alpha_r)$	$f_3 = \frac{0.9451.V_{dc}}{\cos(20° - \theta_a)}.\sin(\theta_a)$
$(30° - \alpha_r) \leq \theta_a \leq (30° + \alpha_r)$	$f_4 = \frac{0.9451.V_{dc}}{\cos(10° - \alpha_r)}.\sin(\theta_a)$
$(30° + \alpha_r) \leq \theta_a \leq (50° - \alpha_r)$	$f_5 = \frac{0.9451.V_{dc}}{\cos(40° - \theta_a)}.\sin(\theta_a)$
$(50° - \alpha_r) \leq \theta_a \leq (50° + \alpha_r)$	$f_6 = \frac{0.9451.V_{dc}}{\cos(10° - \alpha_r)}.\sin(\theta_a)$
$(50° + \alpha_r) \leq \theta_a \leq (70° - \alpha_r)$	$f_7 = \frac{0.9451.V_{dc}}{\cos(60° - \theta_a)}.\sin(\theta_a)$
$(70° - \alpha_r) \leq \theta_a \leq (70° + \alpha_r)$	$f_8 = \frac{0.9451.V_{dc}}{\cos(10° - \alpha_r)}.\sin(\theta_a)$
$(70° + \alpha_r) \leq \theta_a \leq (90° - \alpha_r)$	$f_9 = \frac{0.9451.V_{dc}}{\cos(80° - \theta_a)}.\sin(\theta_a)$
$(90° - \alpha_r) \leq \theta_a \leq (90° + \alpha_r)$	$f_{10} = \frac{0.9451.V_{dc}}{\cos(10° - \alpha_r)}.\sin(\theta_a)$

Table 4.9. Hardware Specification

Sub-system	Specifications
Three-phase Inverter	1200 Volts, 75 Amps
Three-phase induction motor	415 volts, 50 Hz, 3.7 kW
Three-phase rectifier modules	415 Volts, 60 Amps
Three-phase auto-transformer	415 Volts, 50 Hz, 10 Amps
DSP (TI C2000, TMS320F28069M)	clk=90 MHz
FPGA (Xilinx, Spartan-6)	clk=50MHz

voltages based on the voltage space vector schemes. The machine parameters used for the simulation of an open-end winding 4-pole induction machine are listed in table 4.10.

Hardware prototype is implemented using two inverters with SKM75GB12T4 IGBT half bridge modules and TMS320F28069S digital signal controller on a 3.7 kW three-phase IM. The details of the hardware setup are specified in Table. 4.9. The block diagram of the various hardware components used as well as the functions performed are shown in fig 4.15a. From the figure, it can be seen that DSP and FPGA together implement the switching scheme used to generate the 12 gate pulses, six for each inverter, inverter-1, and inverter-2. The reference speed is the input to the DSP. Using V/f control, the frequency and voltage for the different speeds are calculated. The sampling time for different sets of speeds and hence corresponding supply frequency is calculated. The required time base period value for the PWM and the interrupt is made into a look-up table. Each sector can be divided into different samples. In this experimental setup, each sector of the dodecagon is divided into 4 samples, each sector

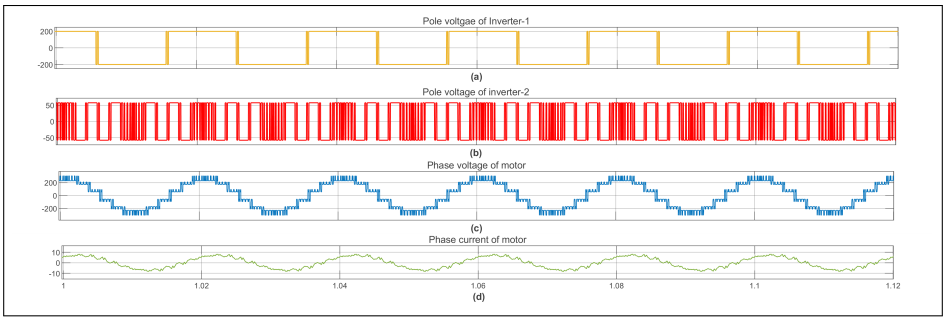

Fig. 4.17. Simulation Results: Region 1- Steady State results: **a.** Pole voltage of inverter-1, **b.** Pole voltage of inverter-2, **c.** Phase voltage of the motor, and **d.** Phase current of open-end winding induction motor.

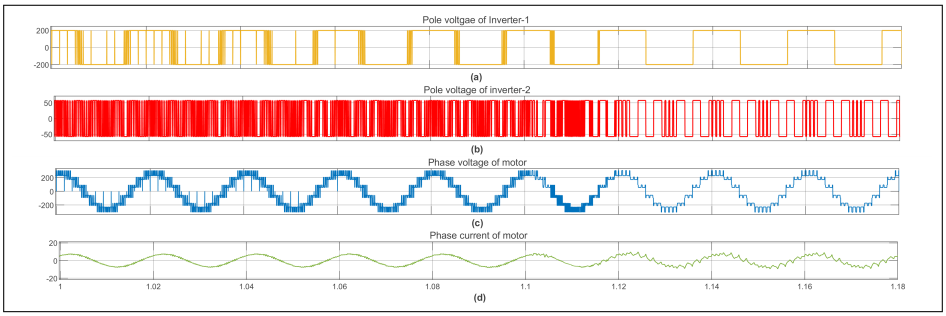

Fig. 4.18. Simulation Result: Transients from Linear region to Region 2: **a.** Pole voltage of inverter-1, **b.** Pole voltage of inverter-2, **c.** Phase voltage of the motor, and **d.** Phase current of open-end winding induction motor.

of 24-sided polygon is divided into three samples and each sector of 18-sided polygon is divided into four samples. The time calculations, T1 and T2 are done for each of these samples in a sector for 50 Hz frequency, and as frequency changes t1 and t2 remain fixed, only the value for T0 and hence Ts varies. The samples are incremented after every sampling time Ts. The modulation index, m_x for each speed is found, where x stands for 12, 18, and 24 in different space vector schemes. The maximum value of modulation in the linear region is defined as m_{lin}, in the over-modulation region-1 is defined as m_{r1} and over-modulation region-2 is defined as m_{r2}. Based on the region of operation, the different switching schemes discussed in the previous sections are implemented as shown in the flowchart in fig 4.16. The timing PWMs, represented as P, and the sector information represented as S in fig 4.15a will be different for the three space vector schemes. These are the inputs to the FPGA from the DSP. The FPGA will then generate the corresponding switching vectors for inverter-1 and inverter-2 for each sampling time and the corresponding gate pulses after providing sufficient dead time. The experimental setup is shown in fig 4.15b.

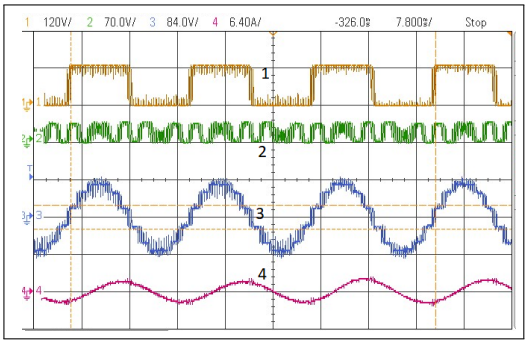

(a) Transient Results: Linear region to Region-1

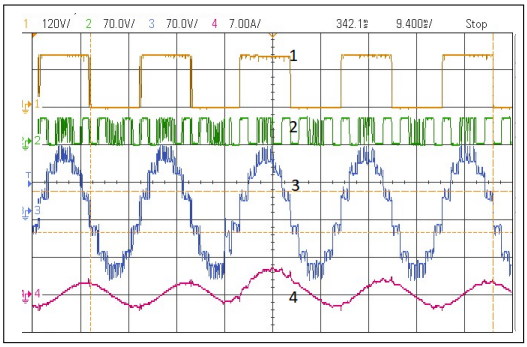

(b) Transient Results: Region-1 to Region-2

Fig. 4.19. 12-sided SVPWM - Transient Results: (1) Pole voltage of inverter-1 (120 V/div), (2) Pole voltage of inverter-2 (70 V/div), (3) Phase voltage of the motor, and (4) Phase current of open-end winding induction motor

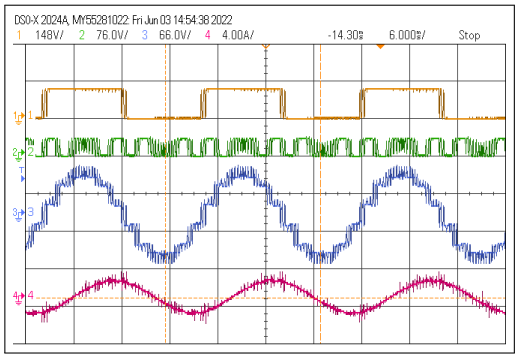

(a) Steady State Results: Region-1

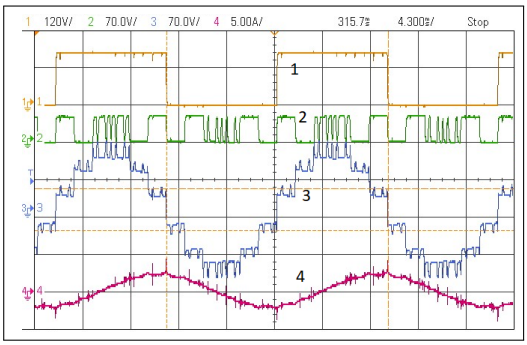

(b) Steady State Results: Region-2

Fig. 4.20. 12-sided SVPWM - Steady State Results: (1) Pole voltage of inverter-1, (2) Pole voltage of inverter-2, (3) Phase voltage of the motor, and (4) Phase current of open-end winding induction motor

Table 4.10. Simulation - Machine parameters

Stator self inductance L_{ss}	0.2596 H
Leakage inductance $\sigma_{12}L_{ss}$	2.8 mH
Mutual inductance between stator and rotor windings L_{sr}	0.2596 H
Stator resistance R_s	1.15 Ω
Rotor resistance R_r	1.97 Ω
Moment of inertia J	0.0165 kgm^2

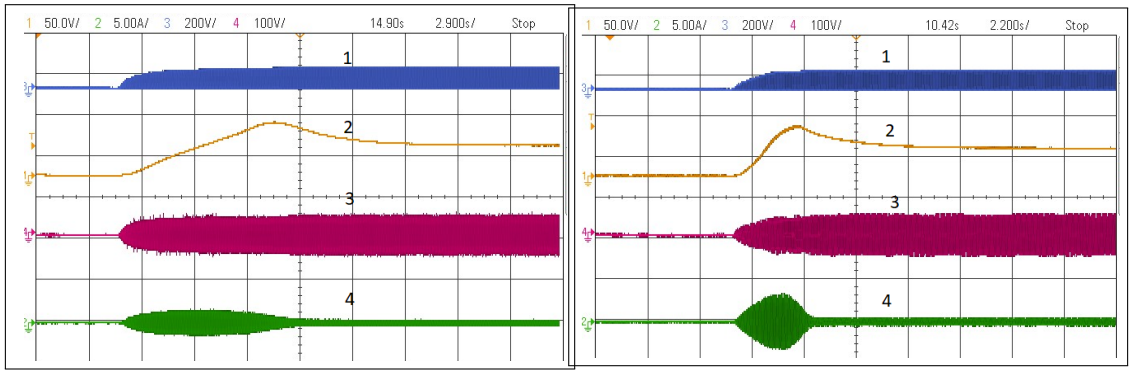

(a) starting to steady state at 50 Hz **(b)** starting to steady state at 25 Hz

Fig. 4.21. 24 side: Starting transient results: (1)Pole voltage of inverter-2 (200 V/div), (2) DC link capacitor voltage of inverter-2 (50 V/div), (3) Motor phase voltage (100 V/div), and (4) Motor phase current (5 A/div).

4.10.1 Dodecagonal voltage space vector modulation scheme

Fig 4.17 provides the steady state results for over-modulation region-I. It shows the waveforms for the pole voltage of inverter-1, inverter-2, multilevel phase voltage across the open-end windings of the machine, and the phase current through the motor winding. It can be seen from the pole voltage waveforms of inverter-1, inverter-2, and the motor phase voltage that the switching frequency has reduced in region -1 operation. Also from the inverter-2 pole voltage, it can be seen that the pole voltage has a different frequency component in some regions (where it follows the hexagonal boundary) and a different frequency component, where it follows pulse width modulation with zero vectors being switched along the vertices of the dodecagon. In fig 4.18 simulation result for the transition from linear region through over-modulation region-I to over-modulation region-2 is shown. The change in frequency components in the pole voltages of inverter -1 and inverter-2 can be seen from this result. It can be noted that there is no change in inverter-2 dc link voltage when there is a transition

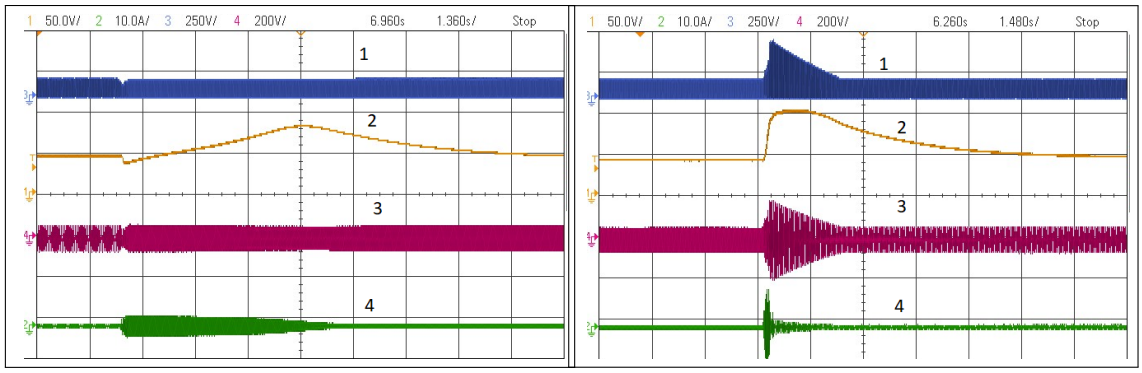

(a) Sudden Change in speed: from 25 Hz to 50 Hz

(b) Sudden Change in speed: from 50 Hz to 25 Hz

Fig. 4.22. 24 side: Sudden change in speed: Transient results: (1)Pole voltage of inverter-2 (250 V/-div), (2) DC link capacitor voltage of inverter-2 (50 V/div), (3) Motor phase voltage (200 V/div), and (4) Motor phase current (10 A/div).

from one region to another.

The hardware results for the dodecagonal space vector scheme are shown below. The steady-state results showing the pole voltages of inverter-1 and inverter-2 and the phase current waveforms for region-1 and region-2 are shown in fig 4.19. Steady-state experimental results for over-modulation region-1 and region-2 are shown in fig 4.20. From these results, it can be seen that the higher frequency component is reducing as the transition happens from linear region to region-1 and to region-2. When the system is operating in region-2, the inverter-1 only has a 50 Hz component in its pole voltage waveform, inverter two pole voltage has a different frequency component when it remains fixed along the vertices of the polygon for a duration equivalent to the holding angle, and then a different frequency pattern when it switches along the polygonal boundary during the remaining time duration.

4.10.2 24-sided voltage space vector modulation scheme

The experimental results showing the transient change at starting to a steady state operation at 50 Hz is shown in fig 4.21a and the transient change at starting to a steady state operation at 25 Hz is shown in fig 4.21b. It can be seen that the DC link capacitor voltage of inverter-2 builds up at the start and settles to the steady state value by following the proposed switching scheme. The transient results for the sudden change in speed are shown in fig 4.22a and fig 4.22b. It can be seen from the figure that the capacitor voltage settles back to the steady state value using the

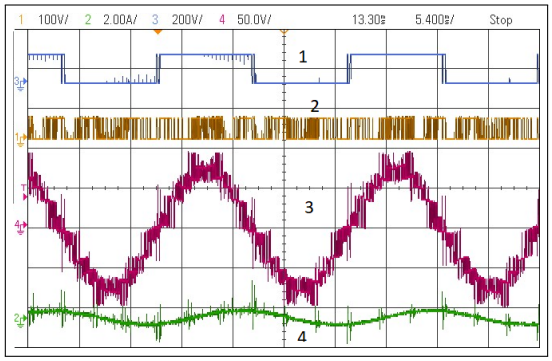

(a) 24 Sides: Transition from linear region to region-1

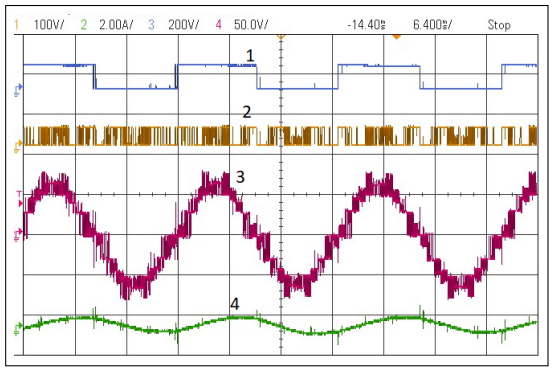

(b) 24 Sides: Transition from region-1 to region-2

Fig. 4.23. 24-sided SVPWM: (1) Pole voltage of inverter-1(200 V/div), (2) Pole voltage of inverter-2 (100 V/div), (3) Phase voltage of the motor (50 V/div), and (4) Phase current of open-end winding induction motor (2 A/div).

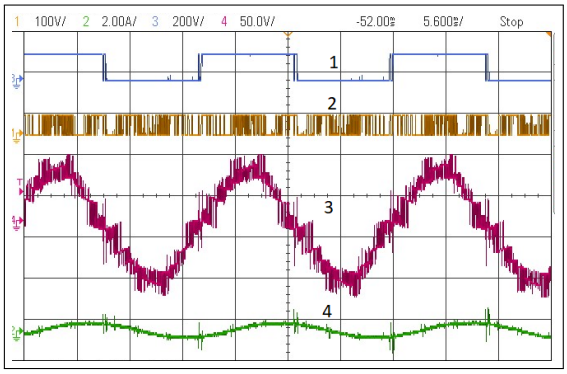

(a) 24 SVPWM: Region-1

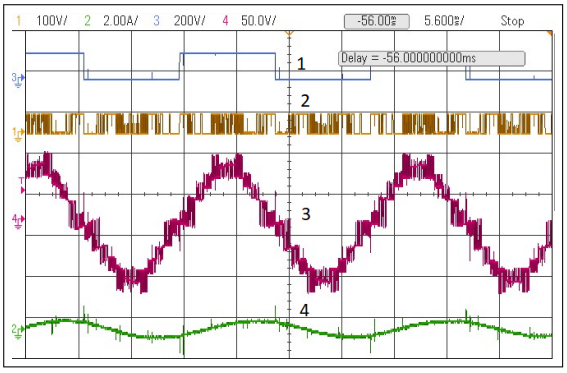

(b) 24 SVPWM: Region-2

Fig. 4.24. 24-sided SVPWM: (1) Pole voltage of inverter-1 (200 V/div), (2) Pole voltage of inverter-2 (100 V/div), (3) Phase voltage of the motor (50 V/div), and (4) Phase current of open-end winding induction motor (2 A/div).

switching scheme. When there is a sudden increase in speed, the capacitor voltage will drop suddenly, but it will come back to its steady state value naturally. Similarly, when there is a sudden reduction in speed, the capacitor voltage suddenly rises, but it will settle back to its steady state value naturally, after a short duration. The transition from linear region to region-1 is shown in fig 4.23a and the transition from region-1 to region-2 is shown in fig 4.23b. The steady-state waveforms for region-1 and region-2 are shown in fig 4.24. The reduction in switching frequency as the mode of operation changes from the linear region to the over-modulation region is visible from the experimental results.

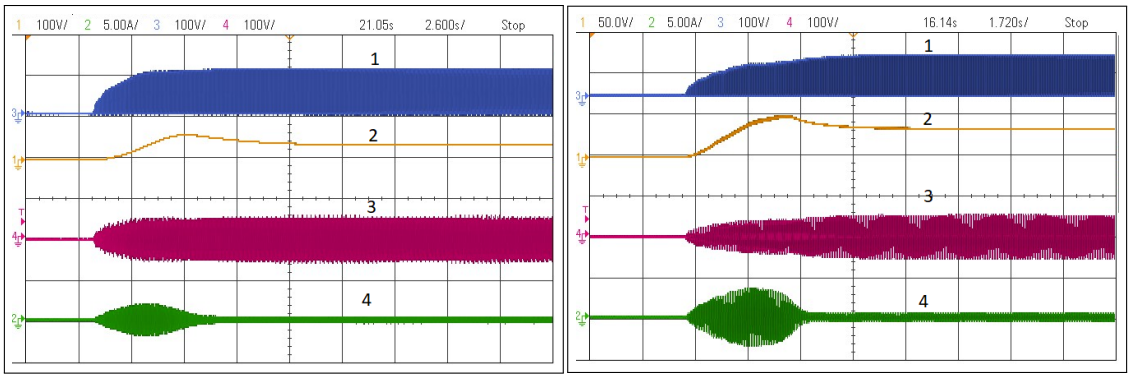

(a) Starting to steady state at 50 Hz **(b)** Starting to steady state at 25 Hz

Fig. 4.25. 18 side: Starting Transient results: (1)Pole voltage of inverter-2, (2) DC link capacitor voltage of inverter-2, (3) Motor phase voltage, and (4)Motor phase current.

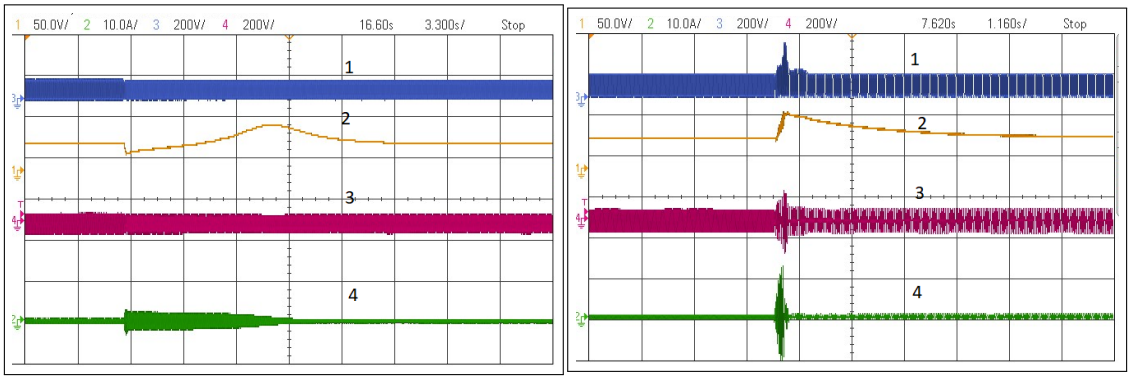

(a) Sudden Change in speed: from 25 Hz to 50 Hz **(b)** Sudden Change in speed: from 50 Hz to 25 Hz

Fig. 4.26. 18 side: Sudden change in speed: Transient results: (1)Pole voltage of inverter-2 (100 V/-div), (2) DC link capacitor voltage of inverter-2, (3) Motor phase voltage (100 V/div), and (4) Motor phase current (5 A/div).

4.10.3 18-sided voltage space vector modulation scheme

The experimental results showing the transient change at starting to a steady state operation at 50 Hz is shown in fig 4.25a and the transient change at starting to a steady state operation at 25 Hz is shown in fig 4.25b. It can be seen from these results that the capacitor voltage naturally builds up from zero to the steady state value without any closed-loop control effort. The transient results for the sudden change in speed are shown in fig 4.26a and fig 4.26b. It can be seen from the figure that the capacitor voltage suddenly changes but settles back to the steady state value using the switching scheme. The steady-state waveforms for linear region and region-2 are shown in fig 4.27. The reduction in switching frequency as it changes from linear

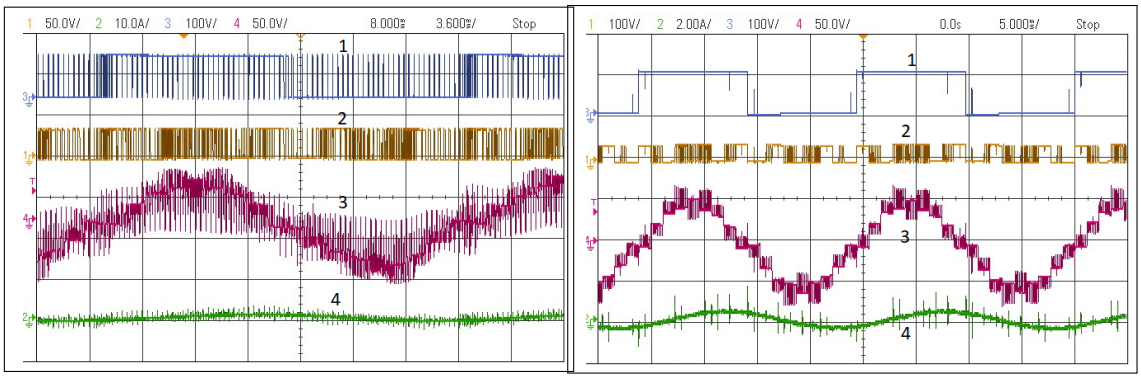

(a) 18 SVPWM: Linear Region **(b)** 18 SVPWM: Region-2

Fig. 4.27. 18-sided SVPWM: (1) Pole voltage of inverter-1 (100 V/div), (2) Pole voltage of inverter-2 (100 V/div), (3) Phase voltage of the motor (50 V/div), and (4) Phase current of open-end winding induction motor.

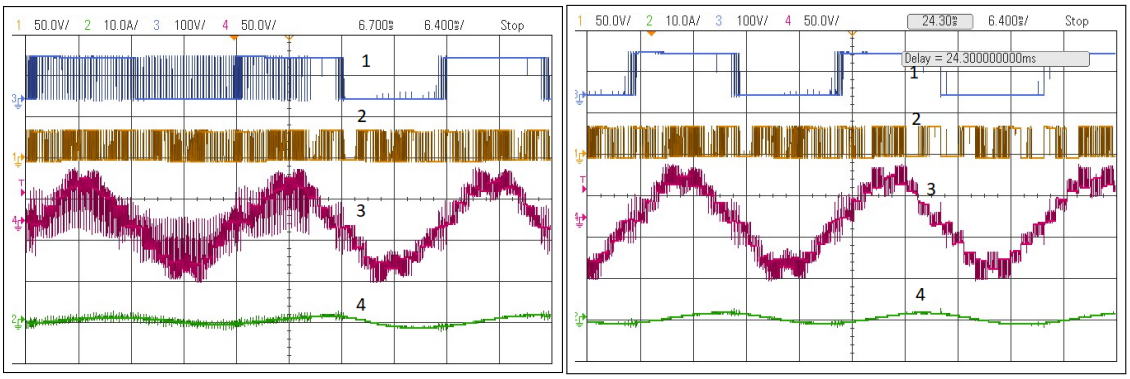

(a) 18 Sides: Transition from linear region to region-1 **(b)** 18 Sides: Transition from region-1 to region-2

Fig. 4.28. 18-sided SVPWM: (1) Pole voltage of inverter-1 ((100 V/div), (2) Pole voltage of inverter-2 (50 V/div), (3) Phase voltage of the motor (50 V/div), and (4) Phase current of open-end winding induction motor (10 A/div).

to over-modulation region is visible from the pole voltage waveforms of inverter-1, inverter-2, and the motor phase voltage waveforms. The transition from linear region to region-1 is shown in fig 4.28a and the transition from region-1 to region-2 is shown in fig 4.28b.

4.11 Conclusion

This chapter discusses in detail an efficient driving scheme that can be utilized for an all-wheel drive EV, which has two power trains in both axles. Usually either one of the power trains is fully engaged while the other drive is turned on when an

external torque is required. Thus in this method the main motor is configured as an open-end winding machine and energized by using the two inverters, one available in the rear wheel axle and the other available in the front wheel axle. Thus three different multi-sided SVM schemes are implemented in this thesis, using two two-level inverters but with a single DC source. The other inverter acts as a switched capacitor which will generate voltages that do not have any fundamental frequency component in it. Hence, during steady-state conditions, the capacitor will not absorb any real power in an average sense, thus maintaining a constant voltage naturally without any closed loop controller.

12-sided, 18-sided, and 24-sided SVM schemes are implemented in this chapter using a single DC source and this theory can be generalized for any multi-sided converter. The mathematical proof for this concept is derived in detail for all three switching schemes. It is proved that the capacitor at a steady state will not absorb any average real power. Also under transient conditions, the capacitor will build up the voltage to its steady state value naturally without any external control effort.

Also, the linear region of operation is larger as the number of sides of the space vector increases, thus better battery utilization can with this scheme. There is a reduction in torque ripple in multi-sided space vector schemes when compared with two levels of inverter-based hexagonal space vector schemes.

Also, a switching scheme is implemented for the linearisation of the over-modulation region for all three multi-sided space vector schemes. Thus for a higher speed of operation, the existing battery can be better utilized. Simulation and experimental results are included to verify the proposed concepts.

Chapter 5

Summary and Critical Overview of Thesis

5.1 Introduction

In recent decades, advancements in battery technology, environmental concerns, and supportive policies have spurred interest in electric vehicles around the world. Two and three-wheeler EVs dominate the EV market in developing countries like India, Thailand, and Indonesia, while Battery Electric Vehicles (BEVs), mainly electric-Sports Utility Vehicles (e-SUVs) which are mainly all-wheel drive vehicles are in the top sales in developed countries like the US and Europe. All-wheel drive EVs include two motor drives, one in their front axle and the other in their rear axle, mainly to have better performance by giving power to all wheels when driving on slippery, icy, or muddy roads. Some of the All-Wheel Drive (AWD) EVs include the Audi e-tron, Mercedes Benz EQB, Porsche Taycan Turbo S, Tesla Model X, Jaguar i Pace, BMW iX and BMW i7.

With improvement in traction technology, the performance of electric cars has reached on par with Internal Combustion Engine (ICE) cars. However, the cost of EVs and the life cycle of batteries are issues that still need to be addressed.

As an EV user, the main concerns are range anxiety, and the time required to charge the battery. Presently, there are two types of chargers for EVs. On-board AC slow chargers and Off-board DC fast chargers. The on-board chargers are limited by their power capability as they need to be placed inside the vehicle having a fixed dimension. The maximum power rating of the available on-board charger is only 22 kW. DC fast chargers have power rating up to 360 kW and they are available only at sparsely placed charging stations.

5.2 Objectives of the Thesis

This thesis deals with the charging and driving schemes for AWD EVs. A new on-board charger is proposed which utilizes the existing driving hardware for charging the battery, hence the name integrated battery charger. There were many IBCs in the literature using multiphase machines and/or multi-leg inverters, but the proposed IBC utilizes the existing three-phase machine and the three-legged inverter. Thus, compared to existing on-board chargers, IBC is not limited by the size or weight requirements inside the vehicle as it re-utilizes the existing hardware with minimal external hardware.

Also, AWD EVs have two sets of powertrains, one on the front wheel axle and the other on the rear wheel axle. So an integrated charger can be developed by utilizing the two motors and inverters and connecting them as a parallel combination of IBCs using the split-phase machine. The power capability of the charger is doubled compared to a single IBC using the split-phase machine.

Finally, a driving scheme is introduced in AWD EVs for better utilization of the existing DC source. In AWD EVs only one powertrain is constantly engaged, while the other is energized only when there is a need for an extra torque for the wheels. A new driving scheme is proposed wherein the neutral of the constantly engaged motor is disconnected and it is made to run as an open-end winding motor using the two inverters (of both axles) under normal driving conditions. When there is a need for extra torque, both motors are energized as three-phase machines with the corresponding three-leg inverters. The advantage of using the OEW space vector scheme for the constantly engaged motor is that there is a reduction in the phase voltage harmonics across the machine windings with multi-sided SVM schemes and thus a reduction in torque ripple for the motor. Using the two, two-level inverters, 12-sided, 18-sided, and 24-sided modulation schemes are discussed in this thesis.

5.3 IBC using split phase machine

A new and fast integrated battery charging scheme is developed for EVs with the existing three-phase machine and three-legged powertrain inverter. While charging the battery, the inverter acts as a front-end converter and the machine windings act as the grid interface inductance. However, the machine should not rotate while drawing grid currents.

The torque developed inside the machine while charging should be zero. Hence the windings are given supply in such a way that only pulsating flux is produced inside the machine and the instantaneous torque is zero

This charger can be used to charge the EV from any place where AC power is available and is based on the power capability of the Electric Vehicle Supply Equipment (EVSE). Furthermore, the power rating of the IBC can be up to twice the power rating of the motor inside the vehicle. As the proposed IBC scheme is bidirectional, the system can also be used for vehicle-to-grid applications.

However, due to the asymmetrical structure of the split-phase machine, the parallel combination of inductance (phase windings of the motor) for each phase is not equal to the other phases. Also, the pulsating flux that links each winding is different. Hence, even if the grid voltages are balanced, the current drawn from the grid is not balanced. It will be distorted in shape due to harmonics. To limit the unbalance of the grid currents, the model of the system is derived in a-b-c, stationary $\alpha - \beta$, and synchronously rotating d-q reference frames.

From the mathematical model, it has been derived that there exists a mutual inductance term, L_{dq} between the d and q axis of the synchronously rotating reference frame. Also, all the inductance terms are varying with grid angle θ. Thus it was seen that the d-q components of the grid currents will have high even harmonic components along with DC terms, unlike a balanced system which will only have DC terms.

To limit the unbalance new current control methods were included like using feed-forward terms (which are mathematically derived) which will take care of the even harmonic terms in the d-q components of the grid voltage. This control method can be extended to any generalized front-end converters with unbalanced inductances. In this thesis, the IBC is implemented for induction machine drives based on EVs. Further research can be done for implementing this topology using permanent magnet synchronous machines as it has become a popular motor in EVs.

5.4 Parallel combination of IBC using split phase machine for AWD EVs

A high-power integrated charging scheme is proposed for All-Wheel Drive EVs, using the two motor drives inside the vehicle. This charging scheme can also be implemented for heavy-duty electric trucks, which are always on the run, and this scheme helps

users to charge the battery from any location where the AC supply is available.

The main objective of this scheme is to find a proper winding configuration of the two motors such that the unbalance in the grid currents can be limited without using any external control effort. The split-phase windings can be connected to the grid in six different ways. Similarly, the grid windings of the other split-phase machine in AWD can be connected in six different ways to the grid. Thus all together there can be 36 different combinations in which the two IBCs can be connected in parallel. Among these, it is found that three combinations can reduce the unbalance in grid currents to a large extent. A mathematical proof is also derived to prove the cancellation of unbalance in the grid currents. Among the three possible configurations, the $R-Y-B$ $/Y-R-B$ configuration is implemented in this thesis.

Also, there is a path for the circulating current to flow when two converters are connected in parallel because of the difference in the pole voltage between the same phase of two converters, either due to the interleaving of carriers (which causes the flow of a high frequency circulating current) or due to the difference in interface inductance between the same phase of IBC-1 and IBC-2. In the proposed system, there is no high-frequency circulating current as the carriers are not interleaved but there is a low-frequency circulating current due to the presence of unbalanced grid interface inductances. The factors contributing to the flow of circulating current need to be figured out.

A common mode model of the system was developed and it was found that the common mode current of IBC-1 depends on the difference in common mode voltage of IBC-1 and IBC-2 and on the leakage inductance of the machine. It is not influenced by the mutual inductance and its varying effects. This current is minimized by using a PI controller as the zero sequence current controller.

Furthermore, this scheme can be used for vehicle-to-grid applications because of its bidirectional nature. In cases where front-axle and rear-axle powers are different, unbalance in current is mitigated as opposed to complete elimination.

In future work, the parallel combination of IBCs can be implemented by using two different machines with different power ratings. Most of the AWD EVs that exists in the present market uses two different types of motors with unequal power rating for the front and rear wheel axle. Hence the parallel combination of these systems for charging the battery can be considered as a future work.

5.5 An OEW IM with space vector modulation scheme for better performance of AWD EVs

An efficient driving mechanism that can be implemented in EVs, especially in the AWDs is developed. In AWDs, there are two motor drive systems in which only one system is engaged all the time. The other system is powered only in limited conditions. Here, a driving scheme is proposed, wherein the main motor(which is always engaged) is driven by using the two inverters(present in both the rear axle and front axle) as an open-end winding motor using multi-sided voltage space vector schemes and thus increase the efficiency of the system. Here, using the existing two, two-level inverters, 12-sided, 18-sided, and 24-sided OEW space vector voltage schemes using a single DC source are discussed in detail.

The topology utilizes two, two-level inverters, Inverter 1 and Inverter 2. Inverter 1 is provided with a DC source of magnitude V_{dc} and Inverter 2 is connected with a capacitor. The capacitor voltage is maintained constant without any voltage controller irrespective of different load conditions, using the proper modulation method.

For the capacitor voltage to be maintained automatically, the voltage vectors switched by inverter 2 at every instant should be such that the average active power absorbed by the capacitor is zero, irrespective of the load conditions.

The mathematical proof for the same is derived in detail using instantaneous p-q theory. The following conditions are derived from the mathematical proof.

Firstly, the average real power absorbed or delivered by inverter 2 is zero. Hence the average real power given by inverter 1 should be absorbed by the motor under steady state conditions. For this, the maximum fundamental voltage of the multi-sided voltage space vector (12-side, 18-side, or 24-side) should be equal to the maximum fundamental voltage of the hexagonal voltage space vector. Thus the magnitude of each of the multi-sided voltage space vectors is decided on this criteria.

Secondly, the inverter 2 should generate a vector in an average sense such that it will be perpendicular to the resultant multi-sided vector. Then inverter 2 will not absorb any average real power.

Also, a switching scheme is implemented to get a linear relationship between the fundamental voltage across the motor and the DC link voltage for the region above the linear region of operation in the space vector modulation scheme. The advantage of multi-sided SVM schemes compared to hexagonal SVM schemes will be visible only

when working in a square wave mode of operation. Normally the SVM schemes work till the linear mode of operation as there is no linear relationship between the required fundamental voltage and DC source voltage in the over-modulation region. In this work, this over-modulation region is linearized by using a different switching scheme compared to the linear region.

Exhaustive experimental results are included to verify the above concepts.

5.6 Conclusion

This work aims to solve a few significant problems that impede EV adoption. An Integrated Battery Charger to enable high-power (level-3) charging of the battery inside the electric vehicle wherever AC power is available is attempted. This charging method will also effectively reduce the capital cost of EV charging facilities as powertrain equipment is reused as the AC-DC converter. The existing three-phase machine is reconfigured as a split phase machine and proper winding arrangement is done to develop zero instantaneous torque inside the machine while charging the battery. The three-legged inverter works as a front-end converter and draws current at unity power factor. New control schemes are implemented to reduce the unbalanced issues in the grid currents using the derived mathematical model.

The proposed scheme is adaptable to be used for AWD vehicles. As e-SUVs typically have larger batteries, the high power capabilities of e-SUV powertrains as parallel IBCs should be exploited for the benefit of fast charging. A new winding configuration for split phase machines is proposed which will naturally mitigate the unbalance in grid currents without any extra control effort. The issue of circulating current in parallel configuration of converters is also taken care of.

Furthermore, a new driving scheme is proposed for AWD EVs using the existing powertrains. The motor is driven as an open-end winding machine with the two inverters already present in the vehicle and a 12, 18, and 24-sided voltage space vector modulation technique is implemented which can increase the linear region of modulation and hence the battery utilization. A stability analysis for the switched capacitor of the second inverter is done and the capacitor voltage is maintained without the use of any voltage controllers. Also, a linearization switching scheme is implemented for 12, 18, and 24-sided voltage polygons, so that a linear relationship is maintained between the output voltage and input battery voltage from the linear region up to the extreme square wave modulation.

As a future work, a similar IBC scheme can be implemented using permanent magnet synchronous machine as they are being popularly used in EVs. Compared to IBC using induction machine, there may be a chance of vibration in PMSM machines, which need to be taken care of. Also other control options for IBC can be considered like digital control using state space analysis as the model is already derived, or current error space vector control schemes. Similarly this work can be extended including the battery, DC-DC converter and the battery management system, with its total control. Also the parallel combination of IBCs using different machines can be considered as a future work, as some AWDs consists of two different types of motors in its front and rear-wheel axis.

In summary, this thesis proposes methods to use existing power electronic hardware in an EV for charging batteries and driving motors more efficiently. As the cost of adopting these schemes is relatively minimal, the proposed schemes are a viable alternative to traditional charging and driving methods. The proposed methods are validated through mathematical models, simulations, and exhaustive experimental results.

Bibliography

[1] "https://www.marketsandmarkets.com/market-reports/electric-vehicle-market."

[2] "https://www.iea.org/reports/global-ev-outlook-2023."

[3] "https://www.tesla.com/semi."

[4] "https://www.volvotrucks.us/trucks/vnr-electric."

[5] "https://www.fortunebusinessinsights.com/india-electric-vehicle-market-106623."

[6] "https://www.volkswagen.co.uk/files/live/sites/vwuk/files/pdf/brochures/id4-brochure-pricelist-p11d.pdf."

[7] "https://www.audi-mediacenter.com/en/electric-suvs-in-the-premium-compact-segment-the-audi-q4-e-tron-and-the-q4-sportback-e-tron-13887/electric-motors-and-electric-all-wheel-drive-13900."

[8] "https://www.audiusa.com/us/web/en/models/e-tron/e-tron-s-sportback/2023."

[9] "https://autoexpo.tatamotors.com/products/electric-vehicles/harrier-ev-features.aspx."

[10] "https://www.audi.in/dam/nemo/in/downloads/e-tron/e-trondigitalbrochure.pdf."

[11] "https://www.audi.in/dam/nemo/in/downloads/e-tron/audietrongtdigitalbrochure.pdf."

[12] "https://www.bmw.in/en/all-models/bmw-i/bmw-ix-new/2021/bmw-ix.html."

[13] "https://www.bmw.in/en/all-models/bmw-i/i7/2022/bmw-i7-sedan-highlights.html."

[14] "https://www.mercedes-benz.co.in/passengercars/mercedes-benz-cars/models/eqb/suv-x243/explore/eqb-story.module.html."

[15] "https://www.mercedes-benz.co.in/passengercars/mercedes-benz-cars/models/eqs/saloon-v297/explore.html."

[16] "https://www.kia.com/in/our-vehicles/ev6/showroom.html."

[17] "https://www.porsche.com/international/models/taycan/taycan-models/taycan-turbo-s."

[18] "https://www.volvocars.com/us/cars/xc40-electric/specification/."

[19] "https://evcompare.io/assets/pdf/manuals/model

[20] "https://www.tesla.com/sites/default/files/tesla-model-s.pdf."

[21] "https://evcompare.io/assets/pdf/carspecs/tesla-model-s-85d-specs.pdf."

[22] "https://www.tesla.com/ownersmanual/modelx."

[23] "https://www.jaguar.com/jaguar-range/i-pace/specifications."

[24] *Surface Vehicle Recommended Practice J1772, SAE Electric Vehicle and Plug in Hybrid Electric Vehicle Conductive Charge Coupler*, SAE International, Jan. 2010.

[25] M. Yilmaz and P. T. Krein, "Review of battery charger topologies, charging power levels, and infrastructure for plug-in electric and hybrid vehicles," *IEEE Transactions on Power Electronics*, vol. 28, no. 5, pp. 2151–2169, 2013.

[26] S. S. Williamson, A. K. Rathore, and F. Musavi, "Industrial electronics for electric transportation: Current state-of-the-art and future challenges," *IEEE Transactions on Industrial Electronics*, vol. 62, no. 5, pp. 3021–3032, 2015.

[27] H. Tu, H. Feng, S. Srdic, and S. Lukic, "Extreme fast charging of electric vehicles: A technology overview," *IEEE Transactions on Transportation Electrification*, vol. 5, no. 4, pp. 861–878, 2019.

[28] S. International, "Vehicle architecture for data communications standards?class b data communications network interface;," *Standard, SAE International*, Warrendale, PA, USA, 2009.

[29] I. E. Commission, "Plugs, socket-outlets, vehicle couplers and vehicle inlets?conductive charging of electric vehicles?part 1: General requirements;," *Standard; IEC: Geneva, Switzerland*, 2014.

[30] V. G. P. M. F. J. M.-B. J. M. Sanguesa, Julio A.; Torres-Sanz, "A review on electric vehicles: Technologies and challenges." *Smart Cities*, vol. 4, p. 372?404, 2021.

[31] "https://www.chademo.com/wp/pdf/aboutus/brolong.pdf."

[32] "https://heavyindustries.gov.in/writereaddata/uploadfile/standardization

[33] "https://evreporter.com/guide-to-ev-charging-and-standards-in-india/."

[34] "https://e-amrit.niti.gov.in/standards-and-specifications."

[35] "https://www.gogoro.com/in/gogoro-network/."

[36] "https://evreporter.com/battery-swapping-solution-providers-in-india."

[37] "https://www.honda-mpp.com/in/."

[38] H. Rahimi Eichi, U. Ojha, F. Baronti, and M.-Y. Chow, "Battery management system: An overview of its application in the smart grid and electric vehicles," *Industrial Electronics Magazine, IEEE*, vol. 7, pp. 4–16, 06 2013.

[39] N. Chaturvedi, R. Klein, J. Christensen, J. Ahmed, and A. Kojic, "Algorithms for advanced battery-management systems," *Control Systems, IEEE*, vol. 30, pp. 49 – 68, 07 2010.

[40] J. Cao, N. Schofield, and A. Emadi, "Battery balancing methods: A comprehensive review," vol. 06, 10 2008, pp. 1 – 6.

[41] B. Xu, A. Oudalov, A. Ulbig, G. Andersson, and D. Kirschen, "Modeling of lithium-ion battery degradation for cell life assessment," *IEEE Transactions on Smart Grid*, vol. 99, pp. 1–1, 06 2016.

[42] L. Romare, M.; Dahllï¿½f, "The life cycle energy consumption and greenhouse gas emissions from lithium-ion batteries: A study with focus on current technology and batteries for light-duty vehicles," in *Technical Report; IVL Swedish Environmental Research Institute: Stockholm, Sweden*, 2017.

[43] T. Hsu, "On the sustainability of electrical vehicles," in *In Proceedings of the IEEE Green Energy and Systems Conference (IGESC),Long Beach, CA, USA*, 25 November 2013, p. 1?7.

[44] K. Gopakumar, V. Ranganthan, and S. Bhat, "Split-phase induction motor operation from pwm voltage source inverter," *IEEE Transactions on Industry Applications*, vol. 29, no. 5, pp. 927–932, 1993.

[45] E. Andresen and K. Bieniek, "6 - phase induction motors for current - source inverter drives," in *1981 Annual Meeting Industry Applications Society*, 1981, pp. 607–618.

[46] T. A. Lipo and L. H. Walker, "Design and control techniques for extending high frequency operation of a csi induction motor drive," *IEEE Transactions on Industry Applications*, vol. IA-19, no. 5, pp. 744–753, 1983.

[47] Y. Zhao and T. Lipo, "Space vector pwm control of dual three-phase induction machine using vector space decomposition," *IEEE Transactions on Industry Applications*, vol. 31, no. 5, pp. 1100–1109, 1995.

[48] G. Pfaff, A. Weschta, and A. F. Wick, "Design and experimental results of a brushless ac servo drive," *IEEE Transactions on Industry Applications*, vol. IA-20, no. 4, pp. 814–821, 1984.

[49] H. van der Broeck, H.-C. Skudelny, and G. Stanke, "Analysis and realization of a pulsewidth modulator based on voltage space vectors," *IEEE Transactions on Industry Applications*, vol. 24, no. 1, pp. 142–150, 1988.

[50] H. Stemmler and P. Guggenbach, "Configurations of high-power voltage source inverter drives," in *1993 Fifth European Conference on Power Electronics and Applications*, 1993, pp. 7–14 vol.5.

[51] V. T. Somasekhar, E. G. Shivakumar, K. Gopakumar, and A. Pittet, "Multi level voltage space phasor generation for an open-end winding induction motor

drive using a dual inverter scheme with asymmetrical dc-link voltages," in *EPE Journal*, vol. 12, no. 3, August 2002, pp. 7–15.

[52] M. Baiju, K. Mohapatra, V. Somasekhar, K. Gopakumar, and L. Umanand, "A five-level inverter voltage space phasor generation for an open-end winding induction motor drive," in *Eighteenth Annual IEEE Applied Power Electronics Conference and Exposition, 2003. APEC '03.*, vol. 2, 2003, pp. 826–832 vol.2.

[53] A. Kshirsagar, R. S. Kaarthik, K. Gopakumar, L. Umanand, and K. Rajashekara, "Low switch count nine-level inverter topology for open-end induction motor drives," *IEEE Transactions on Industrial Electronics*, vol. 64, no. 2, pp. 1009–1017, 2017.

[54] K. Raj R, K. Gopakumar, M. Boby, A. K. Yadav, L. G. Franquelo, and S. S. Williamson, "Multilevel 24-sided polygonal voltage-space-vector structure generation for an im drive using a single dc source," *IEEE Transactions on Industrial Electronics*, vol. 66, no. 2, pp. 1023–1031, 2019.

[55] E. Shivakumar, K. Gopakumar, S. Sinha, A. Pittet, and V. Ranganathan, "Space vector pwm control of dual inverter fed open-end winding induction motor drive," in *APEC 2001. Sixteenth Annual IEEE Applied Power Electronics Conference and Exposition (Cat. No.01CH37181)*, vol. 1, 2001, pp. 399–405 vol.1.

[56] V. Somasekhar, K. Gopakumar, and E. Shivakumar, "A space-vector modulation scheme for a dual two-level inverter fed open-end winding induction motor drive for the elimination of zero-sequence currents," in *EPE Journal*, vol. 12, no. 2, May 2002, pp. 26–36.

[57] M. Baiju, K. Mohapatra, R. Kanchan, and K. Gopakumar, "A dual two-level inverter scheme with common mode voltage elimination for an induction motor drive," *IEEE Transactions on Power Electronics*, vol. 19, no. 3, pp. 794–805, 2004.

[58] K. Mohapatra, K. Gopakumar, V. Somasekhar, and L. Umanand, "A harmonic elimination and suppression scheme for an open-end winding induction motor drive," *IEEE Transactions on Industrial Electronics*, vol. 50, no. 6, pp. 1187–1198, 2003.

[59] S. Pramanick, N. A. Azeez, R. Sudharshan Kaarthik, K. Gopakumar, and C. Cecati, "Low-order harmonic suppression for open-end winding im with dodecagonal space vector using a single dc-link supply," *IEEE Transactions on Industrial Electronics*, vol. 62, no. 9, pp. 5340–5347, 2015.

[60] J. Holtz, "Pulsewidth modulation-a survey," *IEEE Transactions on Industrial Electronics*, vol. 39, no. 5, pp. 410–420, 1992.

[61] R. Kerkman, B. Seibel, D. Brod, T. Rowan, and D. Leggate, "A simplified inverter model for on-line control and simulation," *IEEE Transactions on Industry Applications*, vol. 27, no. 3, pp. 567–573, 1991.

[62] R. Kerkman, T. Rowan, D. Leggate, and B. Seibel, "Control of pwm voltage inverters in the pulse dropping region," *IEEE Industry Applications Magazine*, vol. 2, no. 5, pp. 24–31, 1996.

[63] A. Hava, R. Kerkman, and T. Lipo, "Carrier-based pwm-vsi overmodulation strategies: analysis, comparison, and design," *IEEE Transactions on Power Electronics*, vol. 13, no. 4, pp. 674–689, 1998.

[64] J. A. Houldsworth and D. A. Grant, "The use of harmonic distortion to increase the output voltage of a three-phase pwm inverter," *IEEE Transactions on Industry Applications*, vol. IA-20, no. 5, pp. 1224–1228, 1984.

[65] I. G. Buja. G, "Improvement of pulse width modulation techniques," *Archiv f. Elektrotechnik*, vol. 57, p. 281?289, 1975.

[66] J. Rodriguez, E. Wiechmann, J. Holtz, A. Suarez, and M. Sepulveda, "Igbt inverter with vector modulation," in *Proceedings of 1994 IEEE International Symposium on Industrial Electronics (ISIE'94)*, 1994, pp. 131–136.

[67] H. van der Broeck, H.-C. Skudelny, and G. Stanke, "Analysis and realization of a pulsewidth modulator based on voltage space vectors," *IEEE Transactions on Industry Applications*, vol. 24, no. 1, pp. 142–150, 1988.

[68] J. Holtz, W. Lotzkat, and A. Khambadkone, "On continuous control of pwm inverters in the overmodulation range including the six-step mode," *IEEE Transactions on Power Electronics*, vol. 8, no. 4, pp. 546–553, 1993.

[69] A. Bakhshai, G. Joos, P. Jain, and H. Jin, "Incorporating the overmodulation range in space vector pattern generators using a classification algorithm," *IEEE Transactions on Power Electronics*, vol. 15, no. 1, pp. 83–91, 2000.

[70] S. Bolognani and M. Zigliotto, "Novel digital continuous control of svm inverters in the overmodulation range," *IEEE Transactions on Industry Applications*, vol. 33, no. 2, pp. 525–530, 1997.

[71] D.-C. Lee and G.-M. Lee, "A novel overmodulation technique for space-vector pwm inverters," *IEEE Transactions on Power Electronics*, vol. 13, no. 6, pp. 1144–1151, 1998.

[72] F. Blaabjerg and J. Pedersen, "An integrated high power factor three-phase ac-dc-ac converter for ac-machines implemented in one microcontroller," in *Proceedings of IEEE Power Electronics Specialist Conference - PESC '93*, 1993, pp. 285–292.

[73] J. Prasad, T. Bhavsar, R. Ghosh, and G. Narayanan, "Vector control of three-phase ac/dc front- end converter," 12 2007.

[74] J. Svensson and M. Lindgren, "Vector current controlled grid connected voltage source converter-influence of nonlinearities on the performance," in *PESC 98 Record. 29th Annual IEEE Power Electronics Specialists Conference (Cat. No.98CH36196)*, vol. 1, 1998, pp. 531–537 vol.1.

[75] S. Hiti and D. Boroyevich, "Control of front-end three-phase boost rectifier," in *Proceedings of 1994 IEEE Applied Power Electronics Conference and Exposition - ASPEC'94*, 1994, pp. 927–933 vol.2.

[76] V. Vidya and R. S. Kaarthik, "A control scheme for integrated battery charger with split-phase machine," in *2020 IEEE International Conference on Power Electronics, Smart Grid and Renewable Energy (PESGRE2020)*, 2020, pp. 1–6.

[77] V. Vidya and S. Kaarthik, "Mathematical modeling of split phase machine based integrated battery charger," in *2019 International Transportation Electrification Conference INDIA (ITEC INDIA)*, Dec 2019, pp. 1–5.

[78] S. Ranjith, V. Vidya, and R. S. Kaarthik, "An integrated ev battery charger with retrofit capability," *IEEE Transactions on Transportation Electrification*, vol. 6, no. 3, pp. 985–994, 2020.

[79] V. V and R. S. Kaarthik, "Modeling and control of an integrated battery charger with split-phase machine," *IEEE Transactions on Industry Applications*, vol. 57, no. 2, pp. 1588–1597, 2021.

[80] S. Haghbin, S. Lundmark, M. Alakula, and O. Carlson, "Grid-connected integrated battery chargers in vehicle applications: Review and new solution," *IEEE Transactions on Industrial Electronics*, vol. 60, no. 2, pp. 459–473, 2013.

[81] M. Valente, T. Wijekoon, F. Freijedo, P. Pescetto, G. Pellegrino, and R. Bojoi, "Integrated on-board ev battery chargers: New perspectives and challenges for safety improvement," in *2021 IEEE Workshop on Electrical Machines Design, Control and Diagnosis (WEMDCD)*, 2021, pp. 349–356.

[82] M. Y. Metwly, M. S. Abdel-Majeed, A. S. Abdel-Khalik, R. A. Hamdy, M. S. Hamad, and S. Ahmed, "A review of integrated on-board ev battery chargers: Advanced topologies, recent developments and optimal selection of fscw slot/pole combination," *IEEE Access*, vol. 8, pp. 85 216–85 242, 2020.

[83] I. Subotic and E. Levi, "A review of single-phase on-board integrated battery charging topologies for electric vehicles," in *2015 IEEE Workshop on Electrical Machines Design, Control and Diagnosis (WEMDCD)*, 2015, pp. 136–145.

[84] N. Sakr, D. Sadarnac, and A. Gascher, "A review of on-board integrated chargers for electric vehicles," in *2014 16th European Conference on Power Electronics and Applications*, 2014, pp. 1–10.

[85] B. B. L. De-Sousa, "Combined electric device for powering and charging," *Int. Patent WO 2010/057892 A1*, May 27, 2010.

[86] S.-K. Sul and S.-J. Lee, "An integral battery charger for four-wheel drive electric vehicle," *IEEE Transactions on Industry Applications*, vol. 31, no. 5, pp. 1096–1099, 1995.

[87] Y.-J. Lee, A. Khaligh, and A. Emadi, "Advanced integrated bidirectional ac/dc and dc/dc converter for plug-in hybrid electric vehicles," *IEEE Transactions on Vehicular Technology*, vol. 58, no. 8, pp. 3970–3980, 2009.

[88] D. Thimmesch, "An scr inverter with an integral battery charger for electric vehicles," *IEEE Transactions on Industry Applications*, vol. IA-21, no. 4, pp. 1023–1029, 1985.

[89] W. E. Rippel, "Integrated traction inverter and battery charger apparatus," *U.S. Patent 4 920 475*, Apr. 1990.

[90] W. E. R. A. G. Cocconi, "Integrated motor drive and recharge system," *U.S. Patent 5099186*, Mar. 1992.

[91] A. G. Cocconi, "Combined motor drive and battery recharge system," *U.S. Patent 5 341 075*, Aug. 23, 1994.

[92] C.-S. Lee, J.-B. Jeong, B.-H. Lee, and J. Hur, "Study on 1.5 kw battery chargers for neighborhood electric vehicles," in *2011 IEEE Vehicle Power and Propulsion Conference*, 2011, pp. 1–4.

[93] Y. Jang and M. M. Jovanovic, "Interleaved boost converter with intrinsic voltage-doubler characteristic for universal-line pfc front end," *IEEE Transactions on Power Electronics*, vol. 22, no. 4, pp. 1394–1401, 2007.

[94] P. Kong, S. Wang, F. C. Lee, and C. Wang, "Common-mode emi study and reduction technique for the interleaved multichannel pfc converter," *IEEE Transactions on Power Electronics*, vol. 23, no. 5, pp. 2576–2584, 2008.

[95] M. Kompella, P. Yadav, and R. S. Kaarthik, "A single phase integrated battery charger with active power decoupling for electric vehicles," in *2020 IEEE International Conference on Power Electronics, Drives and Energy Systems (PEDES)*, 2020, pp. 1–6.

[96] H. R. Vangala and R. Kaarthik, "Control of a single phase integrated battery charger with active power decoupling for electric vehicles," in *2021 IEEE Transportation Electrification Conference (ITEC-India)*, 2021, pp. 1–6.

[97] M. Kumar, C. S. Abhishek, and R. S. Kaarthik, "Current hysteresis control of a single phase integrated battery charger with active power decoupling," in *2022 IEEE International Conference on Power Electronics, Smart Grid, and Renewable Energy (PESGRE)*, 2022, pp. 1–7.

[98] V. V, M. Kumar, and R. S. Kaarthik, "Modeling of single phase ibc with active power decoupling," in *2022 IEEE 19th India Council International Conference (INDICON)*, 2022, pp. 1–5.

[99] F. Lacressonniere and B. Cassoret, "Converter used as a battery charger and a motor speed controller in an industrial truck," in *2005 European Conference on Power Electronics and Applications*, 2005, pp. 7 pp.–P.7.

[100] S. Haghbin, S. Lundmark, M. Alakula, and O. Carlson, "An isolated high-power integrated charger in electrified-vehicle applications," *IEEE Transactions on Vehicular Technology*, vol. 60, no. 9, pp. 4115–4126, 2011.

[101] D.-G. Woo, D.-M. Joo, and B.-K. Lee, "On the feasibility of integrated battery charger utilizing traction motor and inverter in plug-in hybrid electric vehicles," *IEEE Transactions on Power Electronics*, vol. 30, no. 12, pp. 7270–7281, 2015.

[102] S. Q. Ali, D. Mascarella, G. Joos, and L. Tan, "Torque cancelation of integrated battery charger based on six-phase permanent magnet synchronous motor drives for electric vehicles," *IEEE Transactions on Transportation Electrification*, vol. 4, no. 2, pp. 344–354, 2018.

[103] C. Shi, Y. Tang, and A. Khaligh, "A three-phase integrated onboard charger for plug-in electric vehicles," *IEEE Transactions on Power Electronics*, vol. 33, no. 6, pp. 4716–4725, 2018.

[104] Y. Xiao, C. Liu, and F. Yu, "An effective charging-torque elimination method for six-phase integrated on-board ev chargers," *IEEE Transactions on Power Electronics*, vol. 35, no. 3, pp. 2776–2786, 2020.

[105] Y. Xiao, L. Chunhua, and F. Yu, "An integrated on-board ev charger with safe charging operation for three-phase ipm motor," *IEEE Transactions on Industrial Electronics*, vol. PP, pp. 1–1, 11 2018.

[106] Y. Hu, X. Song, W. Cao, and B. Ji, "New sr drive with integrated charging capacity for plug-in hybrid electric vehicles (phevs)," *IEEE Transactions on Industrial Electronics*, vol. 61, no. 10, pp. 5722–5731, 2014.

[107] H.-C. Chang and C.-M. Liaw, "An integrated driving/charging switched reluctance motor drive using three-phase power module," *IEEE Transactions on Industrial Electronics*, vol. 58, no. 5, pp. 1763–1775, 2011.

[108] S. Lacroix, E. Laboure, and M. Hilairet, "An integrated fast battery charger for electric vehicle," in *2010 IEEE Vehicle Power and Propulsion Conference*, Sept 2010, pp. 1–6.

[109] I. Subotic, N. Bodo, and E. Levi, "An ev drive-train with integrated fast charging capability," *IEEE Transactions on Power Electronics*, vol. 31, no. 2, pp. 1461–1471, Feb 2016.

[110] L. D. Sousa, B. Silvestre, and B. Bouchez, "A combined multiphase electric drive and fast battery charger for electric vehicles," in *2010 IEEE Vehicle Power and Propulsion Conference*, Sept 2010, pp. 1–6.

[111] I. Subotic, N. Bodo, E. Levi, and M. Jones, "Onboard integrated battery charger for evs using an asymmetrical nine-phase machine," *IEEE Transactions on Industrial Electronics*, vol. 62, no. 5, pp. 3285–3295, May 2015.

[112] I. Subotic and E. Levi, "An integrated battery charger for evs based on a symmetrical six-phase machine," in *2014 IEEE 23rd International Symposium on Industrial Electronics (ISIE)*, June 2014, pp. 2074–2079.

[113] S. Q. Ali, D. Mascarella, G. Joos, and L. Tan, "Torque cancelation of integrated battery charger based on six-phase permanent magnet synchronous motor drives for electric vehicles," *IEEE Transactions on Transportation Electrification*, vol. 4, no. 2, pp. 344–354, June 2018.

[114] A. S. Abdel-Khalik, A. Massoud, and S. Ahmed, "Interior permanent magnet motor-based isolated on-board integrated battery charger for electric vehicles," *IET Electric Power Applications*, vol. 12, no. 1, pp. 124–134, 2018.

[115] C. Shi, Y. Tang, and A. Khaligh, "A three-phase integrated onboard charger for plug-in electric vehicles," *IEEE Transactions on Power Electronics*, vol. 33, no. 6, pp. 4716–4725, June 2018.

[116] Y. Xiao, C. Liu, and F. Yu, "An integrated on-board ev charger with safe charging operation for three-phase ipm motor," *IEEE Transactions on Industrial Electronics*, vol. 66, no. 10, pp. 7551–7560, Oct 2019.

[117] I. Subotic, E. Levi, M. Jones, and D. Graovac, "An integrated battery charger for evs based on an asymmetrical six-phase machine," in *IECON 2013 - 39th Annual Conference of the IEEE Industrial Electronics Society*, Nov 2013, pp. 7244–7249.

[118] I. Subotic, E. Levi, and N. Bodo, "A fast on-board integrated battery charger for evs using an asymmetrical six-phase machine," in *2014 IEEE Vehicle Power and Propulsion Conference (VPPC)*, Oct 2014, pp. 1–6.

[119] S. Sharma, M. Aware, Y. Tatte, J. K. Pandit, and A. Bhowate, "A split three phase induction motor for battery charging application," in *2016 IEEE International Conference on Power Electronics, Drives and Energy Systems (PEDES)*, Dec 2016, pp. 1–6.

[120] J. Prasad, T. Bhavsar, R. Ghosh, and G. Narayanan, "Vector control of three-phase ac/dc front- end converter," in *Sadhana*, 12 2007.

[121] D. N. Zmood, D. G. Holmes, and G. Bode, "Frequency domain analysis of three phase linear current regulators," in *Conference Record of the 1999 IEEE Industry Applications Conference. Thirty-Forth IAS Annual Meeting (Cat. No. 99CH36370)*, vol. 2. IEEE, 1999, pp. 818–825.

[122] D. N. Zmood and D. G. Holmes, "Stationary frame current regulation of pwm inverters with zero steady-state error," *IEEE Transactions on Power Electronics*, vol. 18, no. 3, pp. 814–822, May 2003.

[123] F. Casanellas, "Losses in pwm inverters using igbts," *IEE Proceedings - Electric Power Applications*, vol. 141, no. 5, pp. 235–239, Sep. 1994.

[124] V. V and R. S. Kaarthik, "Parallel operation of ibcs for all wheel drive electric vehicles," in *2022 IEEE International Conference on Power Electronics, Smart Grid, and Renewable Energy (PESGRE)*, 2022, pp. 1–6.

[125] V. Vidya and R. S. Kaarthik, "Parallel operation of integrated battery chargers for all wheel drive electric vehicles," *IEEE Transactions on Transportation Electrification*, vol. 9, no. 2, pp. 3106–3114, 2023.

[126] C.-T. Pan and Y.-H. Liao, "Modeling and coordinate control of circulating currents in parallel three-phase boost rectifiers," *IEEE Transactions on Industrial Electronics*, vol. 54, no. 2, pp. 825–838, 2007.

[127] "https://ackodrive.com/car-guide/awd-vs-4wd/."

[128] M. Terashima, T. Ashikaga, T. Mizuno, K. Natori, N. Fujiwara, and M. Yada, "Novel motors and controllers for high-performance electric vehicle with four

in-wheel motors," *IEEE Transactions on Industrial Electronics*, vol. 44, no. 1, pp. 28–38, 1997.

[129] N. Mutoh and S. Manaka, "Driving performance on low friction coefficient roads which the front-and-rear-wheel-independent-drive-type-electric vehicle (frid ev) has," in *2009 35th Annual Conference of IEEE Industrial Electronics*, 2009, pp. 3791–3796.

[130] N. Mutoh and Y. Takahashi, "Front-and-rear-wheel-independent-drive type electric vehicle (frid ev) with the outstanding driving performance suitable for next-generation adavanced evs," in *2009 IEEE Vehicle Power and Propulsion Conference*, 2009, pp. 1064–1070.

[131] X. Yuan, J. Wang, and K. Colombage, "Torque distribution strategy for a front and rear wheel driven electric vehicle," in *6th IET International Conference on Power Electronics, Machines and Drives (PEMD 2012)*, 2012, pp. 1–6.

[132] "https://www.lexusindia.co.in/content/dam/lexus-v2-in/model-brochures/rx

[133] "https://global.toyota/en/mobility/tnga/powertrain2018/4wd/."

[134] H. Akagi, Y. Kanazawa, and A. Nabae, "Instantaneous reactive power compensators comprising switching devices without energy storage components," *IEEE Transactions on Industry Applications*, vol. IA-20, no. 3, pp. 625–630, 1984.

[135] R. S. and R. S. Kaarthik, "Linearization of over-modulation in dodecagonal space vector pwm," in *2019 IEEE 28th International Symposium on Industrial Electronics (ISIE)*, 2019, pp. 215–220.

List of Publications

Journals

1. V. V and R. S. Kaarthik, "Modeling and Control of an Integrated Battery Charger With Split-Phase Machine," in IEEE Transactions on Industry Applications, vol. 57, no. 2, pp. 1588-1597, March-April 2021, doi: 10.1109/TIA.2020.3047590.

2. V. Vidya and R. S. Kaarthik, "Parallel Operation of Integrated Battery Chargers for All Wheel Drive Electric Vehicles," in IEEE Transactions on Transportation Electrification, vol. 9, no. 2, pp. 3106-3114, June 2023, doi: 10.1109/TTE.2022.3215602.

3. V.Vidya, Balwant Kushwaha, R.S. Kaarthik, "Linearization of Over-modulation Region for 12 and 24-sided Polygonal Space Vector based Inverters with Switched Capacitive Filters," in IEEE Transactions on Industrial Electronics *(under review).*

4. V. Vidya and R. S. Kaarthik, " An 18-sided Voltage Space Vector Modulation scheme for an Open-End Wound Induction Machine using Switched Capacitive Filter," (under preparation)

   Co- authored Journals

5. S. Ranjith, V. Vidya and R. S. Kaarthik, "An Integrated EV Battery Charger With Retrofit Capability," in IEEE Transactions on Transportation Electrification, vol. 6, no. 3, pp. 985-994, Sept. 2020, doi: 10.1109/TTE.2020.2980147.

5.7 International Conference Publications

1. V. Vidya and R. S. Kaarthik, "A Control Scheme for Integrated Battery Charger With Split-Phase Machine," 2020 IEEE International Conference on Power Electronics, Smart Grid and Renewable Energy (PESGRE2020), Cochin, India, 2020, pp. 1-6, doi: 10.1109/PESGRE45664.2020.9070440.

2. V. Vidya and R. S. Kaarthik, "Mathematical Modeling of Split Phase Machine based Integrated Battery Charger," 2019 IEEE Transportation Electrification Conference (ITEC-India), Bengaluru, India, 2019, pp. 1-5, doi: 10.1109/ITEC-India48457 2019 ITECINDIA2019-214.

3. V. Vidya and R. S. Kaarthik, "Parallel Operation of IBCs for All Wheel Drive Electric Vehicles," 2022 IEEE International Conference on Power Electronics, Smart Grid, and Renewable Energy (PESGRE), Trivandrum, India, 2022, pp. 1-6, doi: 10.1109/PESGRE52268.2022.9715867

4. V. Vidya and R. S. Kaarthik, "18 Sided Space Vector Modulation method for Open End Winding Induction Machine Using A Single DC Source", IECON, Singapore, 2023 (accepted).

5. Balwant Kushwaha, V Vidya, R.S. Kaarthik,"Linearization of Over-modulation Region for a Dodecagonal Space Vector Structure with a Single DC Source" ,iTEC India 2023 (accepted).

   Single Phase IBCs

6. P. Yadav, V. Vidya and R. S. Kaarthik, "A Voltage Sensor-less Single-Phase Unity Power Factor AC-DC Front-End Converter," 2019 IEEE Transportation Electrification Conference (ITEC-India), Bengaluru, India, 2019, pp. 1-6, doi: 10.1109/ITEC-India48457 2019 ITECINDIA2019-157.

7. V. Vidya, M. Kumar and R. S. Kaarthik, "Modeling of Single phase IBC with Active Power Decoupling," 2022 IEEE 19th India Council International Conference (INDICON), Kochi, India, 2022, pp. 1-5, doi: 10.1109/INDICON56171.2022.10039839.

Appendix A
Specifications of the Hardware Setup

For implementing the experimental prototype of IBC using split-phase machine, discussed in chapter. 2, a 11 kW, 415 V, 4-pole, three-phase induction motor rewound as split-phase machine was utilized. A three-phase inverter using 75 A, 1200 V IGBT half bridge modules (SKM75GB12T4) were used to work as front-end converter. The gate driver M57962L is used for driving the IGBT modules. LA55P current sensors were used to sense the three-phase grid currents. A level shifter circuit is used to bridge the domain between the sensor and the digital signal processor.

For implementing the experimental prototype for the parallel combination of IBCs, two 11 kW, 415 V, 4-pole, three-phase induction motors rewound as split-phase machine were utilized along with two, three-phase inverters. The control part is implemented using TMS320F28377S digital signal processor.

For implementing the 12, 18 and 24-sided space vector modulation scheme, a 3.7 kW, three-phase 4 pole, induction motor with neutral disconnected was used as an open end winding motor. Spartan-6 Field Programmable Gate Array was used along with TMS320F28377S DSP to generate the gate pulses for both the inverters.

A. 1 Level Shifter and Filter

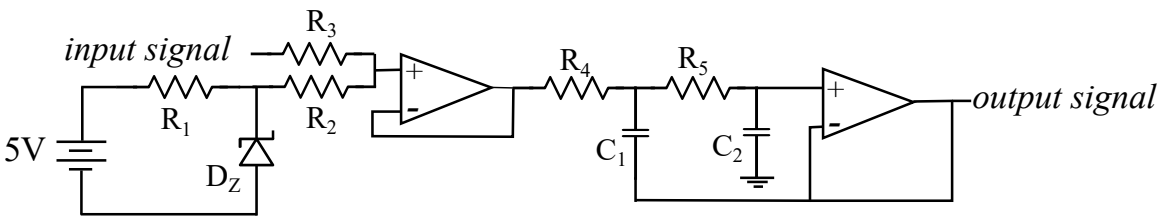

Fig. 5.1. Circuit diagram of the level shifter and Sallenkey filter

Level shifter shifts the bipolar input signal($\pm$ 3V) to unipolar signals of the range (0 to 3 V) which can be given as input to the digital signal processor after passing through a sallenkey filter with cut-off frequency of 5 kHz.

Table 5.1. Level shifter and Filter components

Op-amp	LM341
Zener diode (BZX3V3)	3.3 V, 500 mW
R_1	680Ω
R_2, R_3	12 kΩ
R_4, R_5	10 kΩ
C_1	20 nF
C_2	10 nF

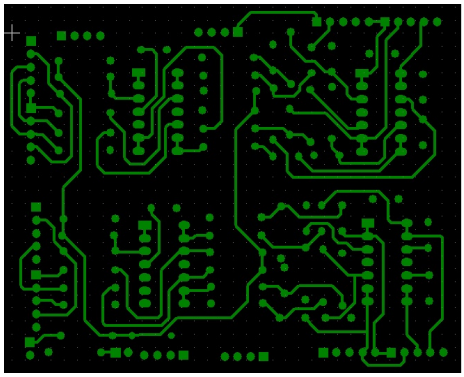

Fig. 5.2. PCB design: Top copper layer of the level shifter

A. 2 TMS320F28377S-Digital Signal Processor

The Digital Signal Processor used for implementing the digital control in the experimental set up was Texas Instruments, 32- bit TMS320F28377S microcontroller. The main features of the board are listed below.

1. 100-pin PowerPAD Thermally Enhanced Thin Quad Flatpack (HTQFP) [PZP suffix].
2. + 5 V supply voltage
3. 200 MHz CPU, with IEEE 754 single precision floating point unit, Trigonometric math unit and Complex math unit.

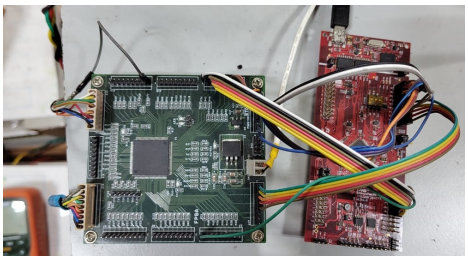

(a) DSP, TMS320F28377S and Spartan-6 FPGA

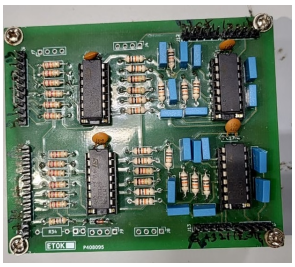

(b) Level shifter circuit with filter

Fig. 5.3. Digital Control and signal processing components

4. 1.2 V core and 3.3 V, input /output design (Unipolar signals).
5. Up to 41 individually programmable, multiplexed General-Purpose Input/Output (GPIO) pins with input filtering.
6. 16-bit flash memory of 1 MB and 16-bit SRAM of 164 kB.
7. ADC 16-bit mode, 14 inputs with 7 channels , or ADC 12-bit mode, 14 inputs with 14 channels.
8. 3 12-bit buffered DAC.
9. 10 Enhanced Pulse Width Modulator (ePWM) channels.
10. 2 eQEP modules.
11. 3 Serial communication interfaces.

Fig. 5.3b shows the digital control components, namely the DSP TMSF28377S and Spartan-6 FPGA.

A. 3 Field Programmable Gate Array

1. Digital Clock Manager (DCM) blocks provides delay, multiply, divide and phase shifting options for clocking signals.
2. Configurable Logic Blocks (CLBs) contain RAM-based Look-Up Tables (LUTs) to implement logic and storage elements that can be used as flip-flops or latches.
3. Block RAMs are fundamentally 18 Kb in size.

Table 5.2. FPGA Spartan-6 XC6SLX4-2TQG144C Attributes

System Pins	144
Equivalent Logic Cells	3840
Total Combinational Logic Blocks (CLB)	600
Dedicated Multipliers	12
Digital Clock Managers (DCM)	4
Maximum User I/O	97

4. Multiplier blocks accept two 18-bit binary numbers as inputs and calculate the product.

A. 4 Split-phase Induction Machine Parameters

Table 5.3. Split-phase induction machine parameters

Rating	11 kW, 415 V, 4-pole
Stator self inductance L_{ss}	80.13 mH
Stator leakage inductance $\sigma_{12}L_{ss}$	1.05 mH
Mutual inductance between stator and rotor windings L_{sr}	76.8 mH
Rotor leakage inductance L_{lr}	2.28 mH
Stator resistance R_s	1.05 Ω
Rotor resistance R_r	1.97 Ω

A. 5 Two-Level voltage source inverter specification

Semicron IGBT modules, SKM75IGB12T4, $V_{CES} = 1200\ V$, $I_{cnom} = 75\ A$.
Gate driver : M57962L
DC link capacitor : $2200\mu F$, 600 V : 2 in series.

A. 6 Current and voltage sensors

LA 55-P LEM : Current transducer ($I_{PN} = 50\ A$).
LV 20-P-LEM : Voltage transducer ($I_{PN} = 10\ mA, V_{PN} = 10$ to $500\ V$).

A. 7 Code for calculating grid angle θ using PLL

The three-phase grid voltages are converted to synchronously rotating reference frame components, V_d and V_q. Grid frequency is calculated for the condition that V_{dref} is zero.

```
e=vdref-vd;
    esum=esum+(ki*e/fs);
    if(esum>wlim)
        esum=wlim;
    ei=esum+(kp*e);
   wsum=wsum+(ei);
    if(wsum>6.28)
  {wsum=wsum-6.28;}
    theta=wsum;
```

A. 7 Code for switch-over from linear to over-modulation region-1 to over-modulation region-2 in DSP

The DSP code for switchover of switching times from linear region to over-modulation regions for 24-sided SVM scheme is listed below. The decision is based on the value of the modulation index. The time duration for switching each vector in a sector, that is $T1, T2,$ and $T0$ are calculated initially.

```
if(m<=0.994)
{
T1_act=T1[sample];
T2_act=T2[sample];
T0_act=TIMER_TBPRD-(T1_act+T2_act);
}
else if (m>0.994 && m<0.997)
{    T1_act = D1[sample]*TIMER_TBPRD;
     T2_act = D2[sample]*TIMER_TBPRD;
     T0_act = 0;
}
else
```

```
{if(T1[sample]<T2[sample])
    {           T1_act = 0;
                T2_act = TIMER_TBPRD;
                T0_act = 0;
    }
    else
    {           T1_act = TIMER_TBPRD;
                T2_act = 0;
                T0_act = 0;
    }
}
```

A. 8 Dead Time - Implemented with FPGA

The dead-time generation to avoid shoot through of the complementary switches in one leg is also done by the FPGA. The logic is to provide a small time delay of the order of 2.50s for the turn-on pulses of each power device and zero time delay for the turn-off pulses. This can be easily achieved by including an up-counter in the gate signal path inside the FPGA, for the required time delay when rising gate pulse arrives (assuming logic level ?1? for ON state).

```
library IEEE;
use IEEE.STD_LOGIC_1164.ALL;
use IEEE.STD_LOGIC_ARITH.ALL;
use IEEE.STD_LOGIC_UNSIGNED.ALL;
entity deadtime is
port(clk,rst:in std_logic; y:out std_logic);
end deadtime;

architecture Behavioral of deadtime is
signal temp: std_logic_vector(7 downto 0):=(others => '0');
signal sig_1: std_logic;
signal sig_2: std_logic;
signal sig_3: std_logic;
signal rst_dt: std_logic;
```

```
begin
-- code for removing gliches
process(clk)
        begin
        if(clk' event and clk='1') then
        sig_1 <= rst;
        sig_2 <= sig_1;
        sig_3 <= sig_2;
        end if;
end process;
rst_dt <= (sig_1 or sig_2 or sig_3);

process(rst_dt,clk,temp)
        begin
                if(rst_dt='0') then temp<=(others=>'0');
                elsif (clk'event and clk='1') then
                        if(temp<="10000000") then
                        temp<=temp+1;
            else
            temp<=temp;
                        end if;
         else temp<=temp;
                end if;
        end process;
        y<=temp(7);
end Behavioral;
```